A PARALLEL MODELLING APPROACH TO RESERVOIR CHARACTERIZATION

A DISSERTATION
SUBMITTED TO THE DEPARTMENT OF PETROLEUM ENGINEERING
AND THE COMMITTEE ON GRADUATE STUDIES
OF STANFORD UNIVERSITY
IN PARTIAL FULFILLMENT OF THE REQUIREMENTS
FOR THE DEGREE OF
DOCTOR OF PHILOSOPHY

Ömer Inanç Türeyen
March 2005

I certify that I have read this dissertation and that, in my opinion, it is fully adequate in scope and quality as a dissertation for the degree of Doctor of Philosophy.

Dr. Jef K. Caers Principal Advisor

I certify that I have read this dissertation and that, in my opinion, it is fully adequate in scope and quality as a dissertation for the degree of Doctor of Philosophy.

Dr. Andre G. Journel

I certify that I have read this dissertation and that, in my opinion, it is fully adequate in scope and quality as a dissertation for the degree of Doctor of Philosophy.

Dr. Louis J. Durlofsky

Approved for the University Committee on Graduate Studies.

Abstract

With the advance of CPU power, numerical models have become an essential part of most engineering applications, especially for modeling subsurface formations. These models in many cases are used for predicting future performance, hence these models must be conditioned to all available data sets as much as possible. This makes data integration an important step in generating such models.

The challenge in data integration lies in the fact that, each data has its own resolution and averaging process. Usually high resolution data have a small area of coverage, while on the other hand, data with a high area of coverage has low resolution. With most current approaches data are integrated independently at their respective scales. High resolution models are used for integrating small scale data while large scale data are integrated on corresponding upscaled models. The drawback of such independent process is that once the scale is changed, the model may no longer honor the data at the lost scale.

In this thesis we propose a general algorithm as a solution to the scaling problem presented above. Instead of proceeding in a series fashion, we propose to construct the model jointly at multiple scales and work with all scales through out the entire data integration process in parallel. This is accomplished by introducing upscaling in the data integration process. As a result all data are honored at their respective scales.

We have introduced a fast optimization step when changing the model resolution. The speed is obtained by using streamline flow simulation. This multiple scales concept was applied to the problem of history matching, where we keep a geostatistical high resolution model and a coarsened flow simulation model in parallel. The perturbations are performed on the high resolution model while the full flow simulations are performed on the coarsened models. Fast flow simulation using streamlines are used to perform gridding optimization while ensuring that both high resolution and coarsened models match the history.

Acknowledgements

I would like to take this opportunity to express my gratitude to the people who have provided endless support throughout my Ph.D. journey. I feel very lucky to have them around me.

I feel very happy to have had Prof. Jef Caers guide me through my Ph.D. study. I am truly grateful for his support and patience. It has been a pleasure working with you Jef. I will do my best to carry on the *structure* and fundamentals that you have taught me.

I would like to thank Prof. Andre Journel for his support and the wonderful discussions that we had. I am very happy to have worked with him at this point in my life.

I would like to thank Prof. Lou Durlofsky for taking time to review my thesis and providing many ideas which I have used in this thesis. He has provided me with a different perspective for looking at things in my Ph.D. work.

I would like to thank my defense committee members Prof. Tony Kovscek and Prof. Atilla Aydin for their time.

Many thanks to the faculty and staff of the Petroleum Engineering department at Stanford University for their help.

Also I would like to thank all my friends from the Petroleum Engineering department. Especially Todd Hoffman for sharing his experience regarding the real field case study, Burc Arpat for the wonderful discussions that we had and for being a great roommate, Yildiray Cinar, Baris Guyaguler, Joe Voelker, Burak Yeten, Deniz Cakici, Umut Ozdogan, Banu Alkaya and last but not least Ozgur Karacali for providing me with lots of help and fun.

Finally I would like to express my endless gratitude to my family for their endless support and love. My dad who has devoted his life to making his children happy, my mom who has provided me with the best care that I could possibly get, my sister for bringing joy

to my life and finally my wife, who has been a part of my Ph.D. journey, for her endless love and support.

Contents

List of Tables

List of Figures

Chapter 1

Introduction and Motivation

1.1 Subjectivity in Reservoir Modelling

With increasing CPU power, numerical models have become an essential part of many engineering applications. One main goal of such models is to make future performance predictions of a physical phenomenon, such as tracking the saturation front of a contaminant in subsurface formations, prediction of tectonic movements for earthquakes, water production from an oil reservoir, type of airflow around an airplane wing, etc.

In petroleum applications, numerical reservoir models are often constructed with a specific end goal in mind. Priority is then given to data relevant to that end goal. For example, if the determination of original oil in place is considered, then emphasis is given to data that provide information regarding the volume, structure, porosity and the initial saturation of the reservoir. Fine tuning permeability values or their anisotropy ratios at this point are of lesser consequence.

In order to construct a numerical reservoir model that accurately predicts future performance of the reservoir, the model must be conditioned to all available relevant data. However, rarely is there enough data to fully constrain the reservoir model. The incompleteness of information forces the modeler to interpret beyond data. Such interpretations are subject to a great deal of uncertainty.

Figure-1.1a illustrates the challenge of constructing a porosity model based on the five porosity measurements. Figure-1.1b shows a model, built from an off-the-shelf interpolation for determining porosity values at unsampled locations, resulting in an unrealistically

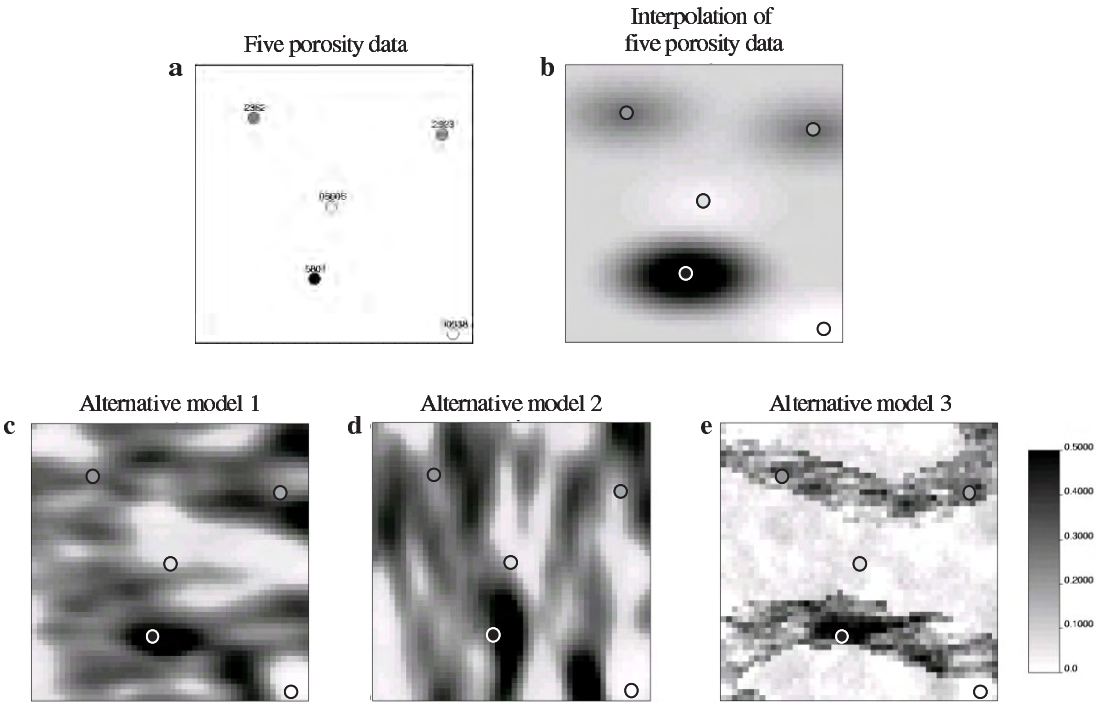

Figure 1.1: (a) Five porosity measurements, (b) Interpolation of the five porosity data, (c,d,e) Alternative models with different spatial relationships (from Caers (2005)).

smooth representation of the porosity. Figures 1.1c, 1.1d and 1.1e provide various alternative models generated from different geostatistical simulation algorithms. Although all models honor the five porosity measurements, they are quite different from each other, each relying on a different interpretation of the underlying geological continuity. Hence a major source of uncertainty lies in the type of geological continuity assumed, in other words, in establishing the link between the measurements and the unsampled locations. A model of geological continuity often needs to be borrowed from sources other than reservoir data, such as outcrops and more generally the geologist' expertise.

1.2 Reservoir Data

When constructing reservoir models, each piece of information has its own characteristic scale at which it provides information. No single source of information determines the reservoir uniquely. Many sources of data are available for constructing reservoir models.

The main challenge in reservoir modelling is to bring such multi-scale data simultaneously into a single numerical model accounting for their difference in scale, their level of accuracy and their redundancy.

Many sources of data are available for reservoir modelling. They may be grouped as follows:

1. **Geological data :** Any data related to the style of geological deposition:
    - Core data : porosity, permeability and relative permeability measurements
    - Well-log data : Any suite of logs that indicate lithology, petro-physics and fluid types near the well-bore
    - Sedimentological and stratigraphic interpretation
    - Outcrop analog data
2. **Geophysical data :** Any data originating from seismic surveys:
    - Surfaces and faults interpreted on 3D seismic
    - Seismic attributes
    - Rock physics data
    - Time lapse 4D seismic data
3. **Reservoir engineering data :** Any data related to testing and production of the reservoir:
    - PVT data
    - Well test data
    - Production data

Figure-1.2 illustrates the most common sources of data along with their scale of information and the resolution of models for comparison. Core data has the smallest scale of information, followed by well-log data. Although core and well-log data provide direct measurements on reservoir petrophysical properties, their scale of information is much

smaller than the resolution of the grid on which we model the reservoir, i.e. the ”3D geo-cellular model” in Figure-1.2. In most cases a scale-up of well-log/core data onto the 3D high resolution geo-cellular model is implicitly assumed although rarely done. This constitutes the ”missing scale” and related problems, Tran (1995). The missing scale may be important in cases where the fine scale heterogeneity has a significant impact on flow.

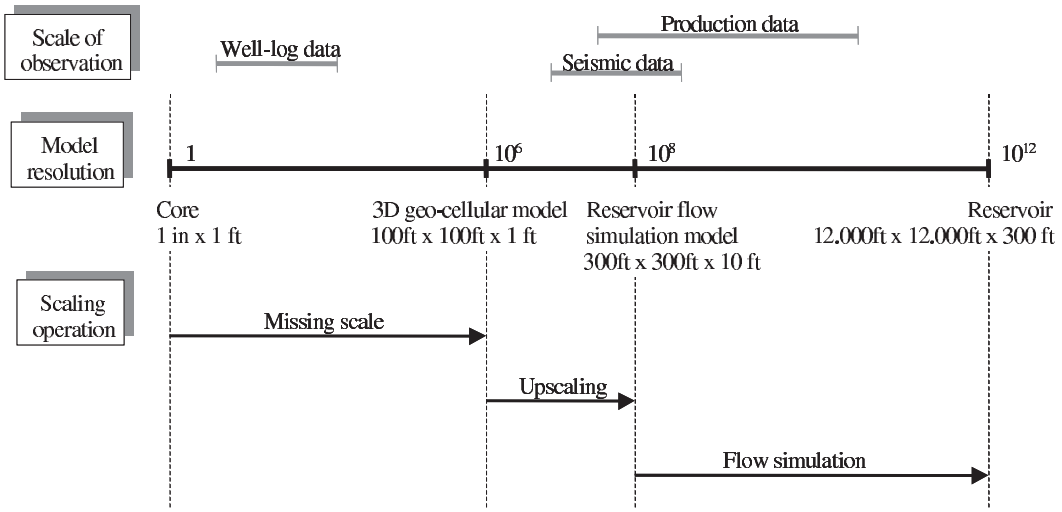

Figure 1.2: Comparison of the scale of observation, model resolution and scaling operation (from Caers (2005)).

1.3 The Reservoir Modelling Workflow

In this section we present the current practice for building a numerical reservoir model. The workflow is given in Figures-1.3 and 1.4. This workflow proceeds with three major frameworks; (1) *the structural and reservoir framework*, (2) *the depositional and geostatistical framework* and (3) *the reservoir flow simulation framework*. Within the structural and reservoir framework, the general architecture of the reservoir is determined. This is the stage at which large scale structures are determined. The depositional and geostatistical framework addresses the facies distribution and petrophysical information. The reservoir flow simulation framework deals with production and PVT data.

The workflow of frameworks (1) and (2) can be summarized as follows:

1. This step calls for determining the top, bottom and style of each layer (if there are

any) and the determination the location of fault blocks. Seismic data is used for this purpose. Well markers are used as ”hard data” to locally constrain surfaces.

2. The next step is to build a 3D stratigraphic grid that is aligned with the surfaces and the faults. These grids are usually corner point geometry and are refined where necessary (such as around the faults).

3. The above steps are typically conducted in the actual reservoir (depositional) coordinates system. The third step calls for mapping this reservoir coordinates system to a depositional coordinate system which is Cartesian. All data, well paths and seismic are mapped onto this Cartesian box.

4. On the Cartesian box, first the facies geometry is simulated. Some of the most common techniques for populating the facies information are: geostatistical indicator simulation (Deutsch and Journel, 1992; Goovaerts, 1997), Boolean techniques (Haldorsen and Damsleth, 1990) and more recently geostatistical simulation using multiple-point geostatistics (Strebelle, 2002; Arpat, 2004; Zhang and Strebelle, 2004). Models or parameters for the facies geometry (such as variogram, training image, or Boolean shape parameters) may be borrowed from outcrop data.

5. At this stage petrophysical properties (such as porosity and permeability) are populated within each facies. This may be performed using standard geostatistical algorithms such as the sequential Gaussian simulation technique (Deutsch and Journel, 1992), which are appropriate for modelling ”homogeneously heterogeneous” permeability and porosity within a layer or within each facies type.

6. Once the petrophysical properties are simulated, they are mapped back into the reservoir coordinates system. A 3D high resolution model is obtained.

The workflow given in Figure-1.3 enables the integration of static data from geological and geophysical sources, see Section-1.2. However, this workflow ignores any dynamic data. The integration of dynamic data, termed ”history matching”, requires an iterative, trial and error process involving multiple runs of numerical flow simulations. The high resolution model (conditioned to seismic and hard data), would be CPU prohibitive for such flow simulations. An upscaling procedure to coarsen the high resolution model is

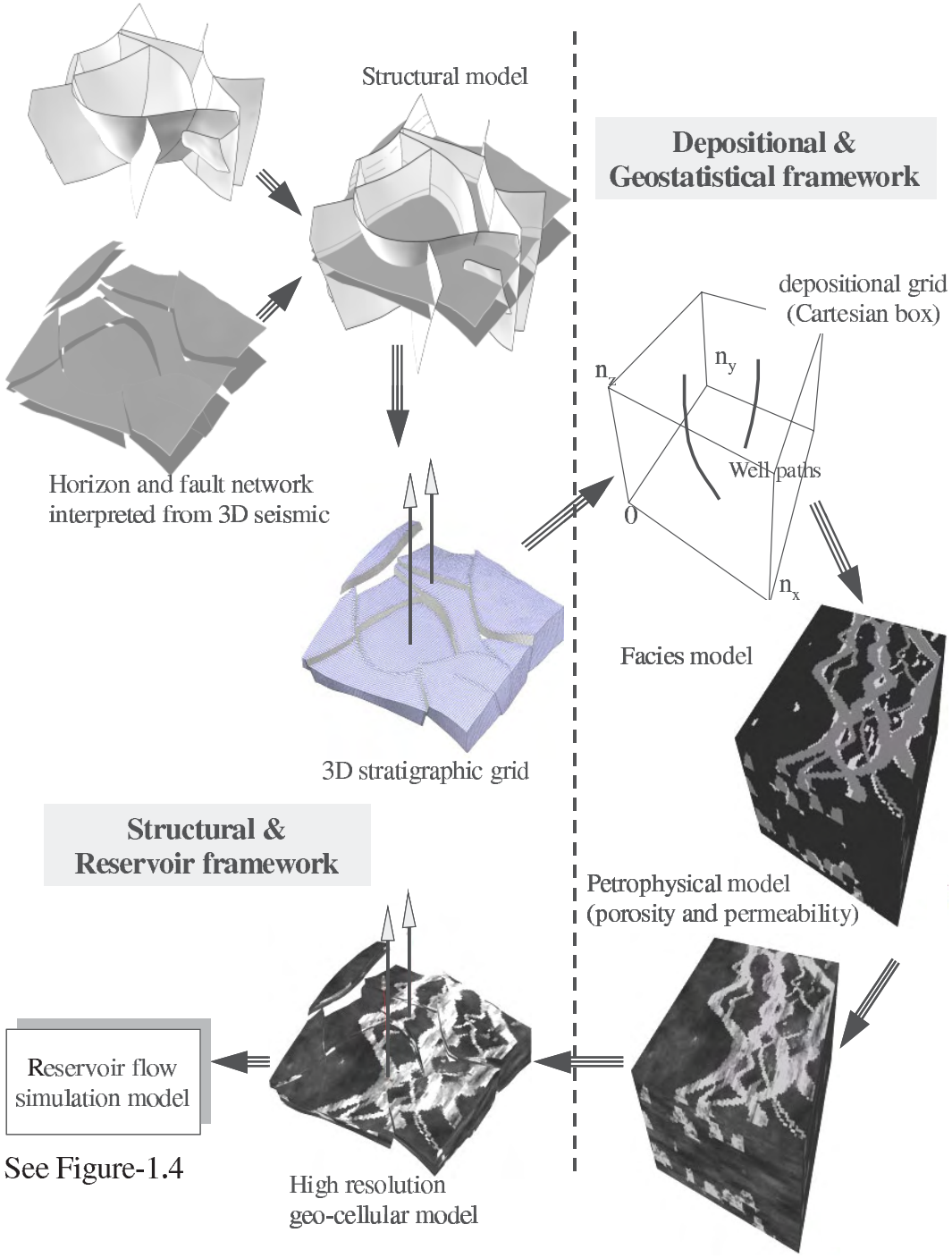

Figure 1.3: Reservoir modelling workflow (from Caers (2005)).

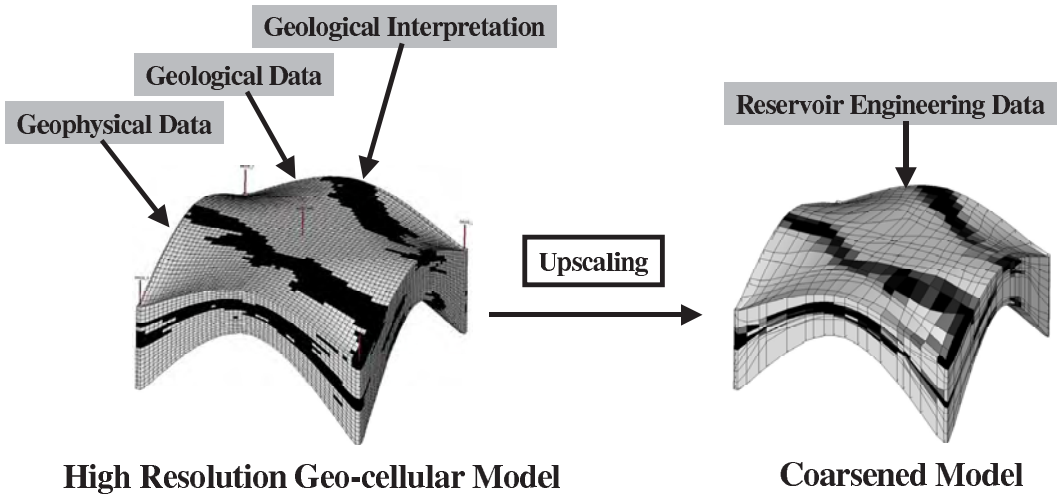

Figure 1.4: Integration of the reservoir dynamic data (The reservoir flow simulation framework).

necessary for making flow simulations feasible. Figure-1.4 represents this procedure. A high resolution model is upscaled to a coarsened model. In the current practice of reservoir modelling it is this coarsened model that is history matched, which involves perturbing the coarsened reservoir properties.

In summary, the current practice of reservoir modelling consists of first building the model using static data (Figure-1.3) then dynamic (Figure-1.4). Using this workflow, important fine scale information may be destroyed while history matching, particularly if the history matching method does not take respect statistics such as variograms or multiple-point statistics. Most history matching techniques arbitrarily change permeability near wells or between wells with little or no regard to the prior model of geological continuity.

A history match can be achieved, but often at the cost of destruction of any prior seismic data conditioning or geological realism. This may lead to poor predictivity of the resulting history matched reservoir models. Preserving geological continuity while history matching has traditionally received little attention, because history match has become a goal on its own, divorced from its original intent, namely prediction of future performance.

Production data should be considered as another piece of information that needs to be integrated ”jointly” with other sources of data. To illustrate the importance of joint integration of static and dynamic data, consider the following synthetic example.

The 2D reservoir given in Figure-1.5a has an injector located at the bottom left corner

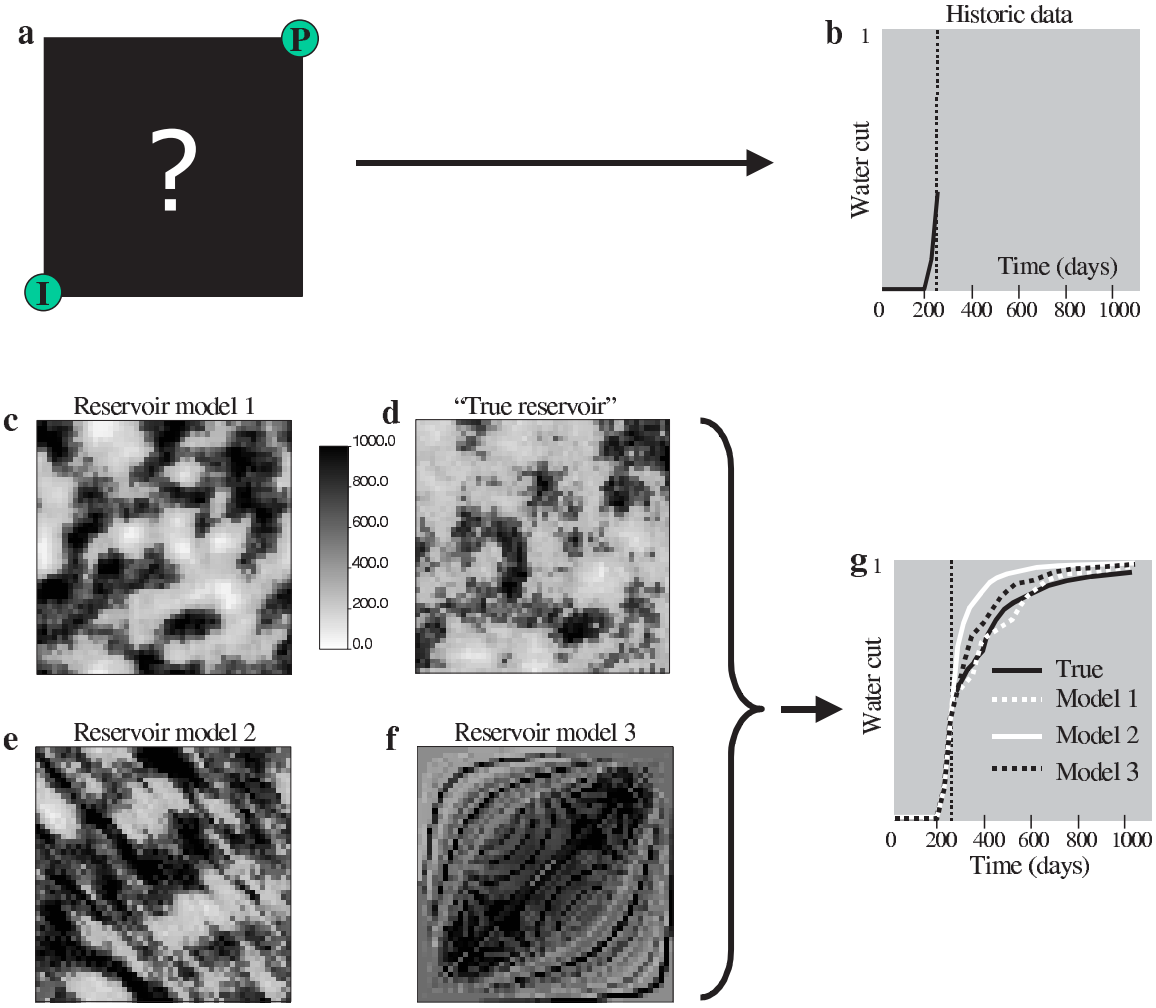

Figure 1.5: Synthetic example showing the non uniqueness of the history matching process. (a) Representation of the true but unknown permeability field, (b) The flow data to be matched, (c) Reservoir model history matched with correct geological interpretation, (d) True permeability field, (e) Reservoir model matched with wrong geological interpretation, (f) Reservoir model matched without any geological interpretation, (g) The flow responses of the various models (from Caers (2005))

.

and a producer located at the top right corner. Water injection is performed on this (initially fully oil saturated) quarter five spot pattern. The resulting water cut curve (for 250 days) is given in Figure-1.5b representing the production data to be matched. Constant porosity is assumed for the model; the goal is to infer the permeability through history matching.

Figures 1.5c, 1.5e and 1.5f give three reservoir models that have been history matched. Figure-1.5g, shows that they all match equally well the history until 250 days yet these permeability fields are very different one from each other. Even in the case of a wrong geological interpretation (Figure-1.5e) or even no geological interpretation (Figure-1.5f) it is still possible to obtain a history match. The difference between these models would appear in the prediction stage. The history matched model that uses the correct geological interpretation would predict the future flow performance best.

The following conclusion can be drawn from this example. History matching is a *non-unique* problem. In realistic cases, history matching alone is not enough to infer the model properties correctly, since multiple models can match the history equally well yet are radically different from each other. The only way to overcome this problem would be to incorporate all available data jointly.

Integrating the dynamic data independently from the other sources of data as done in Figure-1.4 can lead to the problems described above. The end result of the workflow given in Figure-1.3 is a model conditioned to well data and seismic data. However, in order to integrate the production data that model is coarsened first, then perturbed. If this perturbation is done independently, in other words, without taking into account the original well and seismic data, the model might be perturbed to a degree that it would not match any longer the well data and the seismic data.

1.3.1 Some solutions

The shortcoming in the workflow of building the reservoir model first static, then dynamic (in an independent fashion) has been recognized by several authors (amongst which the paper by Tran *et al.* (1999) is pioneering). One solution calls for reintroducing data conditioning from sources such as 3D seismic, well-log/core data and geological interpretation after the history matching phase, through a procedure known as ”downscaling”.

Tran *et al.* (1999) propose the following model building procedure which is termed ”History matching using a downscaling step”:

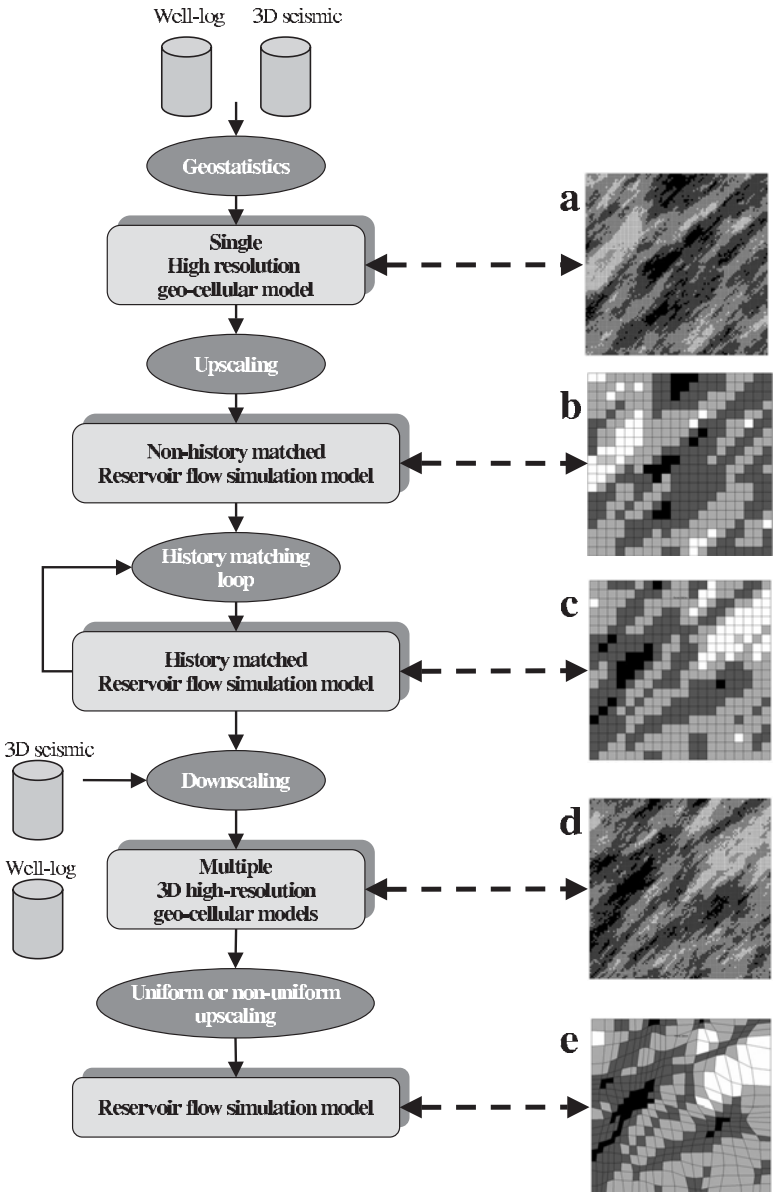

Figure 1.6: The alternative approach shown on a synthetic example. (a) The fine scale model conditioned to 3D seismic and well-log/core data. This can be interpreted as the end result of the traditional workflow given in Figure-1.3, (b) upscaled model not matched to the production data, (c) history matched upscaled model (d) downscaled model, (e) non-uniformly upscaled model.

1. A high resolution (geo-cellular) model is generated conditioned to the 3D seismic and well-log/core data (shown in Figure-1.6a). This high resolution model is obtained as an end result of the workflow given in Figure-1.3.

2. The high resolution model is upscaled to a coarsened model where multiple flow simulations are feasible. This coarsened model does not match history, Figure-1.6b.

3. A history matching algorithm is applied to that coarsened model, Figure-1.6c. Any type of history matching method can be applied. Tran *et al.* (1999) specifically use the self-sequential calibration method that accounts to some degree, for the variogram of the coarse block permeability.

4. The history matched coarsened model (given in Figure-1.6c) is then downscaled to a high resolution model. In this downscaling one accounts for seismic and well-log/core information, as well as any prior geological continuity model, e.g. a variogram, given in Figure-1.6d.

5. Finally the high resolution model is coarsened (possibly to a non-uniform grid) once more to make flow simulations and performance predictions feasible.

There are two drawbacks to this approach:

- Perturbation is applied only to the coarsened model. That coarsened model may not contain any fine scale heterogeneity that could impact flow. Hence, if flow is affected by such features, a history match with predictive properties might not be achieved.

- After the history matching phase, the coarsened models are downscaled for reconditioning to the static data. Hence fine scale heterogeneity is reintroduced. If such fine scale features do impact flow, the downscaling can destroy the history match. Moreover; downscaling is a non-unique problem; multiple downscaled realizations may be obtained from one single coarse model. Hence downscaling may introduce errors / variability in future performance prediction.

In order to demonstrate the non-uniqueness of the downscaling approach, we consider the following synthetic example, where the study field is a cross-section of a reservoir with an injector on the left (injecting water at a constant pressure) and a producer on the

right (producing at constant pressure), as illustrated in Figure-1.7a. The response of the reference permeability is treated as observed field data (given in Figure-1.7b). The task is to generate coarsened realizations that match the reference flow curve. Then the effects of downscaling of the coarsened models on the flow responses will be studied.

Figure-1.8a illustrates the flow responses for three coarsened realizations in addition to the flow response of the reference true field for comparison. The coarsened models are non-uniformly gridded and have dimensions of $5 \times 1 \times 5$. As shown in Figure-1.8a these coarsened models have been history matched until 500 days.

To study the effects of downscaling on the flow responses, the three models are downscaled to a higher resolution of $50 \times 1 \times 50$. The coarsened models and their downscaled versions are given in Figure-1.9.

Flow simulations are performed on these downscaled models and the results are given in Figure-1.8b. The responses are altered significantly when compared with the coarsened responses. The downscaled models do not match the history any longer. A detailed study on the variability of flow responses introduced by downscaling may be found in Ying (2001).

Another alternative to downscaling is to directly work on coarsened unstructured grids. Recent research in geostatistics has shown that simulation of permeability can be performed directly on unstructured grids, without the need for an intermediate Cartesian grid. Deutsch *et al.* (2002) and Manchuk *et al.* (2004) use a direct sequential simulation approach in combination with block kriging for this purpose. Despite the several geostatistical challenges that still linger to do this practically, the major drawback of such an approach is that the grids remain fixed throughout the entire modelling phase. This would present problems for history matching, since during the history matching permeability is perturbed iteratively. A fixed grid whether uniform, structured or unstructured, would not be able to adapt to changes in the fine scale heterogeneities.

Yoon *et al.* (2001) considers a ”multiscale” approach for history matching. The approach starts with a coarsened model which is recursively refined as it is history matched. A coarsened model is first generated and a gradient based inversion is performed to match history as much as possible. Next the model is refined using downscaling, and the inversion is performed again on this refined model. The history match is improved iteratively at each higher resolution. The refinement is performed until a sufficient match is obtained.

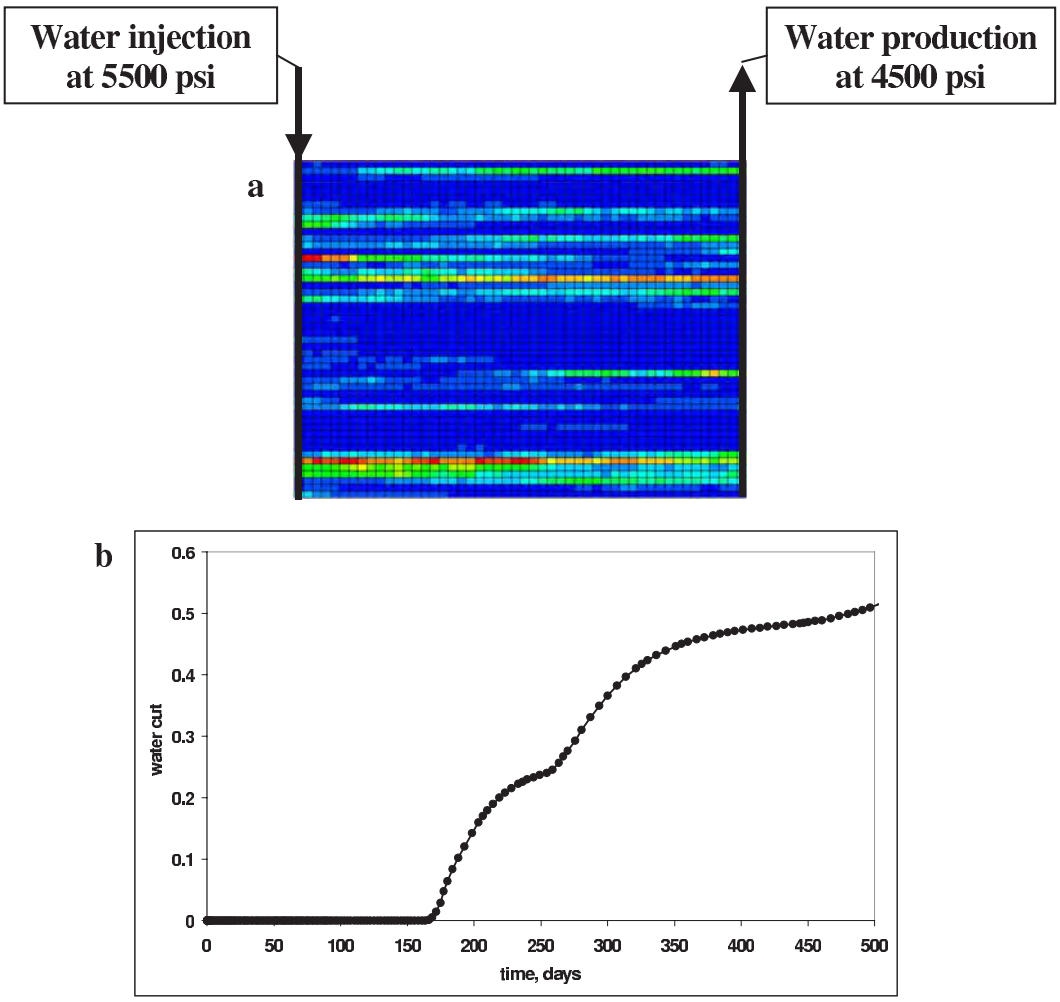

Figure 1.7: (a) The reference permeability field, (b) The flow response of the reference permeability field until 500 days.

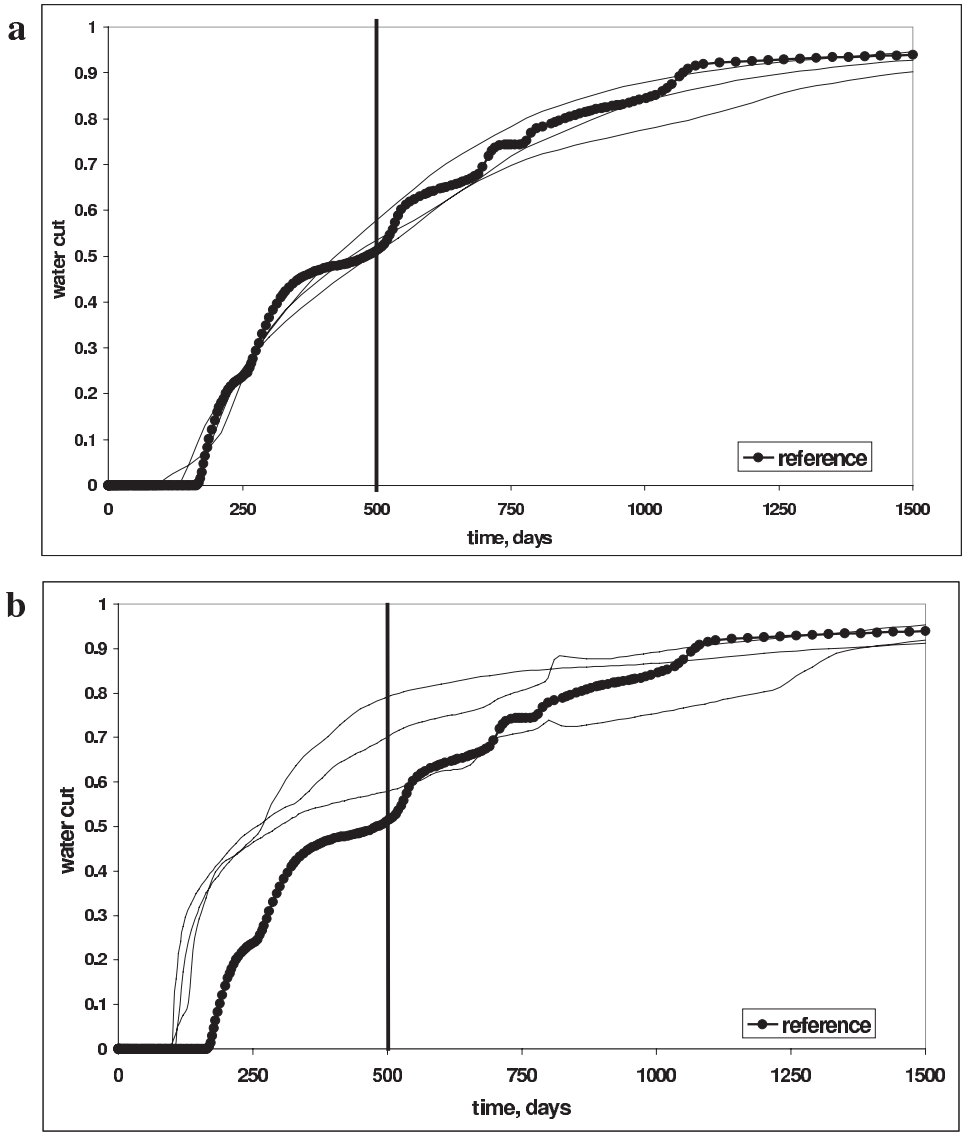

Figure 1.8: (a) The flow responses of three $5 \times 1 \times 5$ coarsened realizations (b) the flow responses of three downscaled $50 \times 1 \times 50$ realizations.

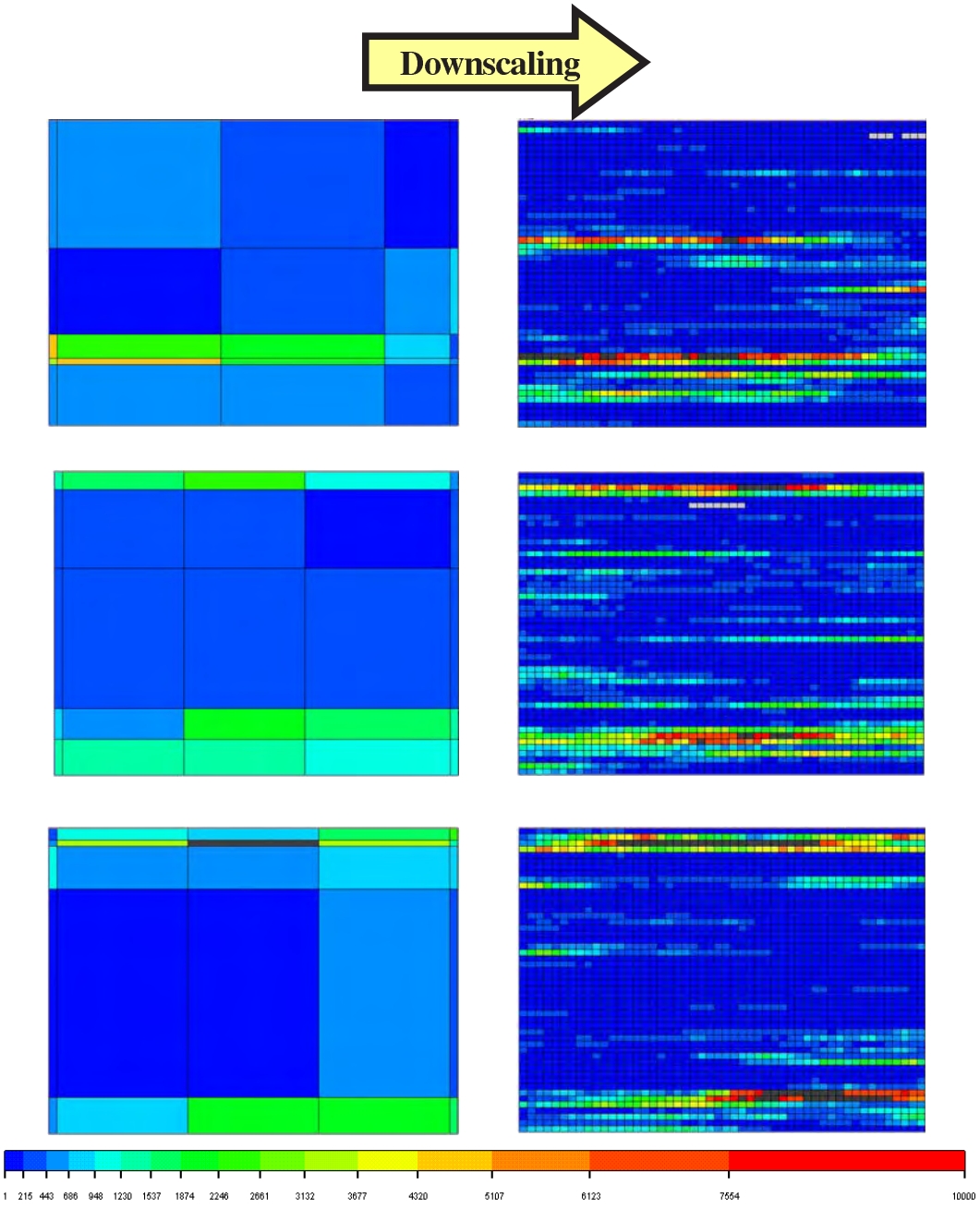

Figure 1.9: Three history matched models and their downscaled high resolution counterparts.

This way, the resolution of the production data is accounted for explicitly, i.e. the resolution of the final grid is an indication of the scale at which the production data inform the reservoir heterogeneity. Even though the inversion is not performed at the highest resolution possible, it is performed multiple times at intermediate resolutions. This could be CPU demanding to obtain a history match. Another drawback of this approach is the way hard data conditioning is handled. Once a model is history matched through an inversion process, ”downscaling” is performed to honor the hard data. The high resolution model is populated by performing conditional sequential simulation with block kriging for conditioning to both the coarsened model block averages (in order to preserve the history) and the hard data. However, the authors point out that the downscaling procedure may introduce a misfit in the match of the production data, similar to the method proposed by Tran *et al.* (1999).

Lø døen *et al.* (2004) approaches the problem of reservoir modelling by quantifying the errors introduced in the upscaling procedure. The upscaling errors are modeled through a calibration procedure where flow simulations are performed several times on pairs of high resolution model and the corresponding coarsened model. Within a history matching context, one can history match the coarsened models and determine the uncertainty in the future predictions of the flow response. Then, the previously calibrated upscaling errors are used to predict the uncertainty of the flow responses of high resolution models. However, such a method requires the flow simulations to be evaluated on multiple high resolution models. In many cases even one single such evaluation might be CPU prohibitive. For highly complex geological systems, with many wells, such modelling of upscaling errors may not be feasible, hence the quantification of uncertainty may not be achieved. Most importantly, this method only targets quantification of the upscaling errors. No attempt is made for reducing these upscaling errors.

In the approach given by Mezghani and Roggero (2001) and later by Schaaf *et al.* (2002), upscaling is made a part of the history matching process. At each perturbation of the high resolution model, upscaling is performed to a predetermined grid configuration (either uniform or non-uniform). Next flow simulations are evaluated on the coarsened model. The approach has similar flavor to some of the methods proposed in this thesis. However, during the upscaling procedure the coarsened model grid remains fixed. This may be limiting for capturing fine scale heterogeneities that might have a considerable

impact on the flow response.

1.4 Structure of the thesis

This thesis proposes a new approach for integrating multi-scale data. The method consists of working on multiple resolutions of models at the same time, therefore avoiding the problem of inconsistent sequences of upscaling or downscaling.

The details of the approach are given in Chapter-2 through a generic workflow. The advantages of using such a workflow are discussed. Various applications are presented using different history matching techniques, different upscaling / upgridding schemes and different types of geological continuity models in 2D and 3D.

Chapter-3 provides an improved workflow based on the concept of ”gridding optimization”. The synthetic examples given in chapter-2 are revisited with this improved workflow. Differences and improvements on the results are discussed.

Chapter-4 presents the application of the proposed parallel modelling methodology to a North Sea Reservoir. The challenge in this case is to model the locations of calcite bodies that have a significant impact on the flow. The application will be given for a portion of the full field.

Finally chapter-5 presents the conclusions obtained from this thesis work. Limitations are discussed followed by suggestions for future work.

Chapter 2

The Parallel Modelling Methodology

2.1 Motivation

The introduction chapter presented the main motivation for the work presented in this thesis. The need for integrating various scales of data into a single numerical model was made clear. Multiple resolutions, from high resolution to coarsened models should be used. But maintaining conditioning to all data (static and dynamic) at all resolutions presents a challenge, since any change made at any given resolution may potentially destroy data conditioning enforced at a different resolution.

The main problem with current practice is that the construction of the high resolution geocellular model is done separately from the history matching performed on the coarsened model. The coarsened model is perturbed using only the production data, and the high resolution model is generated taking into account only static data. In this thesis the problem is attacked from a different perspective. Instead of working on different resolutions of models independently or hierarchically at best, it is proposed to build both high resolution and coarsened models jointly, in parallel. This implies that any perturbation applied to a single resolution of model is reflected onto the other resolution. In the parallel modelling approach all model perturbations (to achieve history matching) are performed on the high resolution geocellular model, and are immediately reflected on the coarsened model. In the parallel modelling approach, flow simulations are still performed on the coarsened model, yet their results are used to perturb the high resolution model. The two resolutions of models are kept in parallel throughout the entire characterization process: A

high resolution model where geostatistics is performed effectively and a coarsened model where flow simulations are performed.

In this chapter, we first introduce the notation used throughout the thesis. Then the parallel modelling workflow is presented in great detail. Finally various synthetic examples are given on which the parallel modelling workflow is applied.

2.2 The Parallel Modelling Methodology

2.2.1 Notations

The following notation is used.

$\mathbf{z}$	$\{z(\mathbf{u}), \forall\, \mathbf{u} \in$ Model$\}$ the set of high resolution model properties at grid blocks $\mathbf{u}$=(x,y,z)
$\mathbf{z}(\mathbf{r})$	A perturbation of the high resolution geocellular model $\mathbf{z}$. The magnitude of perturbation is parameterized using parameters $\mathbf{r}$.
$\mathbf{z}^{up}$	The uniquely determined upscaled model, upscaled from $\mathbf{z}$
$FSM(\mathbf{z})$	A transfer function evaluated on $\mathbf{z}$
$\mathbf{RP}(\mathbf{z})$	The response vector when *FSM* is performed on $\mathbf{z}$.
$S_\theta(\mathbf{z})$	The upscaling method S applied to the high resolution model $\mathbf{z}$. The upscaling method may contain a vector of tuning parameters θ
$\mathbf{D}$	Any type of historical response data to be matched.

2.2.2 The workflow

The workflow for the parallel modelling methodology is given in Figure-2.1. The workflow proceeds as follows:

1. The first step in the workflow is the generation of a high resolution model, $\mathbf{z}$, conditioned to all available static data, such as the one generated as a result of the workflow given in Figure-1.3. The perturbations on $\mathbf{z}$ are parameterized through a set of parameters $\mathbf{r}$ that change the high resolution model $\mathbf{z}$ into a perturbed model $\mathbf{z}(\mathbf{r})$. $\mathbf{r}$ can be a single parameter such as in, the gradual deformation method (Roggero and

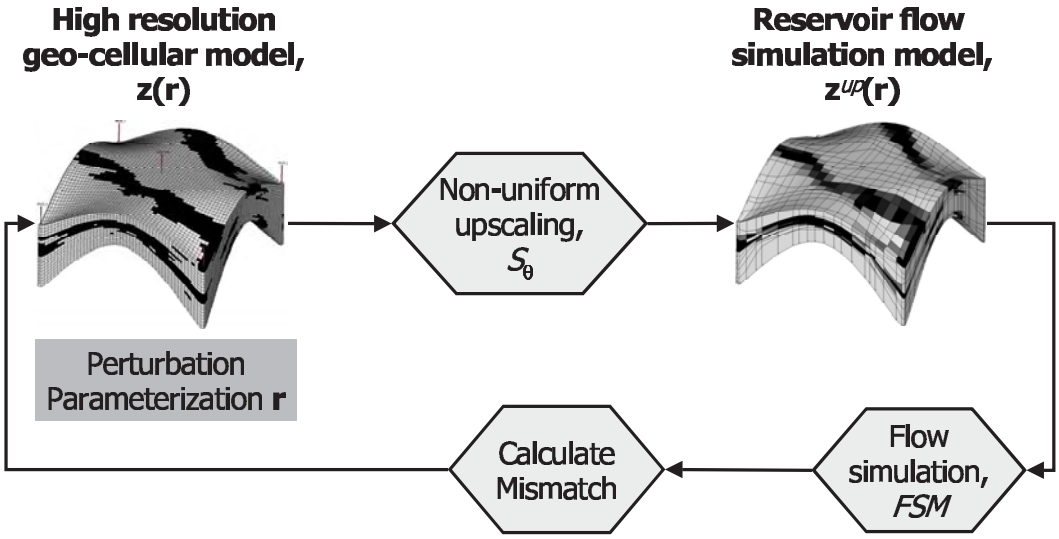

Figure 2.1: Illustration of the basic parallel modelling workflow.

Hu, 1998; Ying and Gomez, 2000), gradual deformation of sequential simulation (Hu *et al.*, 2001; Caers, 2002), the probability perturbation method (Caers, 2003), **r** may be a vector of parameters, as for example in the regional probability perturbation method (Hoffman and Caers, 2003), or **r** may be a parametrization using sensitivity coefficients (Landa and Horne, 1997; Wen *et al.*, 1998). Appendix A provides more details regarding the perturbation / deformation algorithms used in this study. It is important to note that any proposed perturbation is performed on the high resolution model, not the coarsened model.

2. The high resolution model, $\mathbf{z}(\mathbf{r})$ is coarsened to a flow simulation model, $\mathbf{z}^{up}(\mathbf{r})$ through the relation:

$$\mathbf{z}^{up}(\mathbf{r}) = S_\theta(\mathbf{z}(\mathbf{r})) \tag{2.1}$$

S represents the specific coarsening algorithm applied on $\mathbf{z}(\mathbf{r})$ and θ represents the upgridding parameters defining this algorithm S. At this point both S and θ remain fixed throughout the entire characterization process. This constraint will be relaxed in the next chapter. Both S and θ are general and allow the consideration of any upscaling technique such as single phase techniques (Tran, 1995), iterative techniques with

near-well upscaling (Chen *et al.*, 2004), etc. The choice of the upgridding method is also generic, hence dynamic methods (Durlofsky *et al.*, 1997), static methods (Garcia *et al.*, 1992), structured gridding (He, 2004) and unstructured gridding (Prevost, 2003) may be used. The details of the upscaling and upgridding methods used in this study are given in appendices-B and C.

3. Once the coarsened model, $\mathbf{z}^{up}(\mathbf{r})$, is obtained, full flow simulation (*FSM*) is performed and the response is defined by the following relation:

$$\mathbf{RP}_{\mathbf{z}^{up}} = FSM(\mathbf{z}^{up}(\mathbf{r})) \tag{2.2}$$

4. The mismatch between the calculated flow response, $\mathbf{RP}_{\mathbf{z}^{up}}(\mathbf{r})$ and the observed field data is calculated as:

$$O(\mathbf{r}) = |\mathbf{RP}_{\mathbf{z}^{up}}(\mathbf{r}) - \mathbf{D}| \tag{2.3}$$

5. Once the objective function $O(\mathbf{r})$ is calculated, perturbations, obtained by modifying the $\mathbf{r}$ parameters, are applied to the high resolution model. The above steps are repeated until Equation-2.3 is minimized.

Note that the two different resolution models are kept in parallel throughout the entire process. Both the high resolution model and the coarsened simulation model are updated simultaneously during the history matching. The high resolution model is perturbed based on the flow responses of the coarsened simulation model.

2.2.3 Advantages of the parallel modelling methodology

The advantages of the proposed parallel modelling methodology are:

- Fine scale data and coarse scale data are integrated at the same time each at their appropriate resolutions. The well-log/core and the seismic data are introduced via the high resolution model and the production data via the coarsened model. The high resolution models are perturbed such that the mismatch between the flow response of the coarsened model and the observed field data is minimized.

- Relevant geological heterogeneity is maintained at all steps and all scales. Important geological features of the high resolution model can be preserved on the coarsened model through an effective upscaling/upgridding method. Since upscaling / upgridding is performed each time a perturbation is made, the coarsened non-uniform grid is consistent with the fine scale heterogeneities. This allows accounting for the impact of fine scale structures during the history matching process. With the traditional downscaling approach when perturbations are made to the ”coarsened” model, fine scale heterogeneities are not accounted for since the grid was originally built from a different high resolution model.

- The coarsened model is perturbed only as a consequence of the perturbation on the high resolution model. No direct perturbation, possibly geologically inconsistent, is allowed on the coarsened model.

- In ”history matching using downscaling” the grid of the coarsened model is fixed during history matching. Hence the grid cannot adopt itself to the property being perturbed. With the parallel modelling approach, the gridding changes during the entire process. This is a result of the fact that upscaling/upgridding is performed at every step. Hence, the coarsened model is always gridded in a way to account for the distribution of the property being perturbed.

2.3 Examples

In this section we provide applications of the parallel modelling approach on various synthetic examples. The aim is to mainly test if the parallel modelling workflow is successful for different types of geological models, different history matching techniques and different upscaling / upgridding methods. First a Gaussian-type layered case is presented. The gradual deformation, Roggero and Hu (1998); Ying and Gomez (2000) (see Section-A.2 for details), is used as the history matching technique. Flow-based upscaling and upgridding is performed during the coarsening step (see Sections B.1.2 and B.2 respectively for details). The geostatistical simulation is performed by using SGSIM (Deutsch and Journel, 1992). In the second case study another Gaussian field is presented. This case study has different variogram properties and applies a different history matching method, namely gradual

deformation of sequential simulations (see Section-A.3 for details), Hu *et al.* (2001). In the third case study, history matching of a facies model is presented. Unlike the first two examples, where variograms were used as the geological continuity model, geostatistics is performed through a training image based algorithm, SNESIM (Strebelle, 2002). In the fourth case study, we look at a channelized example where the task is to history match the locations of channels using the parallel modelling approach. The history matching method for this problem is the probability perturbation method, Caers (2003) (see Section-A.4 for details). The final case study considers a 3D channel reservoir. This diversity of applications is intended to showcase the generality of the parallel modelling approach.

All examples in this section are synthetic. In other words, first a ”reference” reservoir model is generated and is assumed unknown afterwards for checking the results. The parallel modelling workflow is used to make future flow predictions of the reference model using the data collected, both hard well data and historical production data.

The historical production data considered in all the examples provided in this chapter are the water cut curves. In reality, historical production data is composed of many other components, such as pressure, fluid rates, gas oil ratios, etc. History matching these components is not considered in this thesis. However, note that the parallel modelling workflow is capable of handling such data. Furthermore, in all cases presented in this thesis, we consider the water flooding problem. Primary production is not considered.

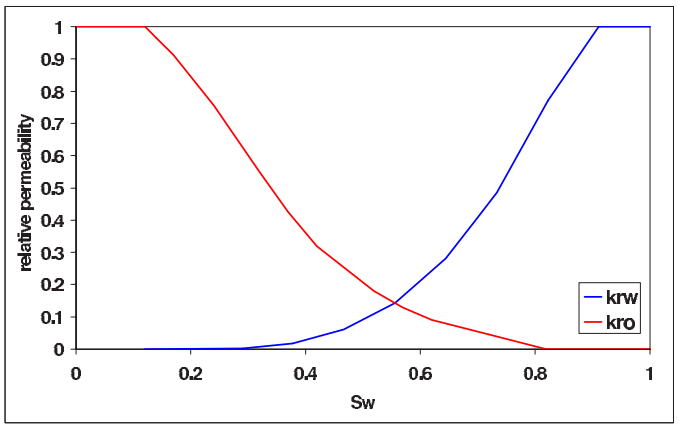

Figure 2.2: The relative permeability curves used in the examples.

The relative permeability curves used in the following examples are given in Figure-2.2. The viscosity of water is 1 and the viscosity of oil is 1.18.

Table 2.1: Summary of the 2D layered example

Geological continuity model	Variogram
Horizontal variogram range	30 blocks
Vertical variogram range	1 block
Geostatistical algorithm	SGSIM
History matching method	Gradual deformation
Reference field grid dimensions	$50 \times 1 \times 50$
Δx, Δz	20ft, 5ft
Porosity	0.2
$\mathbf{k}_{vertical}/\mathbf{k}_{horizontal}$	0.3
Mobility ratio	1
Injection pressure	5500 psi
Production pressure	4500 psi
Simulation Period	500 days
Upscaling	Single phase upscaling
Upgridding	Flow based upgridding

2.3.1 2D layered example

In this case study we perform the parallel modelling approach on a 2D, layered, Gaussian field. A summary of the properties of this model are given in Table-2.1. First a $50 \times 1 \times 50$ Gaussian (permeability) variable is generated by performing an unconditional sequential Gaussian simulation with variogram ranges equal to 30 blocks horizontally and 1 block vertically. The resulting field which has a standard normal distribution is then transformed to a log-normal permeability distribution through a rank preserving transform (Deutsch and Journel, 1992) with a log-mean of 4md and a log-variance of 1.

Each grid block is 20 ft in the horizontal and 5 ft in the vertical direction. An injector well is placed on the left side of the field and a producer well is placed on the right. Water injection is performed at a constant injection pressure of 5500 psi using the commercial flow simulator ECLIPSE (GeoQuest, 2001). Production is maintained at a constant pressure of 4500 psi. Figure-2.3 gives the reference permeability field. Permeability values are collected along the two wells at every five grid blocks, to be used as hard conditioning data during the parallel modelling workflow.

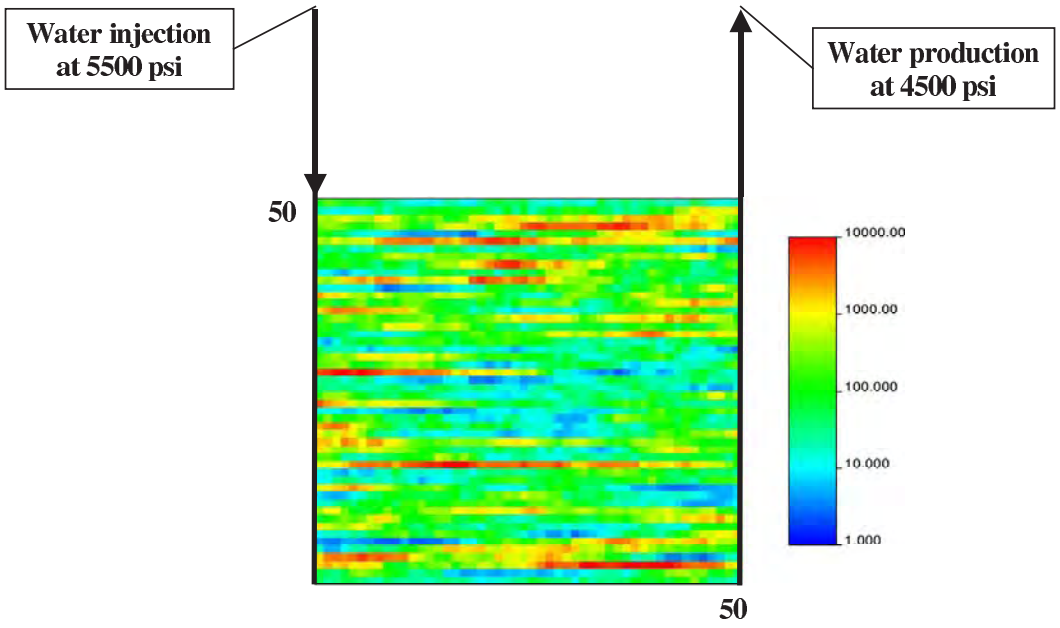

Figure 2.3: The reference permeability and the injection/production scenario.

Flow simulation is performed for 500 days and the reference water cut curve is given in Figure-2.4. The water breakthrough at the producer occurs at around 300 days. The objective of this case study is to generate realizations conditioned to both the hard data and the water cut curve.

Figure-2.5 represents the parallel workflow specifics for this example. The reference permeability field and its corresponding coarsened model are used in the workflow for illustrative purposes. The workflow starts by constructing a high resolution model ($50 \times 1 \times 50$), conditioned to the hard data collected along the wells using SGSIM. The variogram parameters (horizontal range and vertical ranges) and the constant porosity are assumed to be known and are taken as the values that have been used in generating the reference permeability field. The next step is to upgrid the model using the method of Durlofsky *et al.* (1997) (see Appendix-B.2 for details). Four parameters control the gridding, n_x^{max}, n_z^{max}, u_x^{max} and u_z^{max}. The n^{max} parameter determines the maximum number of high resolution grids that are grouped into a single coarse grid. The $u_x^{max}$and u_z^{max} parameters determine the number of high resolution grids that are grouped into a coarsened grid based on average velocity information of the rows and columns of the high resolution permeability field. If the cumulative average velocities of a certain number of rows or columns exceed the u^{max}

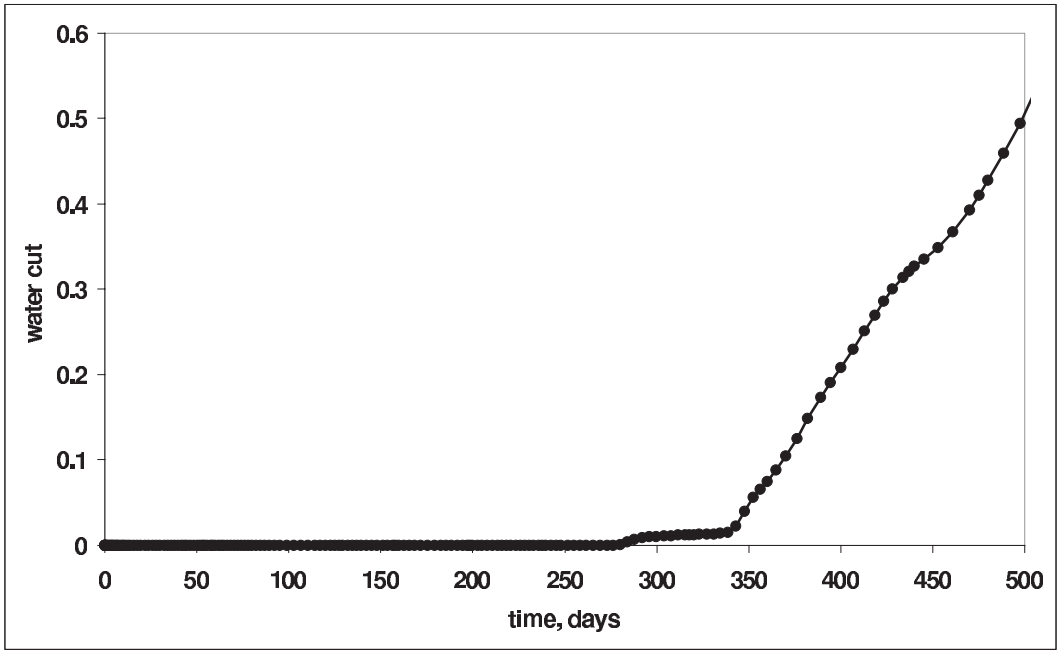

Figure 2.4: The flow response of the reference permeability field.

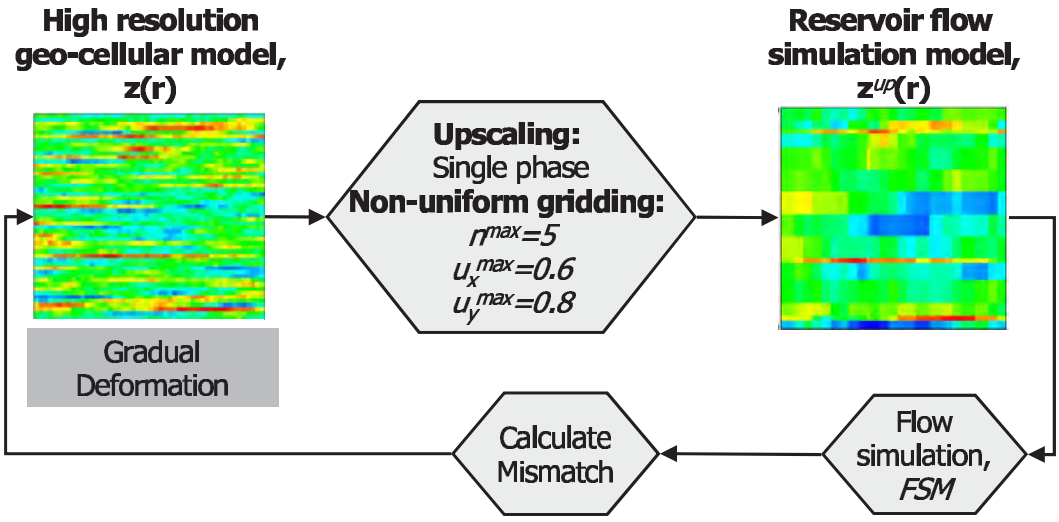

Figure 2.5: The parallel workflow specific to the example.

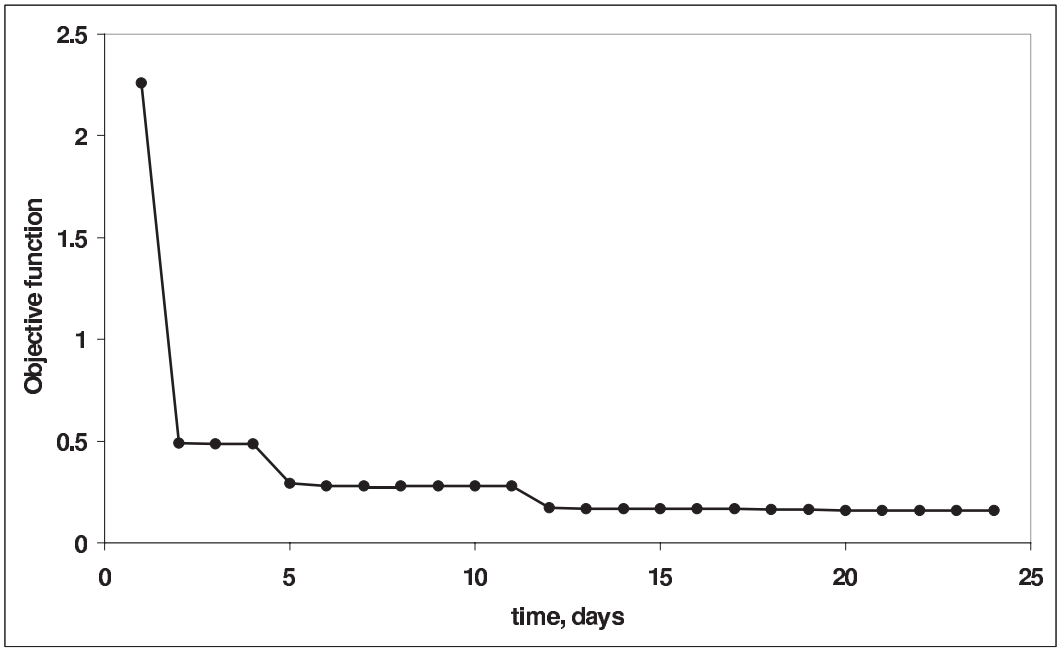

Figure 2.6: The progression of the objective function.

parameter, then they are grouped into a single coarsened grid. Hence, the high velocity rows (or columns) are refined on the coarsened models.

The gridding parameters are taken as $n_x^{max} = n_z^{max} = 5$, $u_x^{max} = 0.6$ and $u_z^{max} = 0.8$. These parameters were chosen to visually preserve the high resolution features when the model is coarsened, leaving high permeability regions refined on the coarsened model using a relatively low number of grid blocks in the coarsened model (see Figure-2.5). Once the coarsened model grid is constructed, the permeability values of the high resolution model are upscaled using a single phase upscaling technique adopted from Deutsch (1985); Tran (1995) (see Appendix-B.1.2 for details).

After the coarsened model is obtained, using the ECLIPSE software (GeoQuest, 2001), flow simulation is performed on the coarsened model using the previous injection/production scheme; this results in the water cut curve for the initial realization. These reference and calculated water cut curves are compared and the mismatch is calculated. If the mismatch is above a predetermined threshold value, the high resolution model is perturbed with a gradual deformation method adapted from Ying and Gomez (2000) (see Appendix-A.2 for details). The above steps are repeated until the mismatch is minimized.

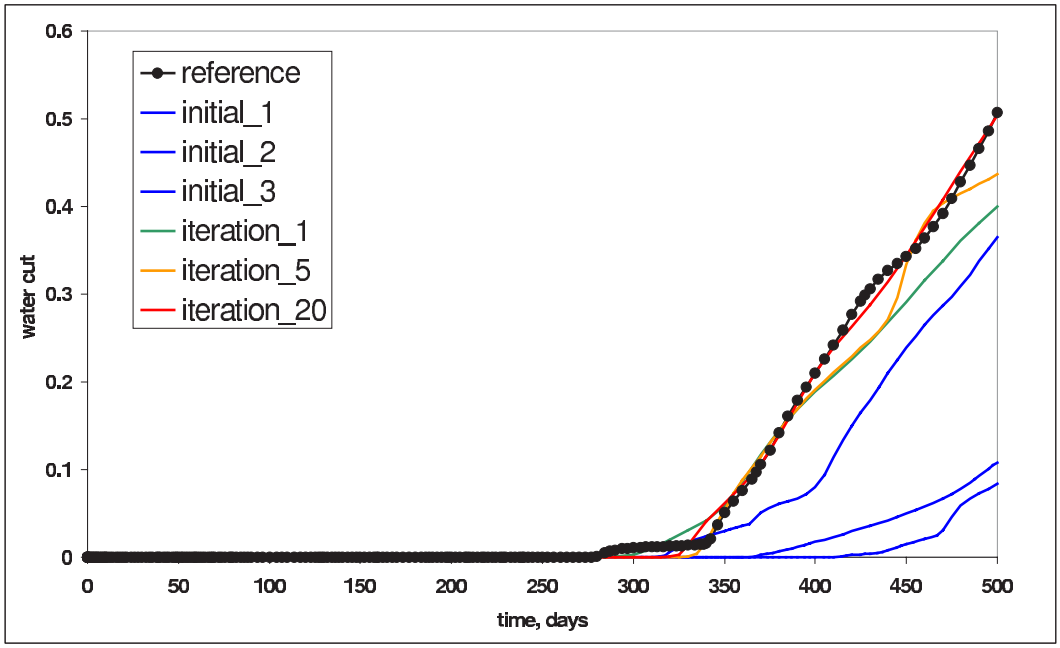

Figure 2.7: The progression of the water cut curve.

Figure-2.6 illustrates the progression of the objective function, $O(r)$ defined in Equation-2.3. The objective function reaches a plateau after 12 iterations. A satisfactory history match is obtained at around 5 iterations. It is important to note that the objective function decreases significantly during the first couple of iterations, this is a typical behavior of the gradual deformation algorithm. Figure-2.7 illustrates how the water cut curves converge to the reference flow response. The blue curves are the water cut curves of the very first three realizations combined through the gradual deformation method. At iteration 5 the water cut curve is already similar to the reference water cut curve. At iteration 20 (red curve in Figure-2.7) a history match is obtained.

Figure-2.8 illustrates the progression of the permeability field during the parallel modelling workflow, both for the high resolution model and the corresponding coarsened model. Snapshots were taken at the end of iterations 1, 5 and 20. At each iteration, the gridding of the coarsened models changes as the high resolution models are perturbed, adapting to the fine scale heterogeneities. At the end of the first, the fifth and the twentieth iterations, the coarsened models have grid dimensions of $13 \times 1 \times 19$, $30 \times 1 \times 23$ and $17 \times 1 \times 21$ respectively.

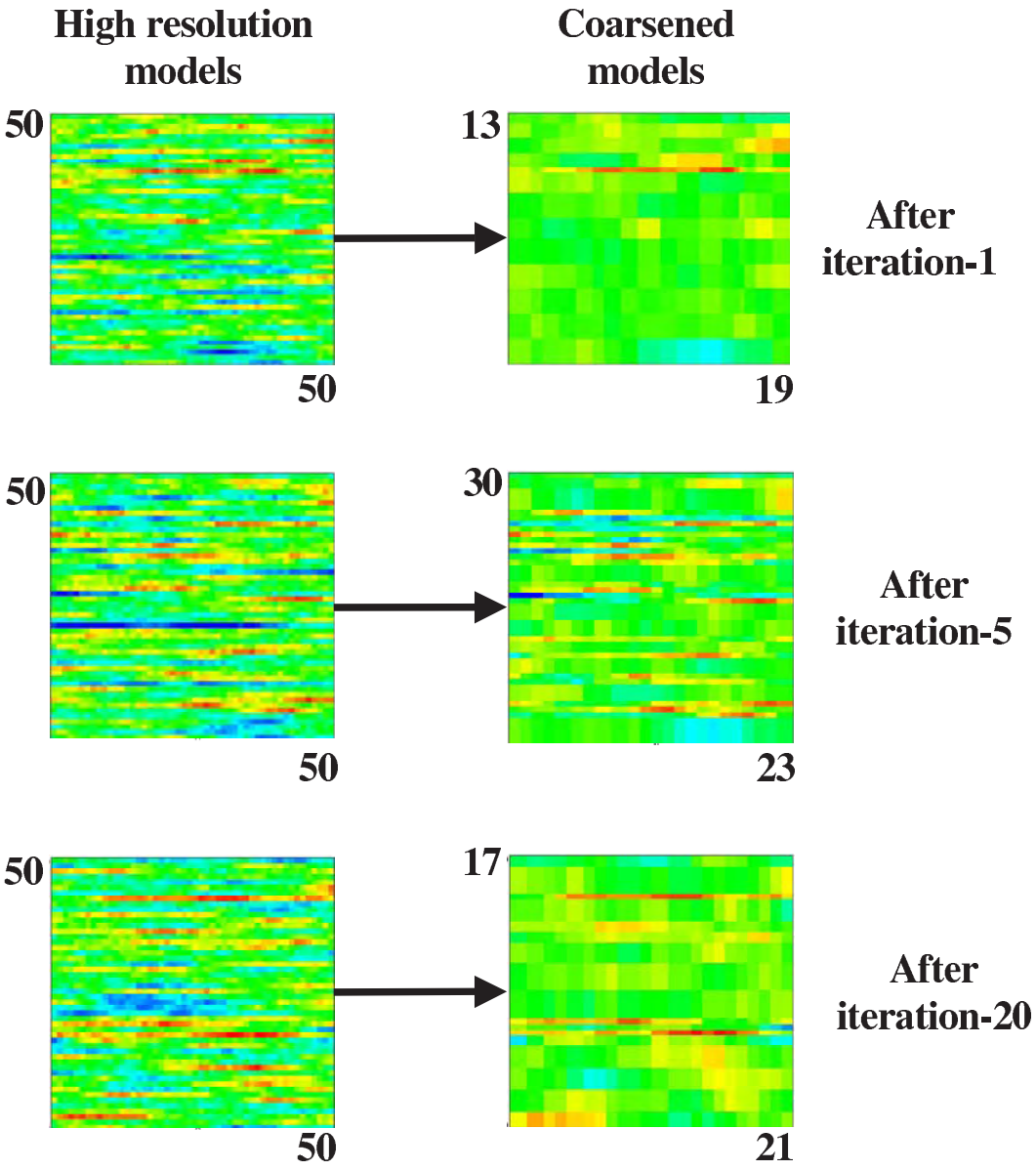

Figure 2.8: The progression of the permeability field.

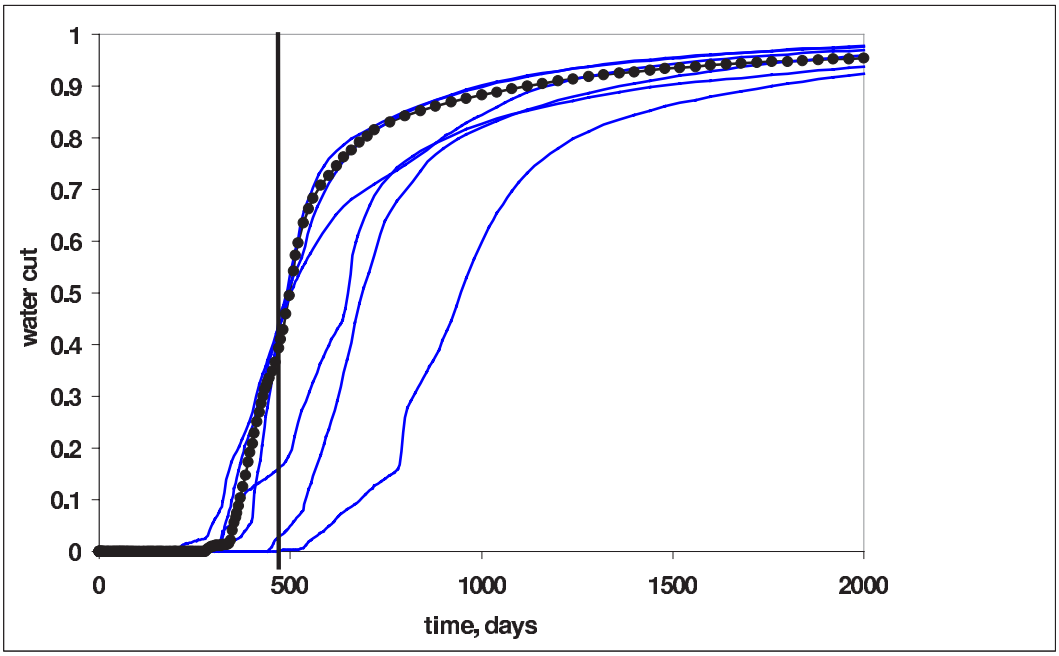

Figure 2.9: Flow responses of 9 realizations conditioned only to hard data.

Consider now the contribution of the historical production data on the uncertainty of the future flow performance predictions. Figure-2.9 gives the flow responses of 6 high resolution realizations conditioned only to hard data. The injection/production period is taken as 2000 days. As apparent in Figure-2.9, a wide scatter is observed especially with regard to the breakthrough times. As expected, the responses are very different from the reference water cut curve, since history matching has not been performed.

Figure-2.10 illustrates the flow responses of the 6 coarsened realizations conditioned to both hard data and the historical production data. Until 500 days, the reference curve and the responses of the 6 realizations are in very good agreement. Uncertainty with regard to the future predictions has also been reduced considerably (compare with Figure-2.9 until 2000 days). Figure-2.11 shows some of the end results of the parallel modelling workflow. Two end results are obtained; a high resolution model and a coarsened model which represents the fine scale heterogeneity through non-uniform gridding. The coarsened models are gridded differently and have different grid dimensions.

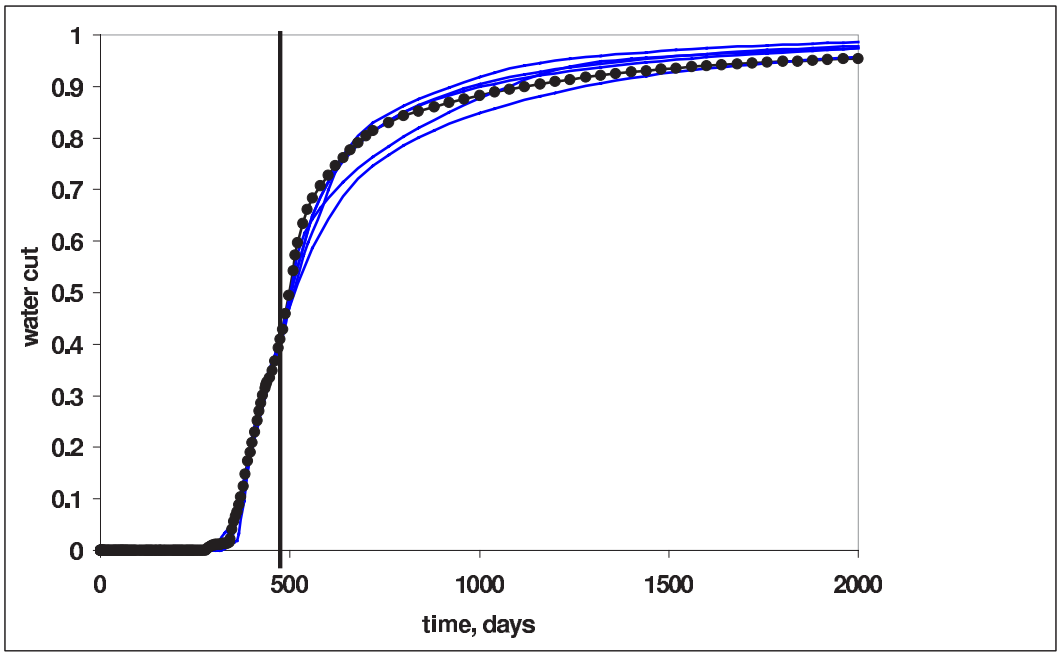

Figure 2.10: Flow responses of 5 realizations conditioned to both hard data and the historical production data.

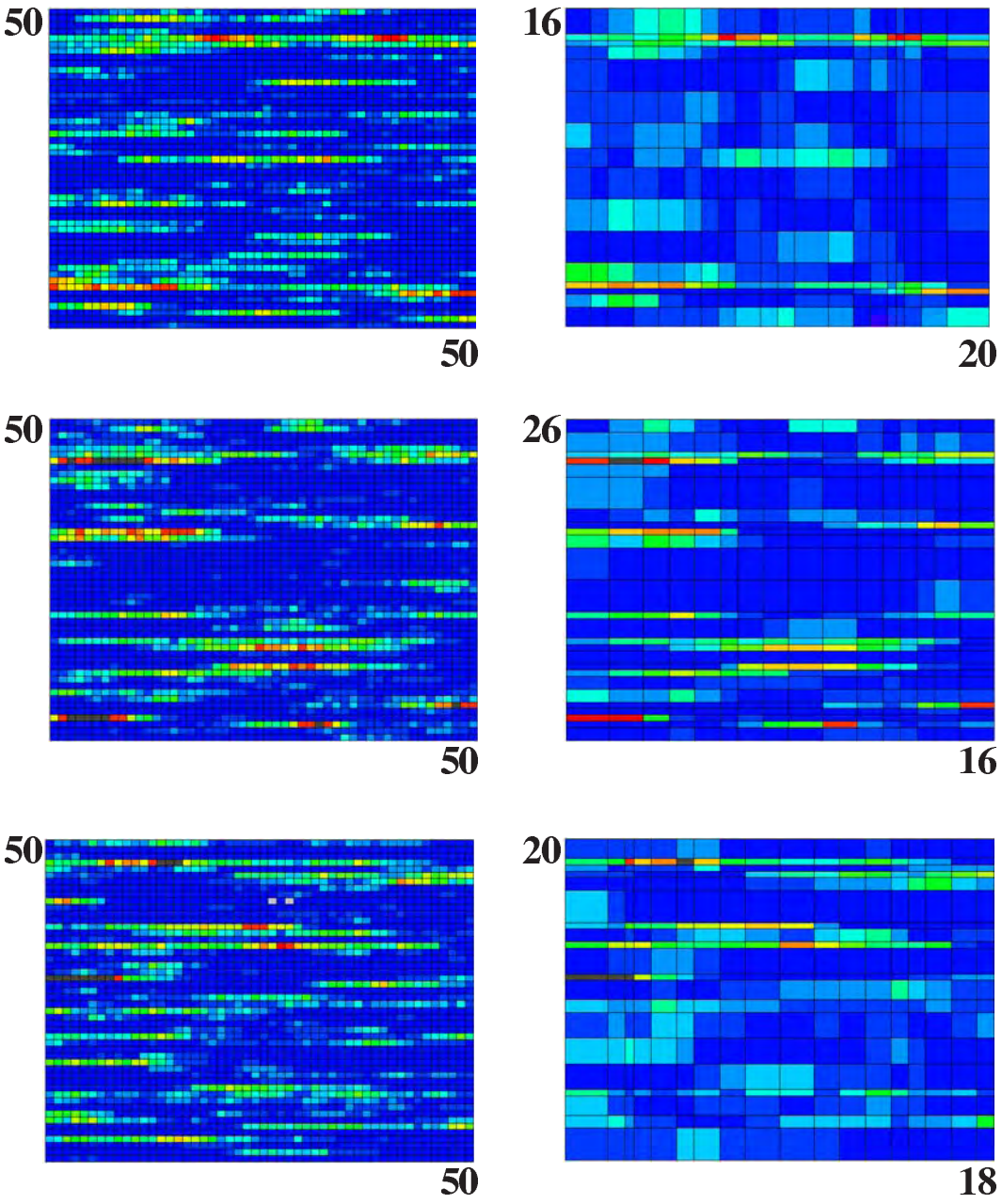

Figure 2.11: Sample end results of the parallel modelling workflow. Left: final high resolution models, right: final coarsened models.

Table 2.2: Summary of the 2D Gaussian example

Geological continuity model	Variogram
Horizontal variogram range	20 blocks
Vertical variogram range	10 block
Geostatistical algorithm	SGSIM
History matching method	Gradual deformation of sequential simulation
Reference field grid dimensions	$50 \times 1 \times 50$
Δx, Δz	20ft, 5ft
Porosity	0.2
$\mathbf{k}_{vertical}/\mathbf{k}_{horizontal}$	0.3
Mobility ratio	1
Injection pressure	5500 psi
Production pressure	4500 psi
Simulation Period	1500 days
Upscaling	Single phase upscaling
Upgridding	Flow based upgridding restricted to $25 \times 1 \times 25$

2.3.2 2D Gaussian example

This second case study differs from the first one in terms of variogram range, injection / production periods and the history matching technique. A summary of the example properties are given in Table-2.2. For this case we have chosen to use a less anisotropic variogram for the permeability field, with ranges 20 grid cells in the horizontal and 10 grid cells in the vertical direction. The flow simulation is performed over a longer period of time, 1500 days, and the resulting water cut curve is used as the reference production data. Hard data is collected along the two wells at every fifth grid block to be used as hard conditioning data. The future predictions will be made by running the model for 5000 days. The history matching technique for this case is the gradual deformation of sequential simulations adapted from Hu *et al.* (2001) (see Appendix-A.3 for more details).

The $50 \times 1 \times 50$ reference permeability field, generated using the SGSIM algorithm, is given in Figure-2.12. Each grid block is of 20ft in the horizontal and 5ft in the vertical. Due to the shorter variogram ranges, the permeability field appears more patchy, unlike the previous example with a layered system. Water injection is performed at a constant

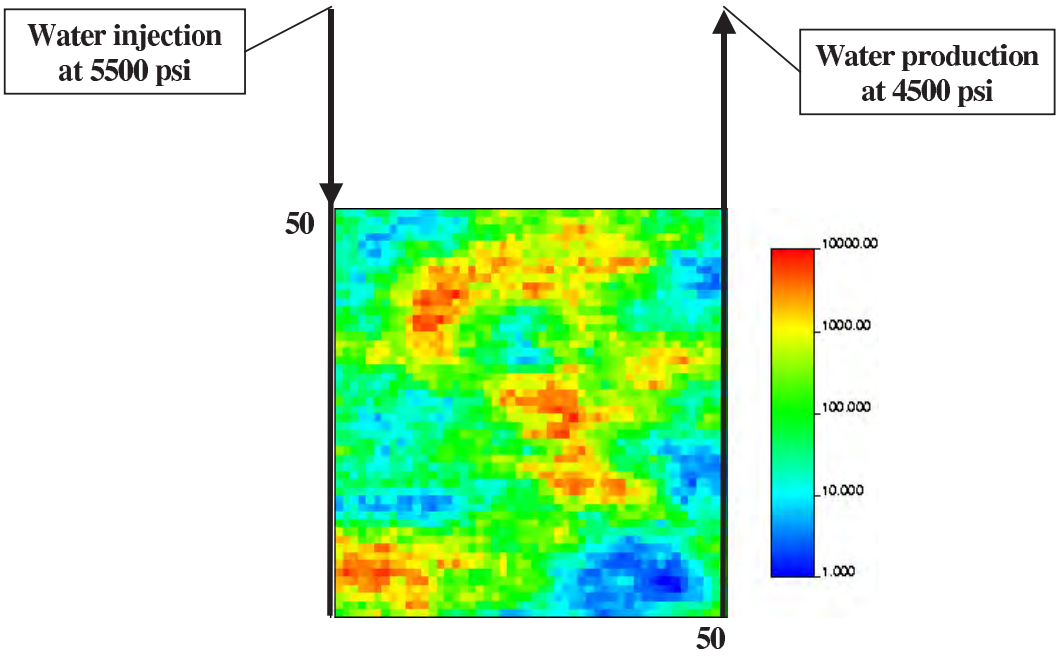

Figure 2.12: The reference permeability field.

pressure of 5500 psi and production is maintained under a constant pressure of 4500 psi. Figure-2.13 shows the resulting reference water cut curve. The breakthrough occurs close to 1000 days.

In the previous example, we define the gridding parameters n^{max}, u_x^{max} and u_y^{max} prior to applying the parallel modelling approach. These values were determined by trial and error, basically the reference permeability field was upgridded and upscaled using these parameters many times. Based on visual appreciation, the parameters were chosen such as to reproduce the high permeability regions best on the coarse model grid while keeping the number of coarse grid blocks as low as possible. For this example a simpler approach is proposed: Instead of fixing the gridding parameters beforehand, we fix the coarsening ratio. Hence for this example, the high resolution model is upscaled from dimensions of $50 \times 1 \times 50$ to a $25 \times 1 \times 25$ coarsened model. This is achieved by adjusting the u_x^{max} and u_z^{max} parameters, such that they provide a coarsened model of $25 \times 1 \times 25$ at each perturbation of the high resolution model.

Consider the plot of u_x^{max} versus the z dimension of the coarsened model given in Figure-2.14. When the u_x^{max} parameter is set to zero, the high resolution model is obtained.

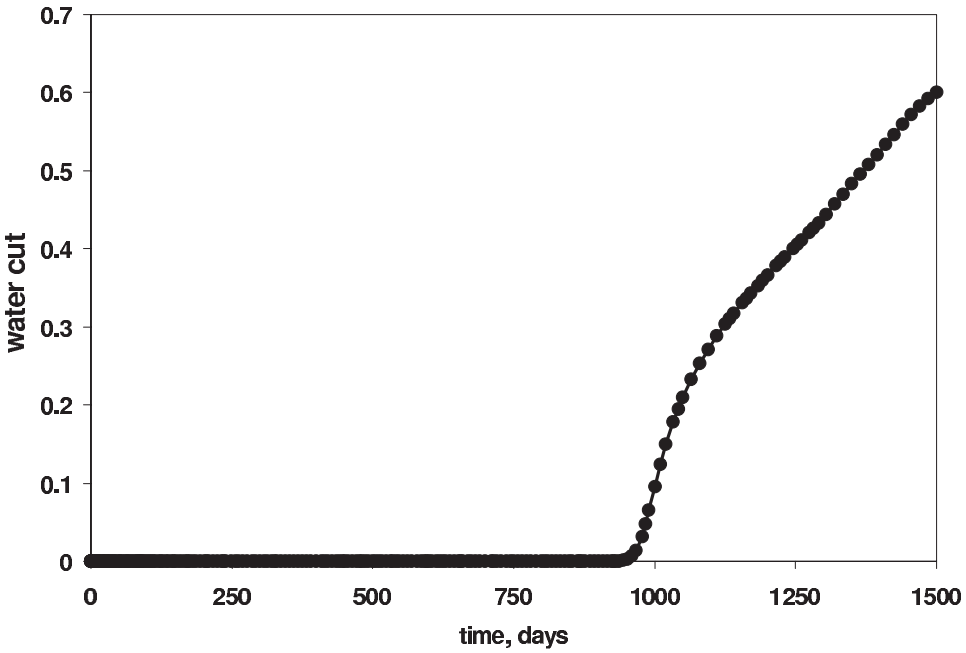

Figure 2.13: The flow response of the reference permeability field.

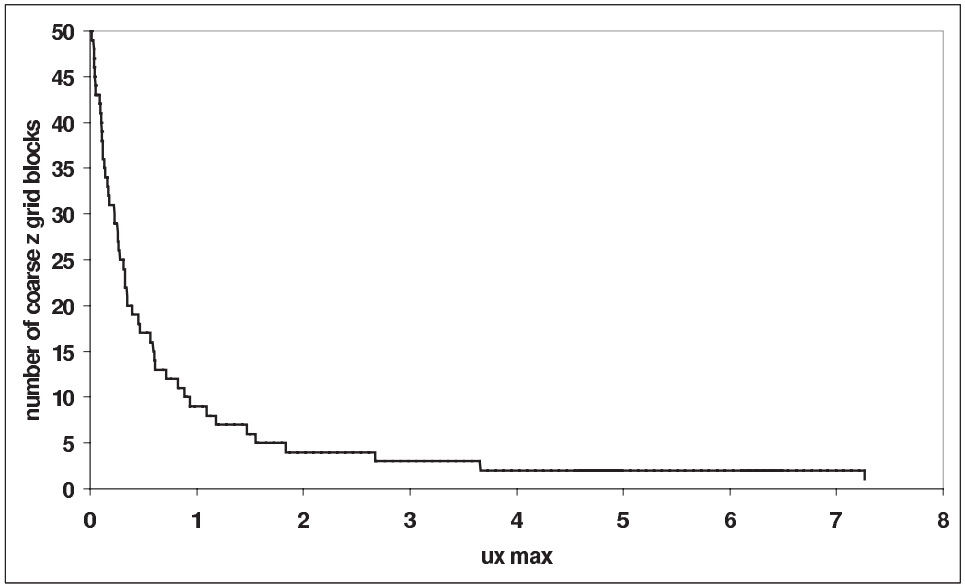

Figure 2.14: The relationship between u_x^{max} and the z dimension of the coarsened model.

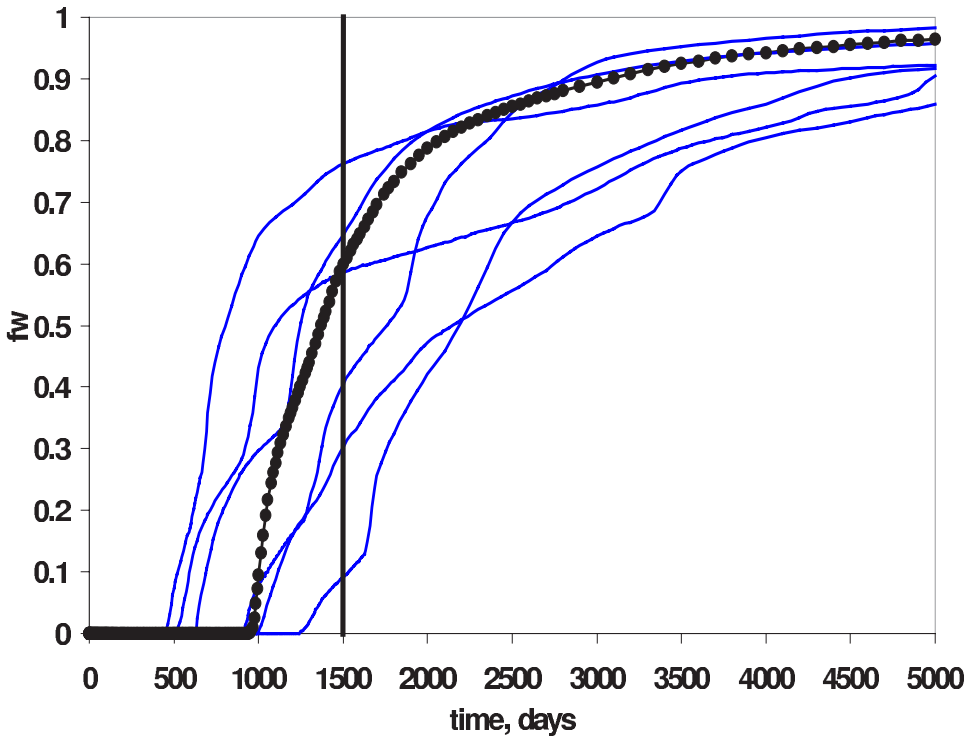

Figure 2.15: Flow responses of 6 realizations conditioned only to hard data.

When a high value for the u_x^{max} parameter is set, this allows for grouping many high resolution layers in to a single coarsened grid block. As seen from Figure-2.14, when the u_x^{max} parameter is set to 7.3, the coarsened model has a z grid dimension of 1.

Using such a plot, if the z grid dimension is predefined, then a corresponding u_x^{max} parameter can be determined. Hence at each perturbation of the high resolution model, the u_x^{max} and u_z^{max} parameters are determined such that the coarsened model has grid dimensions of $25 \times 1 \times 25$. Note that, even though the coarsened model dimensions are fixed, the gridding does change to adapt to the underlying heterogeneity at each perturbation of the high resolution model.

For comparison, Figure-2.15 represents the flow responses of 6 high resolution realizations conditioned only to the hard data showing a wide scatter. Figure-2.16 represents the flow responses of 6 coarsened realizations that are the end results of the parallel modelling approach. The flow responses match the history until 1500 days and a reduction in the

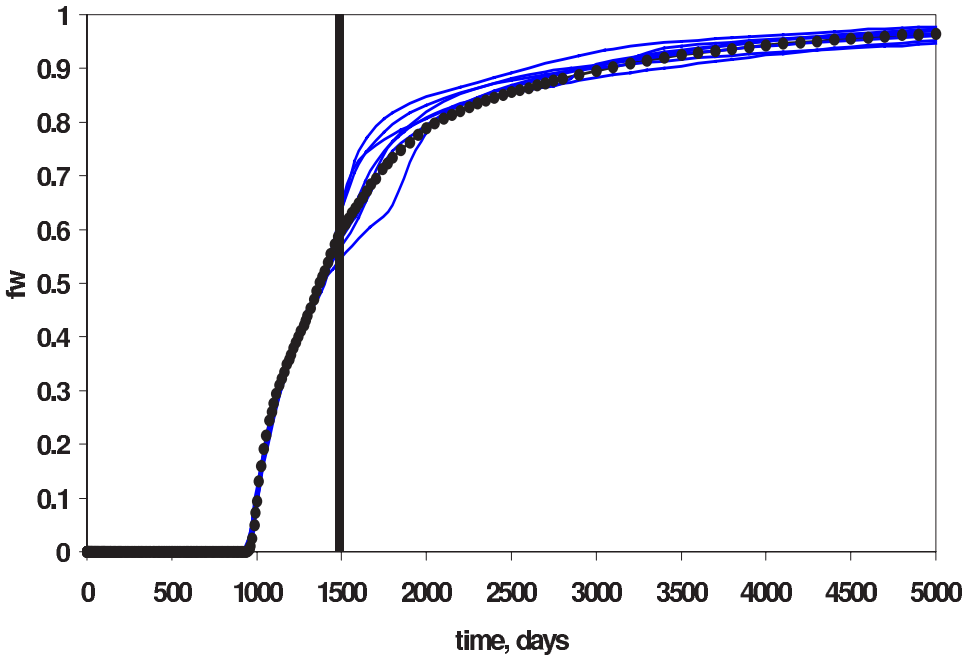

Figure 2.16: Flow responses of 6 realizations conditioned to both hard data and the production history.

uncertainty of the future predictions is apparent. Figure-2.17 shows some of the resulting high resolution and coarsened permeability fields. It is important to note that the high permeability regions are preserved on the coarsened models.

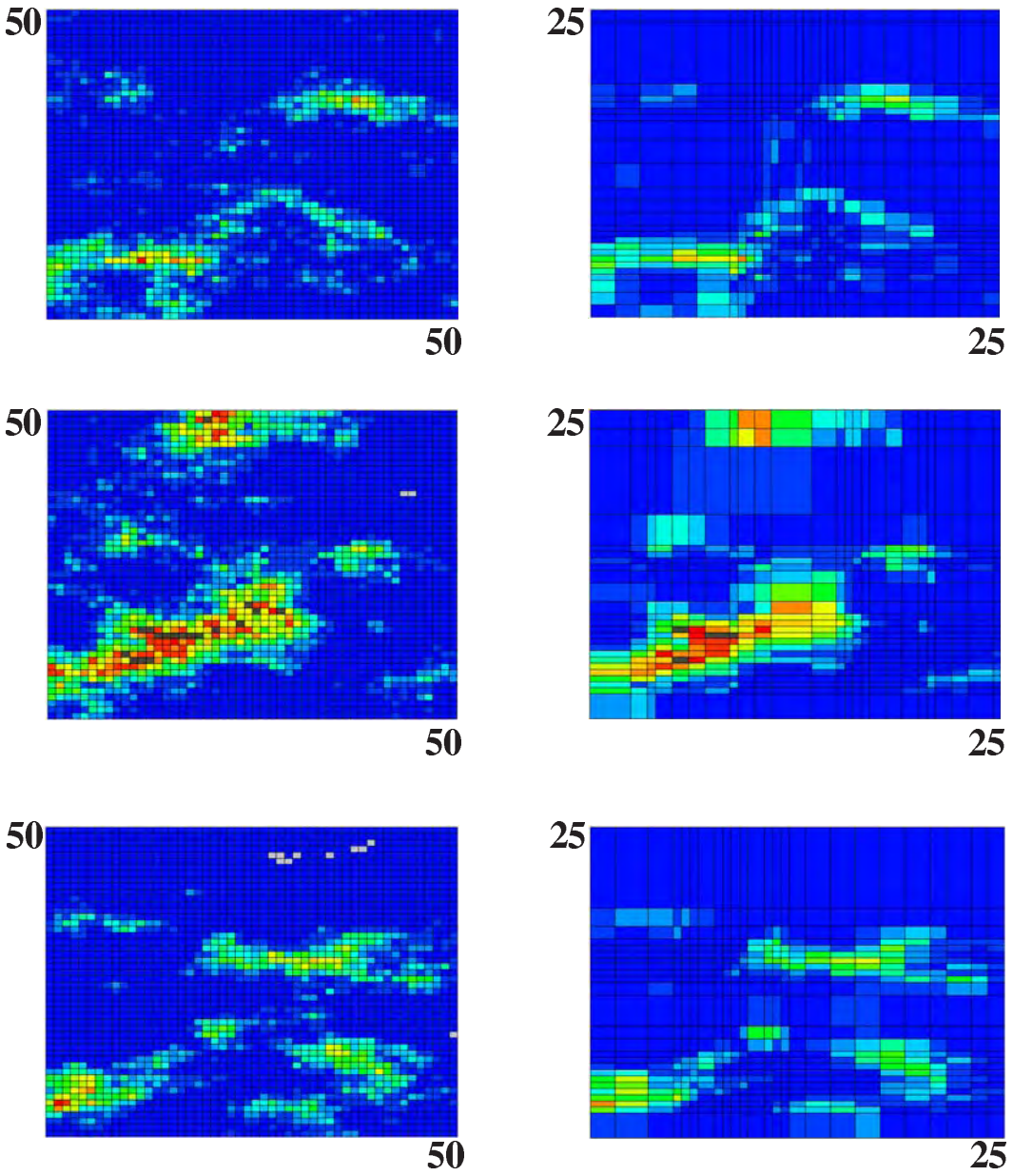

Figure 2.17: Sample end results of the parallel modelling workflow. Left: resulting high resolution models, right: resulting coarsened models.

2.3.3 2D facies model

In the previous two case studies, the parallel modelling approach was applied to continuous permeability models. In this example, the parallel modelling approach is applied to a facies model with four facies. The underlying geological continuity model is given through the $400 \times 1 \times 150$ training image in Figure-2.18a. Figure-2.18b represents the reference permeability field, obtained by running the multiple-point simulation algorithm SNESIM (Strebelle, 2002). The field has grid dimensions of $50 \times 1 \times 50$. Each of the four facies is assigned a constant permeability of 3md, 30md 300md and 3000md. Layering is emphasized by assigning the highest and lowest permeability values to the facies that extend horizontally. The injection / production scheme is for 500 days, with water injection taking place at 5500 psi and production at 4500 psi. Hard data is collected at every fifth grid block along the two wells to be used as conditioning data during the parallel modelling workflow. Each grid block is 20ft in the horizontal and 5ft in the vertical. A summary of the properties for this example are given in Table-2.3.

Table 2.3: Summary of the 2D facies example

Geological continuity model	Training image $400 \times 1 \times 150$
Geostatistical algorithm	SNESIM
History matching method	Gradual deformation of sequential simulation
Reference field grid dimensions	$50 \times 1 \times 50$
Δx, Δz	20ft, 5ft
Porosity	0.2
$\mathbf{k}_{vertical}/\mathbf{k}_{horizontal}$	1.0
Mobility ratio	1
Injection pressure	5500 psi
Production pressure	4500 psi
Simulation Period	500 days
Upscaling	Single phase upscaling
Upgridding	Flow based upgridding restricted to $25 \times 1 \times 25$

Figure-2.19 gives the flow response of the reference permeability field. The breakthrough occurs around 250 days. The flow responses of 6 high resolution models conditioned only to hard data are given in Figure-2.20. Figure-2.21 shows the flow responses

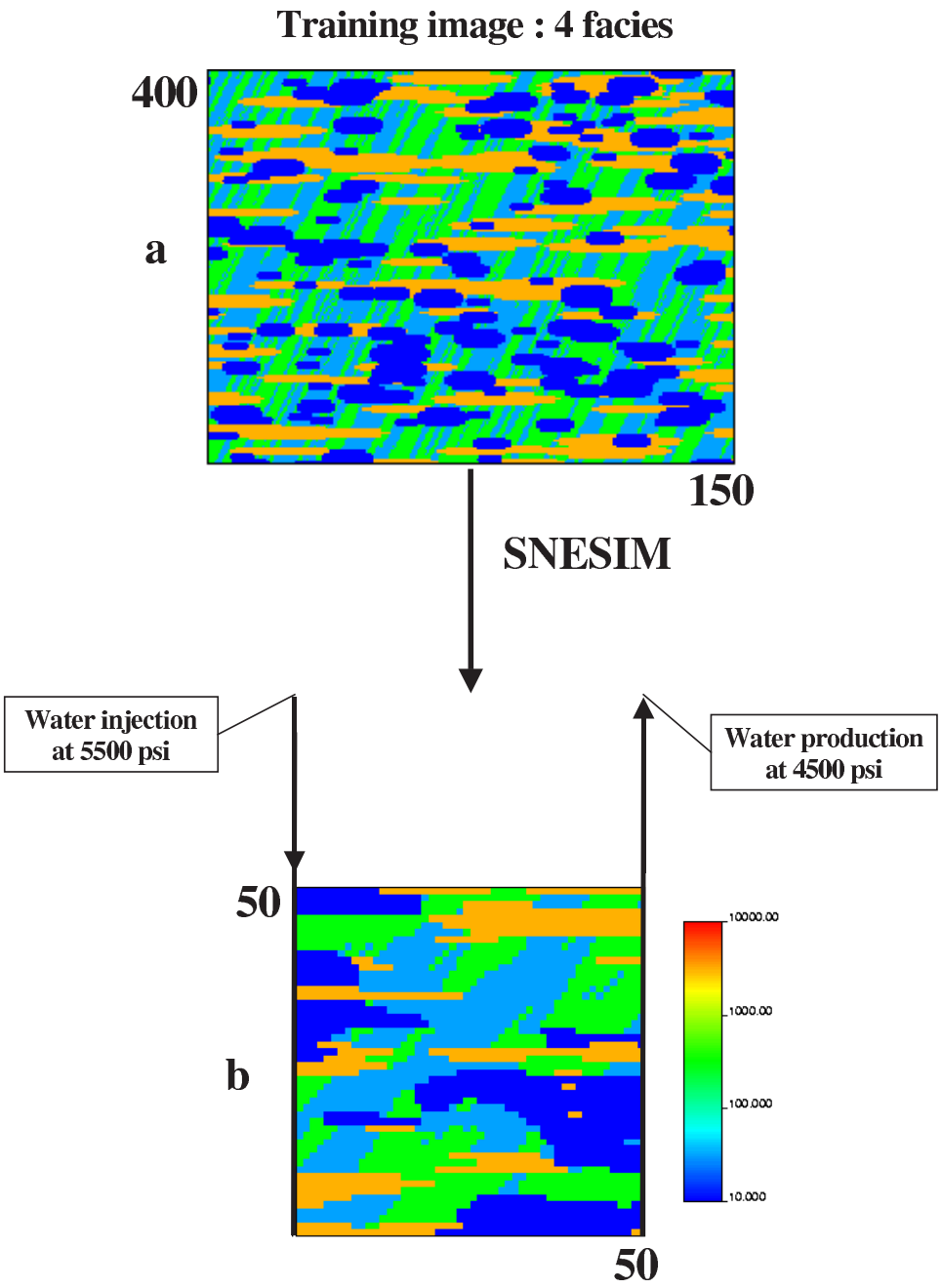

Figure 2.18: (a) The training image for the four facies model (b) the reference permeability field obtained through the given training image.

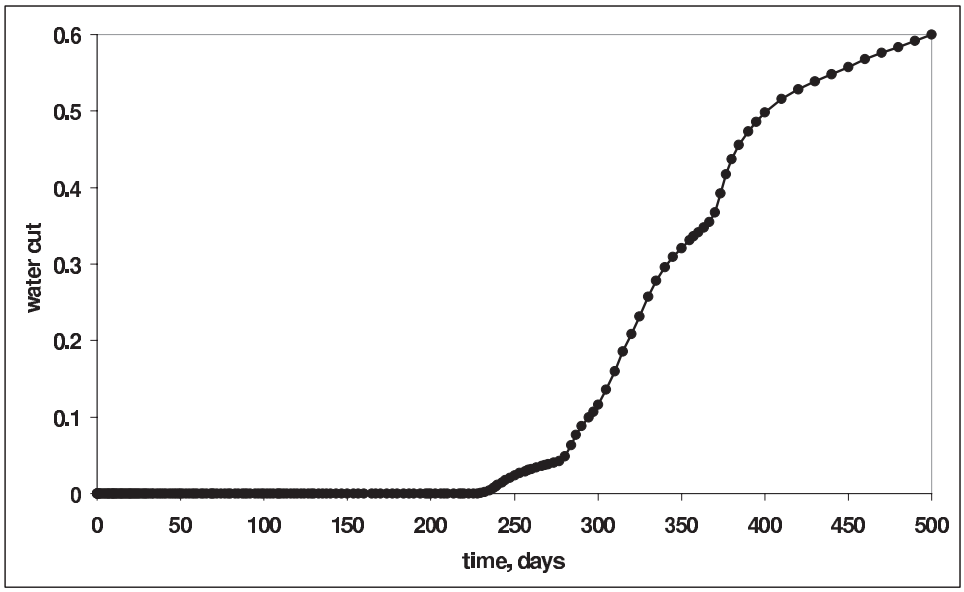

Figure 2.19: The flow response of the reference permeability field.

of 6 realizations that are the end results of the parallel modelling workflow. Comparing Figures 2.20 and 2.21 shows that the parallel modelling workflow significantly improves the flow responses.

Figure-2.22 shows samples of the resulting permeability fields. Note that the structure of the facies remain similar to that of the reference permeability field. This is expected since the history matching method ensures that the perturbed models keep their underlying geological continuity, that depicted the training image. The coarsened models preserve the high permeability facies since these are the ones most important to flow.

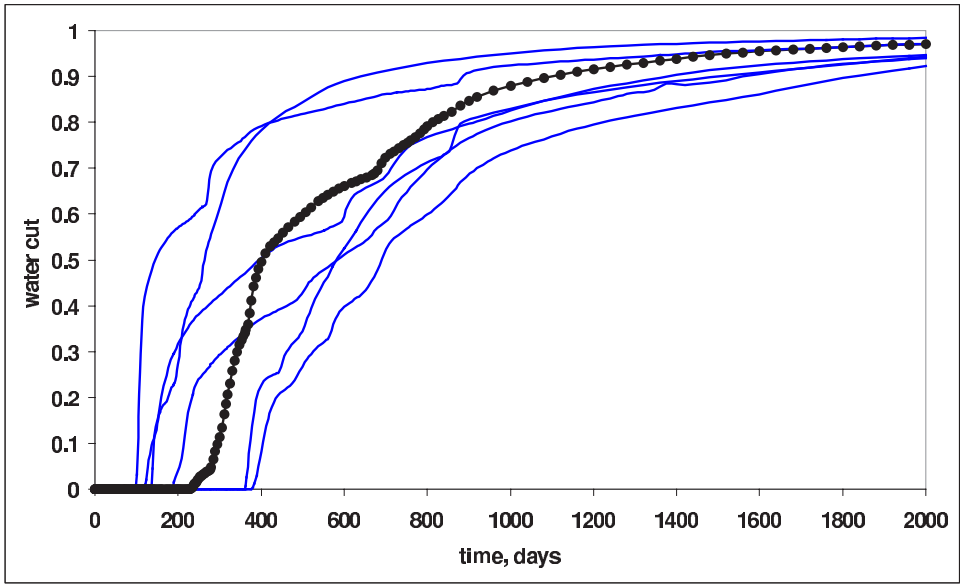

Figure 2.20: Flow responses of 6 realizations conditioned only to hard data.

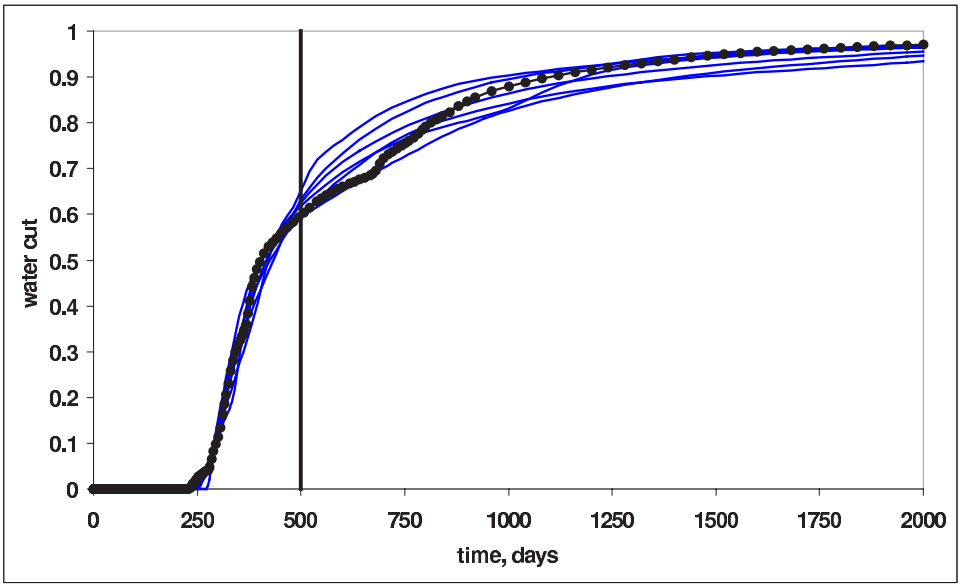

Figure 2.21: Flow responses of 6 realizations conditioned to both hard data and the production data.

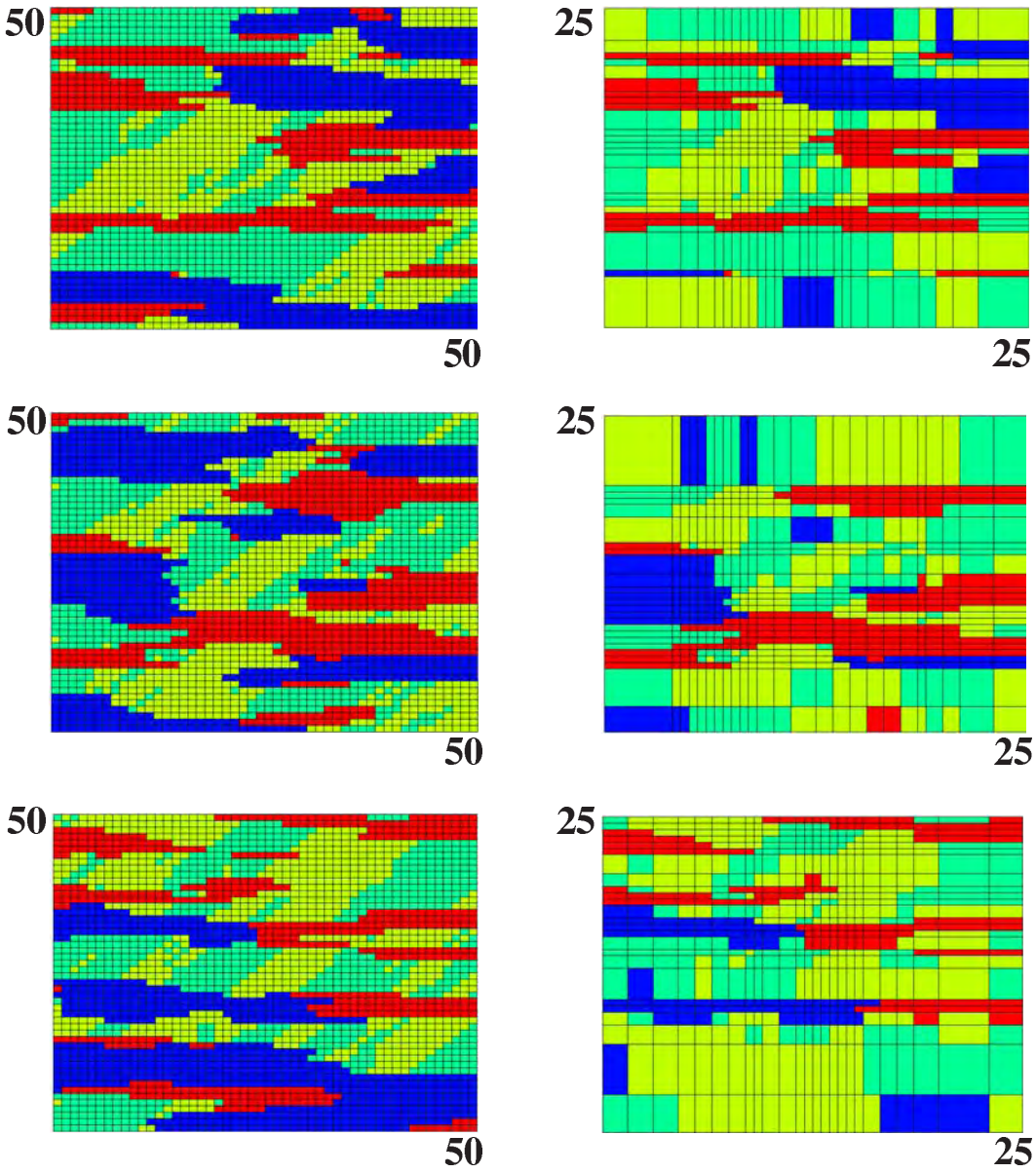

Figure 2.22: Sample end results of the parallel modelling workflow. Left: resulting high resolution models, right: resulting coarsened models.

2.3.4 2D channel example

In this example we apply the parallel modelling approach to a more realistic geological scenario, mainly a 2D channel system. A summary of the properties of this example is given in Table-2.4. The SNESIM algorithm (Strebelle, 2002) is used to generate a high resolution reference model using the training image given in Figure-2.23a. The reference permeability field has dimensions of $100 \times 100 \times 1$ and water flooding is simulated on a quarter five spot pattern as shown in Figure-2.23b. The two facies (channel and non-channel) are assigned constant permeability values of 10000md for the channel facies and 100md for the non-channel facies. The permeability values at the two well locations are collected for hard data conditioning during the modelling phase. The flow simulation is conducted for 500 days and the corresponding water cut curve is given in Figure-2.24 with breakthrough occurring at around 400 days. Water injection is performed at a constant pressure of 5500 psi and production is maintained at 4500 psi.

Table 2.4: Summary of the 2D channel example

Geological continuity model	Training image with two facies
Geostatistical algorithm	SNESIM
History matching method	Probability perturbation method
Reference field grid dimensions	$100 \times 100 \times 1$
Δx, Δy	20ft, 20ft
Porosity	0.2
Channel permeability	10000md
Non-Channel permeability	100md
Mobility ratio	1
Injection pressure	5500 psi
Production pressure	4500 psi
Simulation Period	500 days
Upscaling	Arithmetic averaging
Upgridding	3DDEGA ($25 \times 1 \times 25$)

The parallel modelling workflow specific for this example is given in Figure-2.25. The workflow starts by constructing a $100 \times 100 \times 1$ high resolution model conditioned to the hard data using SNESIM with the training image given in Figure-2.23a. Then the model is

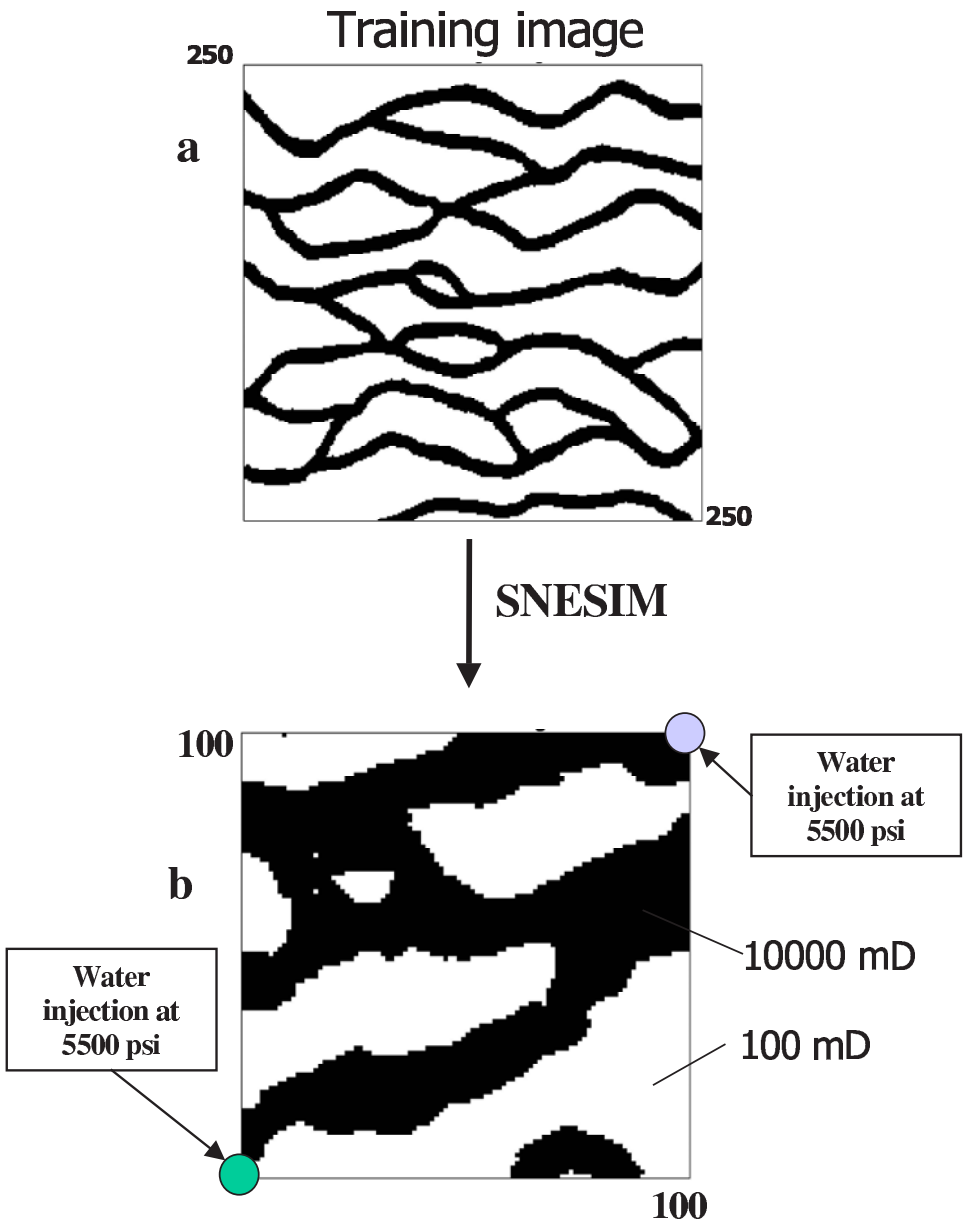

Figure 2.23: (a) The training image depicting the geological continuity model (b) The reference permeability field.

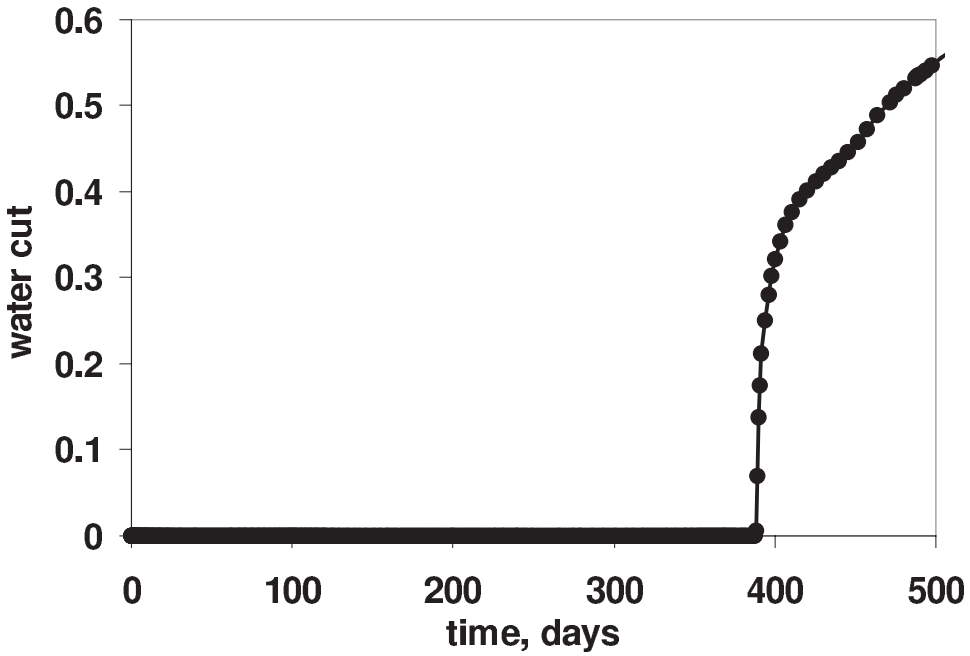

Figure 2.24: The flow response of the reference permeability curve.

non-uniformly coarsened to dimensions of $30 \times 30 \times 1$ using the 3DDEGA (Garcia *et al.*, 1992) algorithm, see Appendix C for more details, 3DDEGA is a gridding algorithm that provides coarsened models with a corner-point geometry grid. The main idea behind the 3DDEGA algorithm is that the grids are adjusted in such a way to make each coarse grid block as homogeneous as possible in terms of the underlying geological heterogeneity.

Upscaling is performed by taking the arithmetic average of the high resolution permeability values. Arithmetic averaging for this example suffices due to the fact that constant permeability values have been assigned to the channel and non-channel facies. 3DDEGA delivers corner point geometry gridding that is well adapted to the overall channel structure. After the coarsening step, flow simulation is performed and the mismatch between the reference flow response and the calculated response is evaluated. If that mismatch is not reduced, the high resolution model is perturbed with the probability perturbation method adopted from Caers (2003), see Appendix-A.4 for more details. The probability perturbation method allows for perturbation of the high resolution model without destroying the underlying geological continuity model. The method relies on perturbing the cumulative conditional probability distribution functions used in generating the simulated realization

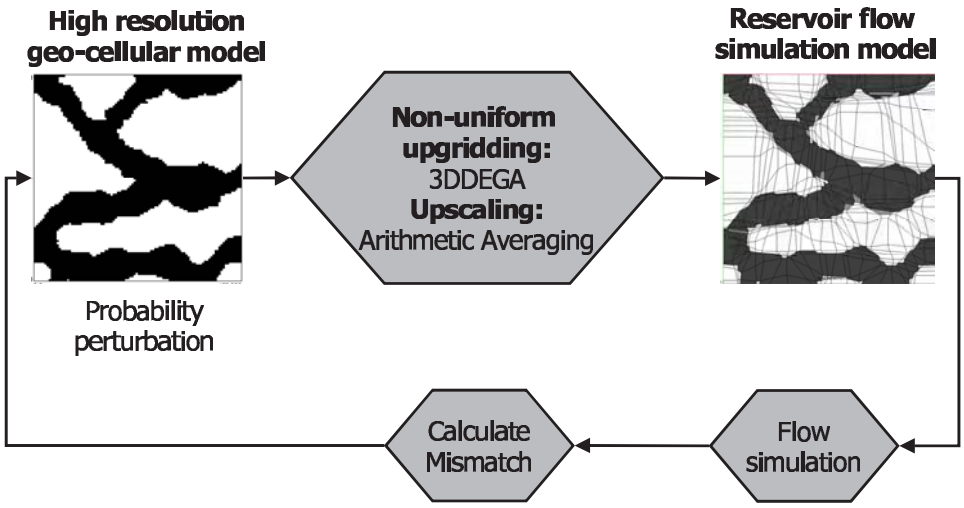

Figure 2.25: The parallel workflow specific for the 2D channel example.

in a sequential simulation approach. The above steps are repeated until the mismatch is sufficiently reduced.

To compare the results we first look at the flow responses of 30 realizations conditioned only to the hard data collected form the wells. Figure-2.26 illustrates the results. A wide scatter in the flow responses is observed. This is expected, since most of the flow takes place in the channel regions due to the high permeability contrast between channel and non-channel facies. Binary models can create many channel discontinuities, resulting in later breakthrough times. After we apply the parallel workflow on this example, the future predictions of the flow responses are given in Figure-2.27. Until 500 days history matching is accomplished, and the uncertainty regarding the future predictions until 2000 days has been considerably reduced.

Figure-2.28 illustrates four samples of the realizations conditioned only to the hard data and Figure-2.29 illustrates four samples of realizations conditioned to both hard data and production data. The channel structures are well preserved on the coarsened models. The probability perturbation method ensures that the training image structure is preserved in all realizations generated no matter how much they are perturbed. Furthermore, the 3DDEGA upgridding algorithm ensures preservation of the channel structures on the coarsened models.

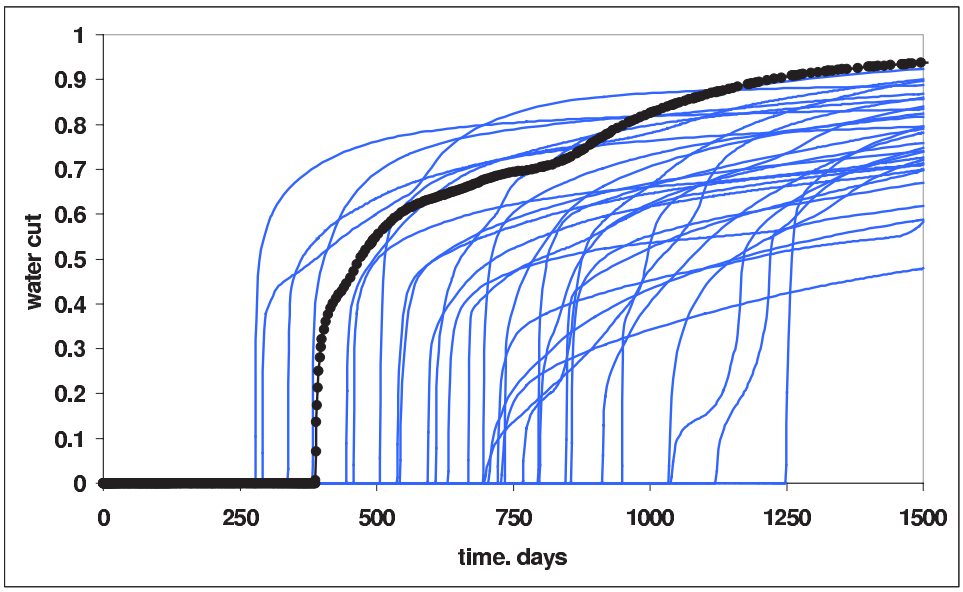

Figure 2.26: The flow responses of 30 realizations conditioned only to the hard data.

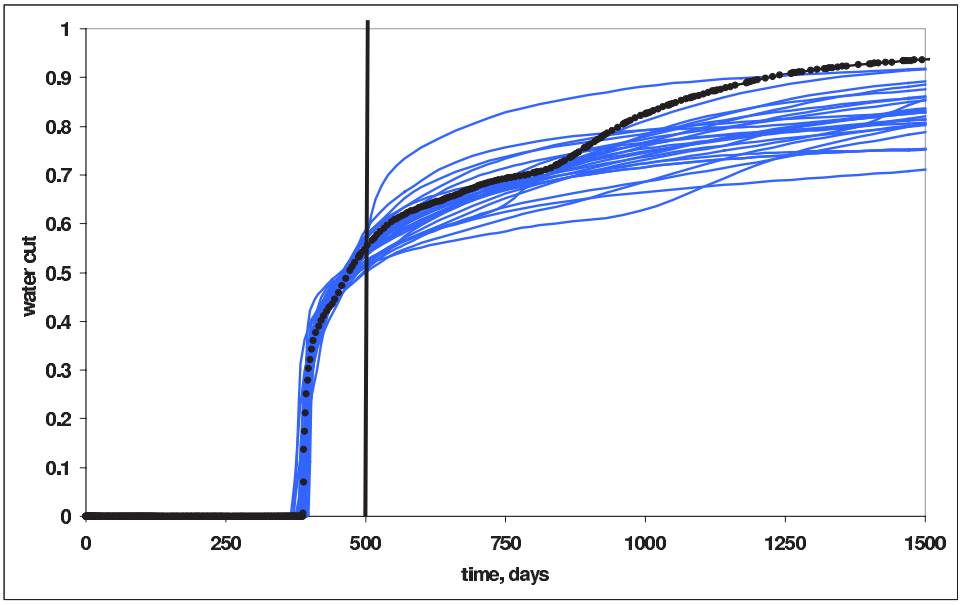

Figure 2.27: The flow responses of 30 realizations conditioned to both hard data and historical production data.

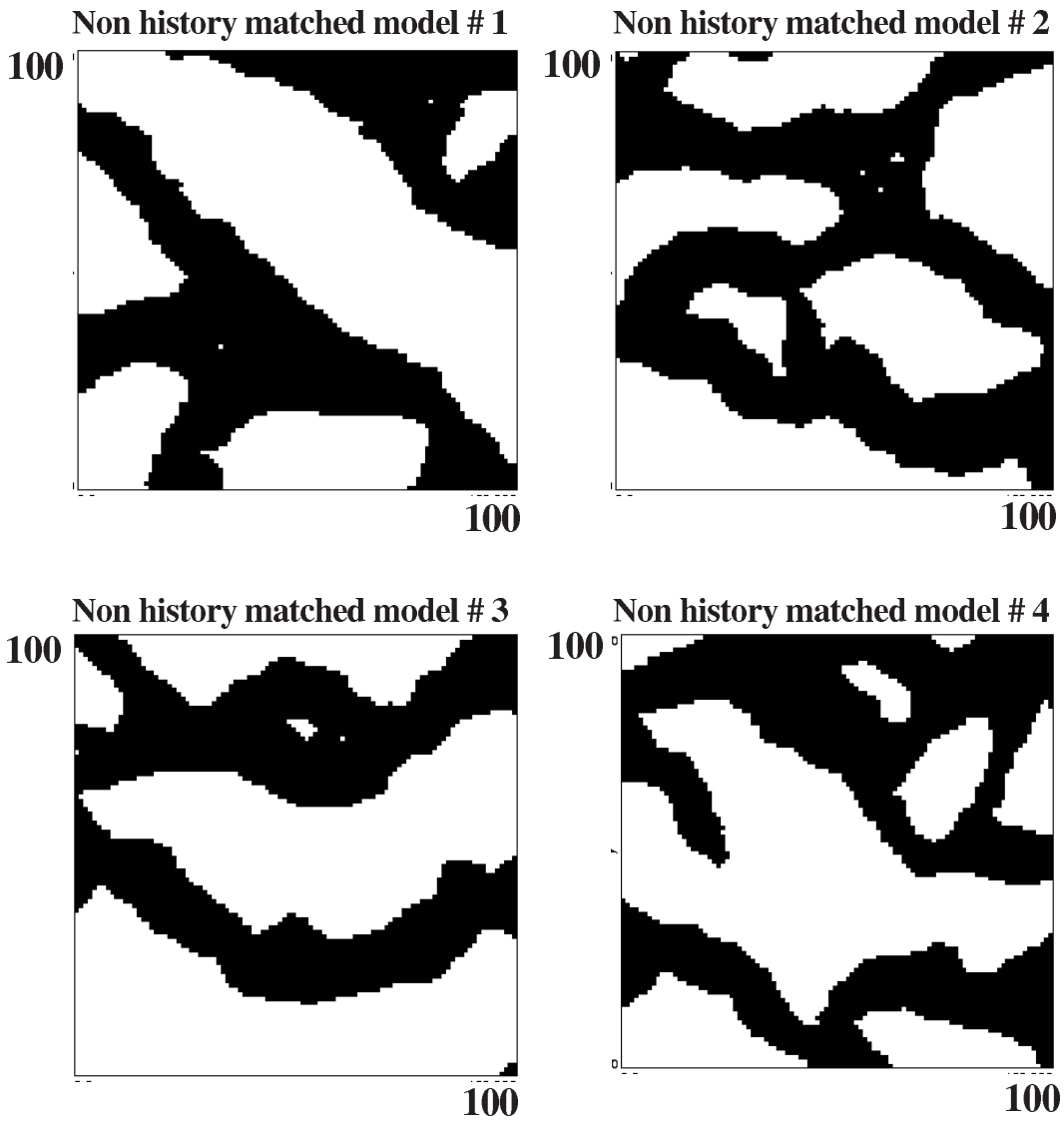

Figure 2.28: Four examples of realization conditioned only to the hard data.

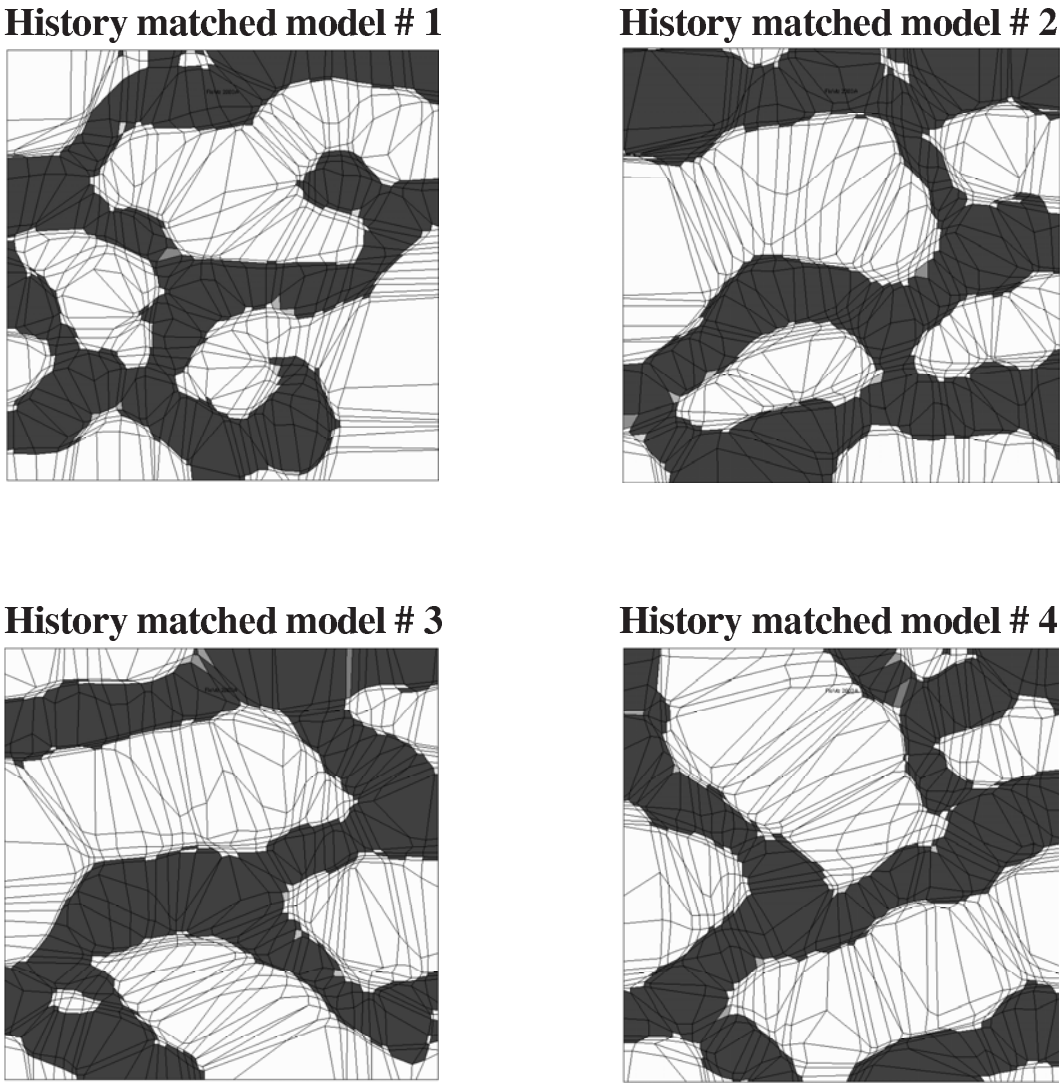

Figure 2.29: Four examples of coarsened realization conditioned to both the hard and the production data.

2.3.5 3D channel example

In this case study, we apply the parallel modelling workflow on a 3D channel system. The underlying geological continuity model is represented with a 3D ($200 \times 200 \times 5$) binary training image. The training image slices for all five horizontal layers is shown Figure-2.30. The underlying geological continuity model has major east-west connectivity of channels.

Table 2.5: Summary of the 3D channel example

Geological continuity model	3D Training image with two facies
Geostatistical algorithm	SNESIM
History matching method	Probability perturbation method
Reference field grid dimensions	$51 \times 51 \times 10$
Δx, Δy, Δz	20ft, 20ft, 20ft
Porosity	0.2
Channel permeability	1000md
Non-Channel permeability	100md
Mobility ratio	1
Injection pressure	5500 psi
Production pressure	4500 psi
Simulation Period	500 days
Upscaling	Arithmetic averaging
Upgridding	3DDEGA ($20 \times 20 \times 10$)

A quarter five spot pattern is simulated on the reference permeability field given in Figure-2.31a. The channel structure of the field is shown in Figure-2.31b. The reference permeability field is generated using the SNESIM algorithm (Strebelle, 2002). The two facies, channel and non-channel, are assigned constant permeability values of 1000md and 100 md respectively. Water injection is simulated on the reference field with a flow period of 500 days. The resulting water cut curve is given in Figure-2.32. The breakthrough is observed at around 300 days. The injection pressure is 5500 psi and the production pressure is taken to be 4500 psi. Hard data is collected along the two wells at every five grid blocks in the vertical. The summary for this case study is summarized in Table-2.5.

In order to compare the results, we first look at the flow responses of 6 high resolution realizations conditioned only to hard data, given in Figure-2.33. These flow responses

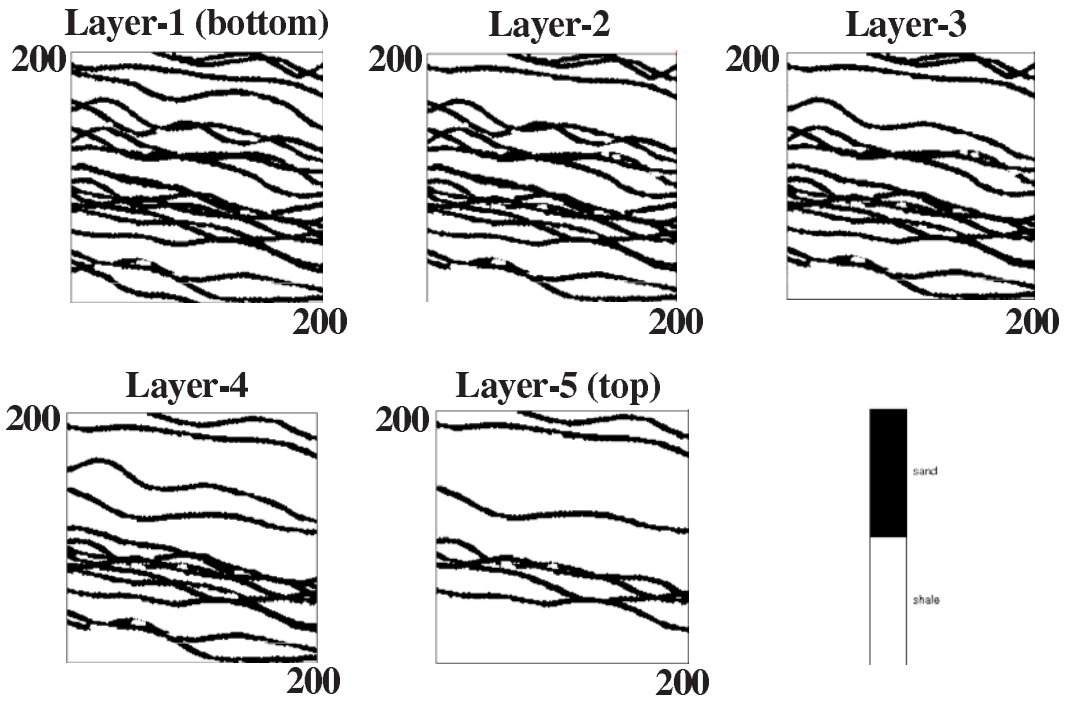

Figure 2.30: Slices of the 3D training image for all five layers.

do not represent the flow responses of the reference permeability field and show a wide scatter. Figure-2.34 shows the flow responses of the resulting realizations once the parallel modelling workflow is applied. A history match until 500 days is achieved. A significant reduction in the future performance predictions is also obtained when compared with Figure-2.33. Four sample history matched models are given in Figure-2.35. Note that the overall channel structure remains consistent with that of the training image shown in Figure-2.30.

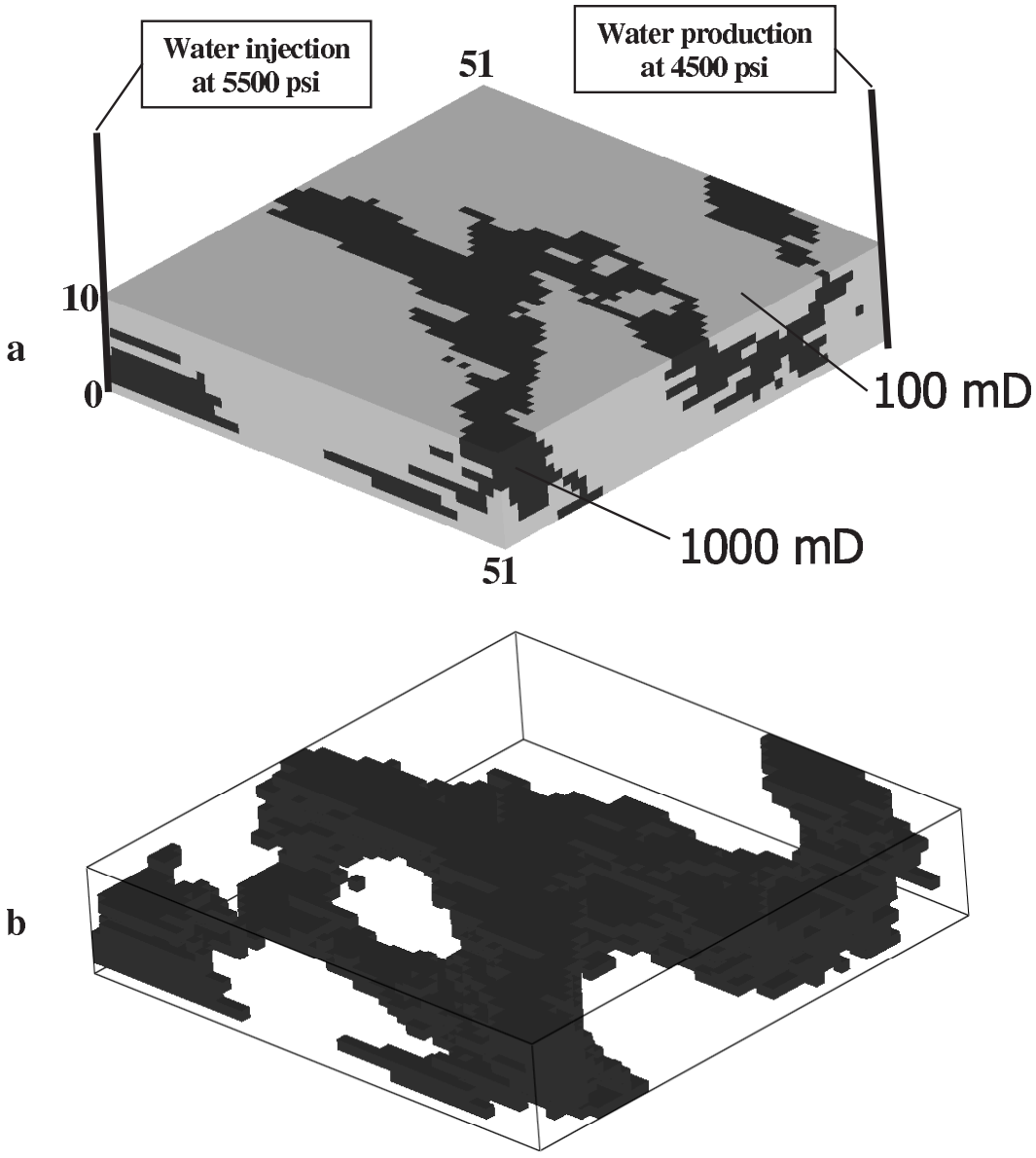

Figure 2.31: (a) The reference permeability field (b) The channel structure of the reference permeability field.

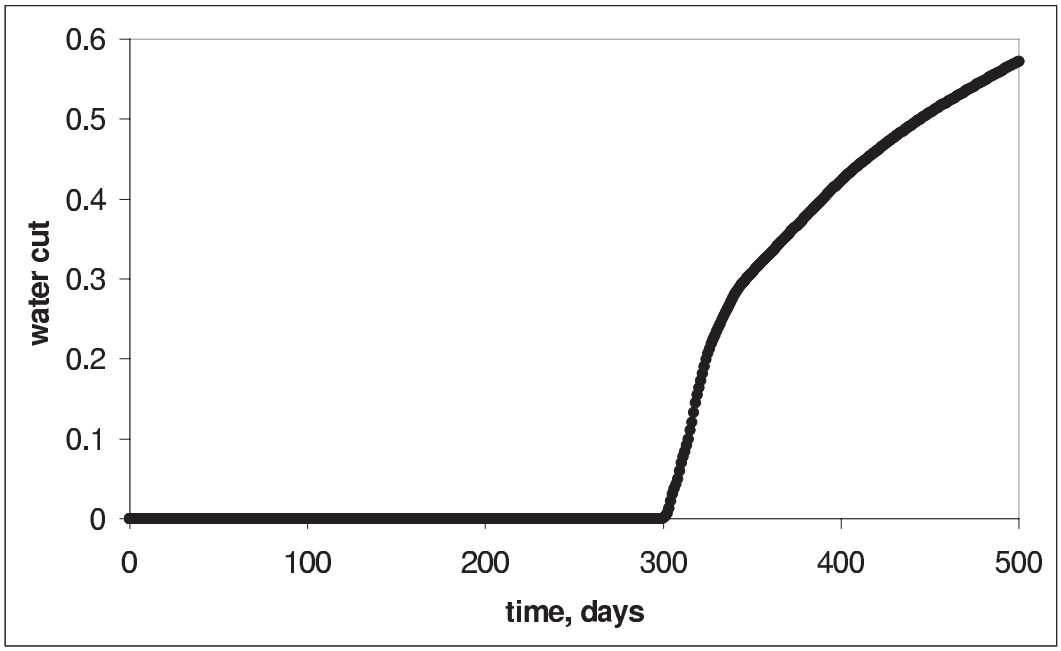

Figure 2.32: The flow response of the reference permeability field.

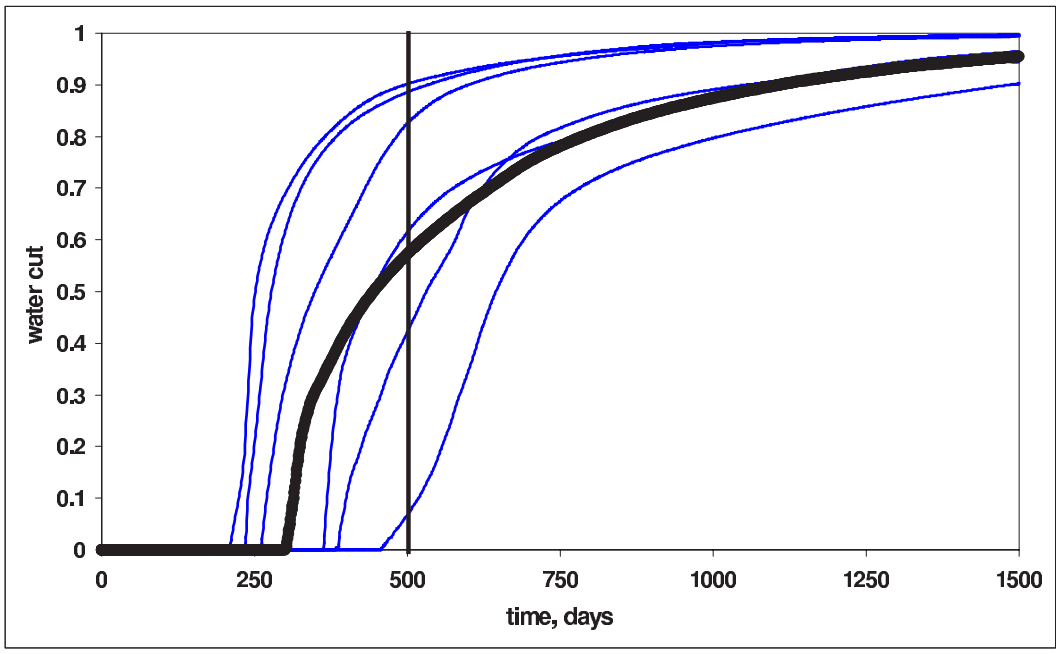

Figure 2.33: Flow responses of high resolution realizations conditioned only to hard data.

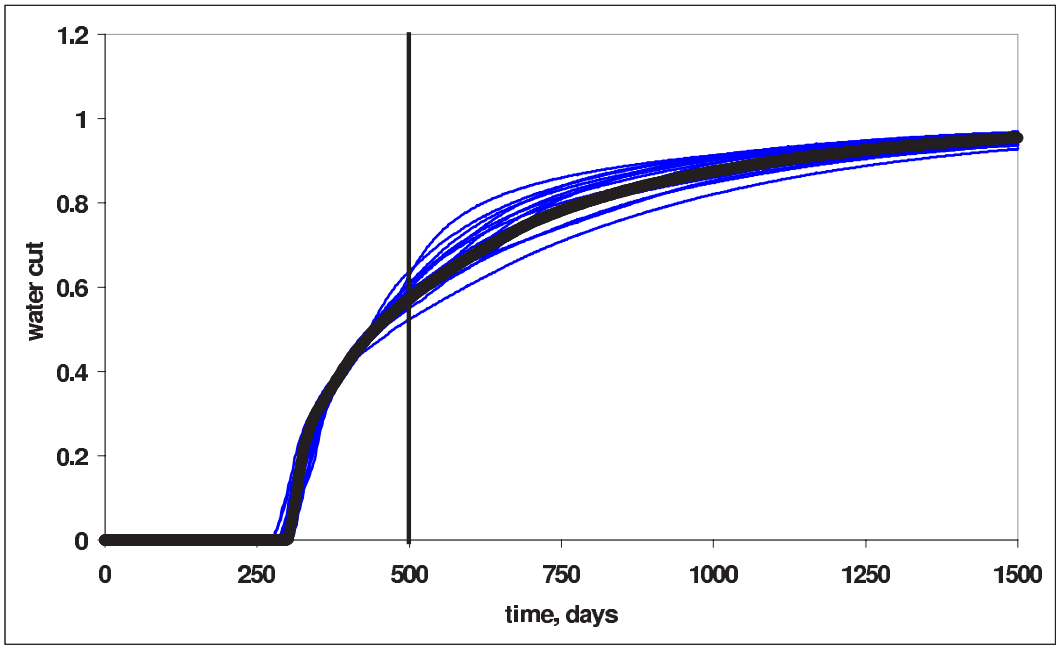

Figure 2.34: Flow responses of coarsened models conditioned to both hard data and the production data.

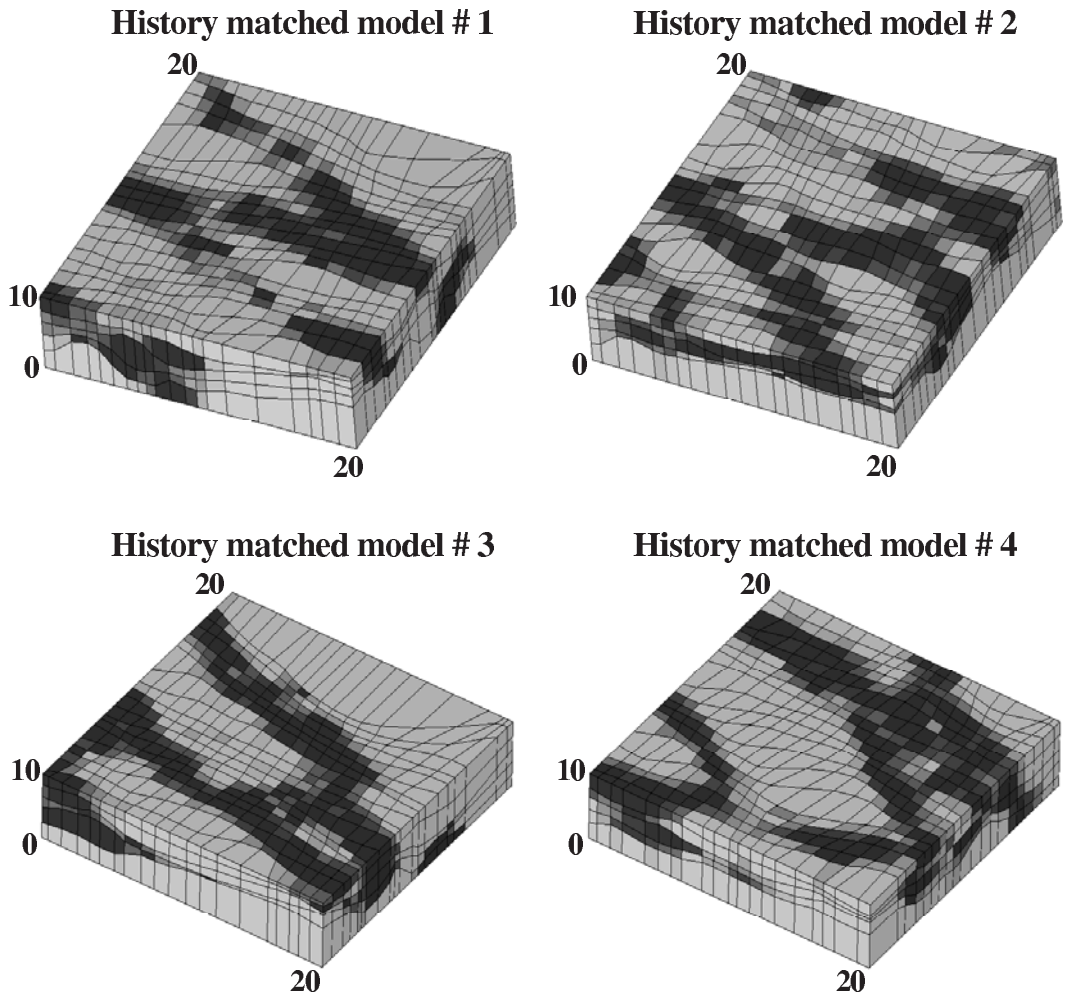

Figure 2.35: Sample history matched models.

2.4 Discussion

This chapter presented the basics of the parallel modelling workflow. Applications were given using synthetic examples. These applications show that the parallel modelling workflow offers an effective alternative for data integration in reservoir modelling. However there are some limitations to the approach that have not been addressed in this chapter.

From the structure of the workflow it appears that the scale change (upscaling) plays an important role in the parallel modelling methodology. In the first example, the upgridding parameters were fixed based on visual appreciation. Upscaling parameters were chosen such that they preserve the fine scale heterogeneities on the coarsened model. However, during the parallel modelling workflow, the high resolution models change when perturbed. These perturbed models can be significantly different from each other. Hence a predetermined set of gridding parameters may not be always appropriate.

In the second and third case examples an alternative approach is taken where by, instead of predetermining and fixing the gridding parameters, the upscaling ratios are fixed. In the examples provided, the high resolution models had grid dimensions of $50 \times 1 \times 50$ from which they were upscaled to fixed coarsened grid dimensions of $25 \times 1 \times 25$. It is shown that history matching can be obtained with the $25 \times 1 \times 25$ coarsened models. It has not been investigated if the parallel modelling workflow would still be applicable for higher coarsening ratios, for example upscaled to a $15 \times 1 \times 15$ or $10 \times 1 \times 10$ or even a $5 \times 1 \times 5$ model. In other words: How coarse can one go?

As stressed throughout this chapter, the parallel modelling workflow results in coarsened models that are non-uniformly gridded and match the history. Hence future predictions can be made directly without any posterior downscaling or upscaling. Also resulting from the parallel modelling workflow is also a high resolution model, where all static data are honored. There remains to investigate whether the resulting high resolution model honors the production data.

Nor is the impact of upscaling errors investigated: The question ”How does upscaling errors affect the parallel modelling workflow?” has not been addressed.

The next chapter will focus in greater depth on these issues. The effects of upscaling on the results is first analyzed. Then, an improved workflow is presented.

Through the use of current reservoir modelling workflows these synthetic examples might be handled using the following procedure. First a number of high resolution models

would be generated which would then be upscaled either uniformly or non-uniformly. Next these models would be ranked based on how closely they represent the historical production data. The models that closely match the production data would be further history matched. In the case of non-uniform upscaling, although the coarsened models would represent fine scale heterogeneities that impact flow, the history matching techniques used in this chapter may be difficult to apply due to the different sizes of the grid blocks. Hence a different history matching technique would need to be applied. Furthermore, the non-uniform gridding of the coarsened model would be optimal to the initial high resolution model from which it was upscaled. Once the permeability values are perturbed, the coarse grid would no longer be optimal. In the case of uniform upscaling, even though the volume support problem would not be an issue, uniform gridding would fail to capture any fine scale details that might impact flow. As mentioned earlier, perturbing the coarsened model independently of the high resolution model also carries the risk of losing the geological continuity. This is not an issue with the procedure described in this thesis.

Chapter 3

Gridding Optimization

3.1 Motivation

Chapter-2 introduced the parallel modelling approach for jointly integrating static and dynamic data. The methodology relies on upscaling high resolution geological models to a coarsened model, performing flow simulation on the coarsened model but perturbing the high resolution geocellular model based on the flow simulation results. Resulting from this entire process are two separate but consistent models: a high resolution model and a coarsened model. The high resolution model honors all static data (hard and soft), while the coarsened model honors the production data. Furthermore, the final history matched coarsened model is non-uniformly gridded, hence can directly be used for future predictions.

Chapter-2 also illustrated the parallel modelling methodology with various applications on 2D and 3D cases. However, an important issue remained unaddressed. Even though the resulting coarsened model honors the production data, the high resolution model may not. In fact, a strong underlying assumption of this method is that the upscaling errors are small. Flow simulation is evaluated on the coarsened scale, while perturbations are made on the high resolution model; this makes sense only if the flow responses on both resolutions are similar. Otherwise, the adjustments calculated from the coarsened model flow response would not necessarily be relevant to make high resolution model perturbations. However, successful history matches on the coarsened models can be obtained because many models exist that provide the same history (ill-posedness of history matching). In other words, even if the upscaling procedure introduces a considerable error, the optimization procedure will

Table 3.1: Summary of the 2D layered example

Geological continuity model	Variogram
Horizontal variogram range	100 blocks
Vertical variogram range	2 block
Geostatistical algorithm	SGSIM
History matching method	Gradual deformation of sequential simulation
Reference field grid dimensions	$50 \times 1 \times 50$
Δx, Δz	40ft, 5ft
Porosity	0.2
$\mathbf{k}_{vertical}/\mathbf{k}_{horizontal}$	1.0
Mobility ratio	1
Injection pressure	5500 psi
Production pressure	4500 psi
Simulation Period	500 days
Upscaling	Single phase upscaling
Upgridding	Flow based upgridding restricted to $5 \times 1 \times 5$

still select coarse scale model realizations that match history.

The magnitude of the upscaling errors depend, among other factors, on the level of coarsening. Upscaling errors tend to increase as coarsening is increased. Using the parallel modelling approach, one may still reach a satisfactory match, even when applying a large upscaling ratio. Consider the following synthetic example:

Figure-3.1 shows a $50 \times 1 \times 50$ high resolution reference permeability field representing a layered system. The properties of the example are summarized in Table-3.1. Water injection is simulated on this model and the resulting water cut curve is given in Figure-3.2. To illustrate the concern raised above, a high degree of coarsening from a $50 \times 1 \times 50$ to a coarsened model of $5 \times 1 \times 5$ is taken within the parallel modelling approach. The two objectives of this study are:

- Testing the parallel workflow to check the parallel modelling workflow under high upscaling ratio ($5 \times 1 \times 5$).
- Checking if the resulting high resolution models still match history or not.

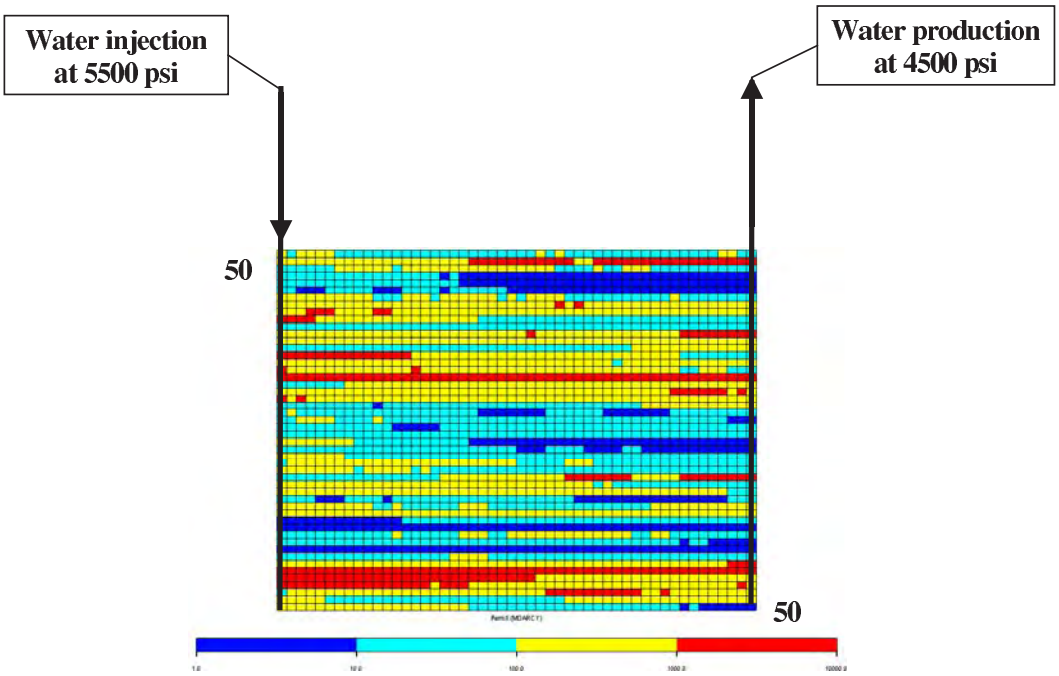

Figure 3.1: The reference permeability field.

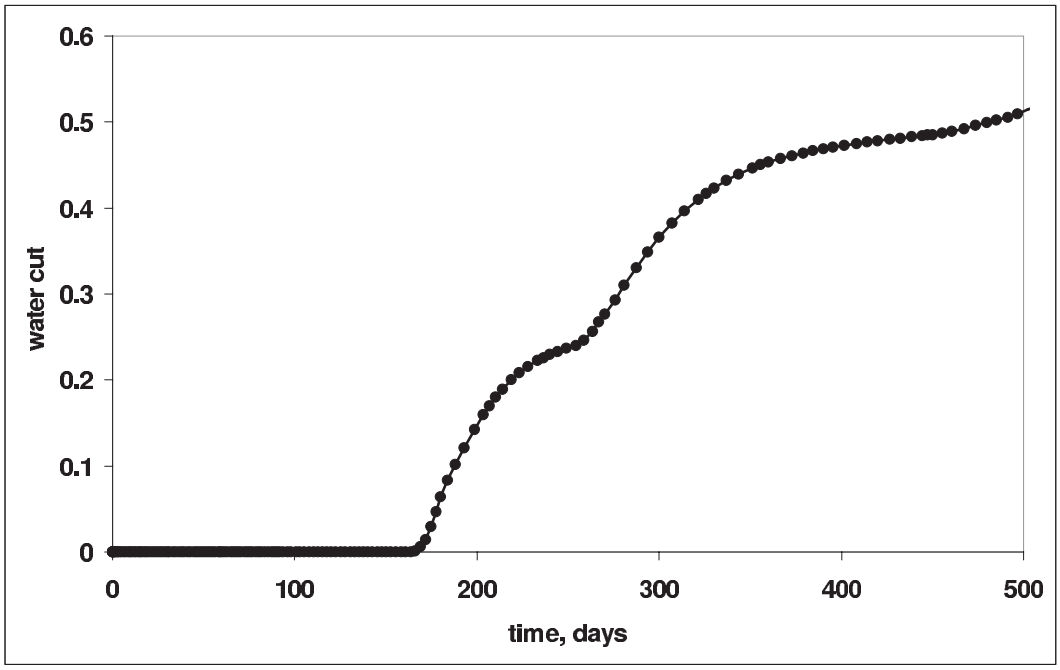

Figure 3.2: The flow response of the reference permeability field.

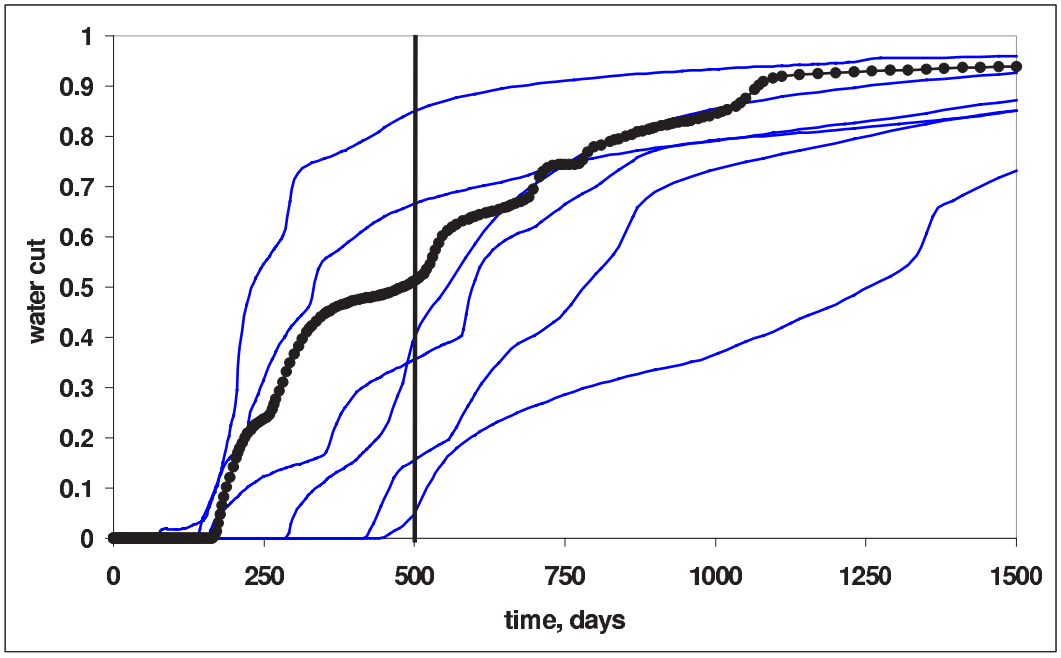

Figure 3.3: Flow responses of 6 high resolution models conditional only to the hard data.

Figure-3.3 provides flow responses of high resolution realizations conditioned only to the hard data. Next we apply the parallel modelling workflow where in each iteration the high resolution model of $50 \times 1 \times 50$ is coarsened to a $5 \times 1 \times 5$. The flow responses of 6 coarsened realizations conditioned to both hard data and production data are given in Figure-3.4. A satisfactory match is obtained despite the high upscaling ratio. There is considerable decrease in the uncertainty of the future performance predictions when compared with Figure-3.3.

Figure-3.5 shows two samples of the output models. Note that the flow responses in Figure-3.4 belong to the coarsened models. The flow responses of the high resolution models are given in Figure-3.6. The high resolution models do not match production data.

Even though the coarsened models satisfactorily honor the production data, it is clear from Figure-3.5 that they fail to represent accurately the underlying geology. The fact that history matching can still be achieved can be attributed to the little constraint that production data carries about the high resolution geological heterogeneity. It appears that in this particular case the production data informs only the larger scale variation of permeability, hence it is possible to match using a coarsened model.

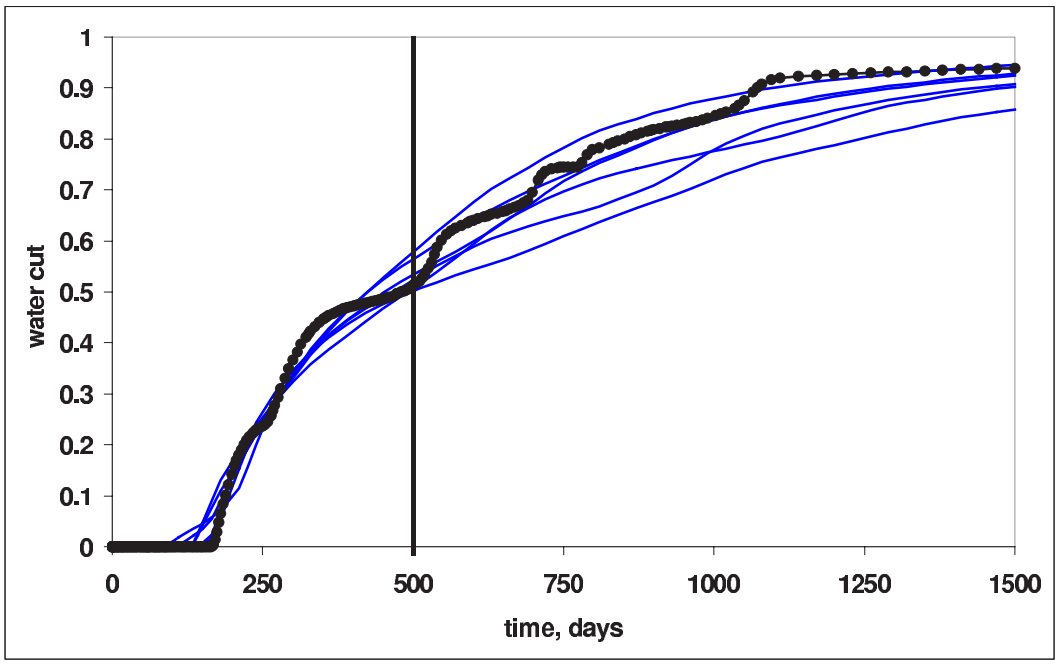

Figure 3.4: Flow responses of 6 coarsened models conditional to both the hard data and the production history.

In many practical applications it would be useful for high resolution models to reflect to some degree, the reservoir flow. Consider, for example, the well placement optimization problem (Guyaguler and Horne, 2001; Yeten and Durlofsky, 2002). Such applications require models that are conditioned to all available data and more importantly the models must be refined enough to depict correctly the underlying geology. Hence, it is important to have a high resolution model which in addition matches the production history.

Performance predictions for infill wells also require a history matched high resolution model. Such applications cannot be conducted on the coarsened model due to the non-uniform gridding, and that gridding did not take into account the location of the infill well. Furthermore in many cases grids are generated using flow based algorithms. In such cases, the resulting coarsened grids are appropriate for the boundary conditions used during the grid generation. Flow performance predictions of infill wells would have to consider new boundary conditions for which the coarsened non-uniform grids may not be appropriate.

Because of the above mentioned reasons, it is important that the high resolution model be informative of the production data to some degree. From a theoretical point of view, as

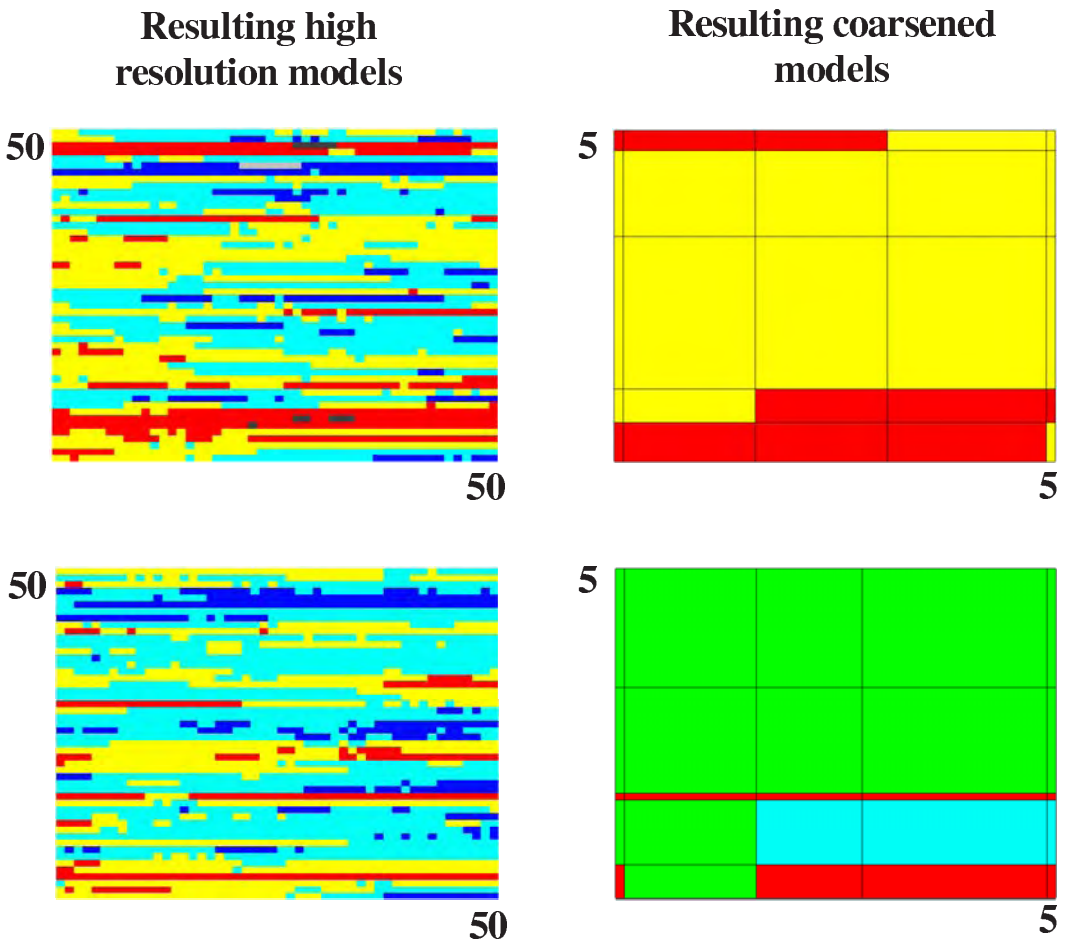

Figure 3.5: Two samples of the end results. A high resolution model and its corresponding coarsened model.

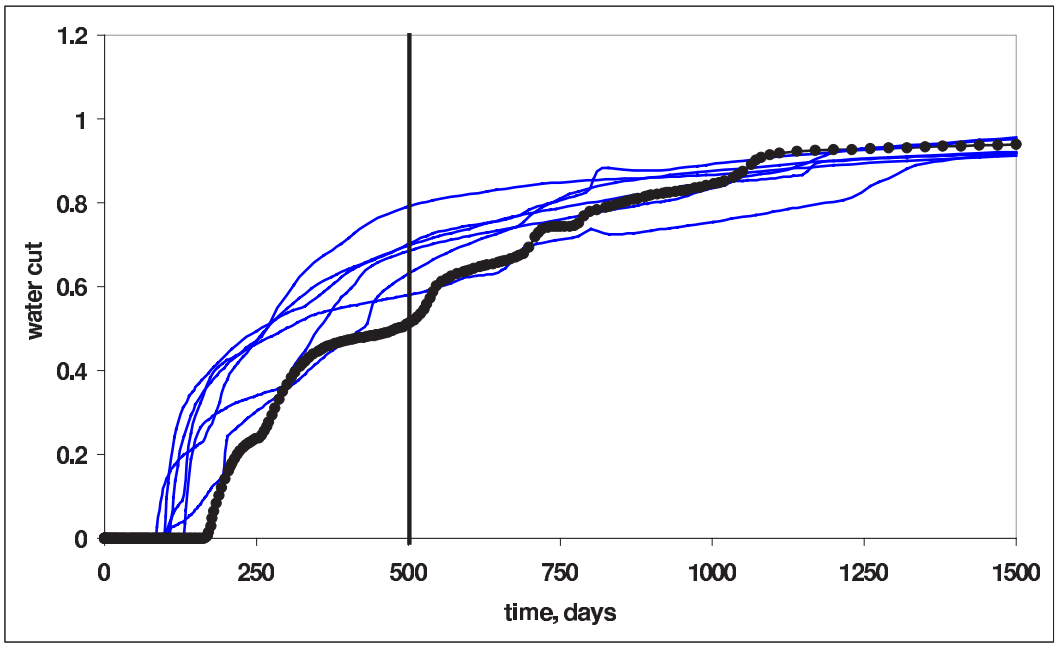

Figure 3.6: The flow responses of the high resolution models.

stated in Chapter-1, the main objective of reservoir modelling is to integrate all available sets of data into one model. The approach proposed in Chapter-2, did not quite achieve this goal. Two end results are retained which are not fully consistent one with each other: A high resolution model that is representative of the geology but is not history matched, and a coarsened model that matches the history but may not necessarily be representative of the geology.

The origin of the problems above are a result of the transition from the high resolution model to the coarsened model: There is no systematic determination of the level of coarsening and corresponding upscaling errors, it is currently arbitrarily fixed by the user. In this chapter we improve on the parallel modelling workflow by relying on a technique for reducing the upscaling error.

3.2 Improved Workflow

In this section we aim at improving the parallel modelling approach by reducing upscaling errors as much as possible. This is achieved by introducing an additional optimization step.

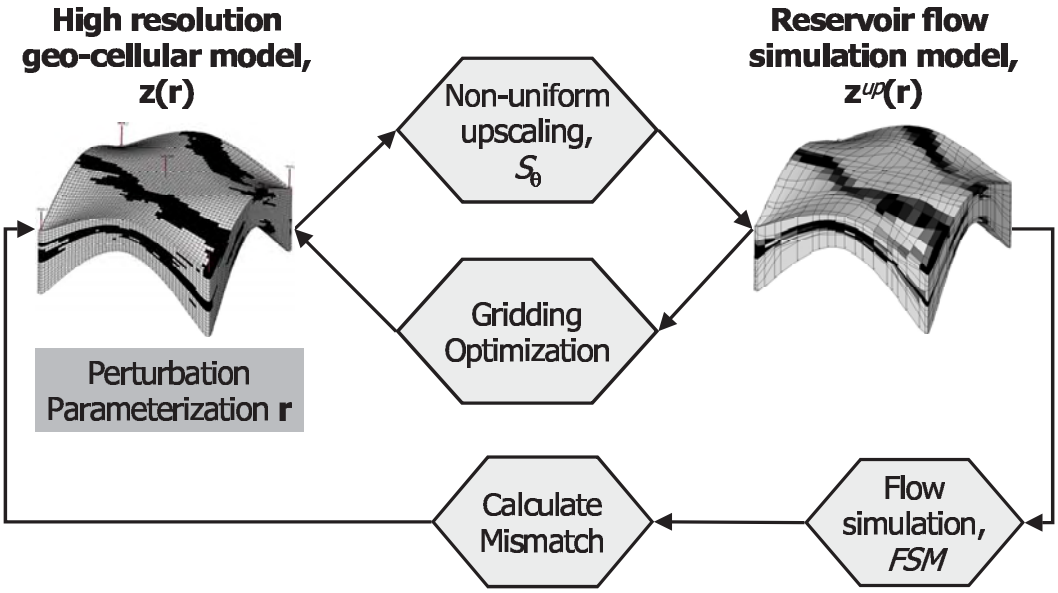

Figure 3.7: The parallel modelling workflow with gridding optimization.

We determine the magnitude of the upscaling errors through an approximate but fast flow simulator. This simulator can be evaluated on the high resolution model, hence allows to quantify the level of error made when upscaling. An optimization method is then used to determine the optimal coarsening parameters. Since the optimal coarsening depends on each particular high resolution model retained, this procedure needs to be applied each time the high resolution model is perturbed.

In this section, we present how this additional optimization process fits in the parallel modelling workflow. First further notation is defined, then the improved workflow is presented.

Additional notation

FSM^*	a flow simulator that is a fast approximation of FSM.
$\mathbf{RP}^*$	the flow response when FSM^* is performed on **z**.

The workflow

The improved parallel modelling workflow is given in Figure-3.7. The workflow proceeds as follows:

1. An initial high resolution model, that honors all available hard data and seismic data is generated.

2. Instead of directly proceeding with the coarsening step, a gridding optimization is performed in order to minimize the differences between the flow responses of the high resolution model and the coarsened model. The true, but unknown upscaling error, termed here as ϵ, is defined as the mismatch between the flow responses of the high resolution model and the coarsened model when using the full flow simulation model FSM:

$$\epsilon = \|FSM(\mathbf{z}^{up}(\mathbf{r})) - FSM(\mathbf{z}(\mathbf{r}))\| \tag{3.1}$$

or

$$\epsilon = \|FSM(S_\theta(\mathbf{z}^{up}(\mathbf{r}))) - FSM(\mathbf{z}(\mathbf{r}))\| \tag{3.2}$$

The aim is to minimize ϵ. However, in practice, we cannot calculate ϵ since the full flow simulation model FSM cannot be evaluated on the high resolution model **z**. This would void the parallel modelling approach in the first place. Hence the challenge is to reduce ϵ without knowing $FSM(\mathbf{z}(\mathbf{r}))$.

To achieve this, an approximate but fast flow simulation model is introduced, denoted FSM^*, one that is fast enough to be evaluated on the high resolution model **z**. We define as ϵ^* the difference between the flow responses of the high resolution model and the coarsened model when using FSM^* for flow simulation:

$$\epsilon^* = \|FSM^*(\mathbf{z}^{up}(\mathbf{r})) - FSM^*(\mathbf{z}(\mathbf{r}))\| \tag{3.3}$$

or

$$\epsilon^* = \|FSM^*(S_\theta(\mathbf{z}^{up}(\mathbf{r}))) - FSM^*(\mathbf{z}(\mathbf{r}))\| \tag{3.4}$$

where the error ϵ^* is a function of the upscaling method S and its parameters θ. ϵ^* can be minimized by finding an optimal set S and θ.

In order to find an optimal θ and S we need to evaluate FSM^* one single time on the high resolution model **z(r)** to obtain a reference fast flow response. Using an iterative optimization procedure, multiple FSM^* evaluations are required on $\mathbf{z}^{up}(\mathbf{r})$ to reduce ϵ^*. The CPU time spent in solving the optimization problem for finding S and θ should be small compared to running FSM on $\mathbf{z}^{up}(\mathbf{r})$, since all FSM^* are evaluated on the coarsened grid.

The assumption made is that, once ϵ^* has been made small enough ϵ has also been reduced, although not by the same amount as ϵ^*. The underlying assumption is that the objective function defined on FSM^* namely ϵ^* is monotonically varying with the objective function defined on FSM namely ϵ. In other words, the ranking of models provided by FSM is the same as the ranking provided by FSM^*: the errors ϵ and ϵ^* need not be the same in absolute magnitude. On a side note: this approach has been used in Ballin *et al.* (1993), in the context of uncertainty quantification.

3. Resulting from the gridding optimization process is a coarsened model that is optimally gridded, hence is also representative of the flow response of the high resolution model. The full flow simulation model, FSM is evaluated on the coarsened model and the mismatch between the flow response and the actual field response is calculated.

4. The high resolution model is perturbed and the above steps repeated until the mismatch between the calculated flow response and the actual field response is deemed small enough.

3.3 Implementation

3.3.1 Gridding optimization

Before explaining how the gridding optimization is performed, we first define the approximate flow model, FSM^*, used in this thesis. The design of the approximate flow model should be based on the problem at hand depending on the type of application, such as primary production, water flooding, gas injection and etc. For the water flooding problem considered in this thesis, the approximate flow model should provide good approximations

to water cut curves. The approximate flow model must be very fast and be feasible on high resolution models and must provide reasonable rank preserving approximations to the actual flow responses.

In this thesis, we have used an incompressible single phase flow simulation for approximate flow model, FSM^*. Due to the incompressible nature of the model, the solution for such a problem needs to be computed only once, since it is not a function of time. This property provides the necessary speed. The result of the incompressible single phase flow simulation is a pressure field, from which the velocity field may be determined. Using this velocity field, a set of streamlines are traced from injector to producer. A pseudo water cut curve (a water cut curve for a unit mobility ratio), f_w^* is obtained by calculating the fraction of streamlines that have broken through at time t at the producer. Note that f_w^* can be calculated on uniform grids as well as non-uniform grids, since streamlines can be traced on any grid type.

The gridding optimization is explained through the following synthetic example. Consider the high resolution $50 \times 1 \times 50$ models given in Figure-3.8. These realizations were generated by making perturbations to an initial realization (the model with $r = 0$ in Figure-3.8) through a single parameter r, where $r \in [-1, 1]$. The history matching technique given in Appendix-A.3 explains in detail how these perturbations were obtained. The realizations given in Figure-3.8 correspond to perturbations with $r = -1.0$, $r = -0.35$, $r = 0.125$, $r = 0.25$, $r = 0.525$ and $r = 0.95$.

Before studying the effects of upgridding / upscaling on ϵ and ϵ^*, we first recall the flow based upgridding method used in terms of the gridding parameters to be optimized. The upgridding method is adapted from Durlofsky *et al.* (1997); details regarding this upgridding method can be found in Appendix-B.2. For a 2D system, such as the ones given in Figure-3.8, four parameters control the gridding of the coarsened models, n_x^{max}, n_z^{max}, u_x^{max} and u_z^{max}. n_x^{max} and n_z^{max} by defining the maximum number of high resolution grid blocks that could be grouped in a single coarsened grid. For this demonstration, both parameters are set to values of 50, in order to eliminate their effects on the gridding. Setting these parameters to 50 eliminates the effects of these parameters, because the coarsened grids in each direction is allowed to contain all high resolution grid cells. In this example the high resolution models have dimensions of $50 \times 1 \times 50$. Hence the gridding of the coarsened

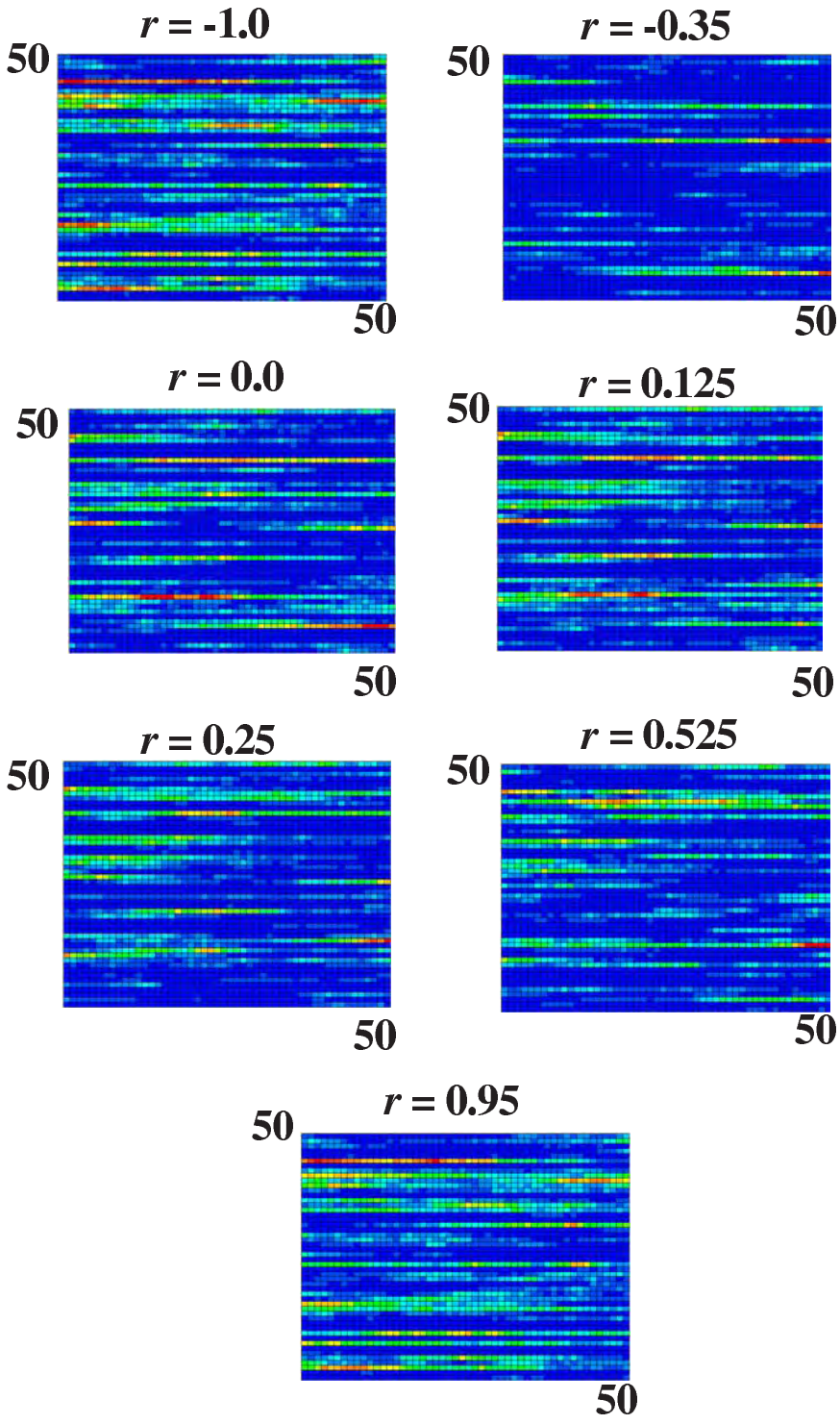

Figure 3.8: The permeability fields that correspond to perturbations of $r = -1.0$, $r = -0.35$, $r = 0.0$, $r = 0.125$, $r = 25$, $r = 0.525$ and $r = 0.95$.

models are controlled by only two parameters, u_x^{max} and u_z^{max}. These parameters determine the maximum number of layers (u_x^{max}) or columns (u_z^{max}) of the 2D high resolution model that can be grouped in a single layer or column of the coarsened model based on the average velocities of the layers or the columns. In other words, if the cumulative average velocities of layers or columns exceed the u^{max} parameter, then these layers or columns are represented as a single layer or a column on the coarsened model. If the u^{max} parameter is set to zero, then the coarsened model will have the same dimensions of the high resolution model. As the u^{max} parameter is increased, the coarsened model dimensions are reduced non-uniformly, refining regions of high velocity.

For each permeability field given in Figure-3.8, an ϵ^* surface is generated. This is accomplished as follows: FSM^* is performed on the high resolution model (on each of the permeability fields given in Figure-3.8) and the approximate flow response (pseudo water cut curve), $f^*_{w_{hrm}}$, is obtained. The u_x^{max} parameter is varied between 0 and 2 with an interval of 0.01 and the u_z^{max} parameter is varied between 0 and 10 with an interval of 0.1. For each combination of u_x^{max} and u_z^{max}, coarsening is applied and FSM^* is performed on the coarsened model, from which a pseudo water cut curve, $f^*_{w_{cm}}$, is obtained. The ϵ^* is then computed through the following relationship:

$$\epsilon^* = |f^*_{w_{hrm}} - f^*_{w_{cm}}| \tag{3.5}$$

ϵ^* is calculated for each combination of u_x^{max} and u_z^{max} and an exhaustive surface is generated. The ϵ^* surfaces for the permeability fields given in Figure-3.8 are given in Figure-3.9. A common feature of all surfaces given in Figure-3.9 is such that ϵ^* is zero when the u_x^{max} and u_z^{max} parameters are zero. This is expected since setting the gridding parameters to zero results in coarsened grid dimensions which are equal to the high resolution model grid dimensions. Hence, since no upscaling is performed, the pseudo water cut curves are identical.

Figure-3.10 shows those values of ϵ^* (given in Figure-3.9) less than 10. Any value larger than 10 is colored red. The ϵ^* surfaces vary significantly between realizations even though the underlying statistics of the reservoir are all the same (same variogram). Hence, an optimal grid for one realization is not necessarily optimal for another, even for realizations that are generated using the same geostatistical algorithm with the same parameter input.

The gridding optimization is performed on these surfaces with the aim to locate a *local*

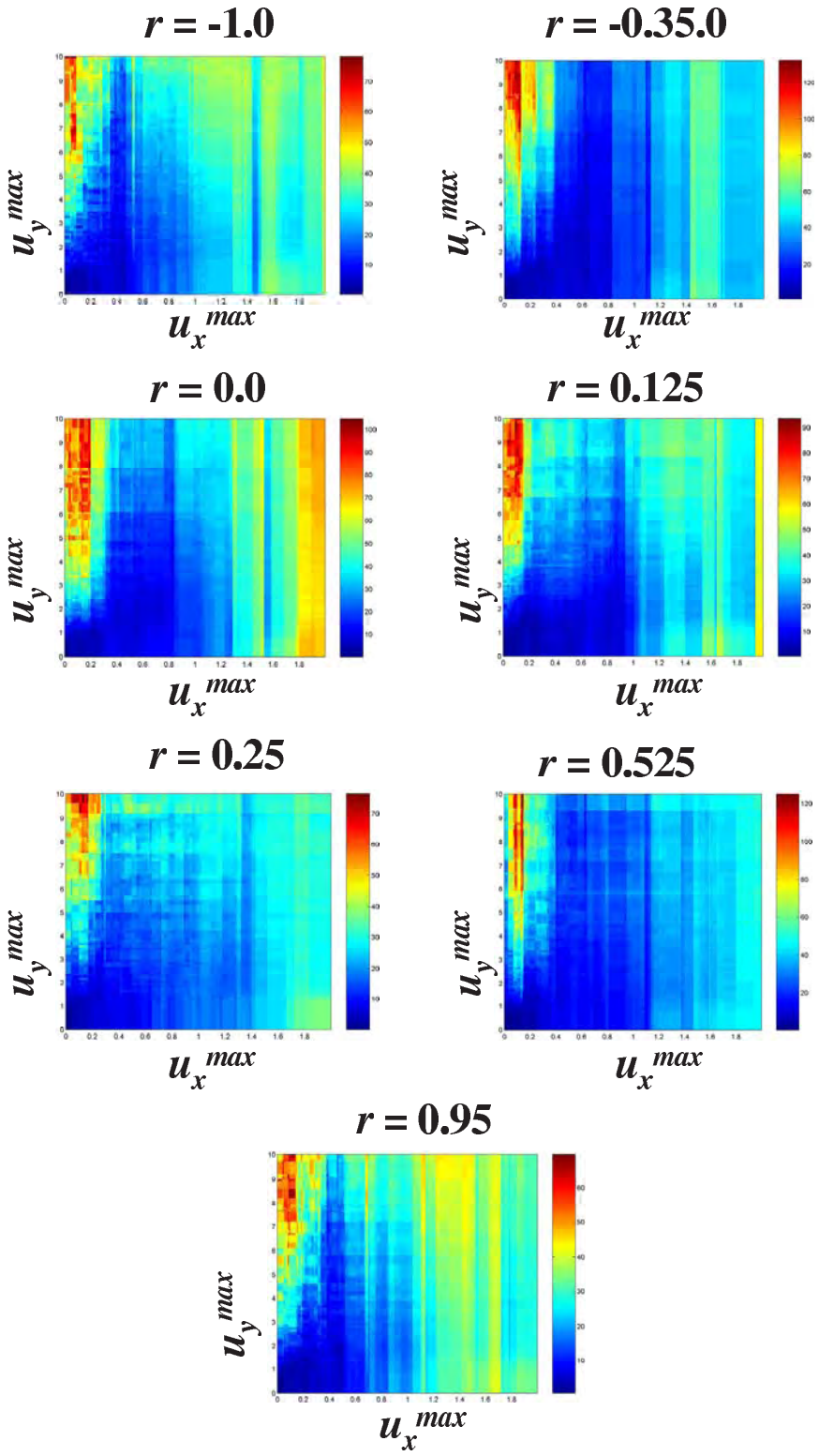

Figure 3.9: The ϵ^* surface for the permeability fields given in Figure-3.8, for parameters $r = -1.0$, $r = -0.35$, $r = 0.0$, $r = 0.125$, $r = 25$, $r = 0.525$ and $r = 0.95$.

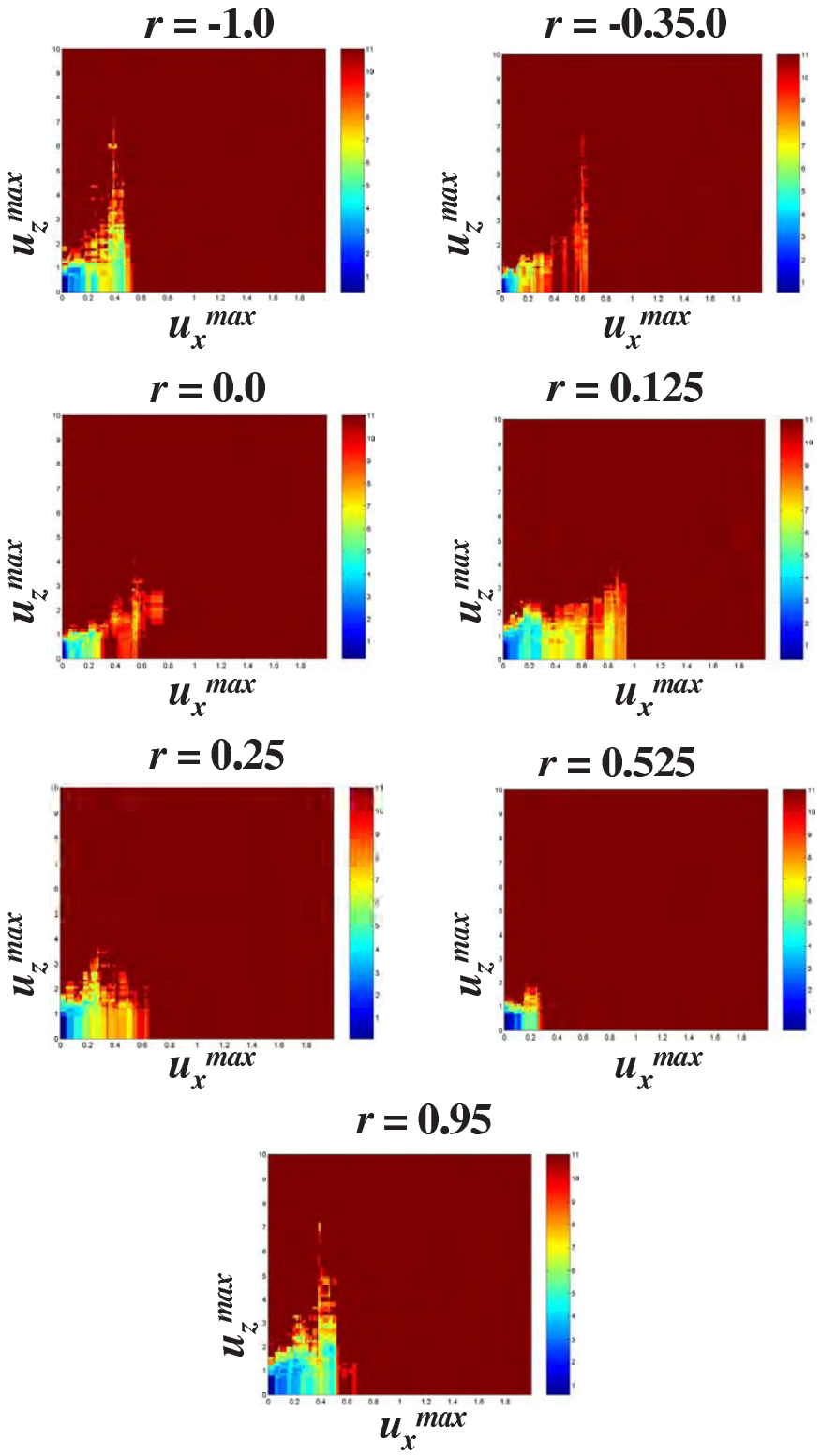

Figure 3.10: The error surfaces given in Figure-3.9 showing only $\epsilon^* < 10$.

minima. As shown in Figures 3.9 and 3.10, the global minimum is located at $u_x^{max} = u_z^{max} = 0$. This point on the ϵ^* surface corresponds to the high resolution model, where $\epsilon^* = 0$ at this point. During the gridding optimization, this global minimum should be avoided. Instead, the aim is to search for a local minimum on the ϵ^* surface, one that provides a coarsened model that contains the least amount of grid lines and yet has a high enough accuracy in terms of representing the high resolution model flow response.

In order to avoid the global minimum, the search for the local minima is performed in a region (on the ϵ^* surface) which excludes the global minima. In order to define this search region, we place constraints on the target dimensions of the coarsened model. Consider a $50 \times 1 \times 50$ high resolution model. For obtaining an optimal coarsened model, constraints may be placed on the coarsened grid dimensions such that, the coarsened grid dimensions would not exceed $30 \times 1 \times 30$. The selection of this threshold is problem specific, depending on the available CPU power. The gridding parameters u_x^{max} and u_z^{max} that correspond to $30 \times 1 \times 30$ dimensions on the coarsened model are then determined with the optimization accounting for the constraints on u_x^{max} and u_z^{max}. Note that a lower limit for the coarsened grid dimensions may also be assigned. In such cases the search for the optimal gridding parameters keeps the coarsened model dimensions within certain limits. For example, the coarsened model grid dimensions can be constrained between $10 \times 1 \times 10$ and $30 \times 1 \times 30$ during the gridding optimization.

Intuitively one would expect that the optimal coarsened model would always have grid dimensions equal to the constrained upper value, in the example presented above this would be dimensions of $30 \times 1 \times 30$. This however is not always the case due to the fact that upscaling does not generally provide monotonic "convergence" behavior. Hence, there stands a good chance for a coarsened model to perform better than a coarsened model with more grid blocks.

The optimization technique used in this study is the polytope method (Gill *et al.*, 1981; Press *et al.*, 1992). This is a non-gradient based algorithm which search for the optimal gridding parameters within the region defined above. The search within this region is accomplished by artificially setting a very high value for ϵ^* whenever points outside the region are used by the polytope algorithm. Hence the polytope algorithm rejects those parameter values that provide coarsened grid dimensions which exceed a certain threshold value.

3.3.2 Reduction of ϵ by reducing ϵ^*

The gridding optimization is always performed on the ϵ^* surface without any knowledge about the actual ϵ surface. The assumption is that if ϵ^* is minimized, the actual error ϵ is also minimized or at least significantly reduced. In reality, information regarding ϵ is never available, since computing ϵ would require the evaluation of the full flow simulation, FSM, on the high resolution model. Here, as a check, we do compute the full ϵ surfaces to investigate how well ϵ^* approximates ϵ.

In this subsection, we compare the actual ϵ^* and ϵ surfaces along with scatter plots of both quantities. Note that the relationship of ϵ with ϵ^* is a strong function of relative permeabilities, viscosity of the fluids and gravity effects. The effects of these factors are not considered in this thesis. In cases where these factors affect the relationship between ϵ and ϵ^*, different rank preserving models may need to be considered. For the demonstration, we will use the ϵ^* surfaces given in the previous section (see Figures 3.9 and 3.10) and compute the corresponding ϵ surfaces. Note that the generation of a single one of the ϵ^* surfaces given in Figure-3.9, requires FSM^* to be evaluated 20000 times (this only takes a couple of hours). Obtaining such surfaces for ϵ by evaluating FSM 20000 times is computationally too costly. Hence we make comparisons of coarser ϵ^* and ϵ surfaces where u_x^{max} is varied between 0 and 2 with an interval of 0.1 and u_z^{max} is varied between 0 and 10 with an interval of 1. Recall that in the previous section, u_x^{max} is varied between 0 and 2 with an interval of 0.01 and u_z^{max} is varied between 0 and 10 with an interval of 0.1.

Figure-3.11 shows the comparison between the ϵ^* and ϵ surfaces for the permeability fields given in Figure-3.8. To complete that comparison, we construct scatter plots between the two variables, as shown in Figure-3.12 and calculate their rank correlation coefficients, ρ_{rank}. If the rank correlation coefficients are high, then this would indicate a rank preserving relationship between ϵ and ϵ^*, a property desired for our gridding optimization. The rank correlation coefficients are summarized in Table-3.2. With the exception of $r = -0.35$, $r = 0.25$ and $r = 0.55$ the overall ρ_{rank} values are satisfactory, in the range $0.7 - 0.75$.

The general trend of the scatter plots are such that, a wider scatter between ϵ and ϵ^* is observed for higher values of ϵ^*. As ϵ^* decreases, the relationship between ϵ and ϵ^* become more linear. The scatter plots given in Figure-3.12 are for the entire ϵ and ϵ^* surfaces given in Figure-3.11. In other words, the range of the u_x^{max} and u_z^{max} are taken such that

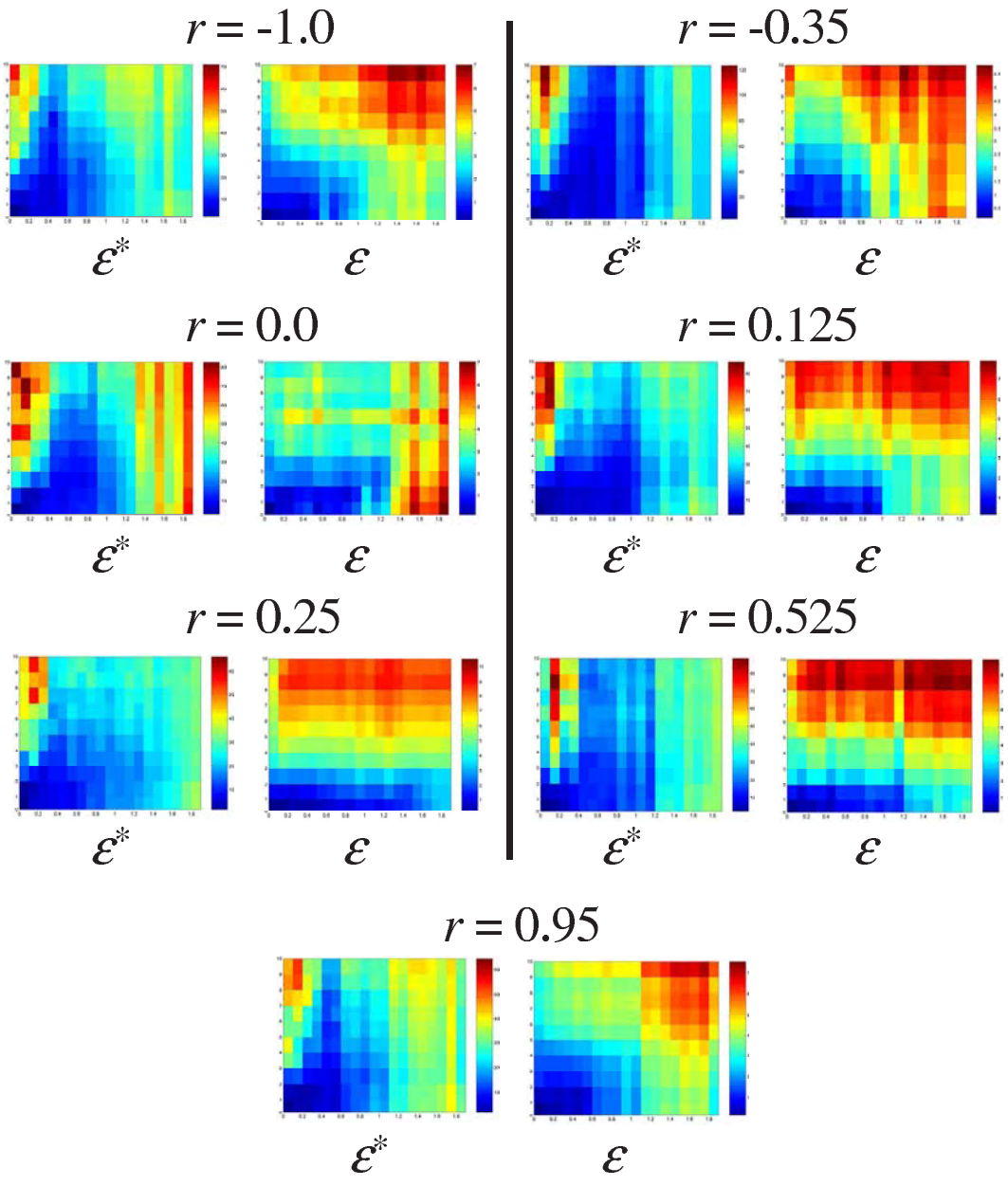

Figure 3.11: Comparison of ϵ^* and ϵ surfaces.

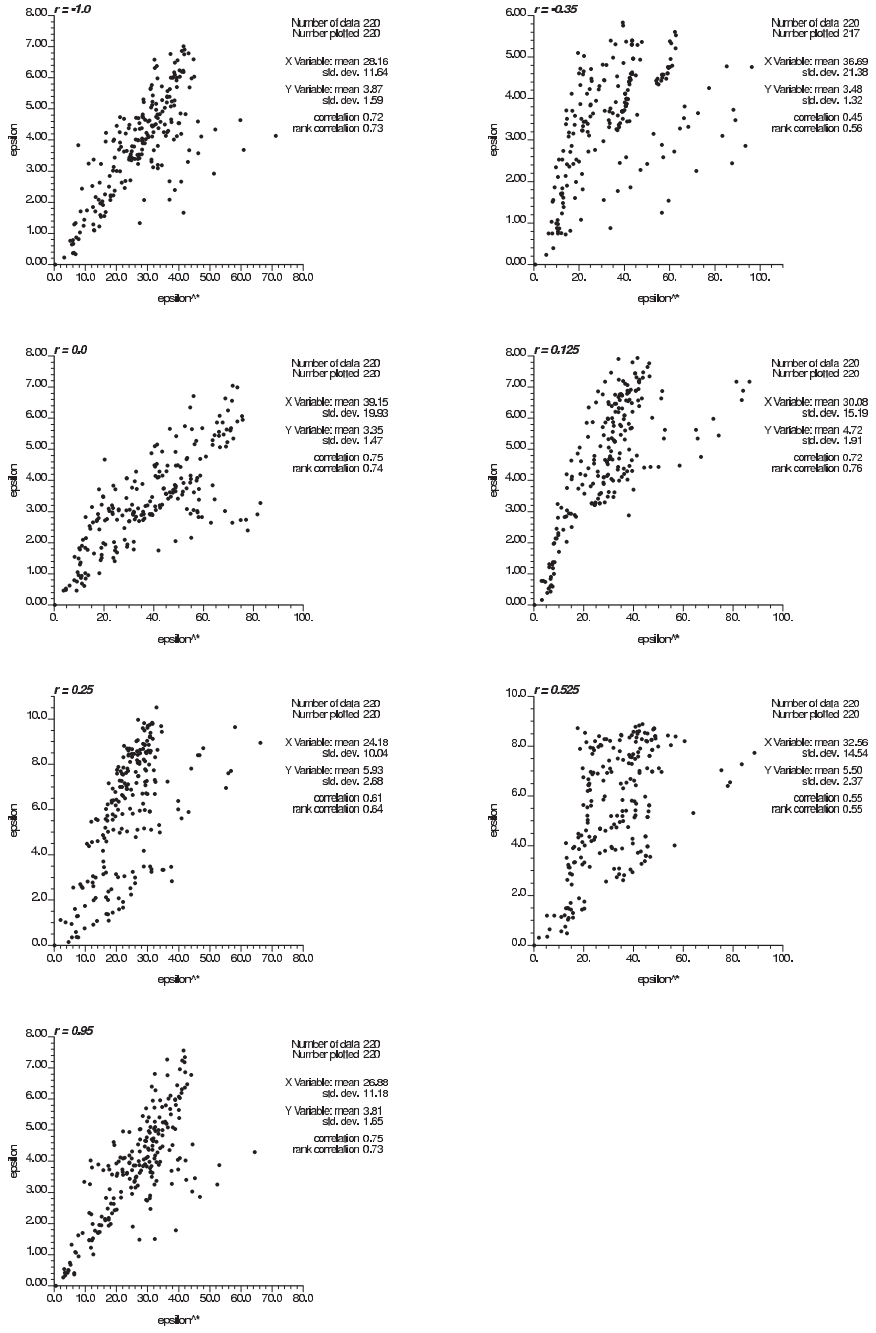

Figure 3.12: Scatter plot of ϵ^* and ϵ.

Table 3.2: The ρ_{rank} values for Figure-3.12.

$0 \leq u_x^{max} \leq 2$ $0 \leq u_x^{max} \leq 1$		$0 \leq u_z^{max} \leq 10$ $0 \leq u_z^{max} \leq 5$	
r	ρ_{rank}	r	ρ_{rank}
-1.0	0.73	-1.0	0.71
-0.35	0.56	-0.35	0.57
0.0	0.74	0.0	0.72
0.125	0.76	0.125	0.90
0.25	0.64	0.25	0.80
0.525	0.55	0.525	0.79
0.95	0.73	0.95	0.75

$0 \leq u_x^{max} \leq 2$ and $0 \leq u_z^{max} \leq 10$. However, the focus should be given to lower values of ϵ^* since the aim is to determine the optimal gridding parameters u_x^{max} and u_z^{max} that provide a local minimum on the ϵ^* surface. Hence we look at the scatter plots of ϵ and ϵ^* values corresponding to a range where $0 \leq u_x^{max} \leq 1$ and $0 \leq u_z^{max} \leq 5$. The scatter plots of ϵ and ϵ^* for this region are given in Figure-3.13. with the rank correlation coefficients summarized in Table-3.2. All ρ_{rank} values with the exception of $r = -0.35$ have improved considerably.

The scatter plot for $r = -0.35$ given in Figure-3.13 still contain high values of ϵ^*. A scatter plot of ϵ versus f is constructed, for values of $\epsilon^* \leq 30$ within the range of parameters $0 \leq u_x^{max} \leq 1$ and $0 \leq u_z^{max} \leq 5$. Figure-3.14 shows this plot, where the rank correlation coefficient has improved to 0.77.

We now consider another synthetic example to test if FSM^* provides rank preserving approximations. A 2D ($100 \times 100 \times 1$) channel model given in Figure-3.15 is used where a quarter five spot pattern is simulated for 500 days.

The upgridding algorithm used for this demonstration is 3DDEGA, adapted from Garcia *et al*. (1992), see Appendix-C for details of the algorithm. The 3DDEGA (3 dimensional discrete elastic grid adjustment) algorithm is applied to the generation of quadrilateral or hexahedral grids suitable for grid adaptation based on reservoir properties (ϕ, k), pressure fields, saturation fields or any other variable. The main idea behind the 3DDEGA algorithm is to generate coarse grid blocks that are as homogeneous as possible in terms of the

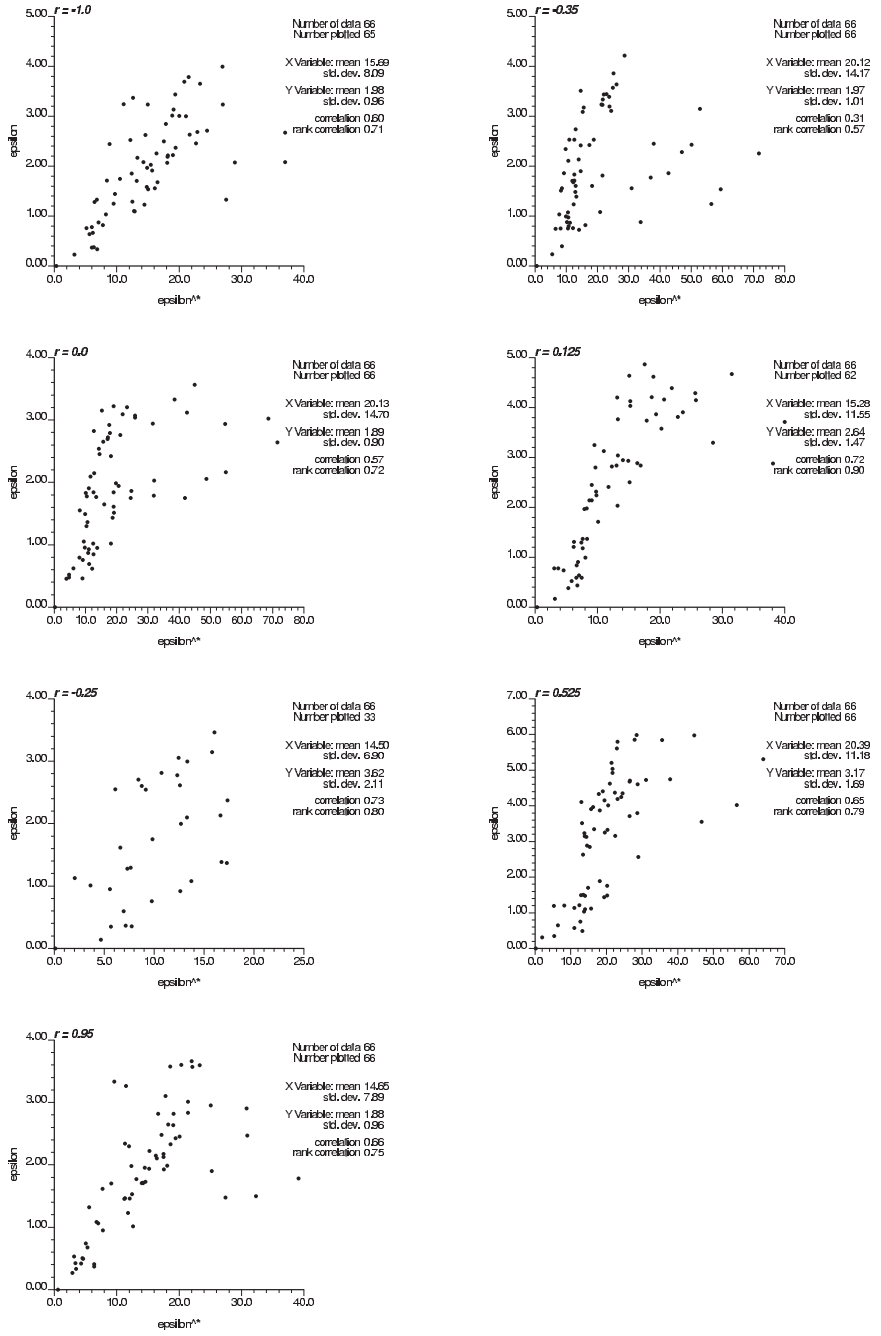

Figure 3.13: Scatter plot of ϵ^* and ϵ for $0 \leq u_x^{max} \leq 1$ and $0 \leq u_z^{max} \leq 5$.

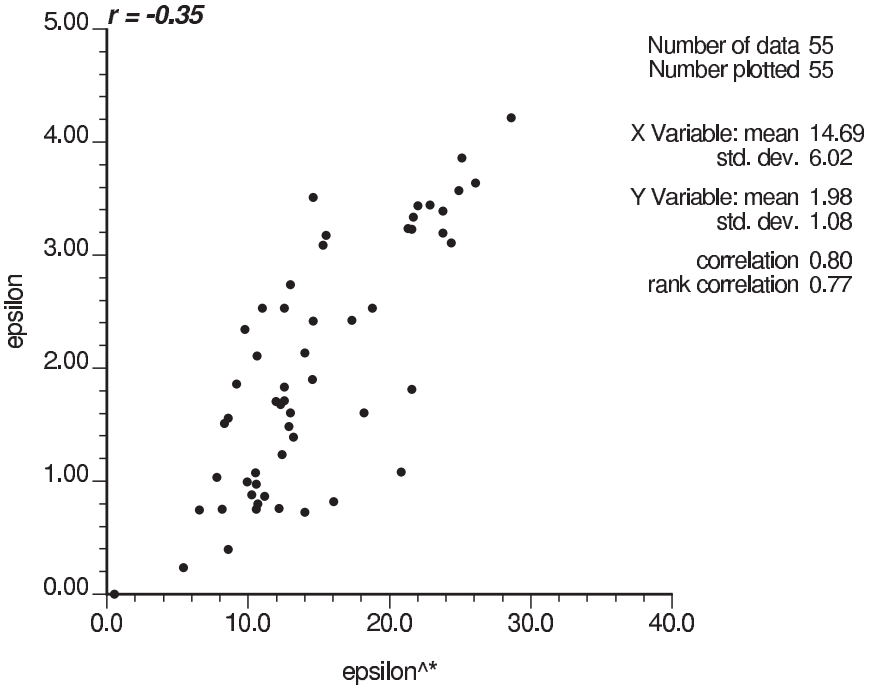

Figure 3.14: The scatter plot of ϵ versus ϵ^* for $r = -0.35$.

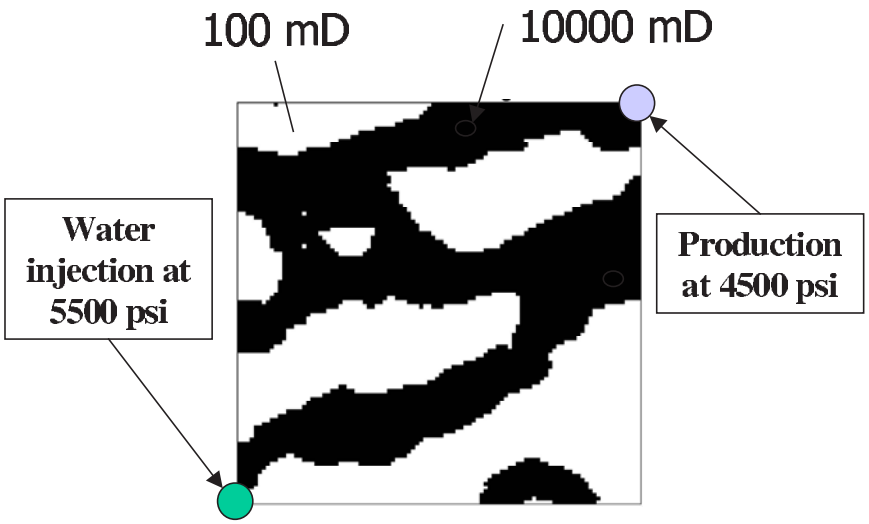

Figure 3.15: The reference permeability field.

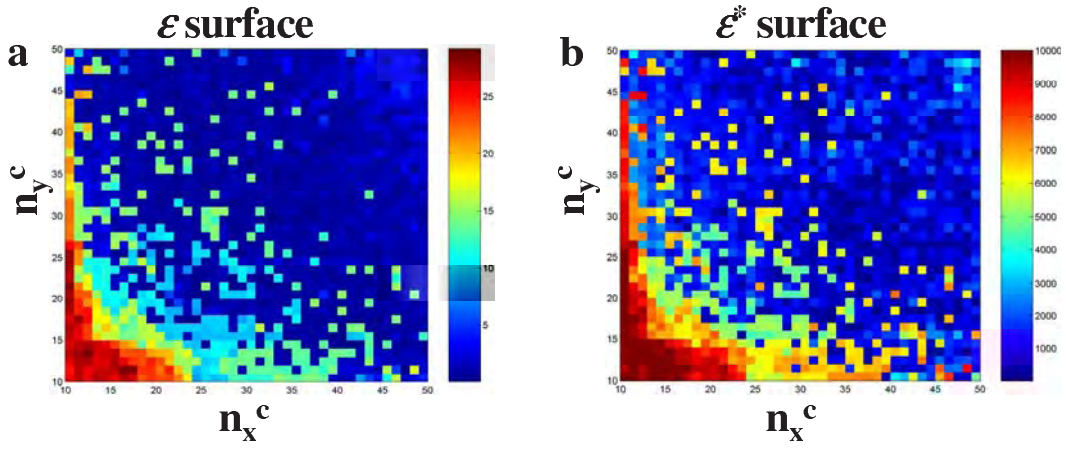

Figure 3.16: Comparison of the ϵ and ϵ^* surface for the channel example, (a) ϵ surface (b) ϵ^* surface.

underlying heterogeneity.

The approximate flow model is performed using the commercial streamline simulator 3dsl (Streamsim, 2000). 3dsl is run in "TRACER" mode for a single time step and the resulting streamlines are traced to determine the approximate flow response, f_w^*. ϵ and ϵ^* surfaces are generated for different upscaling ratios. The range of the coarsened grid dimensions are $10 \leq n_x^c \leq 50$ and $10 \leq n_y^c \leq 50$. Both surfaces are compared in Figure-3.16. The similarity in the pattern structure is apparent. As the coarsened grid dimensions are decreased, both ϵ and ϵ^* increase. As the model is coarsened, the upscaling errors increase as well.

For a closer analysis, we look at the scatter plot between ϵ and ϵ^* given in Figure-3.17. The correlation coefficient is at a very high value, near 0.98, indicating a strong linear relationship between ϵ and ϵ^*. However, the rank correlation coefficient is much lower of 0.66.

In order to understand the difference between the correlation coefficient and the rank correlation coefficient, we look at the scatter plot of ϵ versus ϵ^* for values of $\epsilon^* \leq 2000$ (given in Figure-3.18a) and for values of $\epsilon^* \geq 2000$ (given in Figure-3.18b). The scatter plot for $\epsilon^* \leq 2000$ displays no correlation at all, while on the other hand the scatter plot for $\epsilon^* \geq 2000$ displays a strong correlation. Both the correlation coefficient and the rank correlation coefficients for Figure-3.18b are high. This indicates that for large upscaling errors, ϵ and ϵ^* are indeed rank preserving. However, for small upscaling errors, the rank

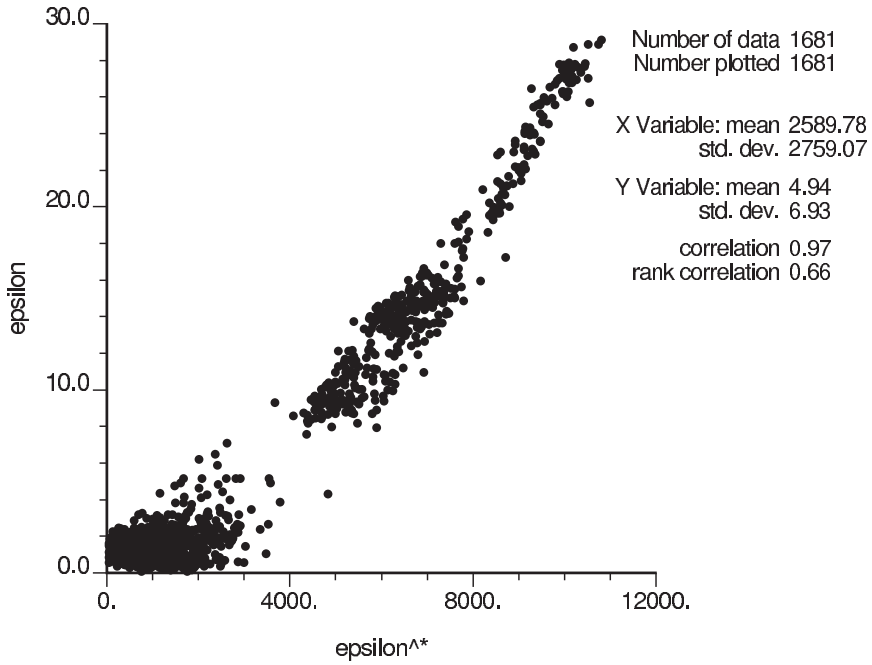

Figure 3.17: Scatter plot of ϵ versus ϵ^*.

preserving property of FSM and FSM^* disappears. In other words, ϵ^* can be used to identify large upscaling errors. However when $\epsilon^* \leq 2000$, ϵ^* is no longer representative of the true upscaling error ϵ. Hence gridding optimization can be applied to reduce the upscaling errors only to a certain degree.

Figure-3.18b also shows that when $\epsilon^* \leq 2000$, ϵ has a range of approximately $0 \leq \epsilon \leq 3$. This leads to the conclusion that rank-preservation approximation of ϵ by ϵ^* is reasonable for $\epsilon \geq 3$. In order to provide visual appreciation regarding the magnitude of ϵ, Figure-3.19 compares the flow responses of various coarsened models along with their ϵ values. The black solid line represents the actual flow response of the high resolution model. First the model is upscaled to grid dimensions of $37 \times 45 \times 1$ and FSM is applied to this coarsened model. The solid blue line in Figure-3.19 is obtained. The difference between the solid blue line and the solid black line represents $\epsilon = 2.2$. Then the model is coarsened to $26 \times 28 \times 1$ and the resulting flow response is given by the green curve in Figure-3.19. In this case $\epsilon = 15.5$. A final comparison is made by coarsening the high resolution model to coarse grid dimensions of $17 \times 12 \times 1$. The solid red line in Figure-3.19 represents the flow response for this last coarsened model. The difference between the high

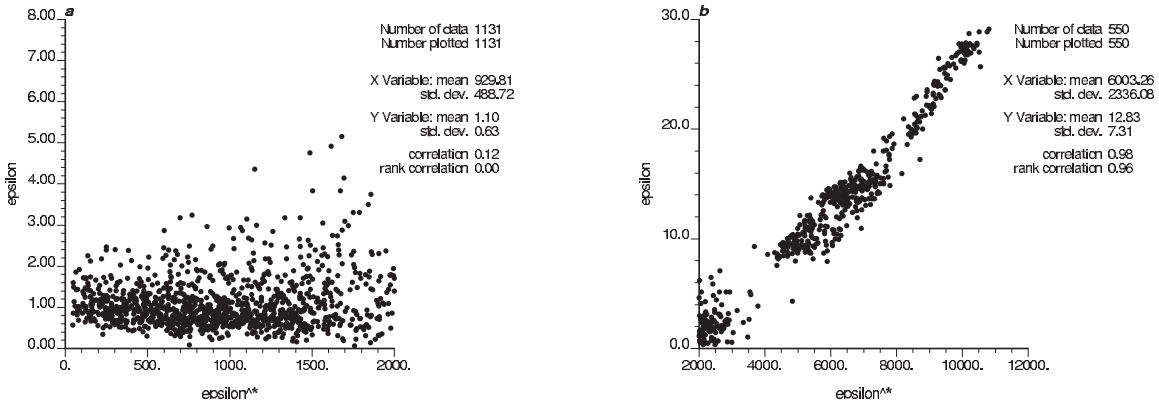

Figure 3.18: (a) scatter plot of ϵ versus ϵ^* for $\epsilon^* \leq 2000$ (b)scatter plot of ϵ versus ϵ^* for $\epsilon^* \geq 2000$.

resolution model flow response is $\epsilon = 26.6$.

It appears from Figure-3.19 that the visual difference between the high resolution flow response and the coarsened model response represented by $\epsilon \leq 3$ (blue curve) is small compared to the other flow responses. The gridding optimization will reduce large upscaling errors for discrete facies models to tolerable values.

In this subsection two synthetic examples have been given to test if the gridding optimization could be performed on the ϵ^* surface. The first test was conducted on a continuous permeability field where the underlying geological continuity model is represented through a variogram model. Comparing ϵ and ϵ^* values on this test case yielded results such that for lower values of ϵ, ϵ^* provided rank preserving approximations from which the gridding optimization could be performed. On the other hand, the second test case which represented a facies model (the geological continuity model is now provided by a training image), yielded results such that ϵ^* provided rank preserving results for ϵ for higher values of ϵ. A gridding optimization in this case would provide the screening of large upscaling/upgridding errors. In both cases, these properties work to the advantage of gridding optimization.

3.3.3 The objective function $O(\mathbf{r})$

The previous subsection studied the relationship between ϵ and ϵ^*. In this subsection we study the impact of the optimally gridded coarsened model on the objective function $O(\mathbf{r})$ representing the mismatch between the calculated data and the observed field data. For this

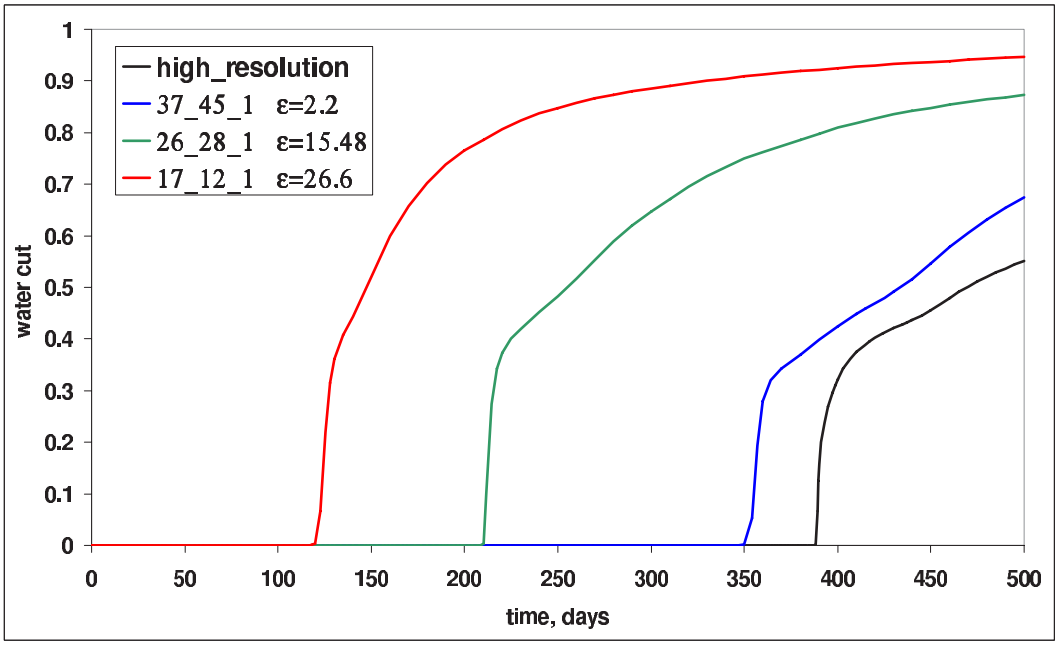

Figure 3.19: Flow responses of the high resolution model and various coarsened models, comparing ϵ values visually.

demonstration, the following synthetic example is used. Figure-3.20 illustrates the high resolution ($50 \times 1 \times 50$) reference permeability field to which flow simulation is applied for a period of 500 days. The flow response corresponding to the reference field is given in Figure-3.21. We now consider the history matching technique given in Appendix-A.3 where the perturbations of an initial guess permeability field are parameterized by a single parameter r, where $r \in [-1, 1]$ (the gradual deformation of sequential simulation method). The task in history matching is to find an optimal value of the r parameter corresponding to a permeability field which flow response minimizes the objective function:

$$O(r) = \|\mathbf{RP}_{\mathbf{z}}(r) - \mathbf{D}\| \tag{3.6}$$

where $\mathbf{RP}_{\mathbf{z}}(r)$ is the flow response of the model $\mathbf{z}(r)$ and $\mathbf{D}$ is the observed field data.

First we calculate exhaustively the objective function as function of the r parameter. This is accomplished by varying the r parameter between -1 and 1 with an interval of 0.01. Flow simulation (with the same boundary conditions shown in Figure-3.20) is performed on each permeability field corresponding to each value of r. The response, $\mathbf{RP}_{\mathbf{z}}(r)$ is

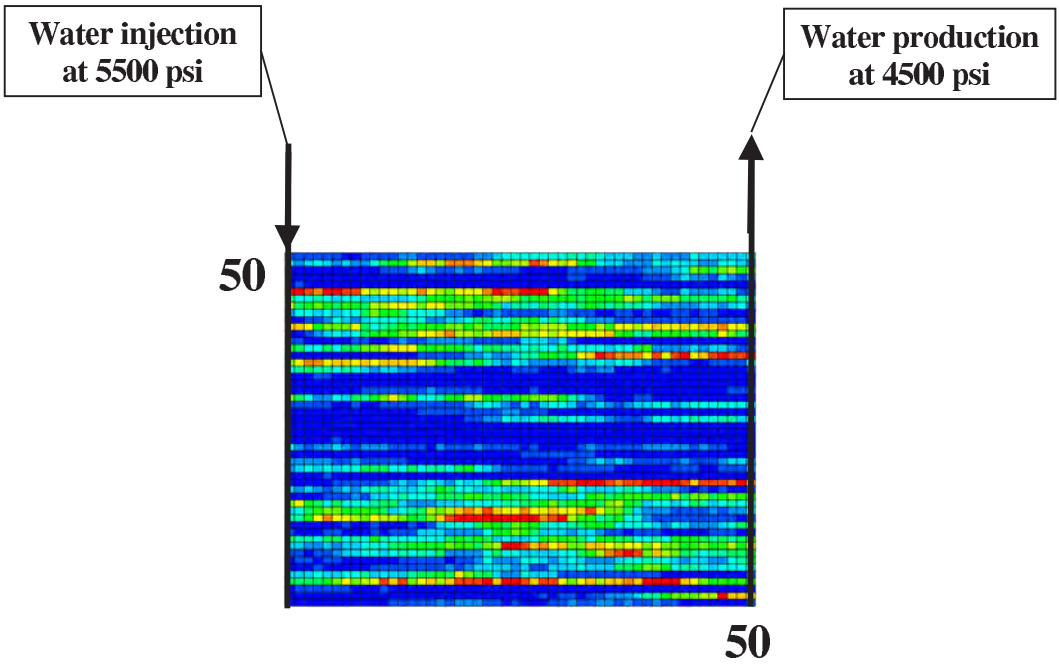

Figure 3.20: The reference permeability field.

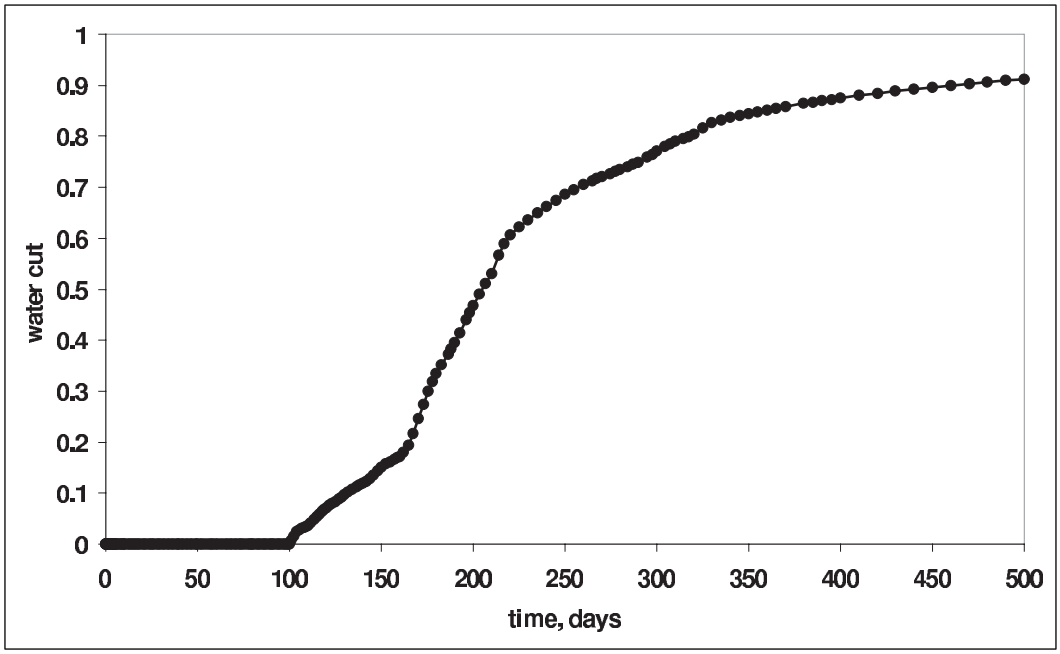

Figure 3.21: The flow response of the reference permeability field for 500 days.

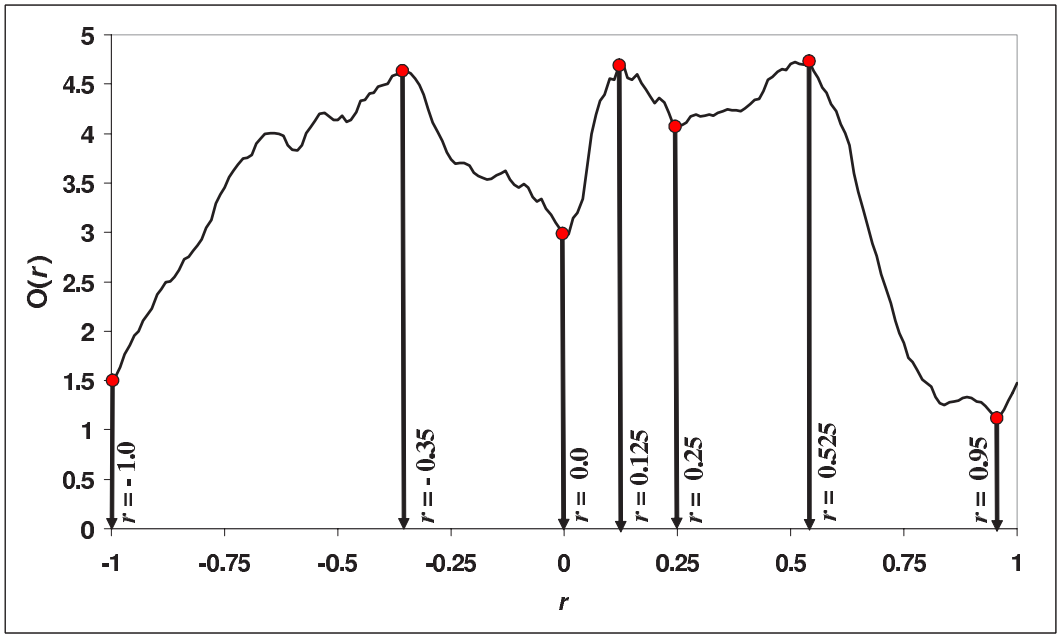

Figure 3.22: The exhaustive objective function evaluated on high resolution models.

obtained and the objective function is calculated where the field response, **D**, in this case is the response given in Figure-3.21.

Some values of r are chosen for closer study, $r = -1.0$, $r = -0.35$, $r = 0.0$, $r = 0.125$, $r = 0.25$, $r = 0.525$ and $r = 0.95$ which are also illustrated in Figure-3.22. The permeability fields corresponding to each r parameter have been given previously in Figure-3.8. Based on the corresponding ϵ^* surfaces given in Figure-3.23, a local minimum is selected for each r-value case. The minima are both shown on the figure, indicated by the black dots and are given in Table-3.3 along with the corresponding grid dimensions.

In order to make a comparison, the high resolution permeability fields under study, given in Figure-3.8, are non-uniformly upscaled to coarsened models of $40 \times 1 \times 40$ and $10 \times 1 \times 10$. The objective of constructing all these coarsened models is to compare their pseudo flow responses ($\mathbf{RP}^*_{z^{up}}(r)$ obtained by evaluating FSM^*), to the full flow responses ($\mathbf{RP}_{z^{up}}(r)$ obtained by evaluating FSM) and their performance in estimating the $O(r)$ curve of the high resolution model given in Figure-3.22. For each r value under study, Figures 3.24 - 3.30 show the high resolution model, the $10 \times 1 \times 10$ coarsened model, the $40 \times 1 \times 40$ coarsened model, the optimally gridded coarsened model (optimal grid

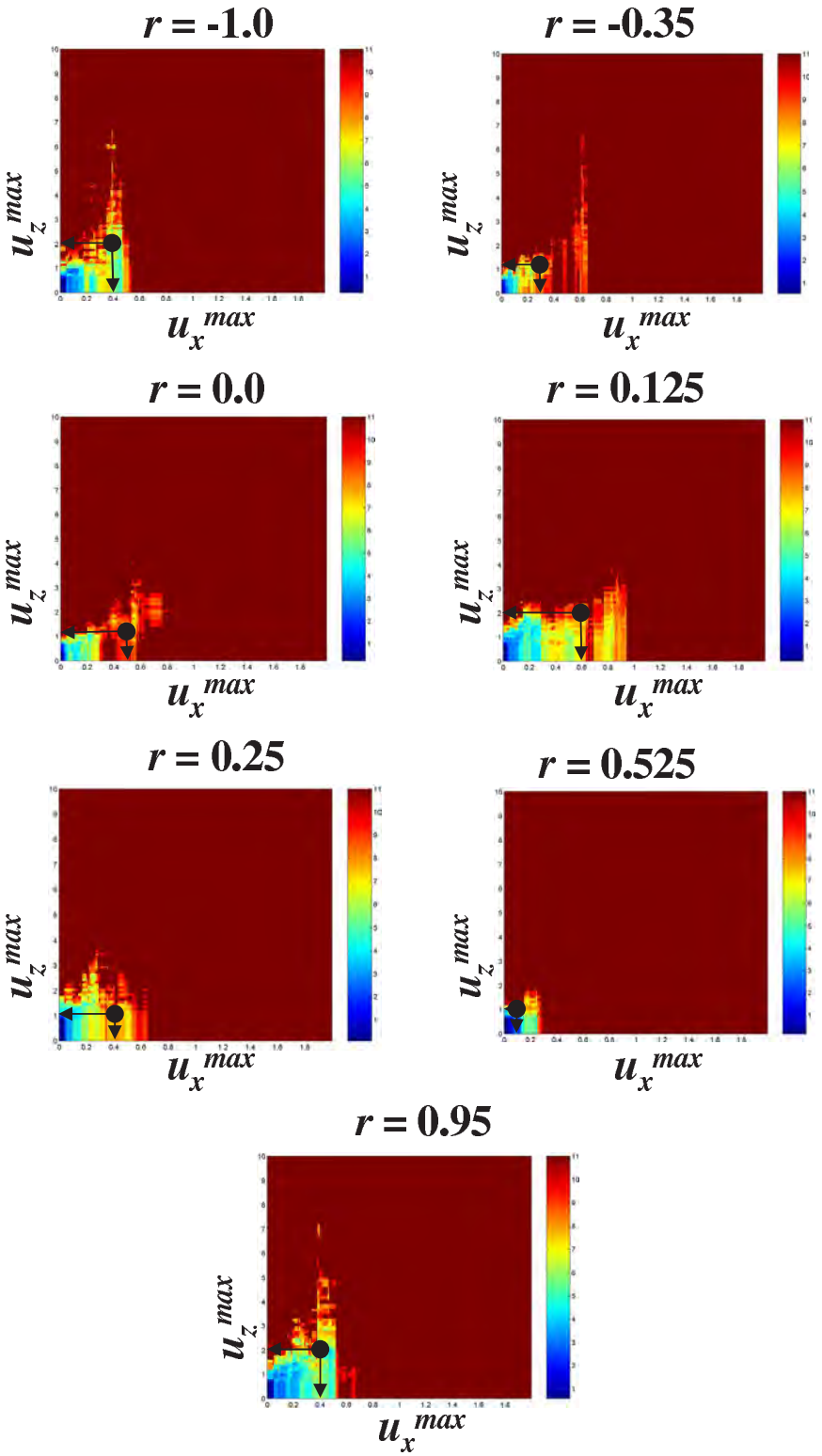

Figure 3.23: The error surfaces for $\epsilon^* < 10$ with sample optimal points.

Table 3.3: u_x^{max} and u_z^{max} values chosen from ϵ^* surfaces given in Figure-3.23.

r	u_x^{max}	u_z^{max}	coarsened model grid dimensions
-1.0	0.4	2.0	$17 \times 1 \times 24$
-0.35	0.3	1.0	$33 \times 1 \times 20$
0.0	0.5	1.1	$27 \times 1 \times 20$
0.125	0.6	2.0	$19 \times 1 \times 21$
0.25	0.4	1.0	$48 \times 1 \times 29$
0.525	0.1	1.0	$33 \times 1 \times 20$
0.95	0.4	2.0	$19 \times 1 \times 27$

dimensions are given in Table-3.3), the pseudo flow responses of all models ($\mathbf{RP}^*$) and the full flow responses of all models ($\mathbf{RP}$).

It appears visually from the figures that in all cases the $10 \times 1 \times 10$ coarsened model is not refined enough to represent the fine scale high permeability layers. On the other hand, the $40 \times 1 \times 40$ models represent the high resolution model rather well, but the coarsening is not significant enough for a significant speedup in evaluating the flow simulations. The optimal coarsened models are refined enough to represent the fine scale high permeability regions and are also coarsened enough for evaluating flow simulations efficiently.

Figures 3.24-3.30 show how the pseudo flow response of the $40 \times 1 \times 40$ model tracks the pseudo flow response of the high resolution model for values of r. The $10 \times 1 \times 10$ model fails to do so. The optimally gridded model on the other hand, tracks the high resolution model pseudo flow response essentially as well as the $40 \times 1 \times 40$ model.

Finally we make a comparison regarding the effects of the above coarsened models on the objective function $O(r)$. For this purpose, we look at the performance of the coarsened models in terms of the $O(r)$. The $O(r)$ of each of the coarsened model is plotted versus the r parameter along with the exhaustive $O(r)$ behavior of the high resolution model previously given in Figure-3.22. Figure-3.31 shows the results. The $40 \times 1 \times 40$ models, track the exhaustive $O(r)$ curve of the high resolution model very well. The $10 \times 1 \times 10$ models fail in this respect. The optimally gridded models have nearly the same level of accuracy in approximating $O(\mathbf{r})$ as the $40 \times 1 \times 40$ models, but with a considerably reduced number of grid blocks.

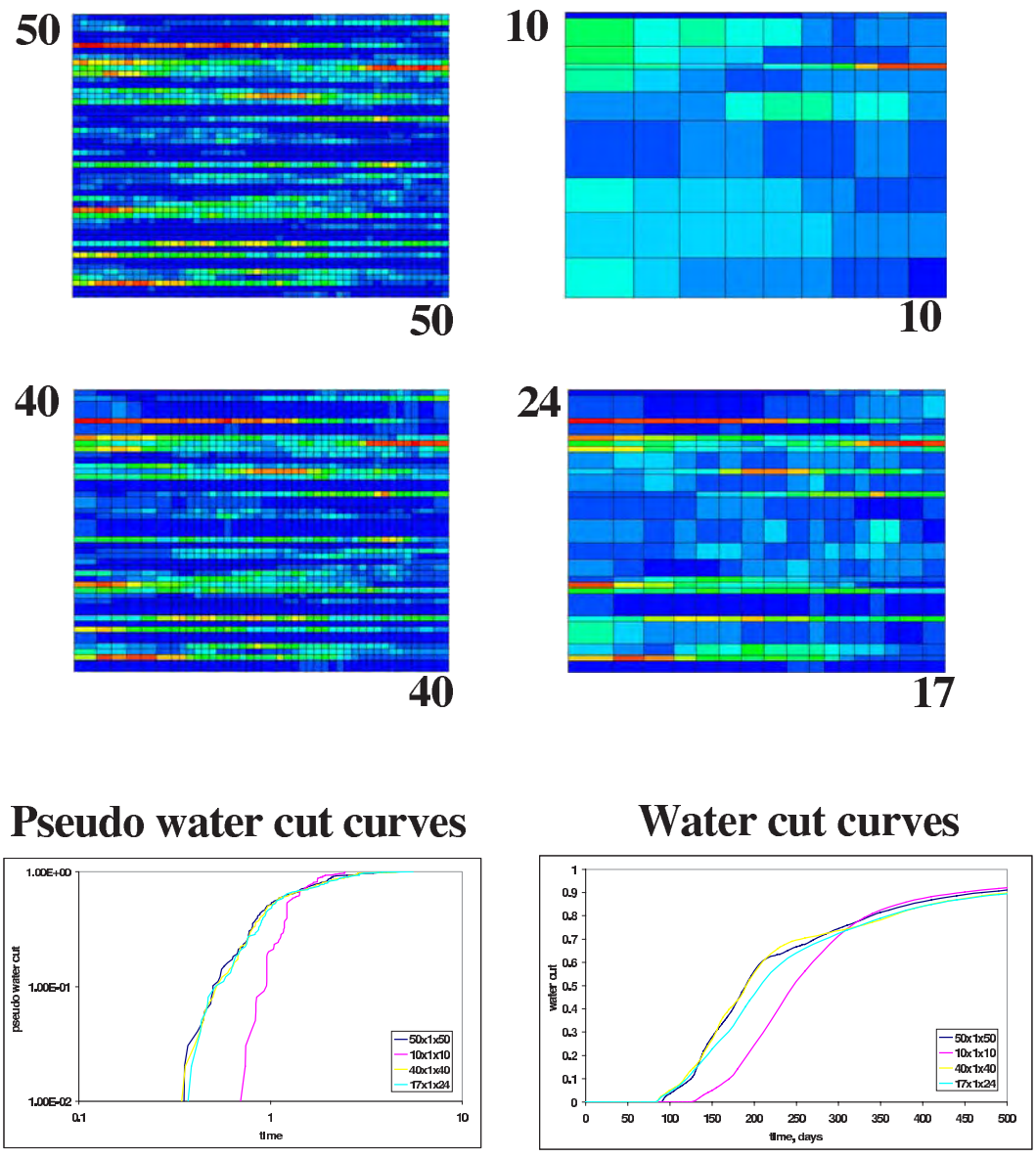

Figure 3.24: Comparison of different model resolutions and their flow responses for $r = -1.0$.

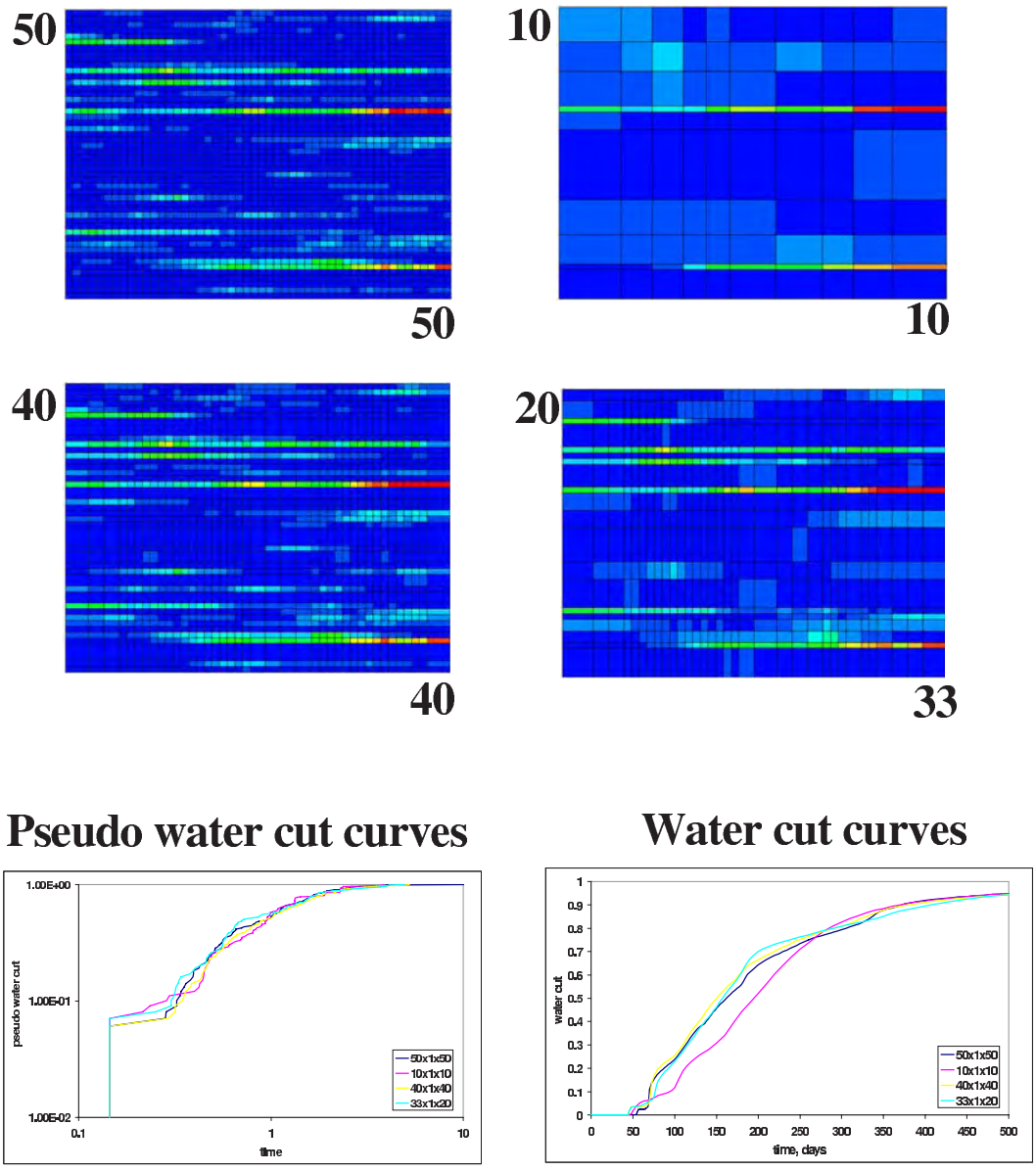

Figure 3.25: Comparison of different model resolutions and their flow responses for $r = -0.35$.

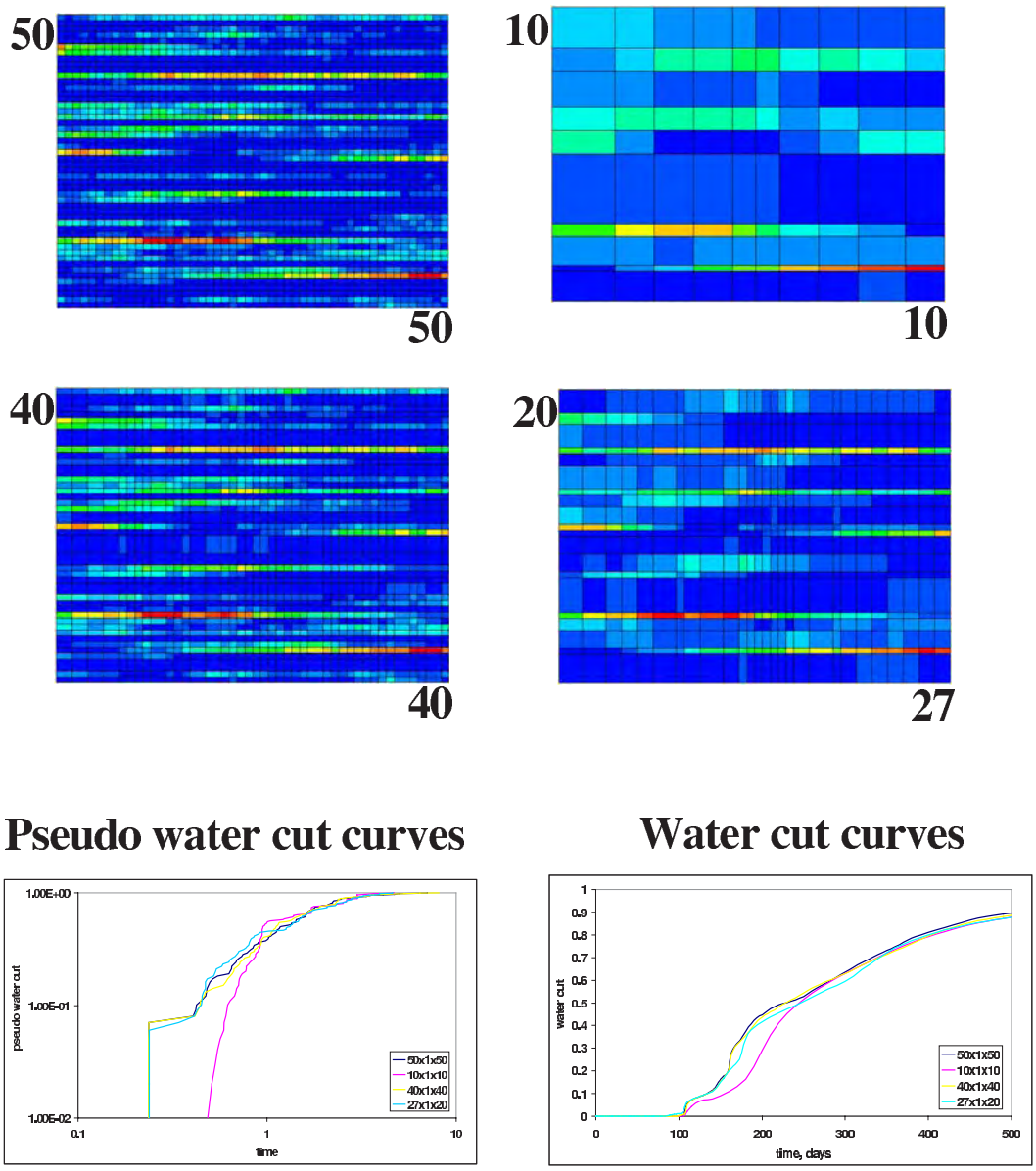

Figure 3.26: Comparison of different model resolutions and their flow responses for $r = 0.0$.

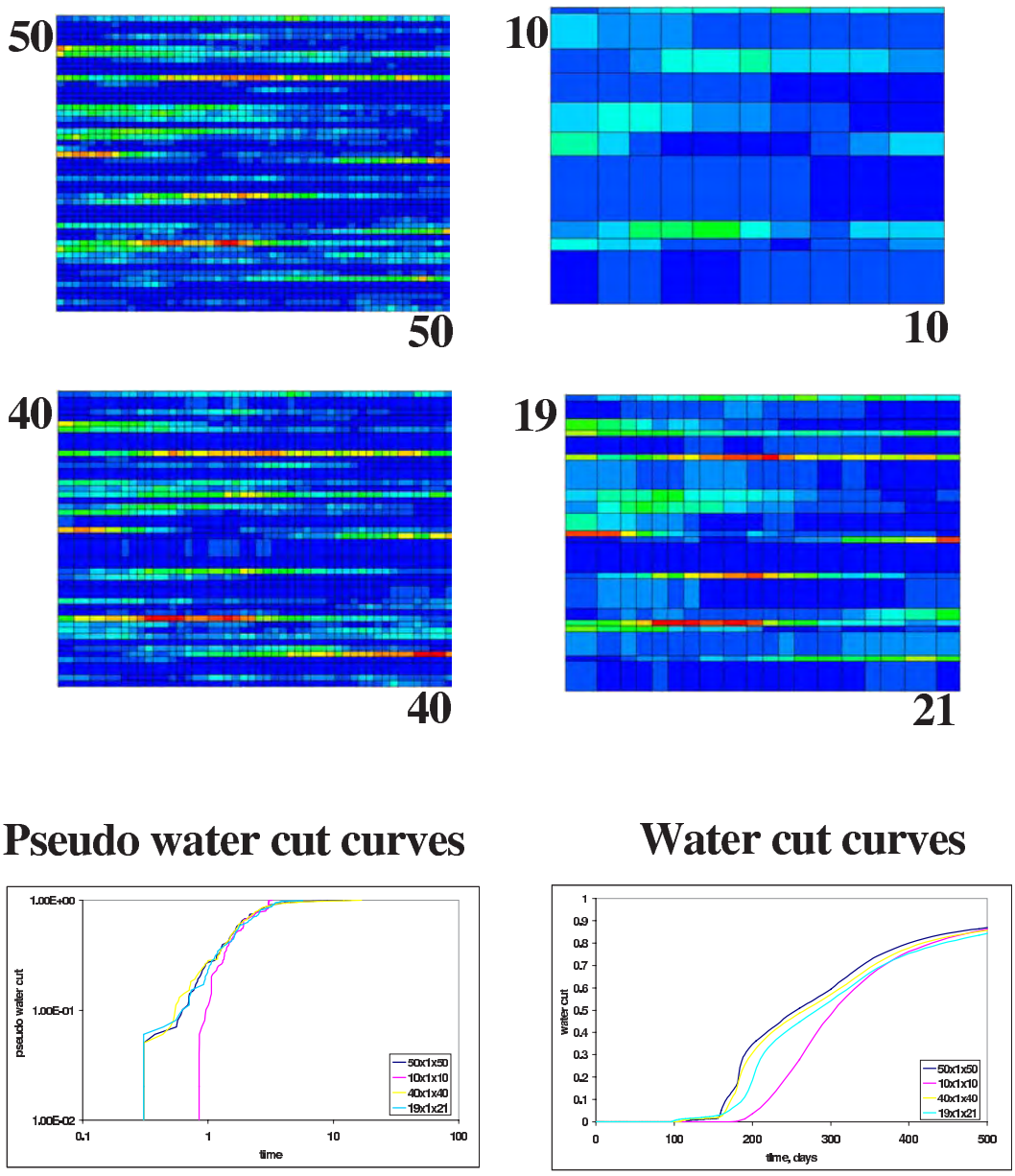

Figure 3.27: Comparison of different model resolutions and their flow responses for $r = 0.125$.

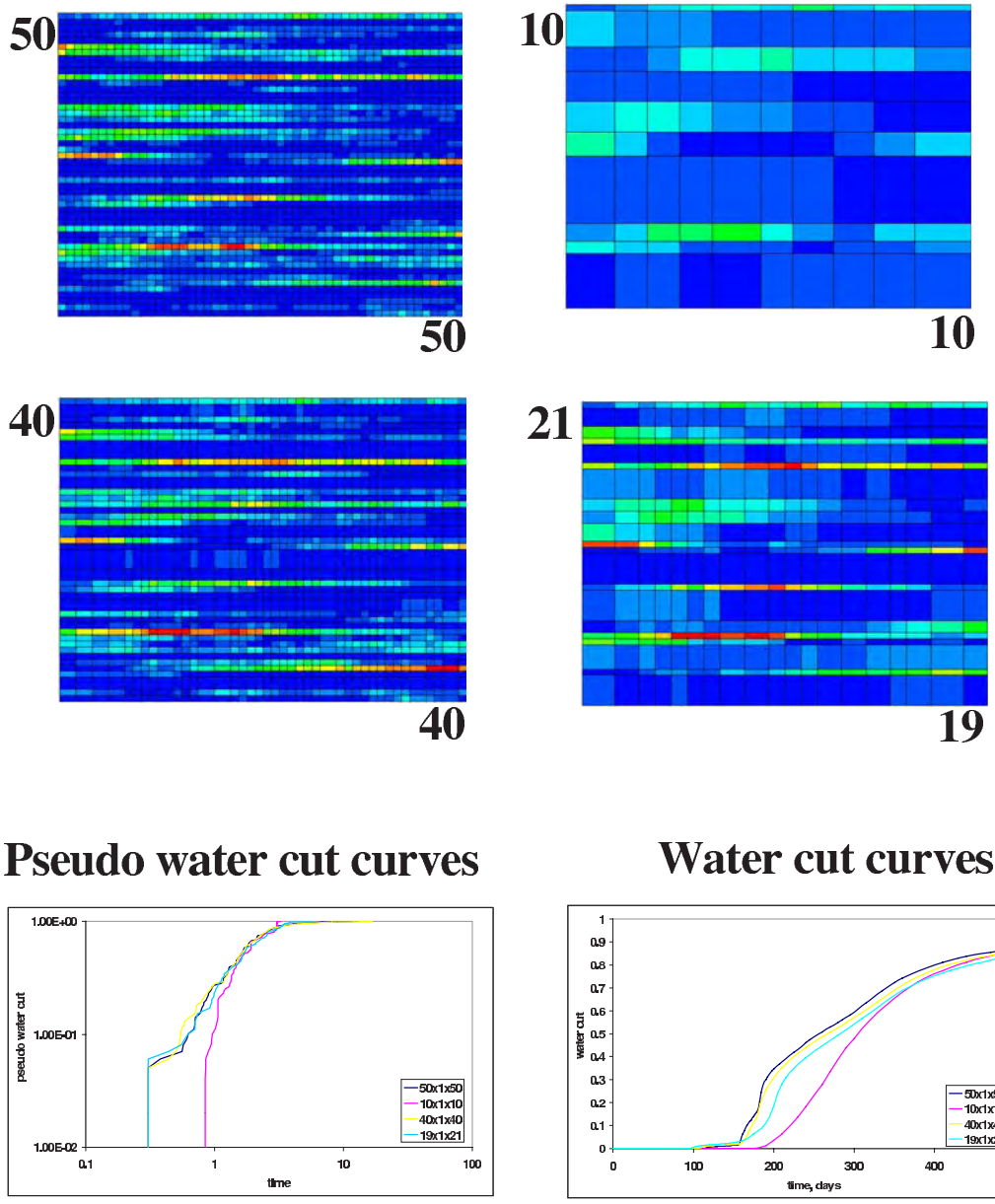

Figure 3.28: Comparison of different model resolutions and their flow responses for $r = 0.25$.

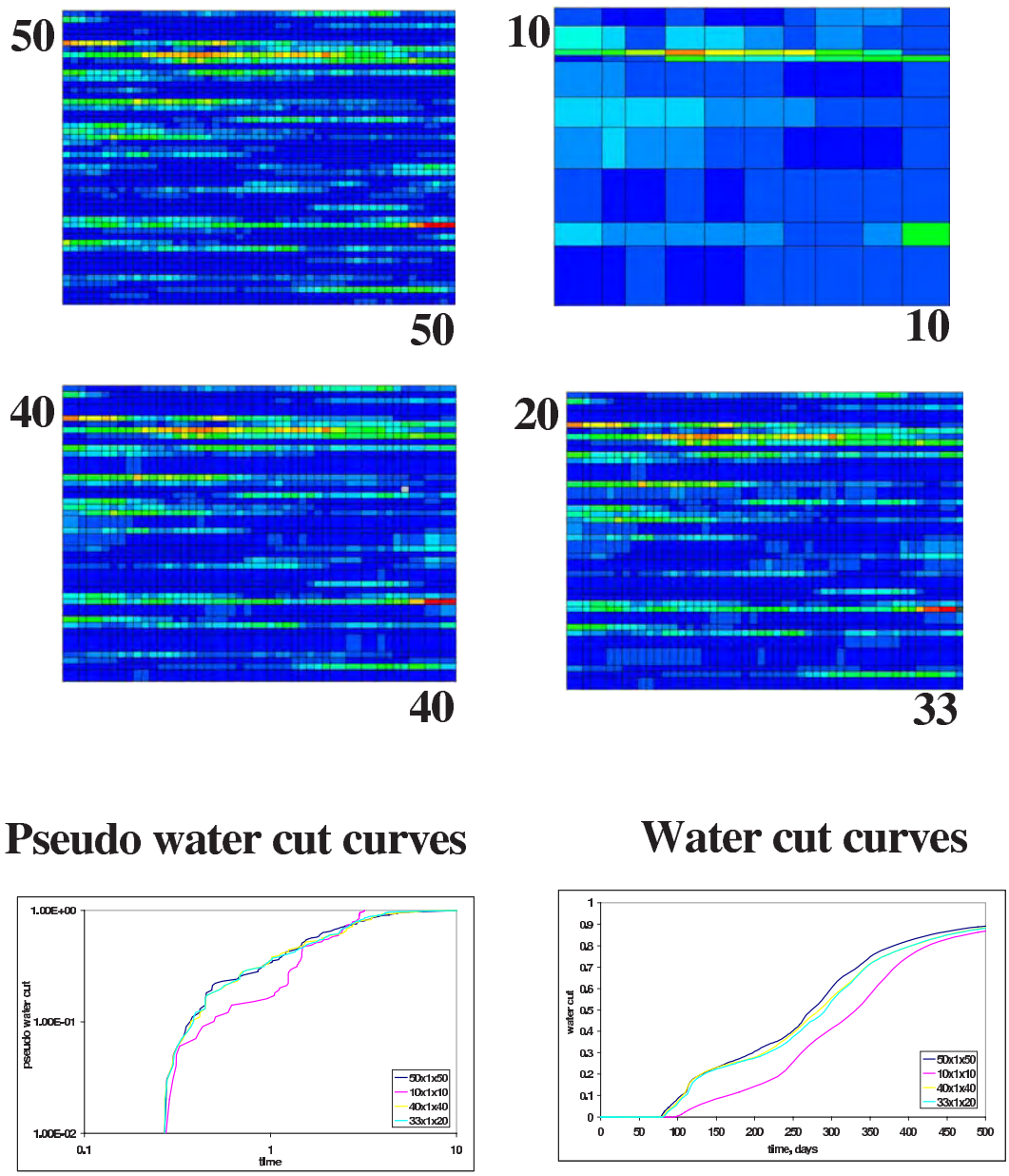

Figure 3.29: Comparison of different model resolutions and their flow responses for $r = 0.525$.

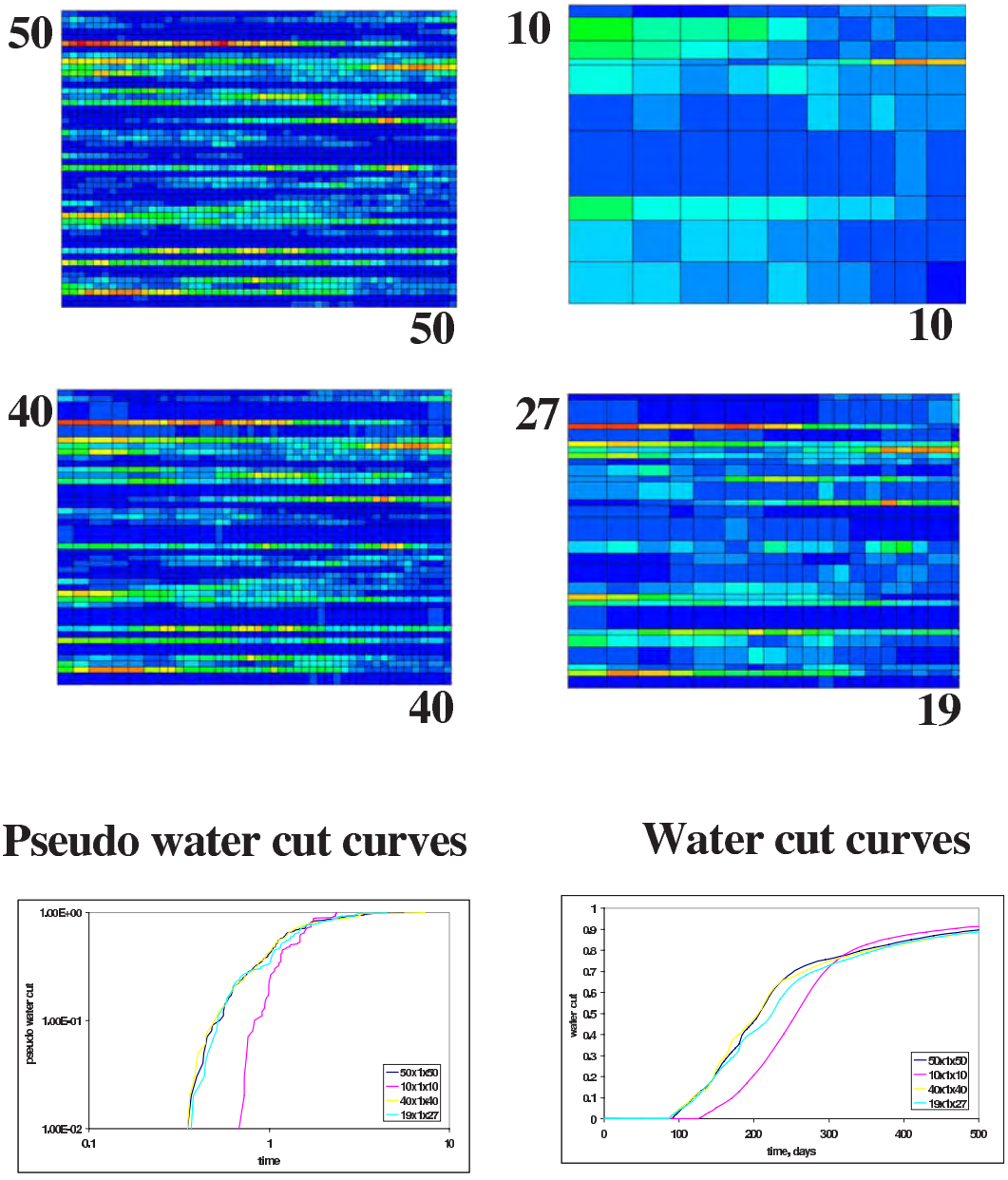

Figure 3.30: Comparison of different model resolutions and their flow responses for $r = 0.95$.

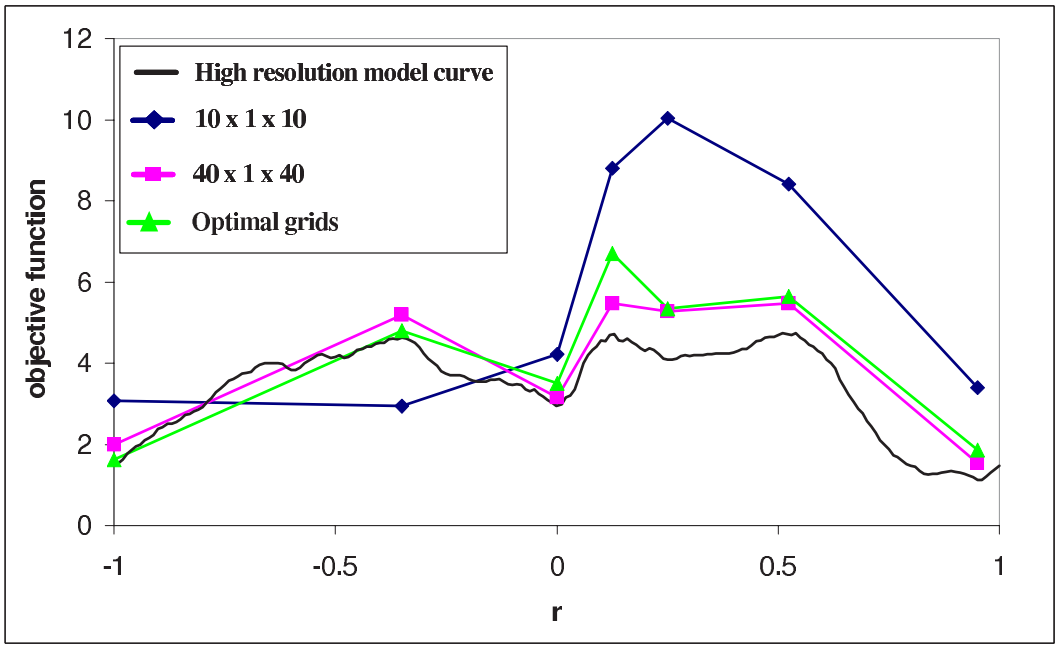

Figure 3.31: The objective function curve for the high resolution model, $10 \times 1 \times 10$ coarsened model, $40 \times 1 \times 40$ coarsened model and the coarsened model with the optimal grids.

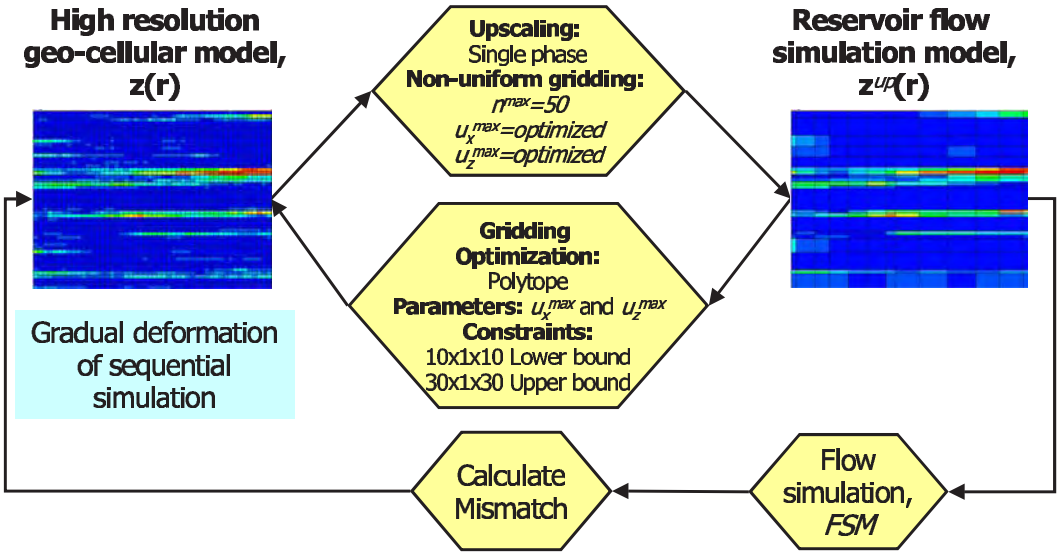

Figure 3.32: The improved workflow specific to example.

3.4 Examples revisited

In this section we revisit some of the examples given previously in Sections 2.3.4, 2.3.5 and 3.1. The improved parallel modelling workflow is applied on these examples and comparisons are made with the results obtained from applying the original parallel modelling workflow.

3.4.1 2D layered example

We first revisit the synthetic application discussed in section-3.1. The reference permeability field for this example is given in Figure-3.1 and the corresponding flow response is given in Figure-3.2. The parallel modelling workflow (without gridding optimization) was able to provide successful history matches on the coarsened realizations (see Figure-3.4 for results). However, the corresponding high resolution models did not match the history (see Figure-3.6 for results).

The improved parallel work flow is applied on this field. The specifics of the example are given in Table-3.1. Before giving the results, we first present the improved parallel workflow specific to this example given in Figure-3.32.

An initial model that honors the hard data and the underlying spatial continuity model

(variogram, for this example) is generated. Next an incompressible single phase flow simulation, FSM^* is performed on the initial high resolution model and the pseudo water cut curve is obtained, $f^*_{w_{hrm}}$. Then a gridding optimization is performed on the u_x^{max} and u_z^{max} parameters. Constraints are given to the coarsened model grid dimensions such that they will be between $10 \times 1 \times 10$ and $30 \times 1 \times 30$. During the gridding optimization FSM^* is evaluated on the coarsened model multiple times, to optimize on the u_x^{max} and u_z^{max} parameters. A pseudo water cut curve $f^*_{w_c}$ is obtained for each evaluation and the mismatch, ϵ^*, is computed. The polytope method adjusts the gridding parameters u_x^{max} and u_z^{max} such that $\epsilon^*$is minimized while at the same time honoring the constraints of the coarsened model grid dimensions ($10 \times 1 \times 10$ and $30 \times 1 \times 30$).

After the gridding optimization, an optimally gridded coarsened model is obtained. Next the full flow simulation model is evaluated on the coarsened model and the difference between the calculated data and the field data, $O(r)$, is obtained. Until this mismatch is minimized, the high resolution model is perturbed by changing the r parameter and the above steps are repeated.

Figure-3.33 illustrates the progression of the high resolution and the coarsened permeability fields at the end of iterations 1, 5, 10, 30 and 50 along with the coarsened model grid dimensions at the end of each iteration. It is important to note that the gridding is dynamic through out the entire modelling process. The coarsened models adapt to the underlying fine scale geology through non-uniform gridding where the grids change each time a perturbation is made to the high resolution model. For the iterations illustrated in Figure-3.33 none of the grid dimensions have reached the maximum allowed dimensions of $30 \times 1 \times 30$.

Next we look at the flow responses of the coarsened models and the corresponding high resolution models. Previously, with the basic parallel modelling workflow (without gridding optimization) the high resolution models did not match the production data. Figure-3.34 illustrates the coarsened model responses for 6 realizations at the end of the improved parallel modelling workflow. All 6 models match the production data until 500 days. The resulting coarsened model dimensions are given in Table-3.4.

Figure-3.35 illustrates the flow responses of the 6 high resolution models. All 6 models match the history. The gridding optimization in this case determines the coarsened model dimensions necessary for the high resolution model to match the history. It is also important to note that, the optimal grid dimensions vary from one model to the other. Even though

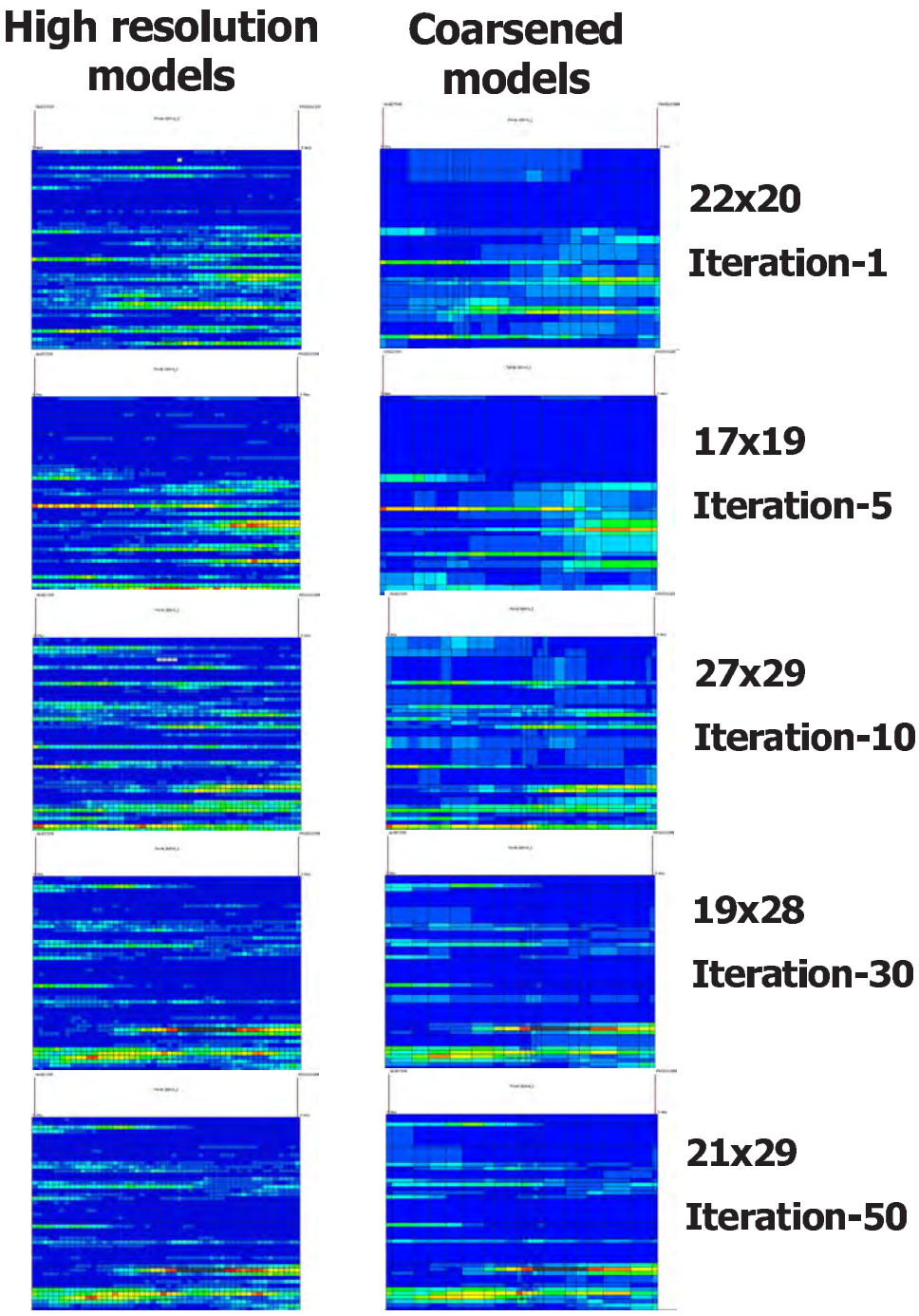

Figure 3.33: The progression of the permeability field during the parallel workflow at the end of iterations 1, 5, 10, 30 and 50.

Table 3.4: The optimal coarsened model dimension.

Model	Optimal coarsened model dimensions
Model # 1	$27 \times 1 \times 28$
Model # 2	$21 \times 1 \times 29$
Model # 3	$13 \times 1 \times 21$
Model # 4	$20 \times 1 \times 30$
Model # 5	$22 \times 1 \times 28$
Model # 6	$25 \times 1 \times 25$

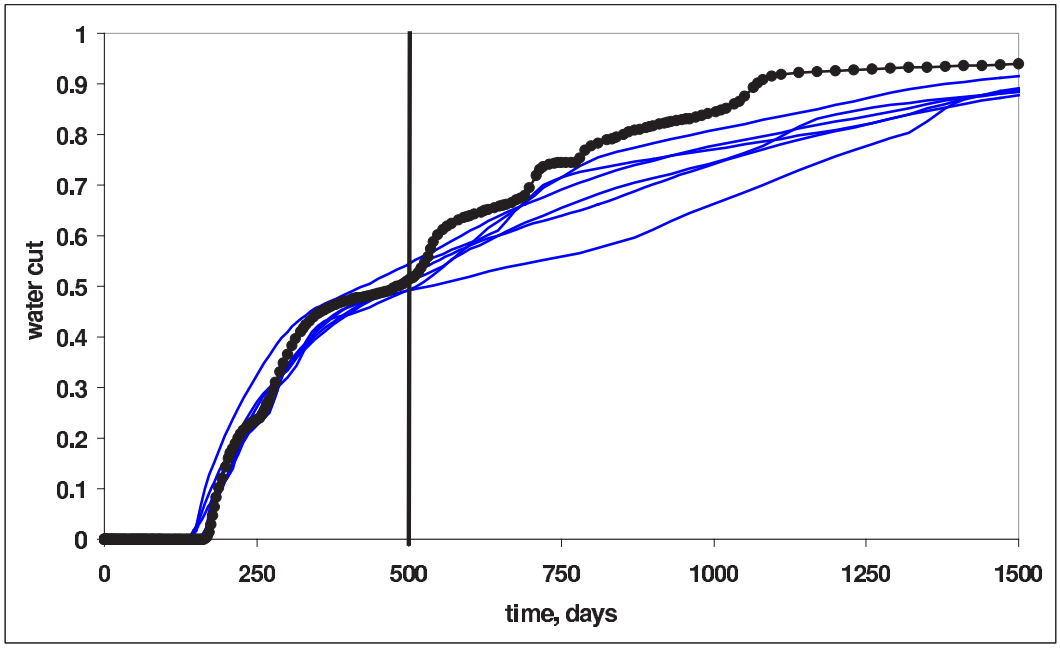

Figure 3.34: The flow responses of the coarsened models.

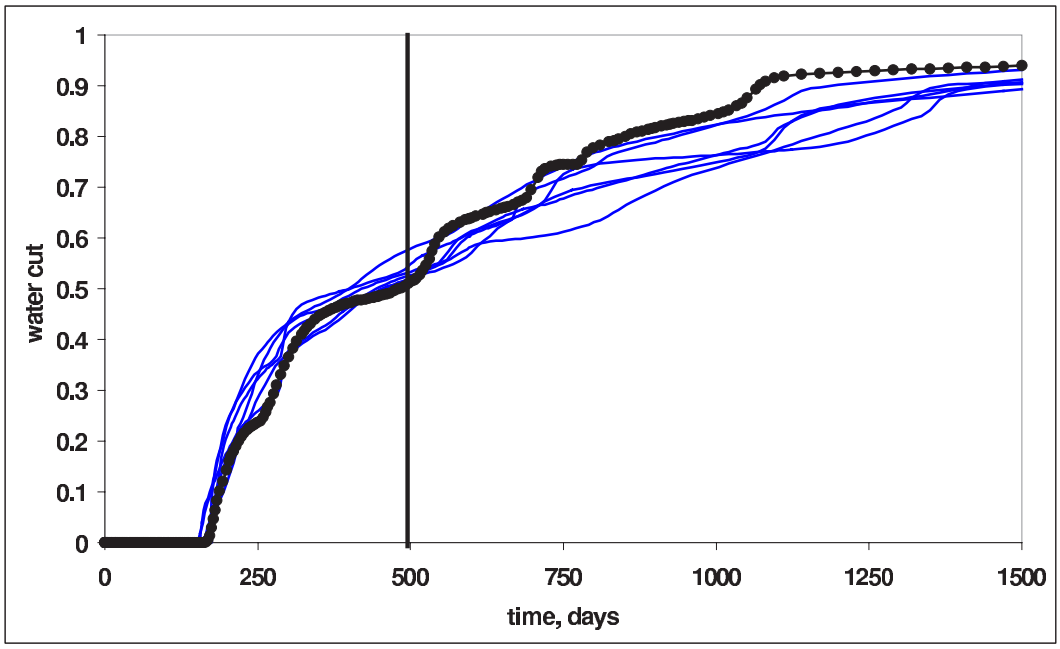

Figure 3.35: The flow responses of the high resolution models.

the same geostatistical input are used (hard data, spatial continuity model, etc.) during the perturbation for history matching, the flow responses of the models may vary significantly.

3.4.2 2D channel example

In this subsection we revisit the example given in Section-2.3.4. When the basic parallel modelling workflow is applied for this case study, the coarsened realizations match the history (see Figure-3.36). The responses of the high resolution do not match the production data as well as the coarsened models see, Figure-3.37.

In order to improve the dynamic response of the high resolution models, we apply the improved parallel modelling workflow on this example. The workflow specific to this example is given in Figure-3.38. The initial guess honors the hard data and the underlying geological continuity model. For this example the underlying geological continuity model is represented through a training image. Hence a training image based algorithm, SNESIM, is used for generating the realizations. Next a gridding optimization is performed in order to obtain the optimally gridded coarsened model. The optimization is performed through the polytope algorithm on the 3DDEGA parameters that control the gridding.

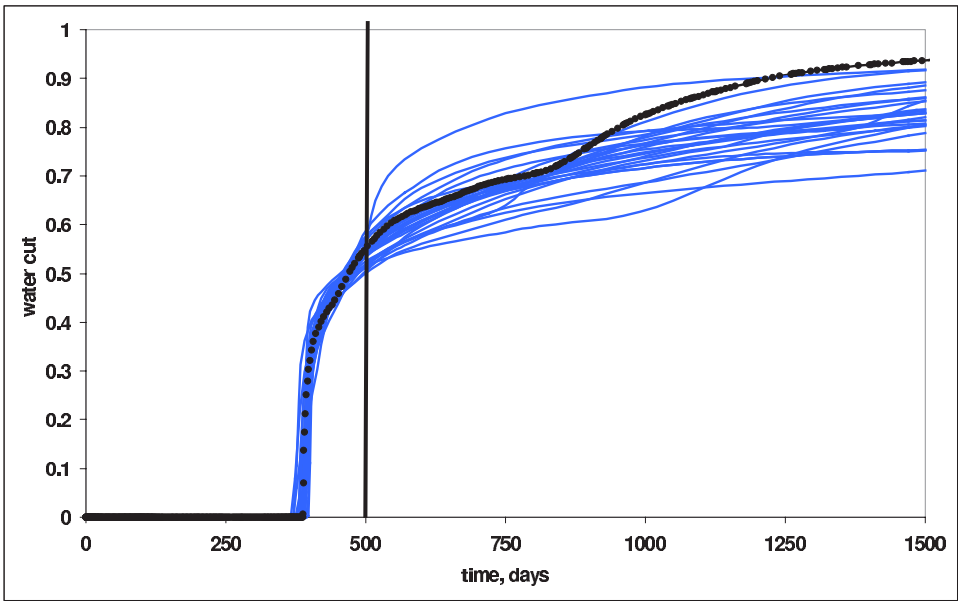

Figure 3.36: The flow responses of 30 realizations conditioned to both hard data and historical production data. Figure-2.27 is revisited for comparison.

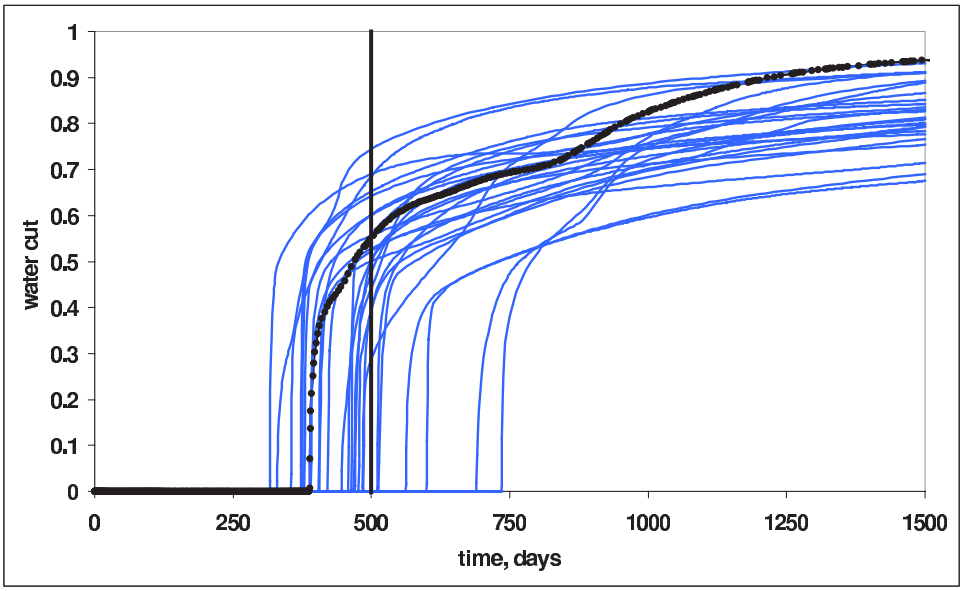

Figure 3.37: The flow responses of the high resolution models in the case no gridding optimization is performed.

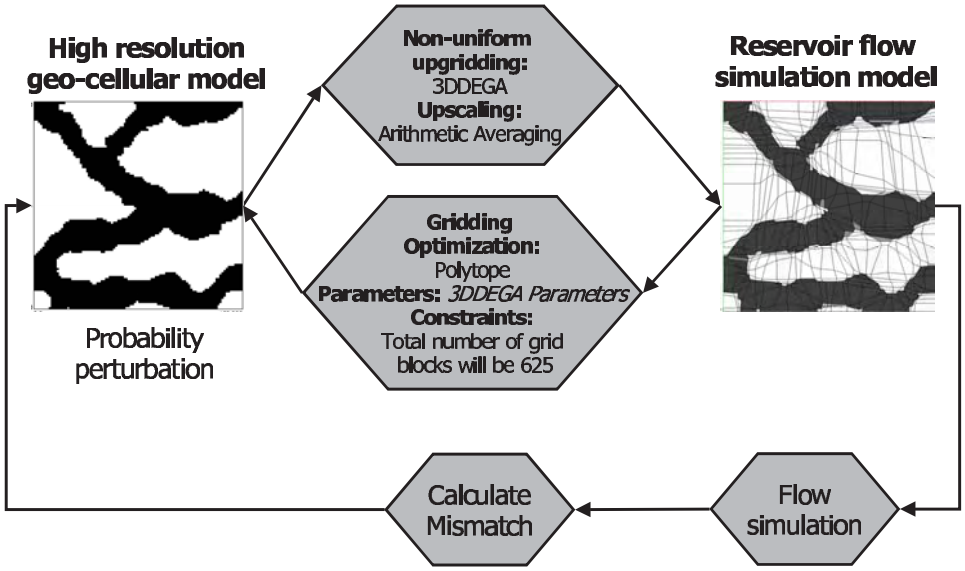

Figure 3.38: The improved parallel modelling workflow specific for this example.

The parameters that are optimized during the gridding optimization are summarized in Table-3.5 along with their constraints. Note that the optimization of the gridding parameters are performed simultaneously, not one after the other. The ω_σ and ω_V parameters represent different impact on the gridding. The ω_σ parameter determines how strong the gridding is a function of the heterogeneity of the underlying property. As ω_σ increases the grids are allowed to deform more to better fit the heterogeneity. The ω_V parameter determines the relationship between volumes of neighboring blocks in the coarsened model. Setting a low value for this parameter allows significantly different volumes for neighboring grid blocks, which may cause numerical instability during flow simulation. Hence increasing this parameter constrains the difference in volumes of neighboring grid blocks. The $cexyratio$, $xsmooth$ and $ysmooth$ parameters are yet other controls that effect the volumes and the straightness of the x and y grid lines respectively. A last parameter to be optimized is the number of coarsened grid blocks in the x direction. A constraint is placed on the total number of grid blocks, to be equal to 625. Hence more grid blocks can be generated in a particular direction if necessary without increasing CPU burden since the total number of coarsened grid blocks remain constant.

Once the optimally gridded coarsened model is determined, the full flow simulation is evaluated on the coarsened model, and the high resolution model is perturbed until the

Table 3.5: Parameters that are optimized during the gridding optimization and constraints placed on them.

Parameter	**Constraint**
ω_σ	$\omega_\sigma \in [0, 2]$
ω_V	$\omega_V \in [-1, 2]$
$cexyratio$	$cexyratio > 0$
$xsmooth$	$xsmooth \geq 0$
$ysmooth$	$ysmooth \geq 0$
n_x^c	$n_x^c \times n_y^c \times n_z^c = 625$

mismatch between the calculated data and the observed field data is minimized. The perturbations in this example have been performed using the probability perturbation method.

The flow responses of the history matched coarsened models are shown in Figure-3.39. As expected, the flow responses match the history for 500 days.

Figure-3.40 illustrates how well the high resolution models match the target flow responses. Although not as good as the coarsened model responses, a reasonable match is still obtained particularly if compared to Figure-3.37 where no gridding optimization is applied.

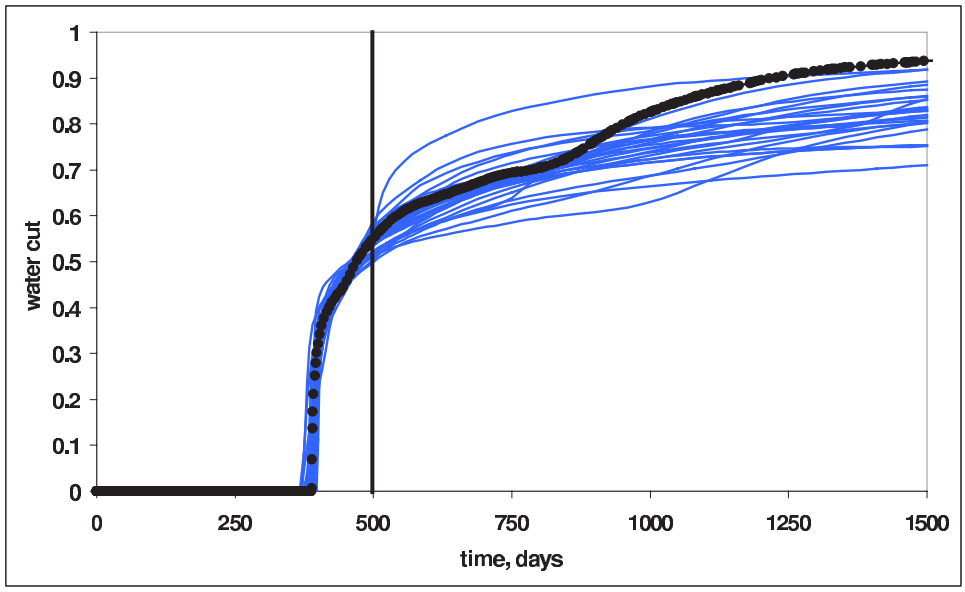

Figure 3.39: The flow responses of the coarsened models when the improved parallel modelling workflow is applied.

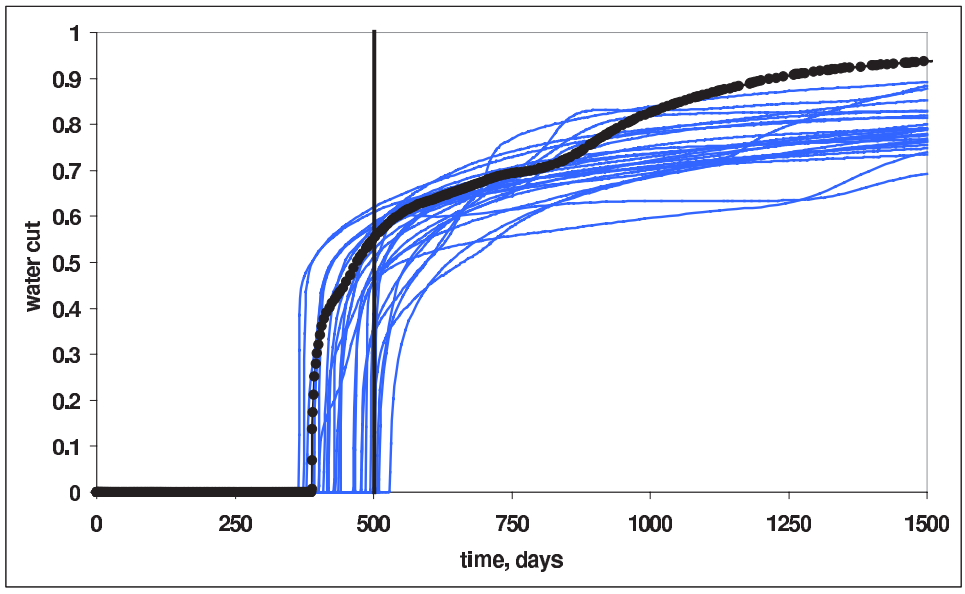

Figure 3.40: The flow responses of the high resolution models when the improved parallel modelling workflow is applied.

3.4.3 Gridding in the near-well region

In this subsection we focus on the important point of ”gridding in the near-well region”. In some cases the flow responses of a high resolution model and a coarsened model can be significantly different even if an efficient upscaling/upgridding technique is used. This is mainly because of the inefficiency of the upscaling/upgridding technique in modelling the near-well region. Special attention needs to be given to these important high flux regions in order to preserve the flow responses on the coarsened models. We first demonstrate what could go wrong if no attention is paid to gridding the wells.

Consider the reference permeability field of the synthetic case given in Section-3.4.2. In this high resolution model, the grid block permeability of the injector is 100 md (located in shale). Figure-3.41 gives two very similar grids obtained by 3D-DEGA along with their flow responses and the flow response of the fine scale reference permeability field. Although the two coarsened models look visually similar, the flow responses of both grids differ considerably. The problem occurs near the injection well. A small change in gridding gives rise to a considerable difference in the injector grid block permeability; 178md vs. 100md. In the case of 178md, the coarse grid block contains a part of fine scale channel running close to the injector, therefore increasing the permeability in that grid block.

One of the solutions to this problem can be near-well upscaling (Ding, 1995; Durlofsky *et al.*, 2000) which is not considered in this thesis. Instead, we propose a solution which improves the gridding in the near-well region. In the example given in Section-3.4.2, the gridding is based only on the static property, namely permeability. As a solution to the well gridding problem shown above, we propose an approach that makes use of both static properties (such as permeability, porosity, etc.) and dynamic information (such as fluxes and velocities) for refining the gridding in the near well region. As mentioned earlier in this chapter, streamlines are used for performing the gridding optimization. We make further use of streamlines for handling the gridding in the near-well region. This is accomplished by constructing a ”streamline count” map once the streamlines are traced on the high resolution model. A streamline count map records the number of streamlines that pass through each grid block. The streamline count map identifies regions with high velocity, often those regions are neighboring wells.

Instead of using solely permeability as a property for gridding criterion, we create a composite of permeability and velocity information as follows: In a region near a well,

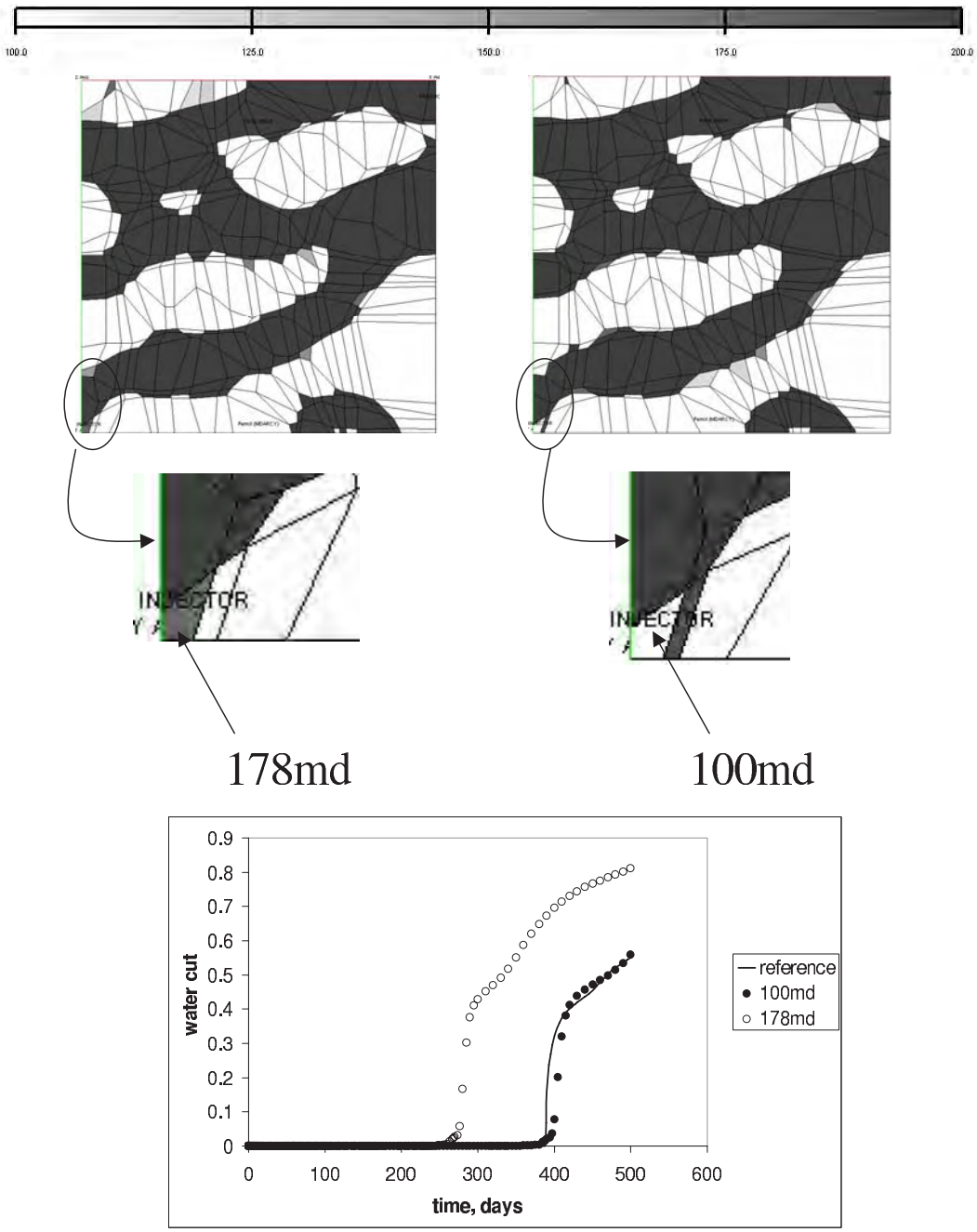

Figure 3.41: Comparison of the flow responses of two similar grids.

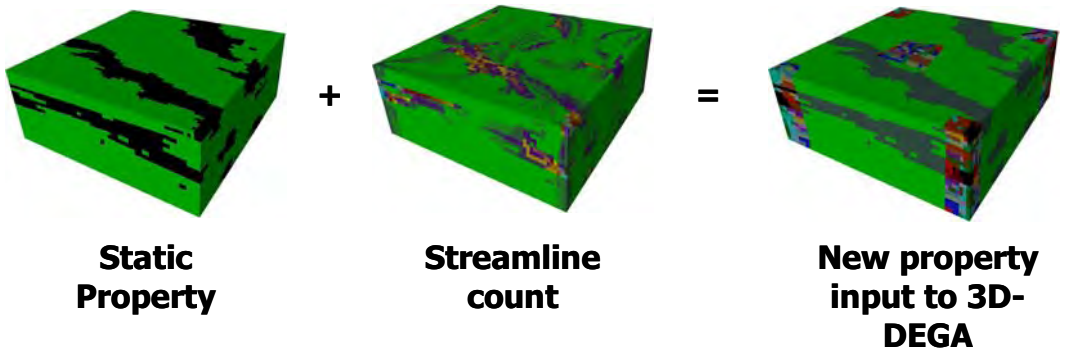

Figure 3.42: The generation of the new property used as input into the 3DDEGA algorithm for managing the gridding in the near-well region.

the streamline count map is used as input to the 3DDEGA algorithm, while in a region further away from a well, permeability is used. As a result instead of supplying the static property into the 3DDEGA algorithm for the gridding, a new property which contains both the streamline count (around the wells) and permeability is used as input into 3DDEGA. Such an approach is illustrated in Figure-3.42. A simple standardization is applied for better classification of streamline count values in order to distinguish between regions of high velocity and low velocity. The standardization procedure consists only of performing a rank preserving transformation of the streamline count values to a uniform distribution. Then this distribution is divided into 20 equally spaced classes and each class is given an indicator. It is this indicator that is used as input into the gridding algorithm.

Important to this approach is to decide the size of the near-well region, i.e. the size of the region where the streamline count map is used for gridding. A parameter s_v (scaled between 0 and 1) is introduced. If this parameter is zero, the streamline count information is used only at the grid blocks completed by the well. If the parameter is set to one, then the size of the near-well region is expanded to cover the entire reservoir, hence upgridding in that case is based only on the streamline count information.

We next perform a sensitivity analysis regarding the effects of the s_v parameter on the gridding. For such a demonstration we use again the 3D synthetic facies model given in Figure-3.42. Gridding is performed using 3DDEGA for $s_v = 0.0$, $s_v = 0.01$, $s_v = 0.02$, $s_v = 0.05$ and $s_v = 0.1$. The results are given in Figures 3.43 - 3.47.

As the s_v parameter is increased, the region around the well where the streamline count information is used expands. If increased too much, such as for $s_v = 0.1$ (Figure-3.47),

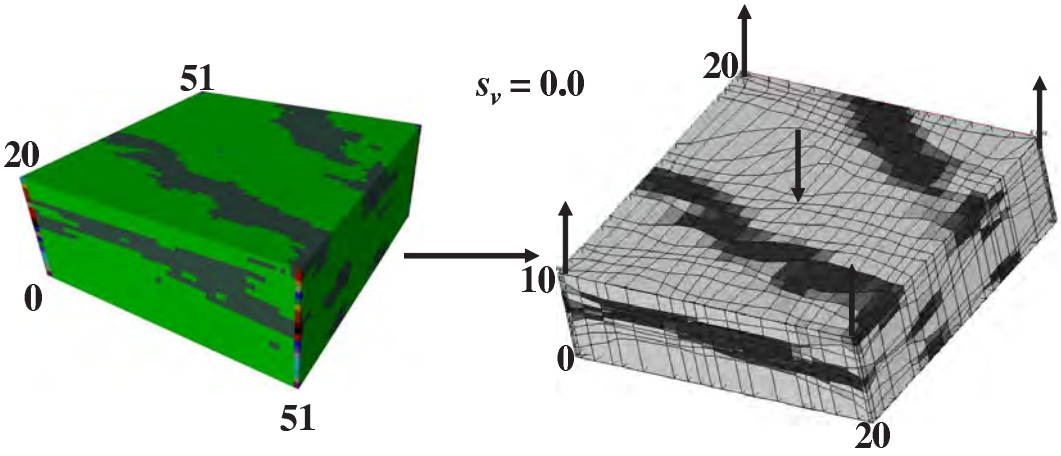

Figure 3.43: Upgridding with 3DDEGA with $s_v = 0.0$.

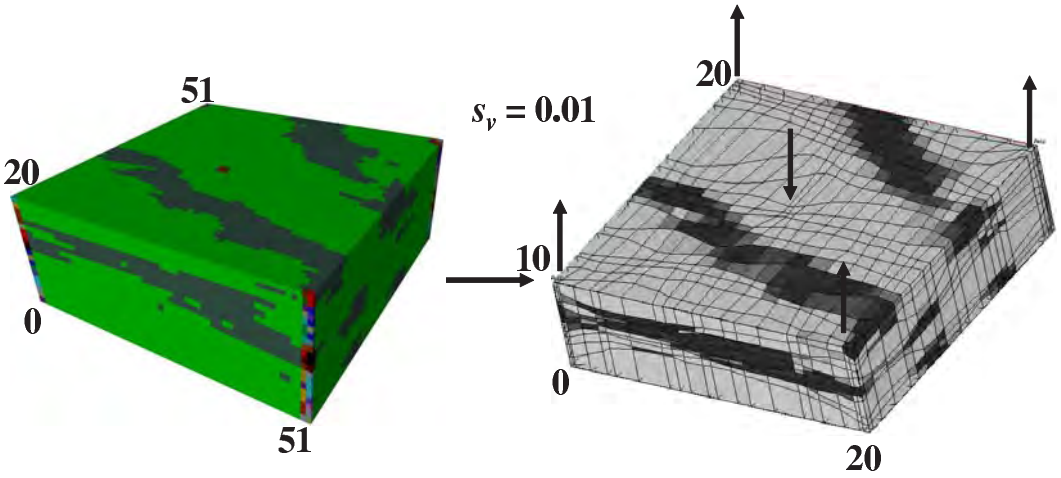

Figure 3.44: Upgridding with 3DDEGA with $s_v = 0.01$.

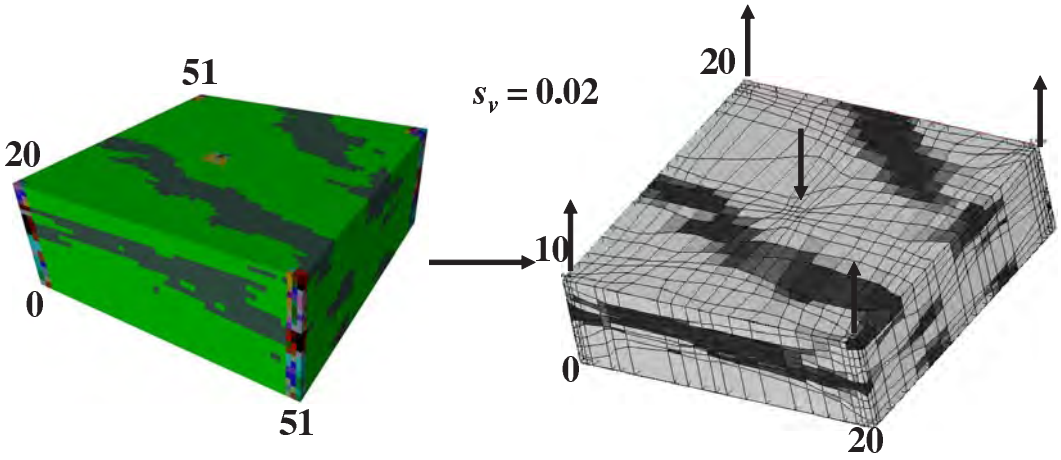

Figure 3.45: Upgridding with 3DDEGA with $s_v = 0.02$.

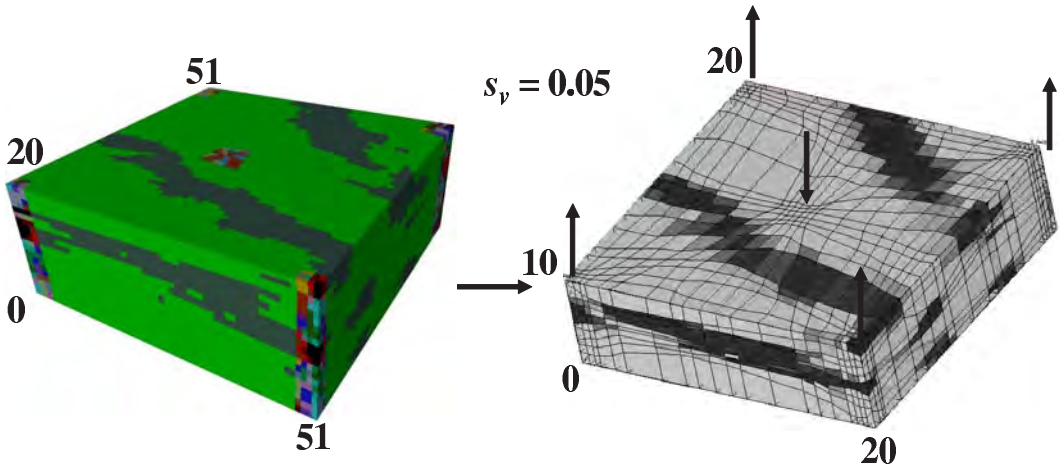

Figure 3.46: Upgridding with 3DDEGA with $s_v = 0.05$.

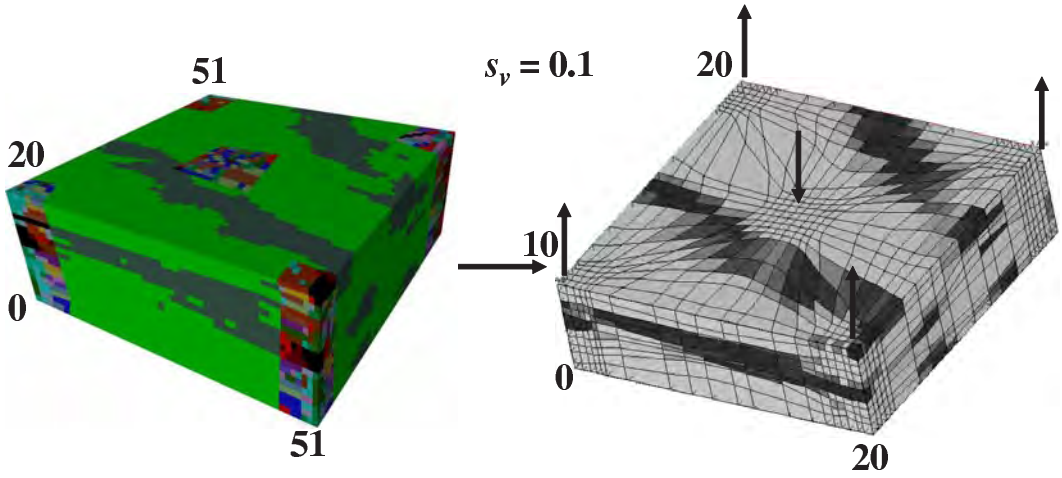

Figure 3.47: Upgridding with 3DDEGA with $s_v = 0.1$.

the gridding is mostly dependent on the streamline count information. This results in over refinement around the wells which results in over-coarsening throughout the rest of the field. Hence the parameter s_v should be included in the list of parameters to be optimized during the gridding optimization. This is demonstrated in the synthetic example given in the next section.

3.4.4 3D channel example

In this section, we revisit the example given in Section-2.3.5 paying special attention to gridding near wells. The improved parallel modelling workflow with well gridding is applied to this example and comparisons are made with the results of the basic parallel modelling workflow (without any gridding optimization). The flow result of the basic parallel workflow given in Figure-2.34 is illustrated again in Figure-3.48. This figure illustrates the flow responses of the coarsened models once the basic parallel modelling workflow is applied. Figure-3.49 shows the flow responses of the resulting high resolution models.

The improved parallel modelling workflow is applied to this synthetic example in an attempt to improve the flow responses of the resulting high resolution models. The gridding parameters that are optimized for this synthetic example are given in Table-3.6. As explained in the previous section, the s_v parameter enables to refine gridding around the near well-bore region through the use of velocity information. This parameter determines

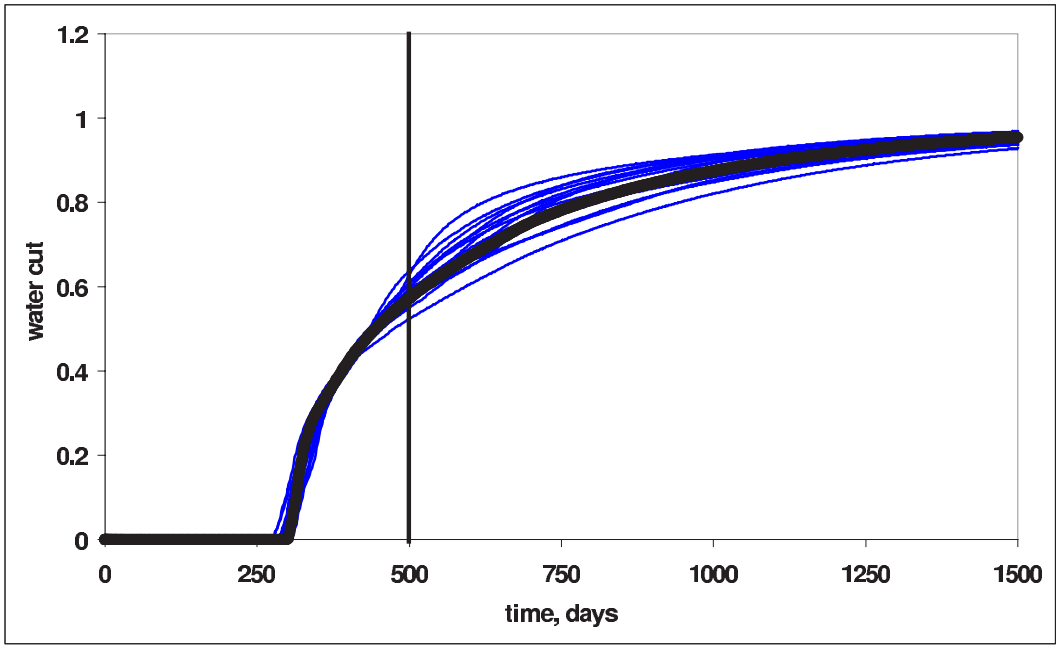

Figure 3.48: Flow responses of coarsened models conditioned to both hard data and the production data.

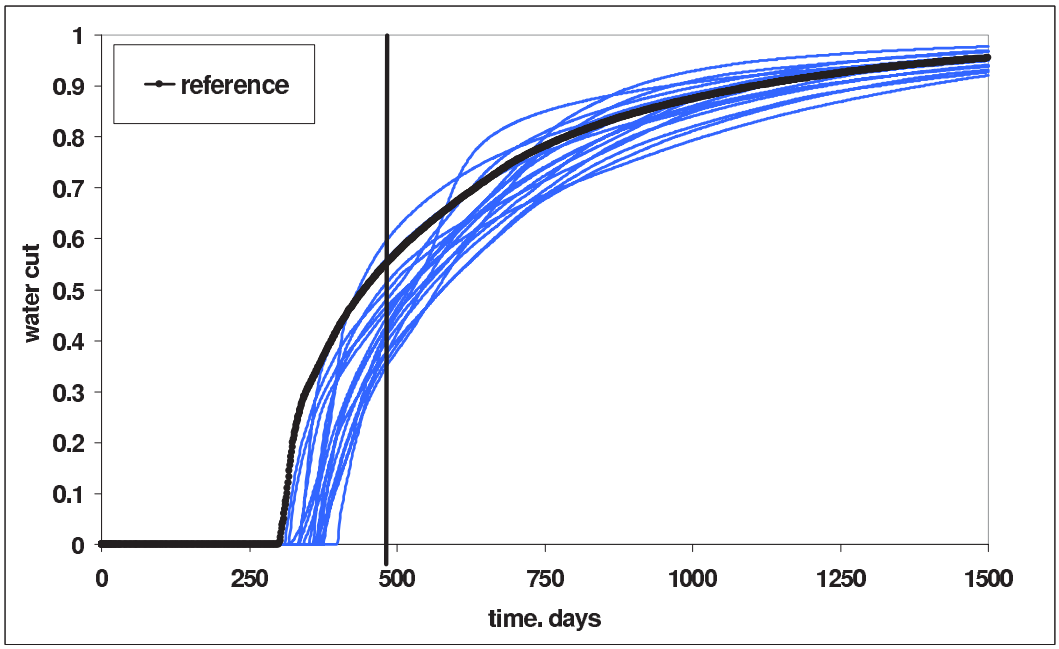

Figure 3.49: Flow responses of coarsened models conditioned to both hard data and the production data.

Table 3.6: Parameters that are optimized during the gridding optimization and constraints placed on them.

Parameter	**Constraint**
ω_σ	$\omega_\sigma \in [0, 2]$
ω_V	$\omega_V \in [-1, 2]$
s_v	$0 \leq s_v \leq 1$

the area around the well where the velocity information is used as input to the gridding algorithm 3DDEGA.

Figure-3.50 shows the flow responses of the resulting coarsened model realizations. As expected, these responses honor the dynamic data until 500 days. A comparison with Figure-3.48 shows no difference for the flow behavior below 500 days and no difference for the scatter of the future performance predictions.

Figure-3.51 shows the resulting flow responses of the high resolution models when the improved parallel modelling workflow is applied. Comparing Figures 3.49 (using the basic parallel modelling) and 3.51 show no significant differences. Applying the improved parallel workflow has not significantly improved the flow responses of the high resolution models. Although, some minor improvement is observed for the breakthrough times of the water cut curves. The sample history matched models are given in Figure-3.52

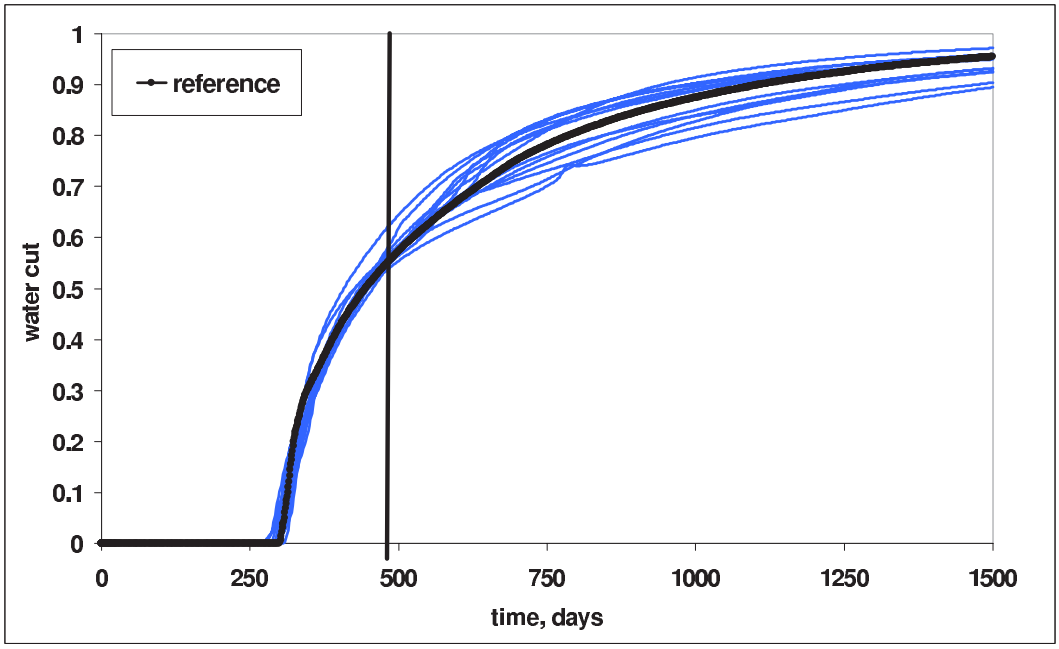

Figure 3.50: Flow responses of coarsened models conditioned to both hard data and the production data.

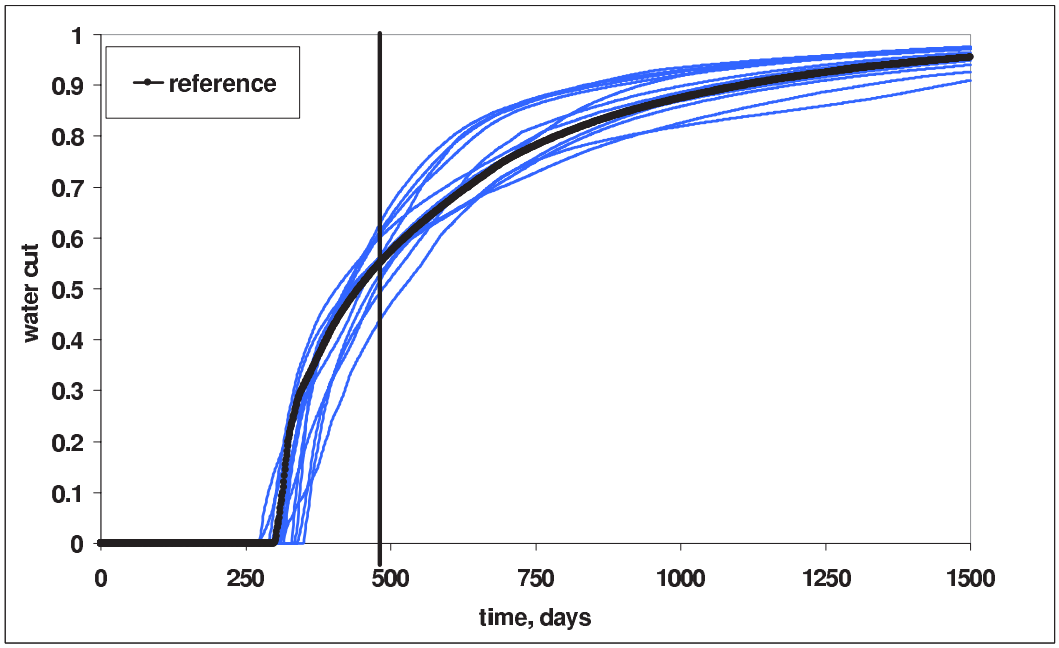

Figure 3.51: Flow responses of coarsened models conditioned to both hard data and the production data.

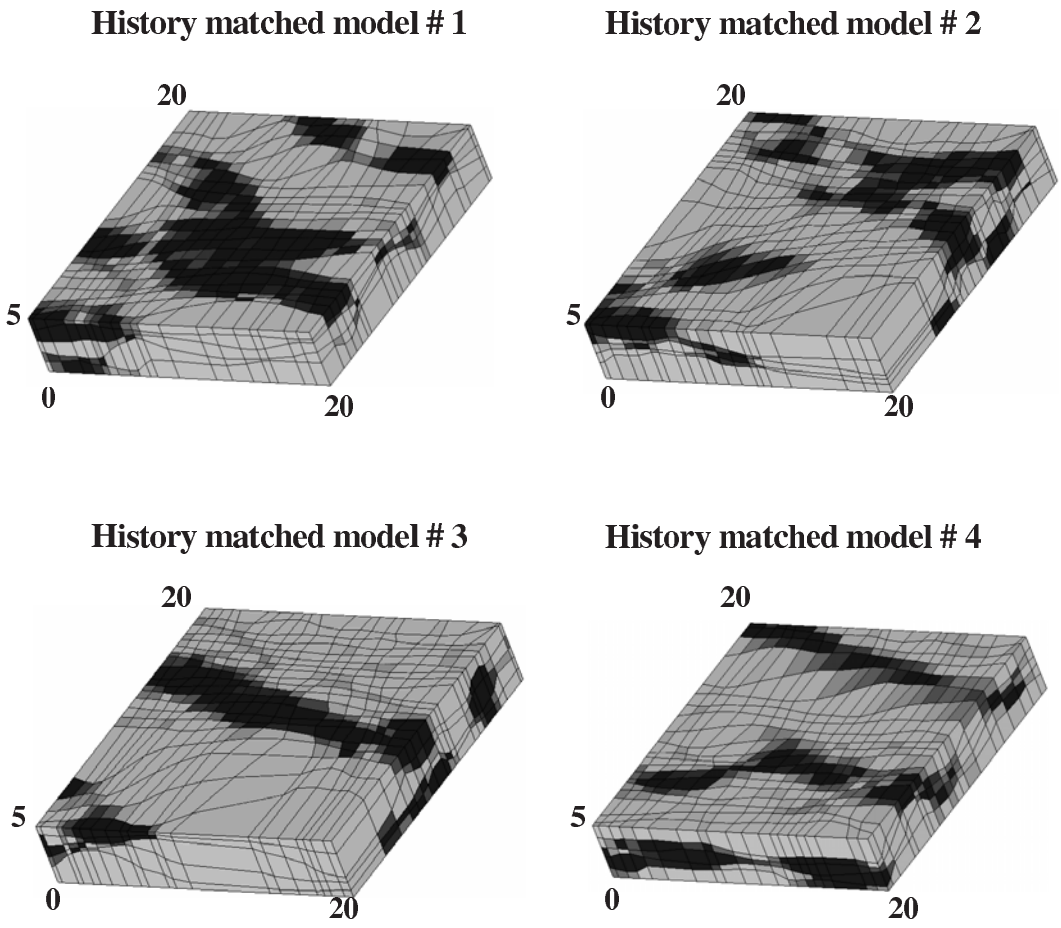

Figure 3.52: Sample history matched models.

Chapter 4

Application to a North Sea Reservoir

4.1 Introduction

In this chapter we present the application of the parallel modelling workflow. The main goal of this case study is to illustrate how this can be applied to real fields.

The methodology is applied to a North Sea reservoir where 5.5 years of production data is available. The production data consists of oil-water rates and pressure data. The reservoir matrix permeability and porosity are fairly homogeneous (layers with uniform porosity and permeability distribution). A number of lenticular calcite bodies exist which affect vertical and horizontal flow are present. The regional variation and local positioning of these calcite bodies is largely unknown since they are too thin (1 ft) to be detected by seismic.

A characterization study has been conducted by Hoffman and Caers (2004) to stochastically model the locations and proportions of these calcite bodies. In their study, Hoffman and Caers (2004) used the regional probability perturbation method to perturb the local configuration and proportions of these bodies to match pressure and flow data. Traditional history matching by perturbing permeability and porosity was unable to history match the field production data. It is crucial to perturb both location and proportions of the calcite bodies.

The challenge in modeling these calcite bodies lies in the fact that they are 1-Stochastic (location of these bodies are mostly unknown) and 2-Extremely thin. It would require a very high resolution geo-cellular model to represent such bodies accurately. Upscaling

without grid refinement near such small bodies, would lead to highly inaccurate flow models since calcite represents a vertical flow barrier. In a traditional reservoir modeling workflow one would generate high resolution geo-cellular models displaying the calcite bodies. Next the model would be upscaled and history matching on the coarsened model would be attempted. However, such history matching would not be able to perturb the location of these bodies due to the coarseness of the upscaled reservoir model. To history match, perturbations will need to be performed on the high resolution grid and any such perturbed high resolution grid will need to be re-upscaled to a coarsened model to re-evaluate the simulated production history. An upscaling method, preserving the high resolution calcite bodies will need to be applied.

Instead, the parallel modelling workflow will be used to model the locations and proportions of the calcite bodies in order to match production history. The probability perturbation method will be used as the primary engine for performing the history match. A high resolution model and a coarsened model will be used in parallel to accomplish the modelling. The high resolution model is used to accurately describe the location and proportions of the calcite bodies. The 3DDEGA algorithm is used to perform the upscaling/upgridding in order to best preserve the calcite bodies on the coarsened model. This coarsened model is then used for flow simulations.

An introduction of the reservoir is given first. Next the work of Hoffman and Caers (2004) is reviewed, followed by a detailed description of the parallel modelling workflow specific to this case study. Finally, results are presented along with final remarks.

4.2 Introduction to the North Sea Reservoir

The North Sea reservoir under study has a faulted structure separating the major segments of the reservoir, see Figure-4.1. The faults are not fully sealing. The top of the reservoir lies at an average depth of 2500m and the reservoir has an average thickness of 230m. The yellow line a-b in Figure-4.1 delineates the cross-section of the reservoir shown in Figure-4.2.

The reservoir is composed of 5 horizons as shown in Figure-4.2. The second horizon is an impermeable shale layer that prevents flow communication between horizon-1 and the rest of the reservoir. The top formation includes a gas cap. The rest of the reservoir has

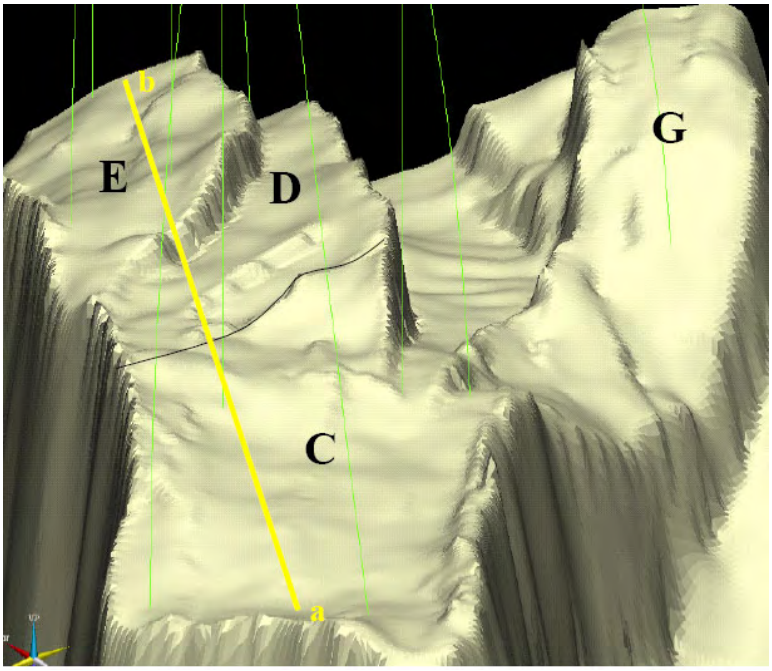

Figure 4.1: The illustration of the top structure along with the major faults and segments, taken from Hoffman and Caers (2004).

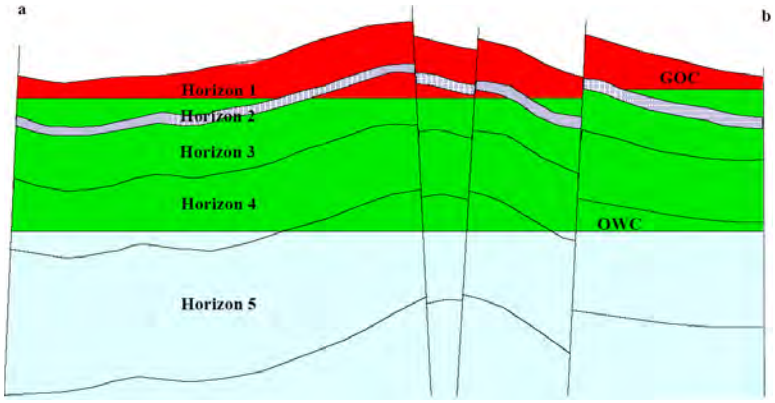

Figure 4.2: The cross section of the reservoir showing the faults, taken from Hoffman and Caers (2004).

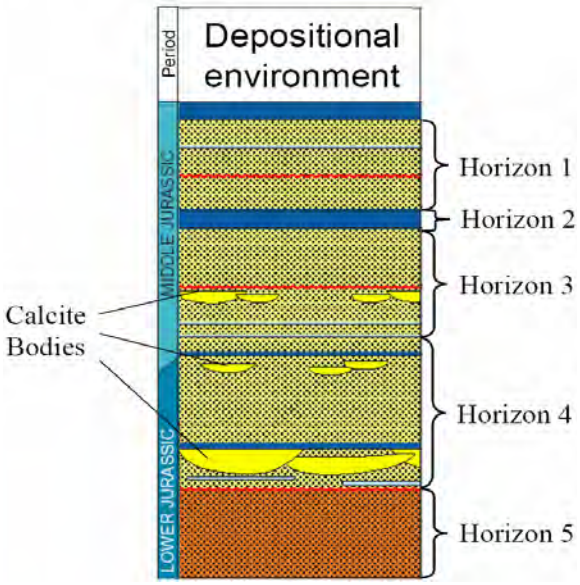

Figure 4.3: Illustration of the calcite bodies, taken from Hoffman and Caers (2004).

only a small amount of gas. Most of the bottom formation accounts for the water zone. There are a total of 22 wells of which 8 are injection wells, injecting mostly water and a small amount of gas. Almost all production wells are either deviated or horizontal.

An important geological characteristic of the reservoir is the presence of calcite bodies that have lenticular shapes and can extend from a couple of meters to tens of meters aereally but are very thin vertically. These bodies impact flow in the vertical as well as horizontal direction. Well log data suggests that these bodies exist mostly within horizon-4, and the lower section of horizon-3. A stratigraphic drawing of the presence of these calcite bodies is shown in Figure-4.3.

The grid dimensions of the existing ECLIPSE numerical model are $39 \times 98 \times 41$. There are 156,702 grid blocks in the reservoir and half of them are active. The reservoir has an initial pressure of 270 bars. 18 separate relative permeability regions exist in the reservoir with relative permeability curves calculated from Corey type curves with different exponential coefficients and end points. The porosity for the numerical model has been obtained by kriging. The permeability map is then obtained by regression from the porosity. These petrophysical properties are fairly homogeneous and have a stationary and low variance statistics within each layer, statistics which can easily be derived from cores and well-log data.

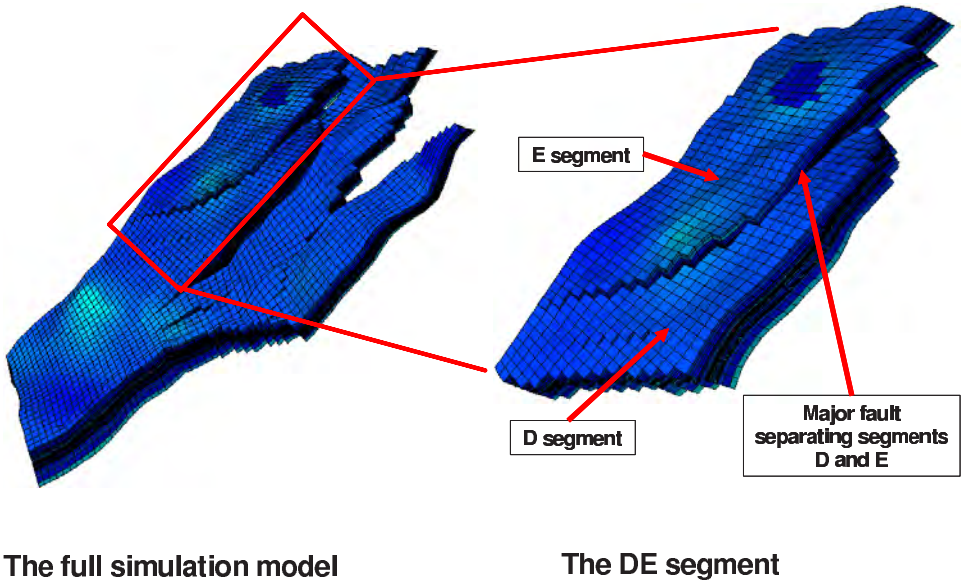

Figure 4.4: The DE segment.

4.2.1 The DE Segment

Both in the characterization study of Hoffman and Caers (2004) and in this study, only the DE segment will be considered. Figure-4.4 shows the full simulation model and the DE segment. A single major fault exists that separates the D segment from the E segment. Once isolated, the DE segment grid dimensions are $15 \times 51 \times 41$ totalling 31365 grid blocks, of which nearly all are active. Although the workflow could be applied to the entire reservoir, we limit ourselves to the DE segment for CPU reasons, since the main goal here is only to illustrate the approach. The DE segment contains 6 production wells and 3 injection wells. The ECLIPSE model was made available for this study, containing all of the completion data as well as an existing coarse grid model.

4.3 Previous modeling efforts

Before explaining the specifics of the parallel modelling approach proposed, we review the study of Hoffman and Caers (2004) which provides useful insights regarding how the history matching should be performed. The study by Hoffman and Caers (2004) aims at determining the locations and proportions of calcite bodies to achieve a history match.

Different perturbations need to be applied to different regions of the reservoir. The regional probability perturbation method (see Appendix-A.4.1 for details) was thus applied. This method perturbs geological properties in different regions without creating discontinuities at the region boundaries (Hoffman and Caers, 2005). In their application streamlines were used to define the regions.

The proportions of the calcite bodies through the following relationship:

$$\mathrm{LP}_{\mathrm{k}}^{\mathrm{NEW}} = \mathrm{LP}_{\mathrm{k}}^{\mathrm{OLD}} + i_k(r_{\mathrm{k}})\mathrm{F_c} \quad \forall \mathrm{k} = 1, 2, \cdots, \mathrm{K} \tag{4.1}$$

where K denotes the total number of regions, k denotes a particular region, $\mathrm{LP_k}$ represents the local proportion of calcite bodies in a particular region and r_{k} is the perturbation parameter for region k. $\mathrm{F_C}$ is a factor which typically takes values between 0.01 and 0.1. This factor is used in order to constrain the amount of perturbation of the local proportions. The term i_{k} determines if the local proportion should decrease or increase. It can only take two values; either -1 (for a decrease in local proportion) or 1 (for an increase). In order to determine the value of i_{k}, two flow simulations are performed at each inner iteration of the probability perturbation method, one run with $i_{\mathrm{k}} = 1$ and one with $i_{\mathrm{k}} = -1$. Based on the flow responses from each region, the value of i_{k} that improves the flow response is used for the third and final run.

The calcite bodies are modeled using the multiple point simulation code SNESIM program (Strebelle, 2002). Information on the size and the distribution of the calcite bodies is limited. A training image (the conceptual geological model), depicting a spatially uniform distribution of low permeability bodies is used. This training image is given in Figure-4.5. The most important characteristic of these bodies is their local clustering. If a large amount of bodies cluster, they form a vertical flow barrier and a horizontal flow conduit. The training image of Figure-4.5 does not show any clustering, the clustering is enforced by regional variation in the proportion of bodies onto the realization generated with SNESIM (see Hoffman and Caers (2004) for details).

Measurements of water rates are available from 6 producers in the reservoir DE segment. The location and proportions of the calcite bodies will be perturbed to match the water rate data. These measurements are given in Figure-4.6. The simulated values of water rates from the ECLIPSE model are also given for comparison. Wells P-10, P-11, P-12 and P-13 match the field response rather well. However, wells P-3 and P-4 are problematic:

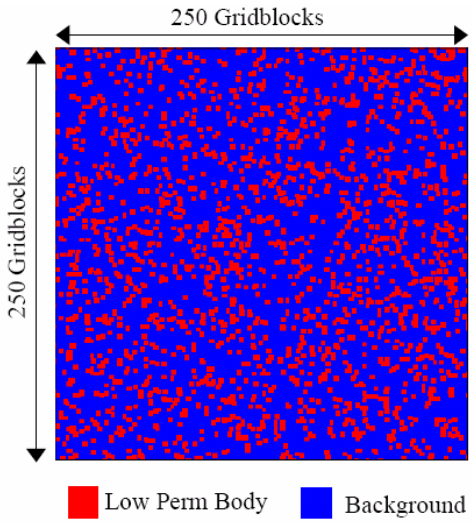

Figure 4.5: The training image (horizontal slice) for modelling the calcite bodies, taken from Hoffman and Caers (2004).

Well P-3 has a much earlier breakthrough and well P-4 displays a later breakthrough than what is measured.

Figure-4.7 shows an example of the regions used in the regional probability perturbation. They were generated from streamline geometry. The streamline regions are updated at each outer iteration of the probability perturbation method.

To isolate the DE segment properly, the effects of the wells located outside the DE segment need to be properly accounted for. This is accomplished by defining flux boundaries around the DE segment. A full flow simulation of the entire reservoir model is performed once where, at this stage, the flux in and out of the DE segment is recorded. Then these fluxes are used for the rest of the history matching process to mimic the effects of all wells in the reservoir.

The final history matched model in Hoffman and Caers (2004) provides proportions of 53% for the region of well P-3, 12% for the region of well P-4, 12% for the region of well P-10, 1% for the region of well P-11, 13% for the region of well P-12 and 22% for the region of well P-13. The flow responses of the wells are given in Figure-4.8.

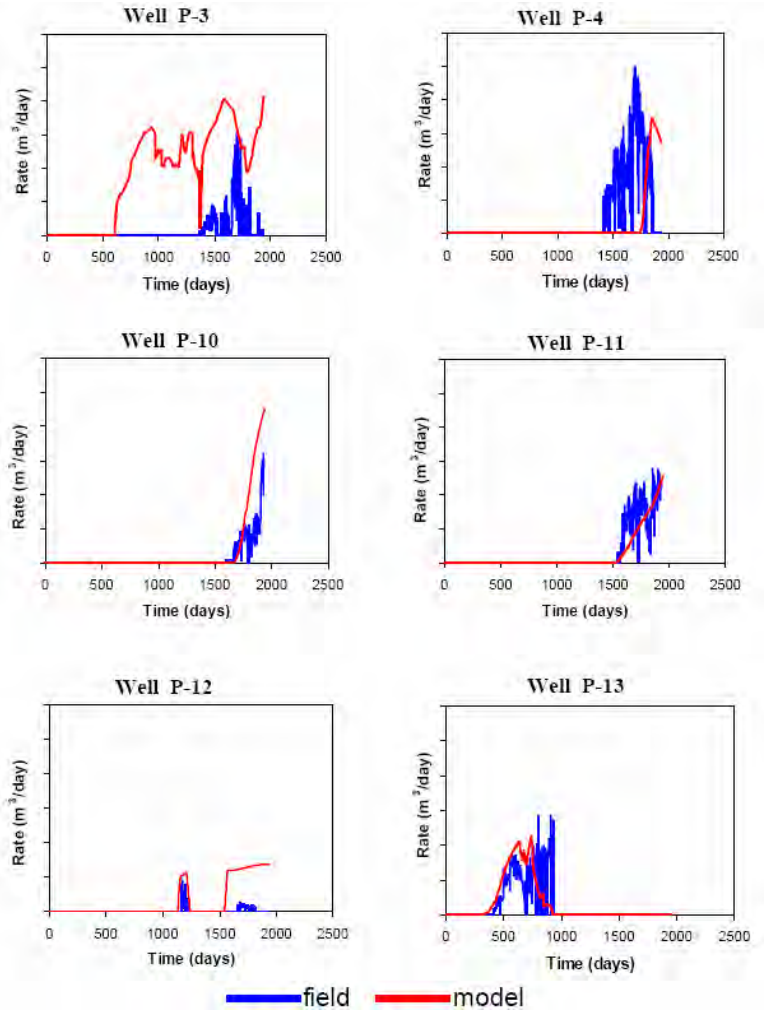

Figure 4.6: The field measurements of water rates from the six producers along with the simulated water rates of the provided numerical model, taken from Hoffman and Caers (2004).

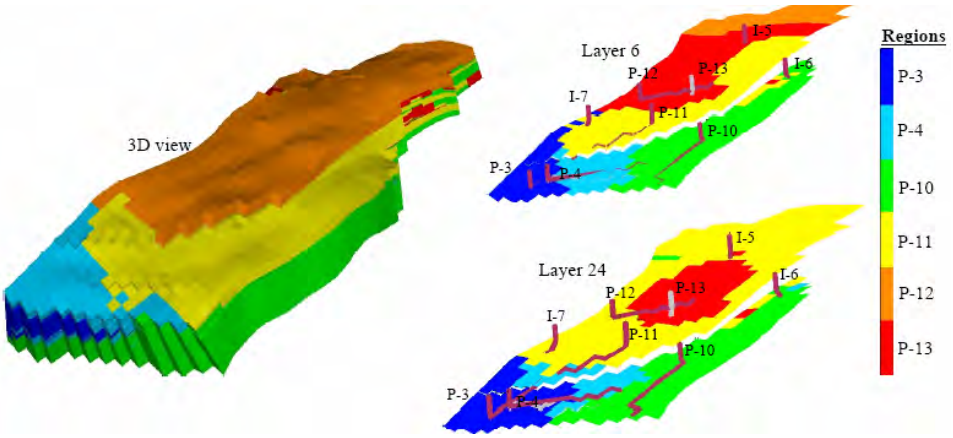

Figure 4.7: The regions defined by streamlines and the location of the wells, taken from Hoffman and Caers (2004).

4.4 The parallel modelling workflow

We have presented in detail the parallel modelling workflow specific to this North Sea reservoir. In the parallel modelling workflow, the gridding is changed to better fit the underlying fine scale heterogeneity (calcite bodies), which are perturbed at each iteration.

In Hoffman and Caers (2004), the calcite bodies were treated as z-transmissibility multipliers in the numerical simulation model. If a body exists in a certain grid block, then the z-transmissibility of that grid block is set to zero, preventing vertical flow. Since the calcite bodies have a very thin structure this is a reasonable approach. However in the approach of Hoffman and Caers (2004), the gridding is fixed. In fact, a prior sensitivity study was required to come up with a reasonable coarse grid that was approximately refined in zones where existence of calcite bodies was suspected. However these zones remained fixed during the history matching iterations.

The parallel modelling workflow offers a solution to the gridding of such fine scale features. Once the calcite bodies are generated on the high-resolution model (this model is fine enough to depict these thin calcite bodies), the coarsened model is gridded such that the physical dimensions of the bodies is accounted for during each iteration of history matching.

As mentioned earlier, Hoffman and Caers (2004) were able to include the boundary effects of the wells outside the DE segment. This was accomplished by imposing flux

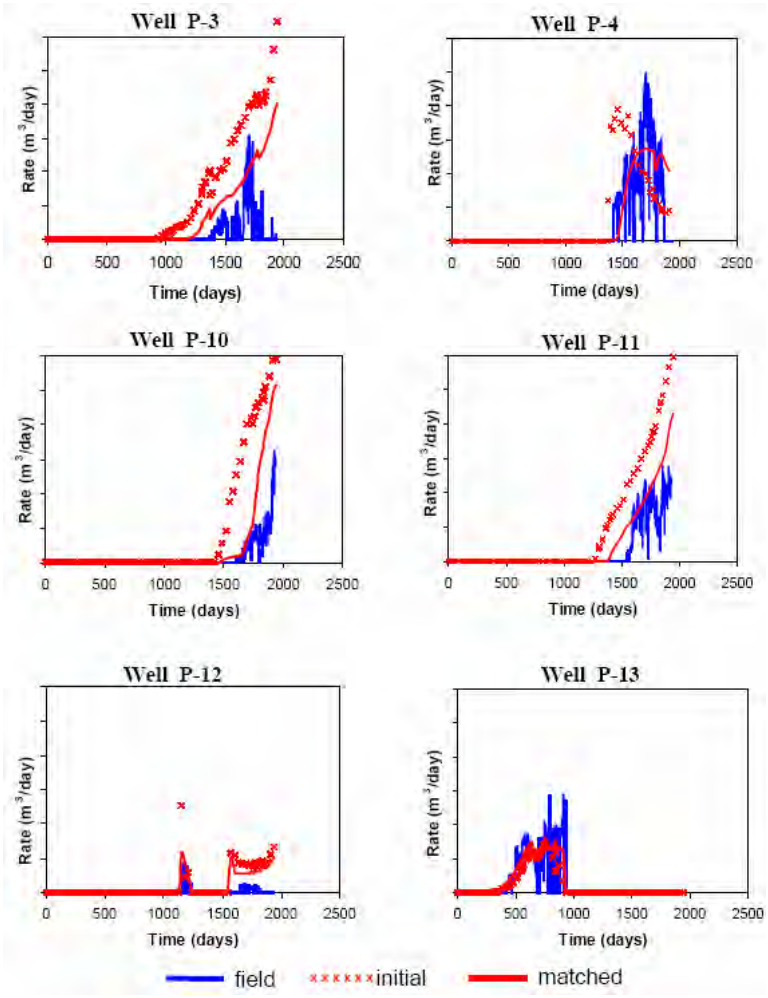

Figure 4.8: The flow responses of the models (both initial and history matched), taken from Hoffman and Caers (2004).

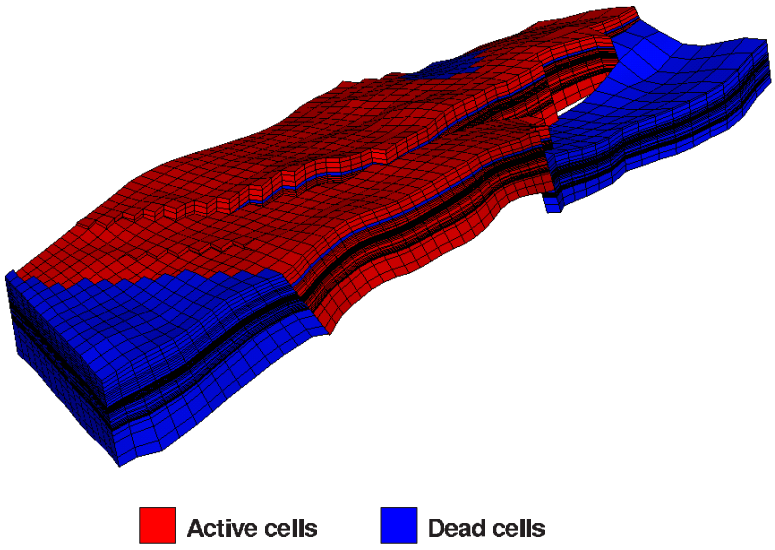

Figure 4.9: The DE segment cut from the full simulation model.

boundaries. This is not feasible in the parallel modelling workflow, because the gridding, hence the fluxes, change during history matching iteration. Hence the DE segment needs to be isolated from the full simulation model. This is accomplished by cookie cutting the DE segment from the full simulation model. The full simulation model grid dimensions are $39 \times 98 \times 41$. From this model, grid cells 6-20 in the x direction, grid cells 28-78 in the y direction and all grid cells in the z direction are isolated. This model is given in Figure-4.9. Once the DE segment is isolated, the model dimensions reduce to $15 \times 51 \times 41$. These coarse grid dimensions are fixed during the entire parallel modelling process. In this isolated model, any grid cell not belonging to the DE segment is treated as a dead cell. These are displayed as blue cells in Figure-4.9. During the isolation step, each property of the grid cell (such as permeability, porosity, net to gross, etc.) is maintained as well as the well indices and well properties.

Next we test if the isolation of the DE segment preserves the flow responses. We accomplish this by comparing the well water production rates of the isolated DE segment and the non-isolated DE segment. Figure-4.10 compares the water production rates of the six producers in the DE segment for the isolated model and the full field model. The flow responses in both cases do not exactly match each other. However, the general trends of the responses for both cases are similar.

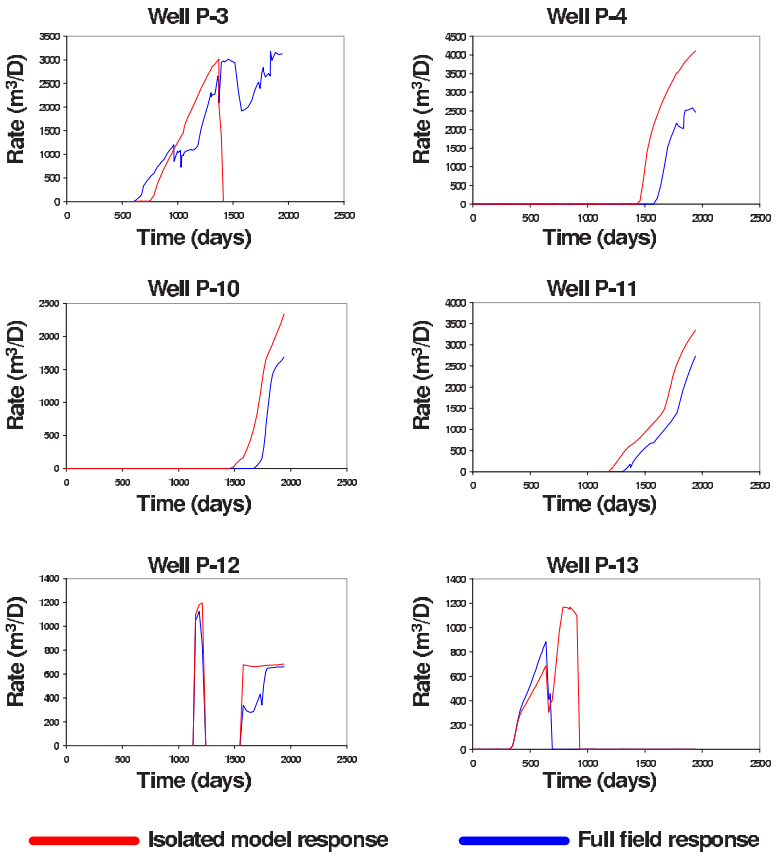

Figure 4.10: Comparison of the flow responses of the production wells of the DE segment for the isolated case and the full field model.

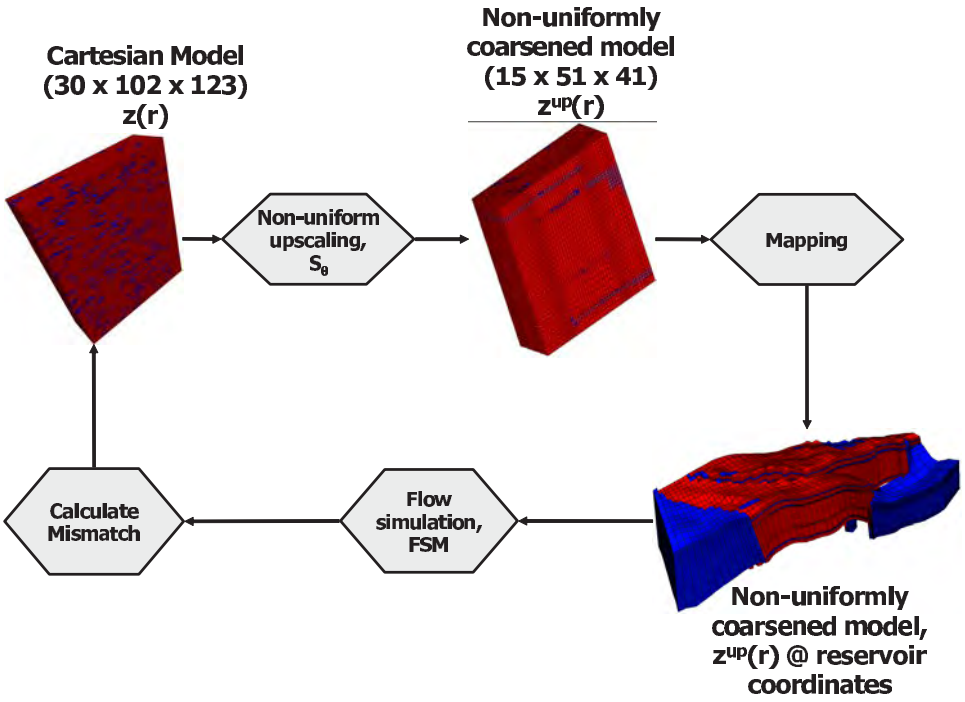

Figure 4.11: The parallel modeling workflow for the North Sea Reservoir.

4.4.1 The workflow

The parallel modeling workflow specific to the North Sea reservoir is given in Figure-4.11. This workflow proceeds as follows (the details of each step is given later):

1. An existing stratigraphic (ECLIPSE model) is available, with grid dimensions $15 \times 51 \times 41$. This stratigraphic model (which is corner point geometry) is refined to grid dimensions of $30 \times 102 \times 123$ still in corner point geometry. Since the gridding is corner point geometry, a corresponding Cartesian grid in original depositional coordinates can be easily created, namely every grid block has the same i, j, k index in both coordinate systems.

2. In the Cartesian grid the calcite bodies are modeled using the multiple-point algorithm SNESIM.

3. Next the gridding algorithm 3DDEGA is used to perform non-uniform upscaling / upgridding, resulting in a coarsened model which is still in Cartesian coordinates.

That gridding is in a corner point geometry in order to better represent the calcite bodies.

4. The non-uniformly gridded model is then mapped to actual reservoir coordinates.
5. Full flow simulation is performed on the coarsened model in the reservoir coordinate system.
6. The mismatch between the flow simulation results and the observed field data are calculated.
7. The calcite bodies in the Cartesian grid are perturbed where using the probability perturbation method.

The upscaling / upgridding is performed on the Cartesian coordinate system. Ideally, these stages should be performed in actual reservoir coordinates. However, the necessary tools were not available to us for performing the upscaling in the actual reservoir coordinates. Hence, upscaling is performed in the Cartesian coordinate system and the resulting coarsened model is then mapped to the actual reservoir coordinate system for performing the flow simulations. The mapping is performed because the flow simulation cannot be run in the Cartesian coordinate system since the reservoir geometry is non-Cartesian.

The generation of the high resolution model

As mentioned in the workflow, a high-resolution geo-cellular model is used to model in detail the calcite bodies. The model utilizes a stratigraphic grid that is easily mapped into a Cartesian box. Non-uniform upscaling is performed in Cartesian coordinates. During that upscaling, the petrophysical properties (permeability, porosity, etc.) need to be upscaled as well. We maintain a model for the petrophysical properties similar to that provided by the operator, i.e. a layer-cake high resolution model of both porosity and permeability.

Due to the corner-point geometry of the grid, a permeability, $k_{i,j,k}$, in reservoir coordinates is the same as permeability $k_{i,j,k}$ in Cartesian coordinates.

Upscaling / upgridding using 3DDEGA

The 3DDEGA (Garcia *et al.*, 1990, 1992) algorithm is used to perform the upscaling / upgridding in Cartesian coordinates. The main objective of the upgridding is to preserve

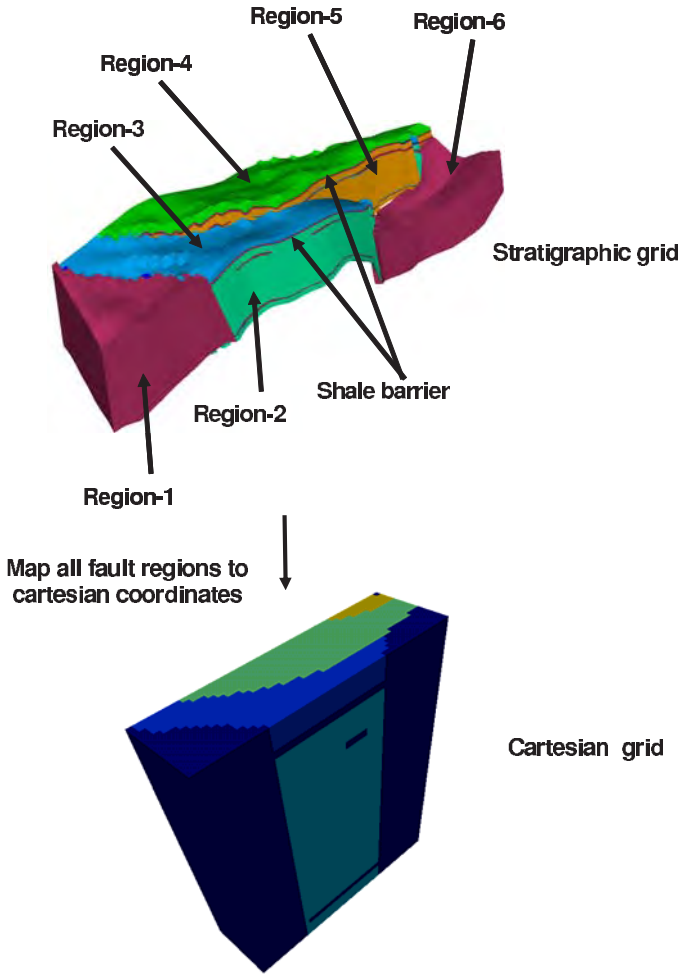

Figure 4.12: Illustration of the fault regions.

as much as possible the shapes of the calcite bodies on the coarsened model. In addition to the calcite bodies, 3DDEGA needs to account for faults as well as the single shale barrier (horizon-2).

Before applying 3DDEGA, a pre-preprocessing of the Cartesian grid is necessary. This preprocessing consists of pasting all necessary petrophysical information, fault information, shale barrier information onto the Cartesian grid. In order to model the location of the faults and the single shale barrier, an indicator code is given to each fault block of the reservoir as well as to the region above and below the shale barrier, see Figure-4.12.

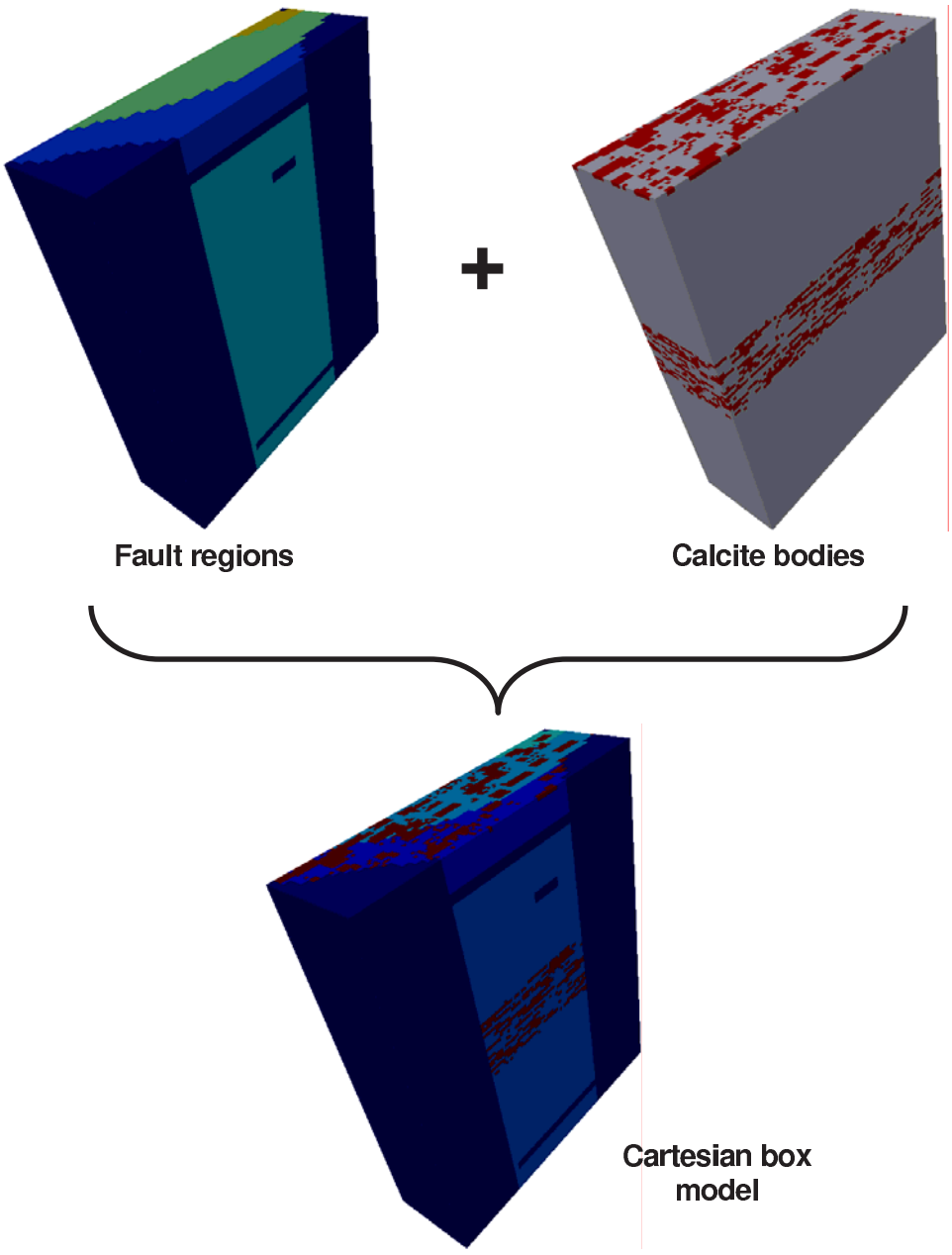

Figure 4.13: The generation of the Cartesian grid.

Next the calcite bodies are simulated in the same Cartesian grid using SNESIM. Figure-4.13 shows how the calcite bodies and fault regions are pasted together onto the same Cartesian grid. For illustrative purposes the bodies are only placed in the very top layer and in the middle layers of the model.

This model is input into the 3DDEGA algorithm. The resulting grid in corner point geometry is shown in Figure-4.14. Both top and side views are provided in order to show that the grids trace the fault lines and refine layers with high proportion of calcite bodies. The permeability values are arithmetically averaged during the upscaling.

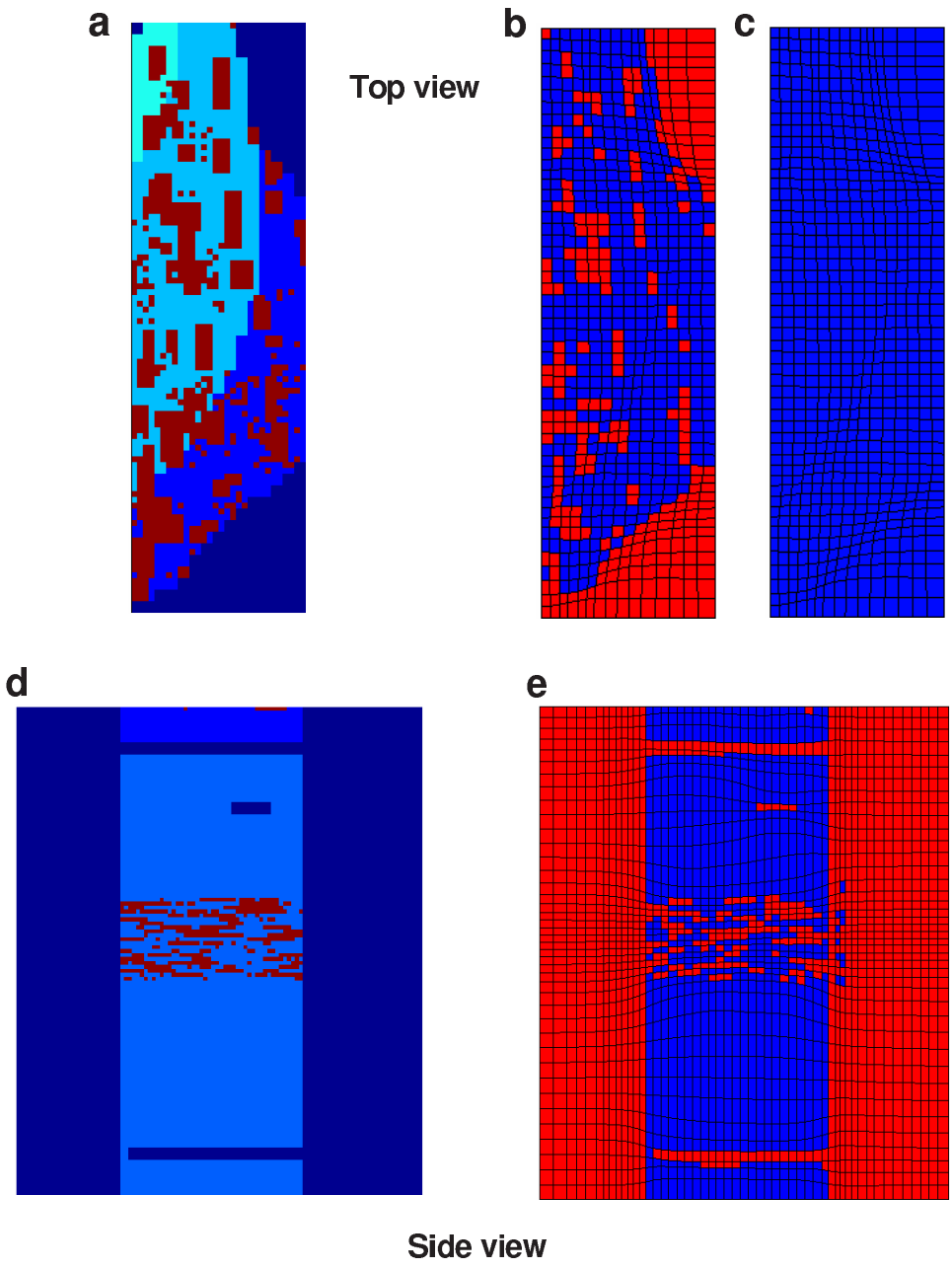

Figure 4.14: (a) The top view of the Cartesian model, (b) The top view of the coarsened 3DDEGA grid with the bodies, (c) The top view of the 3DDEGA grid alone, (d) The side view of the Cartesian model, (e) The side view of the 3DDEGA grid.

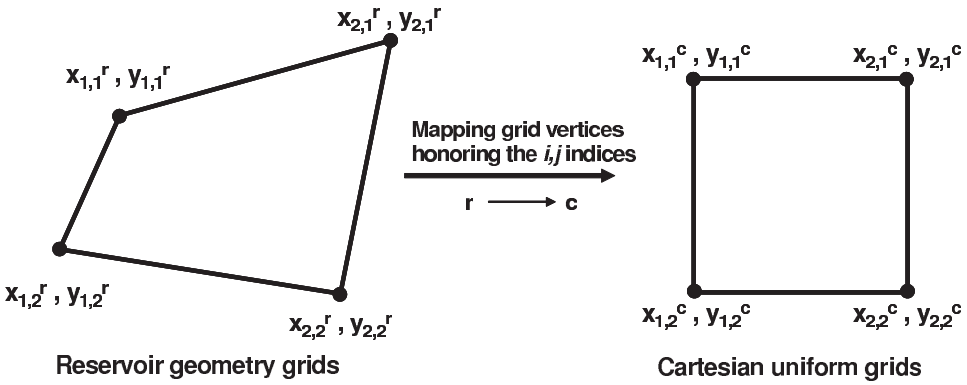

Figure 4.15: The mapping of the grid vertices. The superscript r represents the reservoir coordinates and the superscript c represents the Cartesian (uniform) coordinates.

Mapping

In the mapping phase, the output of 3DDEGA (the coarsened model) which is in Cartesian coordinates, is mapped to the reservoir coordinates. The petrophysical properties of the grid blocks are mapped by honoring the i, j, k indices.

This mapping is composed of three main stages:

1. Mapping the x and y coordinates of the grid vertices for the top and bottom layers.
2. Mapping the z coordinates of the grid vertices for the top and bottom layers.
3. Adjusting all z coordinates of the grid vertices.

In the first step, only the x and y coordinates of the vertices are mapped to the reservoir coordinates. The assumption is that each grid vertex in the reservoir coordinates (these vertices are obtained from the original numerical reservoir model) has a corresponding vertex (with the same i, j index) in Cartesian coordinates. The Cartesian vertices are uniformly distributed in space. This initial mapping is shown in Figure-4.15. Hence in this stage, the x and y coordinates of each vertex are mapped onto their counterparts in the Cartesian (uniform) coordinates.

After the upscaling and upgridding (performed by 3DDEGA), the resulting model vertices, which are still in Cartesian coordinates, are now distributed in space non-uniformly (in corner point geometry). Figure-4.16 shows how the mapping from the Cartesian coordinates to the reservoir coordinates is performed. The red grid in the Cartesian coordinate

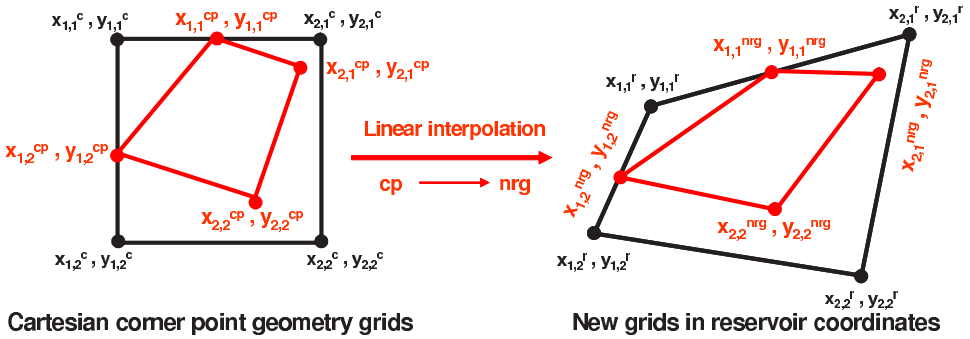

Figure 4.16: The mapping of the grid vertices from Cartesian coordinates to reservoir coordinates. The superscript cp represents the corner point geometry in Cartesian coordinates and the superscript nrg represents the new gridding in the reservoir coordinates.

system represents the 3DDEGA model. These red grids in the Cartesian coordinate system are mapped to the red grids in the reservoir coordinate system through by interpolation.

Next the z coordinates of the vertices that belong to the top and bottom layers are mapped in the same fashion. Figure-4.17 shows the mapping of the x, y and z coordinates for the top surface. Notice that the faults have not been generated so far. At the boundaries of the fault regions the grids are bent in order to accommodate the difference in heights of the segments. Then by using the ”fault regions” a correction is applied to the z-coordinates. The z-coordinates of each fault block are adjusted to account for the major faults, see Figure-4.18.

The rest of the 3DDEGA grid is mapped to the actual reservoir coordinates based on the top and bottom surfaces that have already been mapped. This final stage of the mapping is performed by linear interpolation as well. Once the top and bottom surfaces are interpolated into the actual reservoir coordinates, the grid vertices with corresponding indices are connected from the bottom layer to the top. These lines will be called the z lines. The 3DDEGA algorithm outputs the z lines with the z coordinate of each grid vertex in Cartesian coordinates. Next all z lines along with each grid vertex in the Cartesian coordinate system are linearly interpolated to the actual reservoir coordinates. This mapping is illustrated in Figure-4.19, where the black dots represent the top and bottom layer grid vertices and the red dots represent all grid vertices in the reservoir.

This finalizes the entire mapping providing a model ready for simulation with the commercial flow simulator, ECLIPSE. Figure-4.20 shows the final output of the mapping stage.

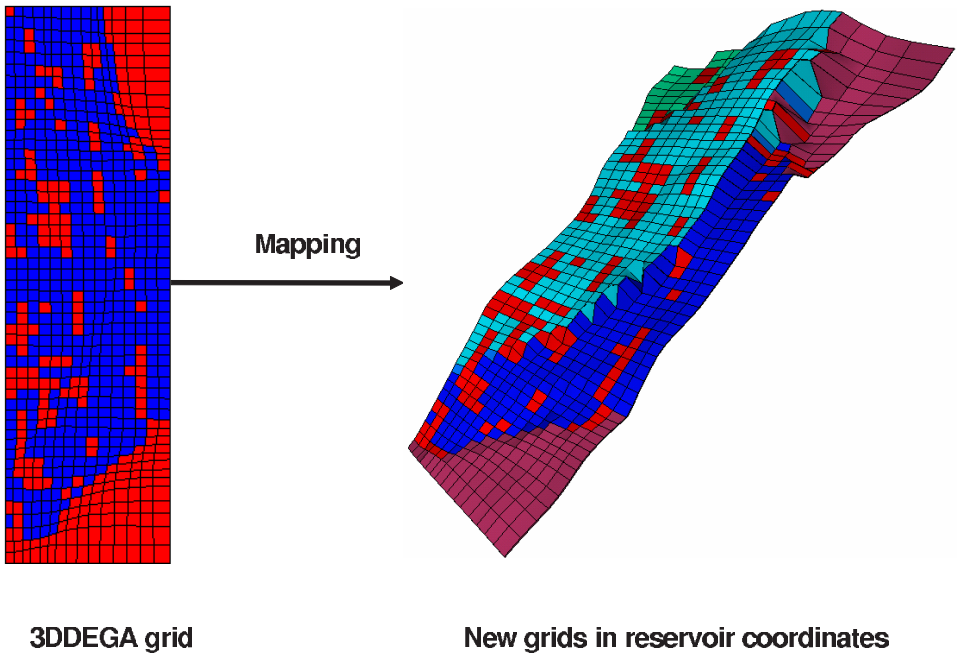

Figure 4.17: The mapping of the top surface from the 3DDEGA grid to the actual reservoir coordinates.

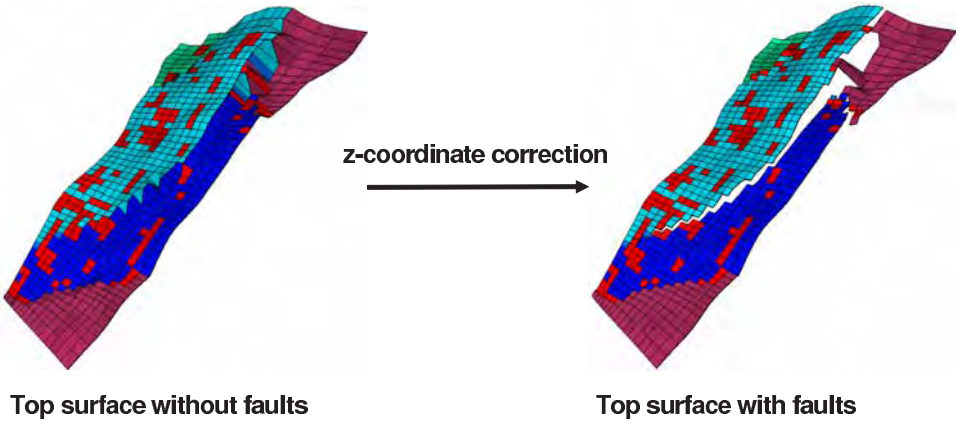

Figure 4.18: Correcting the z coordinates of the grid vertices for the top surface.

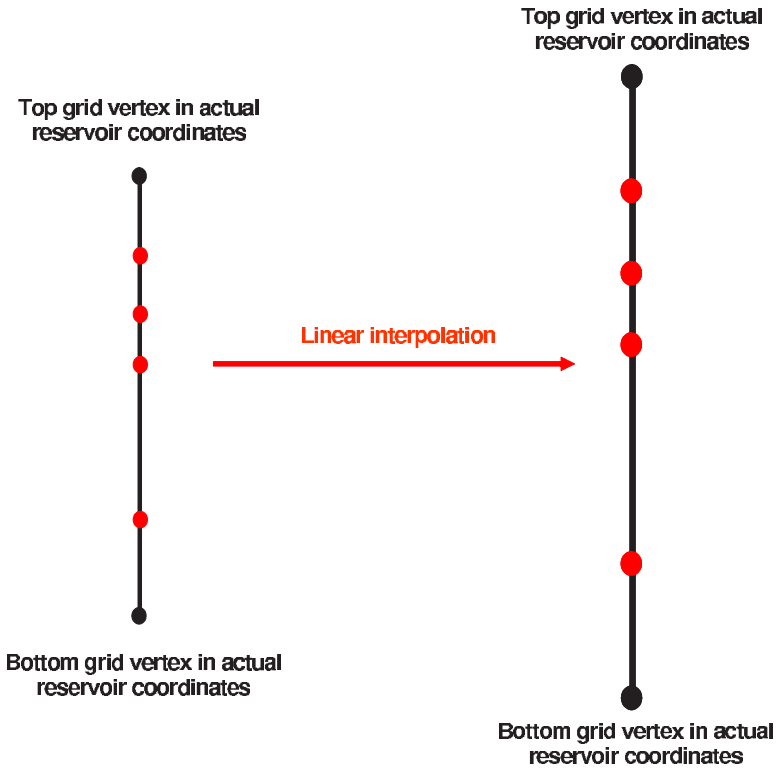

Figure 4.19: Illustration of how all z coordinates of the grid vertices are mapped.

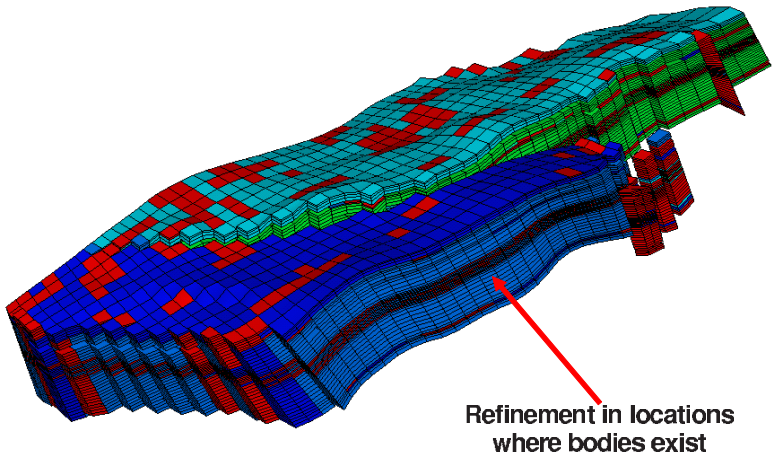

Figure 4.20: The final output of the mapping algorithm. The grids are refined in regions where calcite bodies exist. The dead cells have not been shown in this illustration

The grids are refined in regions where calcite bodies exist.

4.5 Results

We have present the results of the parallel modelling workflow as applied to the North Sea reservoir. The target is to history match the water rates of the problematic wells P-3 and P-4 given in Figure-4.7 by perturbing the location and proportions of the calcite bodies. These perturbations are performed region wise, where in this case only two regions are considered. Unlike the approach by Hoffman and Caers (2004), the regions are predetermined and remain fixed. The first region (region-1) is taken as the area surrounding wells P-3 and P-4. The second region (region-2) is the complement. The local proportions are varied only in the region surrounding the two wells.

The perturbations to the local proportions of the regions are performed with the probability perturbation method through the relation:

$$\mathrm{LP}_{\mathrm{k}}^{\mathrm{NEW}} = \mathrm{LP}_{\mathrm{k}}^{\mathrm{OLD}} + (2r_{\mathrm{k}} - 1)\mathrm{F}_{\mathrm{c}} \tag{4.2}$$

where the term $\mathrm{F_c}$ is taken as 0.1. This relationship allows the local proportions to decrease or increase when necessary. Consider the following three cases: When $r_{\mathrm{k}} = 0$ then $2r_{\mathrm{k}} - 1 = -1$, which causes a decrease in the local proportion. When $r_{\mathrm{k}} = 0.5$ then $2r_{\mathrm{k}} - 1 = 0$, which causes the local proportion to remain same. When $r_{\mathrm{k}} = 1$ then $2r_{\mathrm{k}} - 1 = 1$, which causes an increase in the local proportion.

For this case study the gridding optimization (Chapter-3) is not performed. The various 3DDEGA upgridding parameters were set based on a visual inspection.

The initial local proportion for the region-1 is 1%. The calcite bodies are placed within layers 45 and 65 in the high resolution model (with the bottom layer being the first layer). The initial model is shown in Figure-4.21 and the corresponding flow responses of wells P-3 and P-4 are given in Figure-4.22.

The resulting local proportion of region-1, obtained after history matching, equals 48%, which is in agreement with the results of Hoffman and Caers (2004). The final matched model and its corresponding flow responses are given in Figure-4.23 and Figure-4.24 respectively. As apparent from the flow responses given in Figure-4.24, the flow responses of the wells have improved significantly.

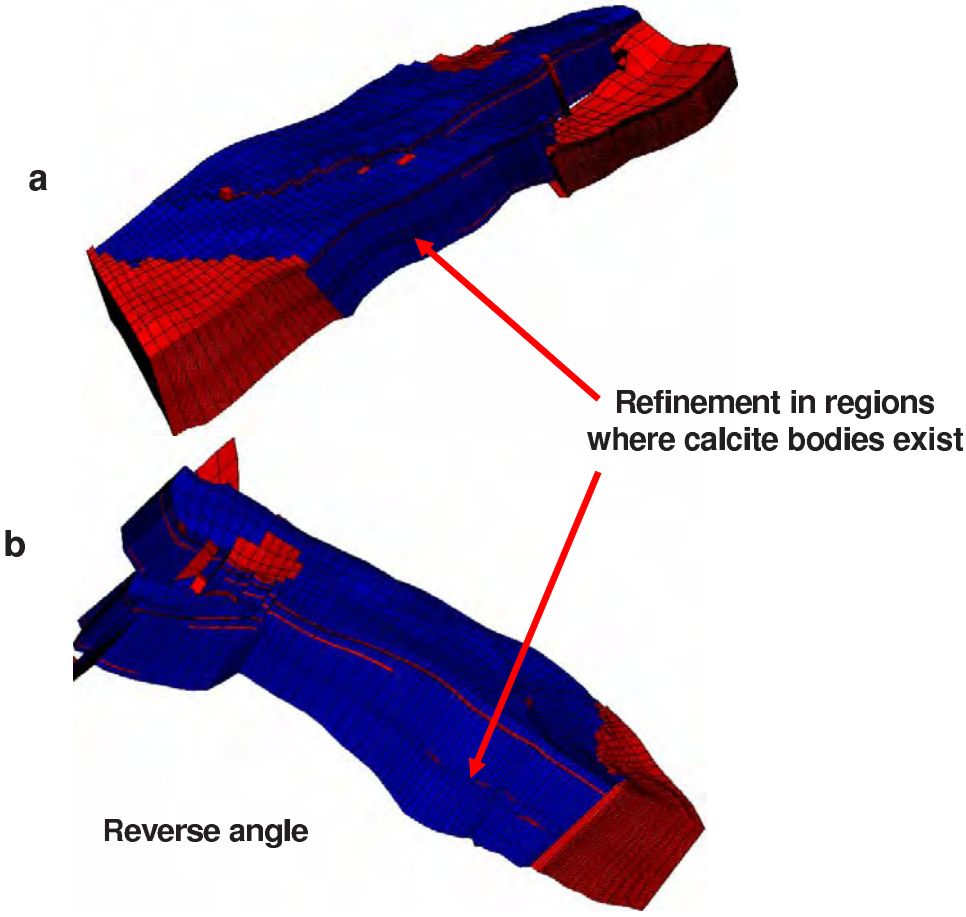

Figure 4.21: The initial model, (a) Forward angle (the calcite bodies are not visible because bodies are placed around wells P-3 and P-4, but refinement is visible), (b) Reverse angle of the model (In this case the calcite bodies are visible).

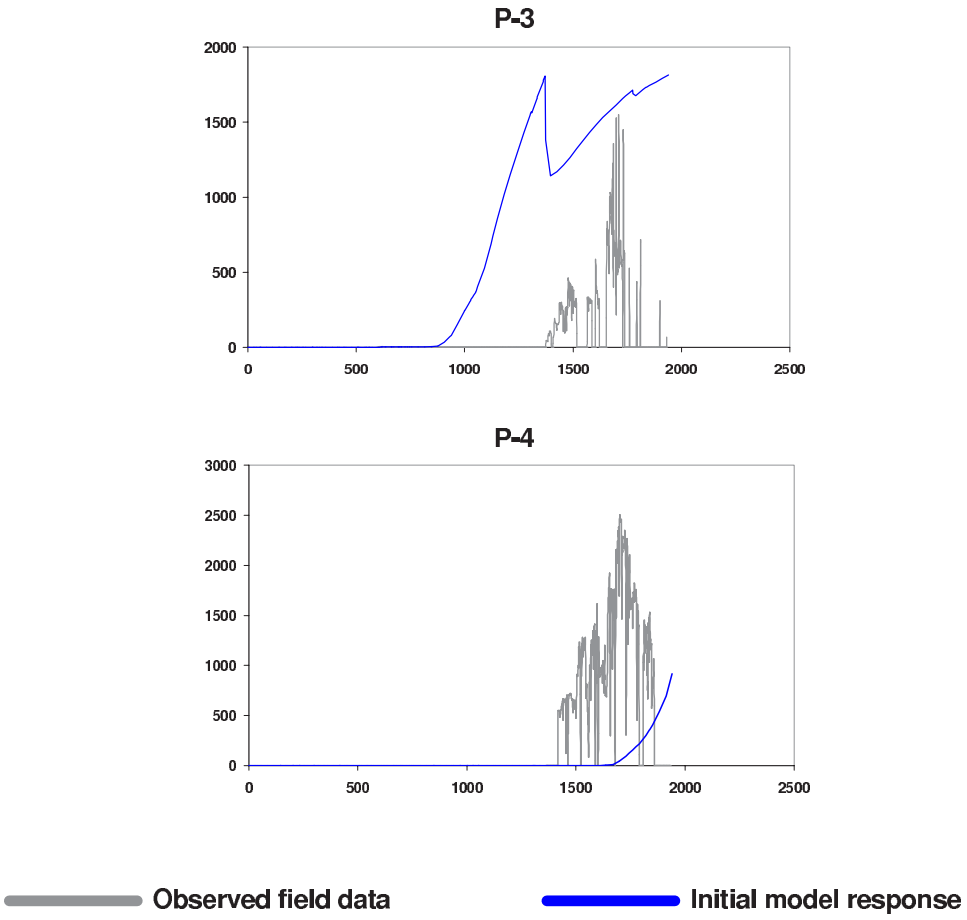

Figure 4.22: The flow response of the initial model for wells P-3 and P-4.

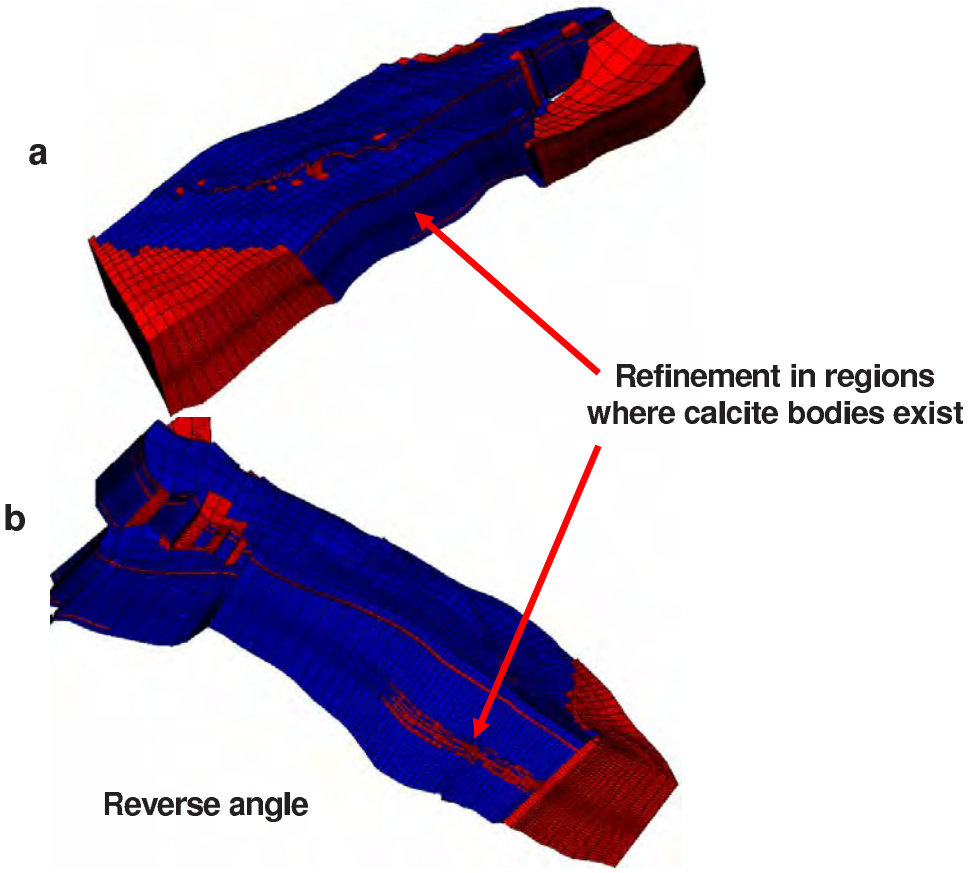

Figure 4.23: The initial model, (a) Forward angle, (b) Reverse angle of the model.

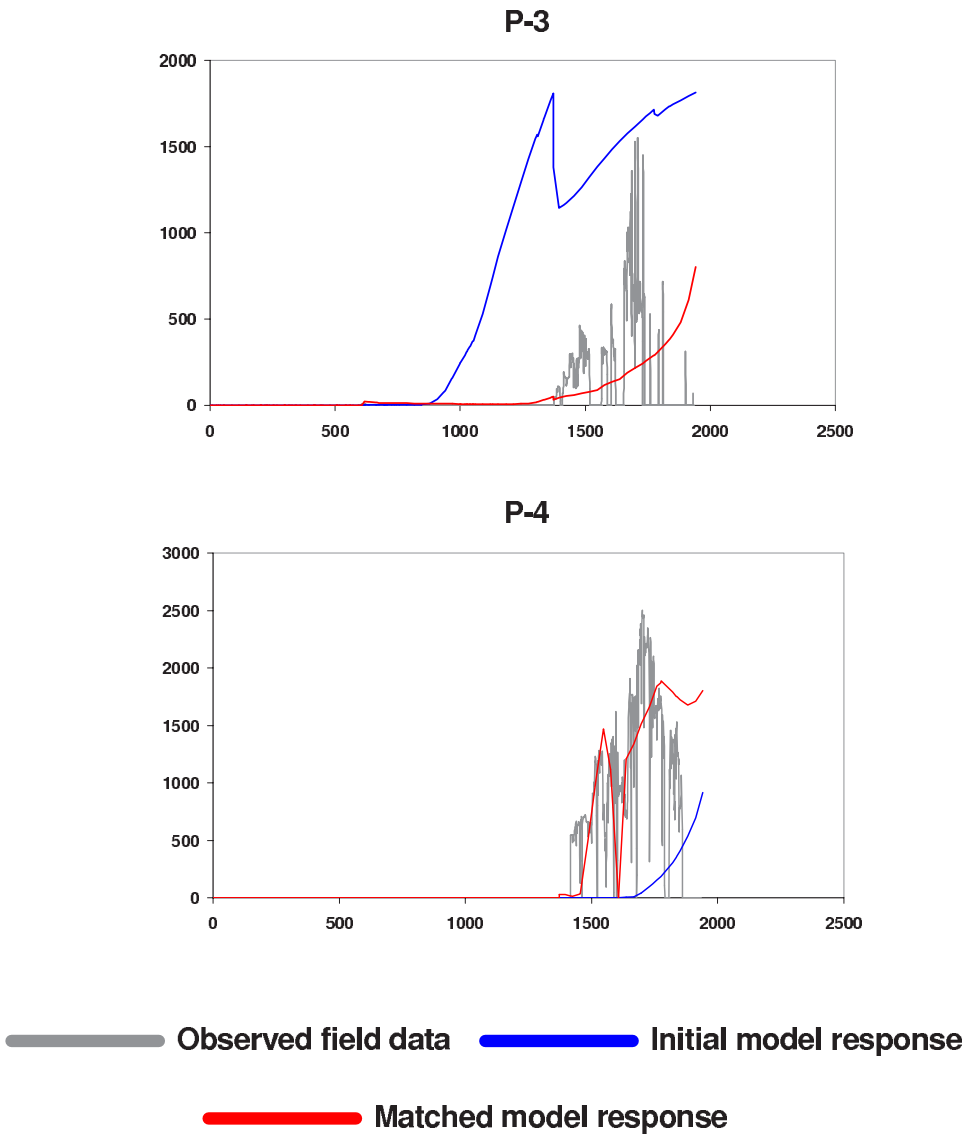

Figure 4.24: The flow response of the matched model for wells P-3 and P-4.

Chapter 5

Conclusions and Future Work

There are mainly two types of data available for reservoir modelling: Static data and dynamic data. Static hard data, such as core measurements and well-logs, inform at a fine scale but are sparse. Static soft data, such as seismic, informs the reservoir at a larger scale. Static data can be directly integrated into a reservoir model using well-established geostatistical methods. The dynamic data (such as pressure and flow data) on the other hand are more difficult to integrate because of their complex and highly non-linear relationships with the properties being modeled. The integration of this type of data is usually treated as an inverse problem and typically requires an iterative method.

The aim of reservoir modelling is to integrate all of the available data into a single numerical model. The challenge is to choose a model resolution (grid spacing) that can accommodate all data. However, such unique resolution does not exist. If the model resolution is too fine, integrating the dynamic data becomes unfeasible CPU-wise. On the other hand, if the resolution is too coarse, important fine-scale geological features as well as fine scale data cannot be accurately represented.

Current reservoir modelling workflows proceed in two stages. The first stage consists of structural modelling (such as horizons and faults), facies modelling and petrophysical modelling. At this stage, there is extensive conditioning to hard data and seismic data. The result of this first stage is a high resolution geo-cellular model which is too fine for any flow simulation to be performed. Hence, an upscaling is performed to coarsen the model in order to make flow simulations feasible. The second stage of modelling mainly addresses the integration of historical production data. The coarsened model is perturbed in some

fashion to obtain a history match. However, this perturbation may lead to the loss of data conditioning (such as hard data or seismic data conditioning) obtained during the previous static modelling. Furthermore, the gridding of the coarsened model typically remains fixed during history matching. This grid is obtained from the initial high resolution geo-cellular model and therefore may not be appropriate where properties are perturbed during a history match. Finally, in a two step workflow such as this, the structural model, which may be one of the greatest sources of uncertainty, also remain fixed. This workflow does not allow for the perturbation of the structural model because the two stages are treated as independent of each other.

This thesis presents an alternative approach to reservoir modelling. The main idea is to work with both a high resolution model and a coarsened model in parallel throughout the entire modelling process. This is accomplished by making upscaling a part of the history matching process. Hence, instead of perturbing the coarsened model independently of the high resolution model, perturbations are performed on the high resolution model and flow simulations are performed on the corresponding coarsened model. The perturbations are done based on the results of the coarse scale model flow response. The upscaling can be performed either uniformly or non-uniformly, depending on which best represents the geological heterogeneity and the response of the high resolution model.

Upscaling / upgridding is required at each perturbation. As a result the gridding adapts itself to the perturbed geological heterogeneity. Resulting from the parallel modelling workflow are two models: a high resolution model, that honors all available static data, and a coarsened model where important geological features are preserved and match the history.

The demonstration of the parallel modelling workflow is given in Chapter-2. The workflow was applied to various cases (in 2D and 3D) using different upscaling techniques, different history matching techniques and considering various types of geology. The workflow appears to work well in all cases history match is obtained while conditioning to hard data.

However, in cases of large upscaling errors, the parallel modelling workflow shows limitations. Hence in Chapter-3, an improved workflow is presented, where instead of directly upscaling the high resolution model, a gridding optimization is performed (to obtain the optimally gridded coarsened model) for minimizing the upscaling errors. As a result, history

match on the high resolution models is improved. This is demonstrated on the synthetic examples given Chapter-2.

The application of the parallel modelling workflow to an actual North Sea reservoir, given in Chapter-4, succeeds to account for calcite bodies which have a considerable impact on the flow response. With the parallel modelling workflow, these calcite bodies are modeled on the high resolution model, and are preserved on the coarsened model at each perturbation. The grid changes to adapt to the changing location of these calcite bodies each time the high resolution model is updated.

Although not addressed in this thesis, it is important to point out that one of the greatest sources of uncertainty could lie in the structural model itself, in other words the locations of the faults or the topology of the horizons. Although not demonstrated, the parallel modeling workflow could be used to perturb the structural model (Mallet, 2002). In the case of the North Sea reservoir, if information regarding the structural model is available, then perturbations of that structural model could be accommodated for if an automatic regridding of the stratigraphic grid is implemented.

Limitations

Some of the limitations of the parallel modelling workflow are:

- The parallel modelling workflow calls for the added cost and complexity of successive upscalings. In some cases this may be time consuming, especially if the improved parallel modelling workflow is considered, where multiple iterations are performed to obtain an optimally gridded coarsened model. This would hold true especially for large reservoirs where such upscaling might take hours of CPU.

- During the parallel modelling workflow, upscaling, upgridding, mapping, structural modelling, etc. are performed automatically. The workflow can accommodate many different tools, but these must be robust enough to be applied automatically without human intervention. Many of the current basic tools, such as gridding, have not yet reached that stage of automation.

- Even though the parallel modelling workflow provides a consistency between the high resolution model and the coarsened model, it is not used to address the missing

scale problem. In the examples presented through out this thesis high resolution models have been constrained with the hard data. However, the hard data which is in many cases provided by cores and well logs comes at a much smaller scale than the resolution of the high resolution model.

- The parallel modelling workflow is a tool and does not address some of the fundamental problems of reservoir modelling. Using this tool does provide means of perturbing a certain property for matching history. However, these perturbations (although providing a history match) could be wrong compensating for other factors such as lack of complete knowledge of fluid properties, underlying heterogeneity model (variogram or training image), etc.

Future work

The following topics may be considered as future work:

- Throughout this thesis, the application of the parallel modelling workflow is demonstrated on mostly corner point geometry gridding. However, in many cases, corner point geometry gridding is not flexible enough to represent the underlying geological heterogeneity. In such cases unstructured gridding would be called for. Unstructured grid allows to represent the fine scale details that would need to be represented on the coarsened model. The parallel modelling workflow should be accommodated to such unstructured gridding.

- Integrating production data is an essential part of reservoir modelling. In order to make accurate production forecasting, the models need to honor all available production data. However, in many cases (especially in reservoirs with few wells), production data is not constraining enough to determine the modeled property (such as permeability). This is because measurements of production are available only at the wells. Hence, there exists many configurations of properties that would provide the same production response during simulation. In other words, production data may not provide enough aereal constraints on the property that is being modeled. One of the recent advances in seismic technology is 4D seismic. 4D seismic consists of multiple 3D seismic surveys conducted at different times. 4D seismic is a function of

the fluid saturations in the reservoir, hence it could provide information with aereal content.

Integrating 4D seismic data requires an iterative inversion approach where a forward seismic run is performed multiple times for minimizing the mismatch between the observed seismic data and the calculated seismic data. As mentioned earlier, 4D seismic is a function of the spatial fluid saturation distributions. Hence, the saturation distributions in the reservoir must also be known in order to perform the inversion process for 4D seismic data integration. These saturation distributions can be obtained from flow simulations, which can only be performed on a coarsened reservoir model due to CPU constraints. Hence a scale problem arises. Current approaches to 4D seismic data integration consist of upscaling the high resolution model and performing flow simulations from which spatial saturation distributions can be obtained. These saturation values are then copied on to the high resolution grid where forward seismic modeling is performed.

The parallel modelling workflow can provide an effective effective way to integrate 4D seismic data. The workflow in this case would start with a high resolution model which would be upscaled to perform the flow simulation from which the saturation distributions for different time slices may be obtained. Next, these saturation distributions can be downscaled back to the high resolution model and the forward seismic run may be performed. Then the mismatch between the calculated seismic data and the observed seismic data can be obtained. In order to minimize the mismatch, perturbations would be performed on the high resolution model and the above steps repeated, until the mismatch is minimized. This could all be performed while conditioning to the production data.

- Throughout the thesis, the parallel modelling workflow is used for modelling permeability (in the synthetic applications) and calcite bodies (in the real field case study). However, as presented in Chapter-1, reservoir modelling consists of much more than just modelling one or more petrophysical properties. One of the main sources of uncertainty is the structural model. If tools are available for perturbing the structural model taking into account the seismic data, then the parallel modelling workflow can be used to model the locations of faults or topology of horizons. However,

as shown in Chapter-1, between the structural model and the high resolution geo-cellular model, there exist many steps of modelling, such as facies modelling and petrophysical modelling. Automatization of the workflow in this case would present serious challenges.

Bibliography

Arpat, G. (2004). A multiple-scale, pattern-based approach to sequential simulation. paper presented at the 7^{th} International Geostatistics Congress. Banff, CANADA, 26 September - 1 October.

Ballin, P. R., Aziz, K., Journel, A. G., and Zuccolo, L. (1993). Quantifying the impact of geological uncertainty on reservoir performing forecasts, paper SPE 25238 presented at the 12th SPE Symposium on Reservoir Simulation, New Orleans, Louisianna, USA, 28 February - 3 March.

Caers, J. (2002). Methods for history matching under geological constraints. paper presented at the VIII European Conference on Mathematics of Oil Recovery. Freiberg, GERMANY, 3-6 September.

Caers, J. K. (2003). History matching under a training image-based geological model constraints. *SPE Journal*, September, pp 218–226.

Caers, J. K. (2005). *Petroleum Geostatictics Primer*. SPE.

Chen, Y., Durlofsky, L. J., and Wen, X. H. (2004). Robust coarse scale modelling of flow and transport in heterogeneous reservoirs. paper presented at the IX European Conference on Mathematics of Oil Recovery. Cannes, FRANCE, 30 August-2 September.

Deutsch, C. V. (1985). Estimating block effective permeability with geostatistics and power averaging, paper SPE 15991 presented at the Unsolicited.

Deutsch, C. V. (1989). Calculating effective absolute permeability in sand-stone/shale sequences. *SPE Formation Evaluation*, September, pp 343–348.

Deutsch, C. V. and Journel, A. G. (1992). *GSLIB user's manual*. Applied Geostatistics. Oxford University Press, New York, second edition.

Deutsch, C. V., Tran, T. T., and Pyrcz, M. J. (2002). Geostatistical assignment of reservoir properties on unstructured grids, paper SPE 77427 presented at the SPE Annual Technical Conference and Exhibition, San Antonio, Texas, USA, 29 September - 2 October.

Ding, Y. (1995). Scaling-up in the vicinity of wells in heterogeneous field, paper SPE 29137 presented at the Reservoir Simulation Symposium, San Antonio, Texas, 12 - 15 February.

Durlofsky, L. J., Jones, R. C., and Milliken, W. J. (1997). A non-uniform coarsening approach for the scale-up of displacement processes in heterogeneous porous media. *Advances in Water Resources*, pp 335–347.

Durlofsky, L. J., Milliken, W. J., and Bernath, A. (2000). Scaleup in the near-well region. *SPE Journal*, March, pp 110 – 117.

Garcia, M. H., Journel, A. G., and Aziz, K. (1990). An automatic grid generation and adjustment method for modelling reservoir heterogeneities. Technical report, Stanford Center For Reservoir Forecasting. 3^{rd} SCRF Annual Report.

Garcia, M. H., Journel, A., and Aziz, K. (1992). Automatic grid generation for modeling reservoir heterogeneities. *SPE Reservoir Engineering*, p 278.

GeoQuest (2001). *ECLIPSE reference manual 2001A*. Schlumberger.

Gill, P. E., Murray, W., and Wright, M. H. (1981). *Practical optimization*. Academic Press, San Diego, USA.

Goovaerts, P. (1997). *Geostatistics for natural resources evaluation*. Applied Geostatistics. Oxford University Press, New York.

Guyaguler, B. and Horne, R. (2001). Uncertainty assesment of well placement optimization, paper SPE 71625 presented at the SPE Annual Technical Conference and Exhibition, New Orleans, Louisiana, USA, 30 September - 3 October.

Haldorsen, H. and Damsleth, E. (1990). Stochastic boolean simulation of fluvial deposits: a new approach combining accuracy with efficiency. *JPT*, April, pp 404–412.

He, C. (2004). *Structured flow-based gridding and upscaling for reservoir simulation*. Phd dissertation, Department of Petroleum Engineering, Stanford University, California.

Hernandez, G. J. J. and Journel, A. G. (1994). Grid block permeabilities: From Point Values to Tensors. *SPEFE*, June.

Hernández, J. (1991). *A stochastic approach to the simulation of block conductivity fields conditional upon data measured at a smaller scale*. Phd dissertation, Department of Applied Earth Sciences, Stanford University, California.

Hoffman, T. and Caers, J. (2004). Regional probability perturbation method applied to a real reservoir. Technical report, Stanford Center For Reservoir Forecasting. 17^{th} SCRF Affiliates meeting.

Hoffman, T. and Caers, J. (2005). Regional probability perturbations for history matching. *Journal of Petroleum Science and Engineering*, pp 53 – 71.

Hoffman, T. B. and Caers, J. (2003). Geostatistical history matching using a regional probability perturbation method, paper SPE 84409 presented at the SPE Annual Technical Conference and Exhibition, Denver, Colorado, USA, 5-8 October.

Hu, L. Y., Blanc, G., and Noetinger, B. (2001). Gradual deformation and iterative calibration of sequential stochastic simulations. *Mathematical Geology*.

Journel, A. G. (2002). Combining knowladge from diverse information sources: an alternative Bayesian analysis. *Mathematical Geology*, July, pp 573–598.

Journel, A. G., Deutsch, C. V., and Desbarats, A. J. (1986). Power averaging for block effective permeability, paper SPE 15128 presented at the 56^{th} California Regional Meeting, California, USA, April.

Landa, L. J. and Horne, R. N. (1997). A procedure to integrate well test data, reservoir performance history and 4-D seismic information into a reservoir description, paper SPE 38653 presented at the SPE Annual Technical Conference and Exhibition, San Antonio, Texas, USA, 5-8 October.

Lø døen, O. P., Omre, H., and Durlofsky, L. J. Chen, Y. (2004). Assesment of uncertainty in reservoir production forecasts using upscaled flow models. paper presented at the 7^{th} International Geostatistics Congress. Banff, CANADA, 26 September - 1 October.

Mallet, J. (2002). *Geomodelling*. Oxford University Press, New York, first edition.

Manchuk, J., Leuangthong, O., and Deutsch, C. V. (2004). Direct geostatistical simulation on unstructured grids. paper presented at the 7^{th} International Geostatistics Congress. Banff, CANADA, 26 September - 1 October.

Mezghani, M. and Roggero, F. (2001). Combining gradual deformation and upscaling techniques for direct conditioning of fine scale reservoir models to dynamic data, paper SPE 71334 presented at the SPE Annual Technical Conference and Exhibition, New Orleans, Louisianna, USA, 30 September - 3 October.

Press, W. H., Teukolsky, S. A., Vetterling, W. T., and Flannery, B. P. (1992). *Numerical recepies in fortran*. Cambridge University Press, Cambridge, second edition.

Prevost, M. (2003). *Accurate coarse reservoir modeling using unstructured grids, flow-based upscaling and streamline simulation*. Phd dissertation, Department of Petroleum Engineering, Stanford University, California.

Roggero, F. and Hu, L. Y. (1998). Gradual deformation of continuous geostatistical models for history matching, paper SPE 49004 presented at the SPE Annual Technical Conference and Exhibition, New Orleans, Louisiana, USA, 27-30 September.

Schaaf, T., Mezghani, M., and Chavent, G. (2002). Direct conditioning of fine-scale facies models to dynamic data by combining gradual deformation and numerical upscaling techniques. paper presented at the VIII European Conference on Mathematics of Oil Recovery. Freiberg, GERMANY, 3-6 September.

Streamsim (2000). *3DSL Three-phase black-oil streamline-based reservoir simulator, Version 1.3, User Guide*.

Strebelle, B. S. (2002). Conditional simulation of complex geological structures using multiple-point geostatistics. *Mathematical Geology*, January, pp 1–22.

Tran, T., Wen, X., and Behrens, R. (1999). Efficient conditioning of 3D fine scale reservoir model to multiphase production data using streamline based coarse-scale inversion and geostatistical downscaling, paper SPE 56518 presented at the SPE Annual Technical Conference and Exhibition, Houston, Texas, USA, 3-6 October.

Tran, T. T. B. (1995). *Stochastic simulation of permeability fields and their scale-up for flow modelling*. Phd dissertation, Department of Petroleum Engineering, Stanford University, California.

Wen, X. H., Deutsch, C. V., and Cullick, A. S. (1998). Integrating pressure and fractional flow data in reservoir modeling with fast streamline-based inverse method, paper SPE 48971 presented at the SPE Annual Technical Conference and Exhibition, New Orleans, Louisiana, USA, 27-30 September.

Yeten, B. and Durlofsky, L. J. Aziz, K. (2002). Optimization of well type, location and trajectory, paper SPE 77565 presented at the SPE Annual Technical Conference and Exhibition, San Antonio, Texas, USA, 29 September - 2 October.

Ying, Z. (2001). Uncertainty of flow responses after conditioning to block averages. Technical report, Stanford Center For Reservoir Forecasting. 14^{th} SCRF Affiliates meeting.

Ying, Z. and Gomez, H. (2000). An improved deformation algorithm for automatic history matching. Technical report, Stanford Center For Reservoir Forecasting. 13^{th} SCRF Affiliates meeting.

Yoon, S., Malallah, A. H., Gupta, A. D., Vasco, D. W., and Behrens, R. A. (2001). A multiscale approach to production-data integration using streamline models. *SPE Journal*, June.

Zhang, T. and Strebelle, S. (2004). Non-stationary multiple-point geostatistical models. paper presented at the 7^{th} International Geostatistics Congress. Banff, CANADA, 26 September - 1 October.

Appendix A

History Matching Under Geological Control

History matching in general is an ill-defined problem with non-unique solutions. Given flow data from an actual field, it is possible to construct many reservoir models that honor this flow data, and these models can be significantly different from each other. Flow data in that sense can not constrain the model fully. Even though a history match can be achieved, the model would lack predictive power if it is not representative of the underlying geology. Hence while conducting history matching, the underlying geological continuity model should always be taken into account. Accurate representation of the underlying geology is of great importance especially for determining the optimal placement of wells (Guyaguler and Horne, 2001; Yeten and Durlofsky, 2002). Without an appropriate prior geological continuity model, representation of that geology is not possible.

In this appendix a collection of history matching methods that account for a prior geological continuity model are discussed. Before presenting the various techniques, we first define the notation used throughout this appendix.

A.1 Notation

z $\{z(\mathbf{u}), \forall\ \mathbf{u} \in \text{Model}\}$ the set of model properties at each grid block **u**=(x,y,z)

y $\{y(\mathbf{u}), \forall\ \mathbf{u} \in \text{Model}\}$ the set of normal score model properties at each grid block **u**=(x,y,z)

z(r) A perturbation of the high resolution geocellular model **z**. The magnitude of perturbation is parameterized using some parameters **r**.

D Historical response data to be matched.

A.2 Gradual Deformation by Linear Combination

The gradual deformation method presented in Roggero and Hu (1998), later improved by Ying and Gomez (2000) to account for hard data, combines linearly a number of Gaussian realizations into a new realization with the same histogram and variogram properties. Figure-A.1 illustrates the method. In a first step, one takes three individual realizations, $\mathbf{z}^1$, $\mathbf{z}^2$ and $\mathbf{z}^3$, which honor the seismic and the hard data, and apply a normal score transform to each of them. Next, the normal score realizations, termed $\mathbf{y}^1$, $\mathbf{y}^2$ and $\mathbf{y}^3$ are pixel-wise linearly combined through the parameters α_1, α_2 and α_3.

$$\mathbf{y} = \alpha_1 \mathbf{y}^1 + \alpha_2 \mathbf{y}^2 + \alpha_3 \mathbf{y}^3 \tag{A.1}$$

The α parameters must satisfy the following constraints.

$$\alpha_1 + \alpha_2 + \alpha_3 = 1 \tag{A.2}$$

$$\alpha_1^2 + \alpha_2^2 + \alpha_3^2 = 1 \tag{A.3}$$

As shown in Ying and Gomez (2000), these constraints guarantee that the mean, variance and variogram of the resulting realization **y** is the same as the ones of the three individual realizations, at the same time honoring the same hard conditioning data. As constraints A.2 and A.3 leave one degree of freedom, the parameters α_1, α_2 and α_3 can in that case be reparametrized as:

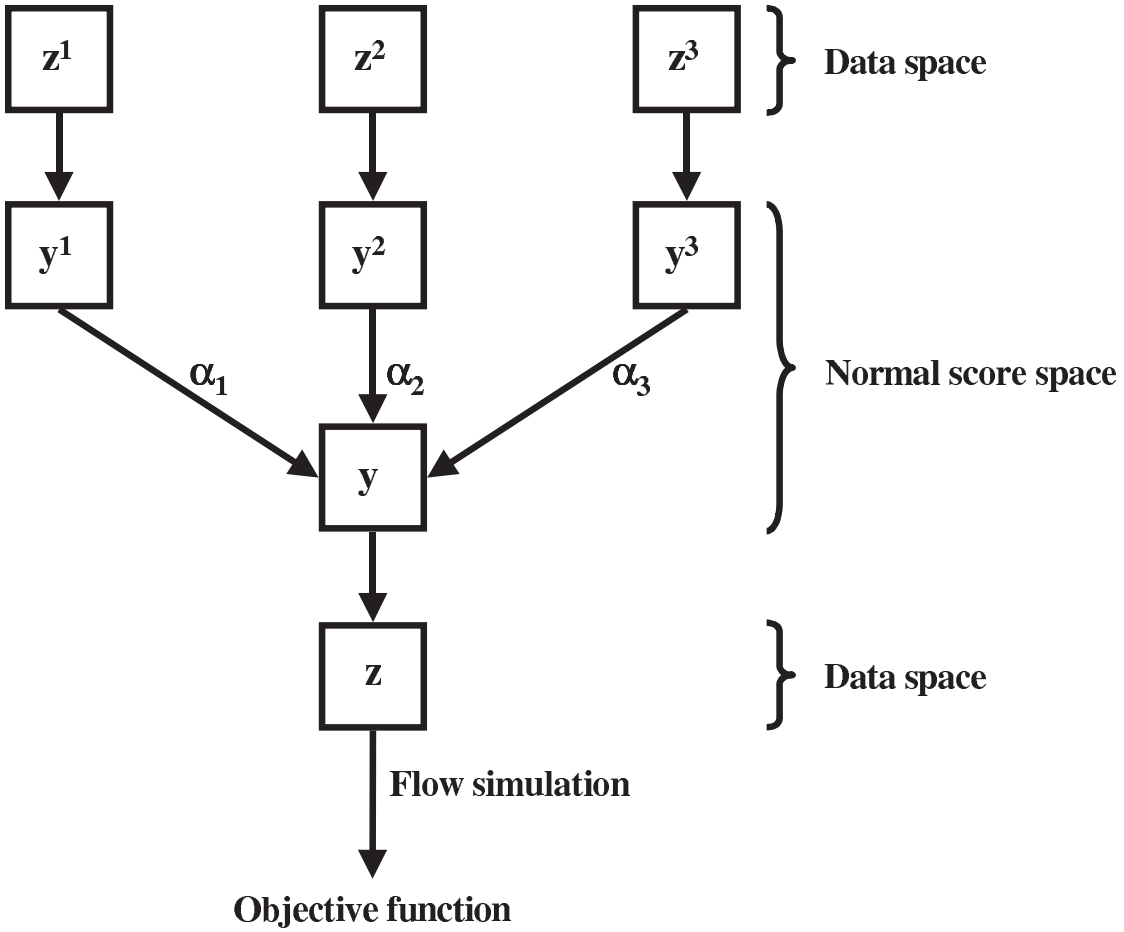

Figure A.1: The inner-loop workflow of the gradual deformation method.

$$\alpha_1 = \frac{1}{3} + \frac{2}{3}\cos r \tag{A.4}$$

$$\alpha_2 = \frac{1}{3} + \frac{2}{3}\sin\left(-\frac{\pi}{6} + r\right) \tag{A.5}$$

$$\alpha_2 = \frac{1}{3} + \frac{2}{3}\sin\left(-\frac{\pi}{6} - r\right) \tag{A.6}$$

where the single parameter *r* represents the available degree of freedom, thus:

$$\mathbf{y}(r) = \alpha_1(r)\mathbf{y}^1 + \alpha_2(r)\mathbf{y}^2 + \alpha_3(r)\mathbf{y}^3 \tag{A.7}$$

The resulting **y**(*r*) is then back transformed into the data space to obtain **z**(*r*). **z**(*r*) is a linear combination of $\mathbf{z}^1$, $\mathbf{z}^2$ and $\mathbf{z}^3$. Taking r values close to 0, provides a realization **z**(*r*) that slightly deviates from $\mathbf{z}^1$, the original realization (when $r = 0$, **z**(*r*)=$\mathbf{z}^1$). This results in a gradual deformation of the initial realizations $\mathbf{z}^1$, $\mathbf{z}^2$ and $\mathbf{z}^3$. For any given parameter value *r* the resulting realization **z**(*r*) is evaluated in a flow simulator resulting in the objective function.

$$O(r) = \|\mathbf{RP}(\mathbf{z}(\mathbf{r})) - \mathbf{D}\| \tag{A.8}$$

where **RP**(**z**) is the calculated flow response obtained by evaluating a flow simulation on **z** and **D** is the observed field data. It is now a matter of finding the optimal value r^{opt} leading to a realization $\mathbf{z}^{opt}$ that matches better the production history, **D**, by minimizing the objective function given in Equation-A.8. Since only one parameter (r) needs to be optimized we can apply any existing one dimensional optimization code, e.g. Dekker Brent (Press *et al.*, 1992). Combining these three realizations may lead to a better match, it does not necessarily provide a completely satisfactory history match. Therefore the resulting optimally combined realization $\mathbf{z}^{r^{opt}}$ is combined with two new equiprobable realizations, see Figure-A.2. The above steps are repeated until a convergence level is achieved. Figure-A.3 gives an alternative way of combining triplets of realizations.

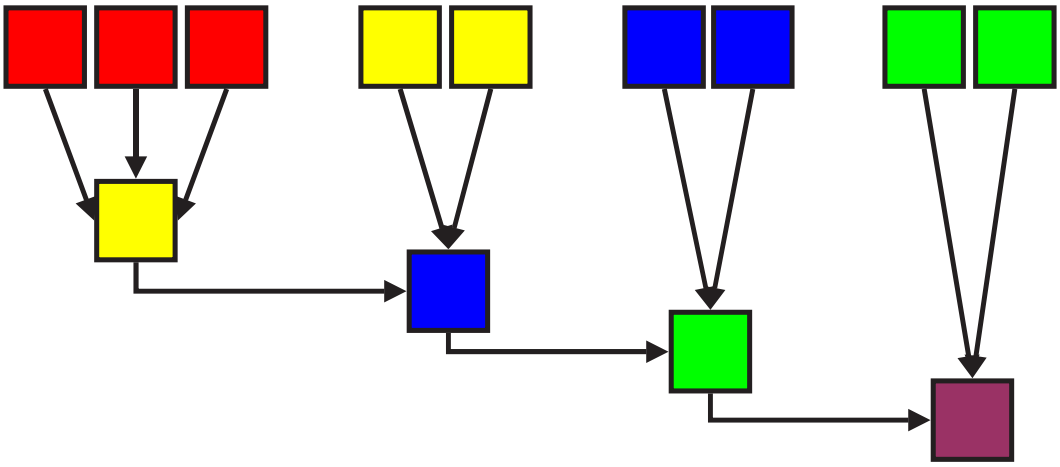

Figure A.2: Progression of the gradual deformation algorithm. Each color represents a new realization. Realizations with the same color are recombined.

The algorithm can be summarized as follows:

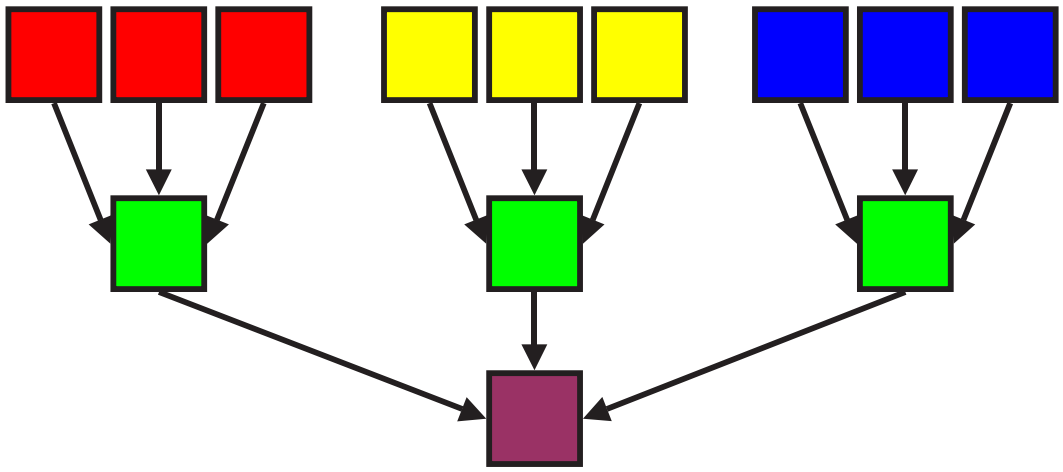

Figure A.3: Progression of the gradual deformation algorithm. Each color represents a new realization. Realizations with the same color are recombined.

1. Simulate three sequential realizations, $\mathbf{z}^1$, $\mathbf{z}^2$ and $\mathbf{z}^3$.
2. Perform a normal score transform and obtain $\mathbf{y}^1$, $\mathbf{y}^2$ and $\mathbf{y}^3$
3. Linearly combine $\mathbf{y}^1$, $\mathbf{y}^2$ and $\mathbf{y}^3$ and obtain $\mathbf{y}$ using relation A.1.
4. Transform $\mathbf{y}$ to obtain $\mathbf{z}$ through the following relationship:
   $\mathbf{z}(r) = G^{-1}(\mathbf{y}(r)) = G^{-1}(\alpha_1(r)\mathbf{y}^1 + \alpha_2(r)\mathbf{y}^2 + \alpha_3(r)\mathbf{y}^3)$
5. Perform flow simulation on $\mathbf{z}$ and calculate objective function given in relation A.8.
6. Goto step-3 and repeat the above steps until r is optimized which gives the optimal realization that minimizes the objective function, $\mathbf{z}$.
7. If the objective function is below a predetermined threshold value then STOP.
8. Set $\mathbf{z}^1$=$\mathbf{z}$ and generate two more individual realizations, $\mathbf{z}^2$ and $\mathbf{z}^3$. Then goto step-2.

A.3 Gradual Deformation of Sequential simulations

The gradual deformation method presented in section-A.2 can only be applied to Gaussian simulations. Hu *et al.* (2001) extended the gradual deformation method to any type of

sequential simulation. Before reviewing the proposed methodology, it is useful to recall the steps of any stochastic sequential simulation, see Deutsch and Journel (1992) and Goovaerts (1997). The basic algorithm of sequential simulation proceeds as follows:

- A random path is used to visit sequentially each unsampled node $\mathbf{u}_i$.
- A conditional cumulative distribution function (ccdf) is modelled at each node $\mathbf{u}_i$. That ccdf is conditioned to the original hard data, the previously simulated nodes and if available, any soft data.
- Using a random number v_i a value is drawn from the ccdf. The series of random numbers used for all nodes $\mathbf{u}_i$ is denoted by the vector **v**$= (v_1, \cdots, v_i, \cdots, v_n)$.

As long as one draws from these conditional distributions with independent random numbers, reproduction of the variogram input is ensured. Hence in order to construct a new realization $\mathbf{z}^r$ slightly different from the previous one, **z**, and at the same time preserve the structural statistics, one could perturb the random numbers. This is done as follows:

Consider a property field **z** that has been generated using a set of random numbers **v**. It is possible to obtain a standard normal distribution, $\mathbf{y}_1$, that corresponds to this set of random numbers by applying a normal score transform to **v**.

$$\mathbf{y}_1 = G^{-1}(\mathbf{v}) \tag{A.9}$$

A new set of numbers can be sampled from a standard normal distribution to obtain $\mathbf{y}_2$. It is possible to combine the standard normal vectors to obtain a third vector, **y**(r), which is also standard normal, through the following relation:

$$\mathbf{y}(r) = \mathbf{y}_1 \cos r + \mathbf{y}_2 \sin r, \qquad r \in [-\pi, \pi] \tag{A.10}$$

By applying a uniform transform to the new standard normal vector, **y**(r), a new set of random numbers, **v**(r), is obtained.

$$\mathbf{v}(r) = G(\mathbf{y}(r)) \tag{A.11}$$

v(r) can be used to generate a new realization **z**(r). To obtain a history match, one needs to minimize the objective function given in Equation-A.8 by optimizing over the r parameter. The history matching algorithm proceeds as follows:

1. Determine a random path which is then fixed.
2. Using that random path and a set of random numbers **v**, perform a sequential simulation resulting in an initial model **z**.
3. Perform flow simulation on the initial model and calculate the objective function. If the objective function is below a predetermined threshold value, then STOP.
4. Transform random numbers **v** to a standard normal distribution $\mathbf{y}_1$ through a normal score transform.
5. Draw a new set of Gaussian deviates, $\mathbf{y}_2$.
6. Determine new set of random numbers through the following relationship:

   $\mathbf{v}(r) = G(\mathbf{y}_1 \cos r^{opt} + \mathbf{y}_2 \sin r^{opt})$
7. With the new set of random numbers, perform a sequential simulation for determining $\mathbf{z}^r$.
8. Perform flow simulation on $\mathbf{z}^r$ and calculate objective function. If the objective function is below a predetermined threshold value, then STOP.
9. Goto step-6 and repeat the above steps until *r* is optimized which gives the optimal realization that minimizes the objective function, $\mathbf{z}^{r^{opt}}$.
10. Set $\mathbf{y}_1 = \mathbf{y}_1 \cos r^{opt} + \mathbf{y}_2 \sin r^{opt}$ and goto 5.

A.3.1 Regional gradual deformation of sequential simulation

Consider a reservoir model with multiple wells. Assume that most of the wells in this model match the production data from the field except for a few. In such a case, instead of perturbing the entire model, we would want to perturb only the regions where flow is affected by those wells that do not match the history. In such cases it is necessary to perform location specific perturbations. However a single parameter does not suffice, due to the fact that different regions may need to be perturbed differently from each other. For example, one would want to perturb regions with wells that do not match history, and not perturb regions where wells match the history. Multiple r parameters are needed to parameterize

perturbations in different regions. The gradual deformation of sequential simulation allows for such flexibility.

The perturbations to the model are made possible by varying r per predefined region in space. The model is partitioned into n predefined regions, and each region is assigned an r parameter. Hence the perturbation of the entire realization is parameterized by a vector of parameters, $\mathbf{r} = r_1, r_2, \cdots, r_n$. The set of random numbers for generating a perturbed realization is determined from the following relation:

$$\mathbf{v}(l, \mathbf{r}) = G(\mathbf{y}_1 \cos r_l + \mathbf{y}_2 \sin r_l), \quad \forall\, l = 1, \cdots, n \tag{A.12}$$

A new realization, **z**(l,**r**) can now be generated using the set of random numbers **v**(l,**r**). Furthermore any region l may be perturbed differently or not perturbed at all by varying the r_l parameter corresponding to the same region. Consider the following synthetic example:

Figure-A.4a illustrates a realization generated using SGSIM (Deutsch and Journel, 1992). This model is split into four regions given in Figure-A.4b. A different r parameter is assigned for each region, r_1, r_2, r_3 and r_4 for regions 1,2,3 and 4 respectively, in order to perturb them differently.

Figures-A.4c, A.4d, A.4e and A.4f illustrates perturbations on the regions defined in Figure-A.4b. Regions 1 and 4 are never perturbed, $r_1 = r_4 = 0.0$. Regions 2 and 3 are perturbed by the same amount. Figures A.4c, A.4d, A.4e and A.4f represent the cases where $r_2 = r_3 = 0.2$, $r_2 = r_3 = 0.5$, $r_2 = r_3 = 0.7$ and $r_2 = r_3 = 1.0$ respectively. As it is clear, as the r parameter increases, more perturbations are performed on regions 2 and 3. In all cases, regions 1 and 4 are never perturbed.

One of the advantages of using the regional deformation of sequential simulation technique is that during the perturbations to different regions, discontinuities are not created along the borders. Figures-A.4c A.4d, A.4e and A.4f illustrate this case well. Even though regions 1 and 4 are never perturbed, discontinuities do not exist between the boundaries of the regions. This is a result of the fact that changes are reflected to the random numbers that are used for generating the realization. The sequential simulation is performed on the entire model and not independently on each region. Also, sequential simulation uses neighborhoods that cross regions. In other words, when the boundaries are simulated, information is used from both sides of the boundaries. Hence discontinuities are avoided.

The drawback of such a method is that, for history matching purposes, optimization

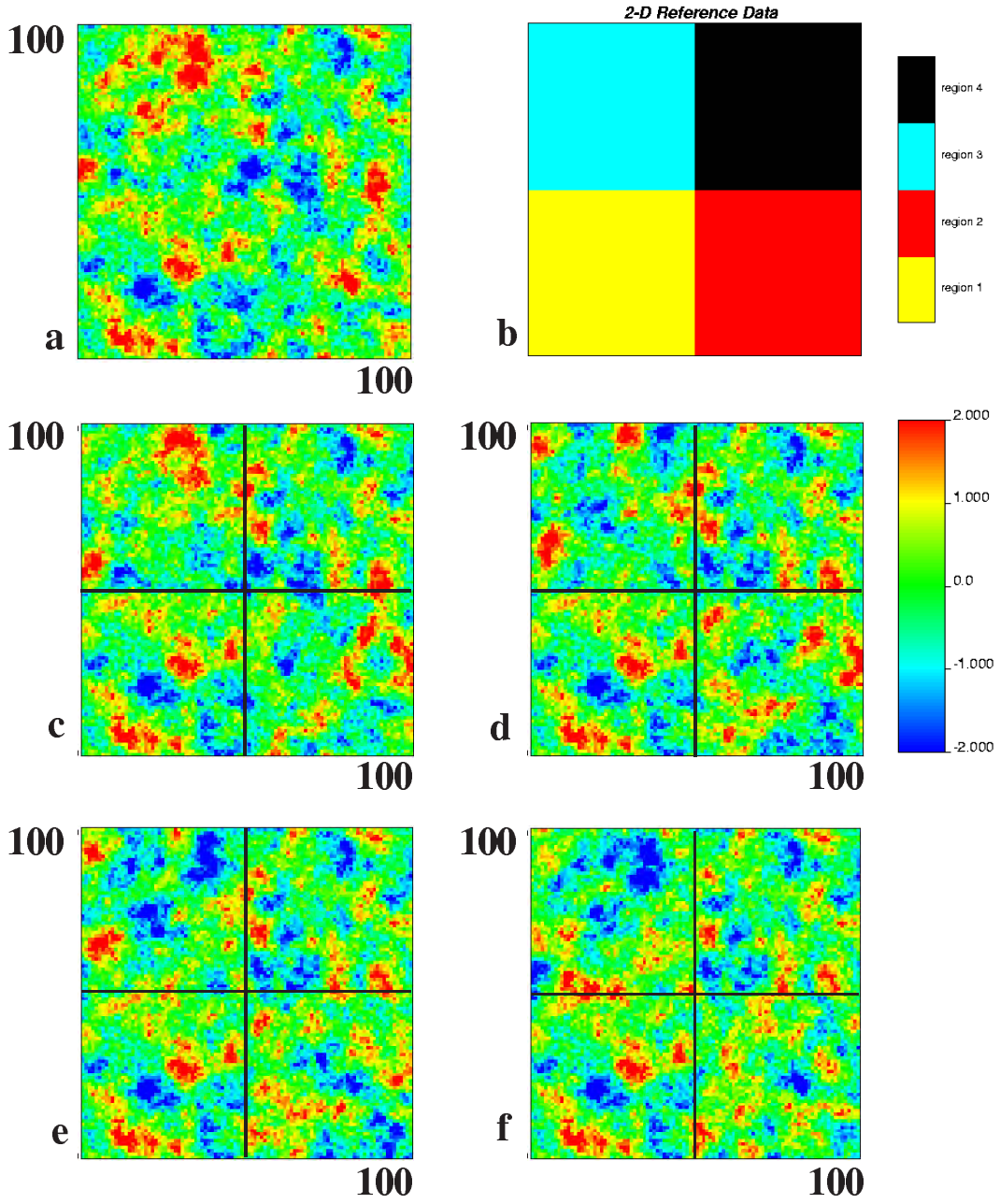

Figure A.4: (a) Initial property model (b) Various regions (c) $r_1 = 0.0, \quad r_2 = 0.2, \quad r_3 = 0.2 \quad r_4 = 0.0$ (d) $r_1 = 0.0, \quad r_2 = 0.5, \quad r_3 = 0.5, \quad r_4 = 0.0$ (e) $r_1 = 0.0, \quad r_2 = 0.7, \quad r_3 = 0.7, \quad r_4 = 0.0$ (f) $r_1 = 0.0, \quad r_2 = 1.0, \quad r_3 = 1.0, \quad r_4 = 0.0$.

needs to be performed on a vector, **r**, instead of a single r parameter. The choice for the regions may also be subjective based on a predefined criteria. Such regions can be determined through streamlines, where a region may be identified with streamlines belonging to an injector-producer pair.

A major drawback of the regional deformation of sequential simulations is that the random path of the sequential simulation is fixed. This is done to preserve the "gradual" nature of the deformation. Equation-A.12 is able to provide a smooth transition as the **r** vector is changed. The resulting field also changes gradually because the random numbers are used for drawing from "fixed" cumulative distribution functions (ccdf) because the random path is fixed. Since a random path represents a discrete geometry, it cannot be gradually changed. Any random path perturbation results in a non-gradual perturbation. When the random path is fixed, we slow the sampling of the space of uncertainty hence potentially slowing the history matching.

A.4 The probability perturbation method

Another route for perturbing the realizations to match history would be to perturb the conditional cumulative distribution functions (Caers, 2003), instead of perturbing the random numbers as shown in section-A.3.

The notation "A" is used for an event occurring at a certain location **u**. This event may be a permeability exceeding a certain value, a type of facies present at **u**, etc. We will consider a binary case for simplicity where A represents a channel or not at a certain location **u**. Such a binary variable is modelled using the indicator $I(\mathbf{u})$.

$$I(\mathbf{u}) = \begin{cases} 1 & \text{if the event occurs at } \mathbf{u} \\ 0 & \text{else} \end{cases}$$

The marginal probability of A occurring at a certain location can be denoted by P(A). Let us also denote "**B**" for representing hard data such as well log/core data. Then the conditional probability of A given the hard data **B** can be written as P(A|**B**). Finally the historical production data is represented by "**D**". Hence the conditional probability of A given the historical production data is P(A|**D**). The main idea behind the probability perturbation method is to perturb P(A|**B**) by taking into account P(A|**D**). If partial relations

P(A|**B**) and P(A|**D**) exist, then they can be combined to obtain the probability P(A|**B**,**D**) (defines the probability which we draw from in sequential simulation) through the method of Journel (2002).

The P(A|**D**) can be defined through the following relation:

$$\mathrm{P}(\mathrm{A}|\mathbf{D}) = (1-r)i^0(\mathbf{u}) + r\mathrm{P}(\mathrm{A}) \tag{A.13}$$

where i^0 is an initial realization conditioned only to P(A|**B**) and r is a parameter that varies between 0 and 1. Two extreme cases exist which are given as:

1. r=0, then P(A|**D**)=i^0(**u**)

2. r=1, then P(A|**D**)=P(A)

As it is clear, the r parameter controls the magnitude of the perturbation performed on a realization. If r=0, then P(A|**D**)=i^0(**u**), which means that P(A|**B**) is fully informative of the production data, hence i^0(**u**) is not perturbed. If r=1, then P(A|**D**)=P(A), which means that P(A|**B**) is not informative of the production data. Hence i^0(**u**) is perturbed. In order to integrate production data, one can take an existing realization, i^0(**u**), and find an optimal value of the r parameter that perturbs the realization to match the history.

Two main advantages exist with such an approach:

1. The overall problem has been parameterized with a single variable, r.

2. The geological continuity is maintained.

To visualize the effects of the r parameter, we consider the following synthetic example.

To create a perturbation of an initial realization i^0(**u**), created using an initial random seed s, one chooses a value for r between [0,1], then generates a new realization i^1(**u**) using

1. A different random seed s′.

2. A probability model P(A|**B**,**D**) obtained by combining P(A|**D**) for the proposed value r with P(A|**B**).

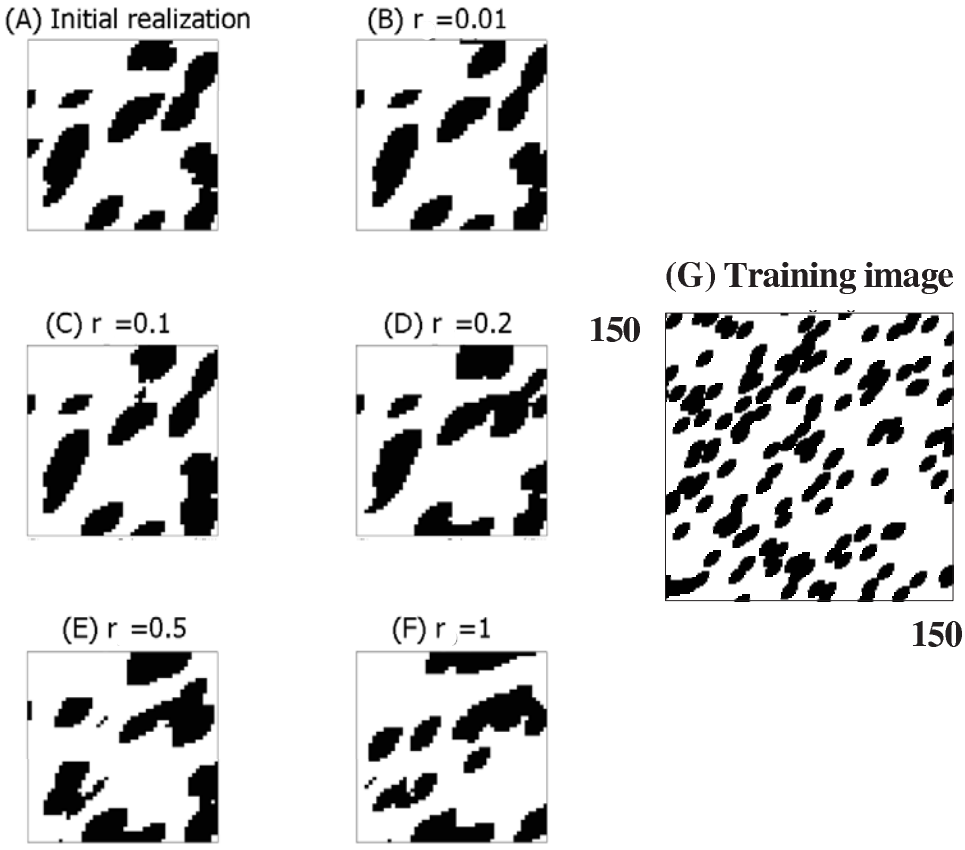

Figure A.5: The magnitude of the perturbations provided by the r parameter.

Figure-A.5 illustrates a sensitivity regarding the effects of the r parameter on the realizations. Figure-A.5a gives the initial seed realization generated using the SNESIM code (Strebelle, 2002) through the training image given in Figure-A.5g. When the r parameter is taken as a small value, then, the initial image is slightly perturbed where the overall structure stays the same (see Figure-A.5b where r=0.01). Increasing the r parameter results in considerable perturbations to the initial image. When r=1.0 (see Figure-A.5f), the image is in this case no longer resembles the initial seed realization. However it is very important to note that, whatever the value of r, the geological continuity (obtained from the training image) is maintained throughout all images.

The workflow for the probability perturbation method is given in Figure-A.6. The algorithm consists of two loops: the outer loop for updating the random seed, and the inner loop where the r parameter is optimized. The workflow is explained as follows:

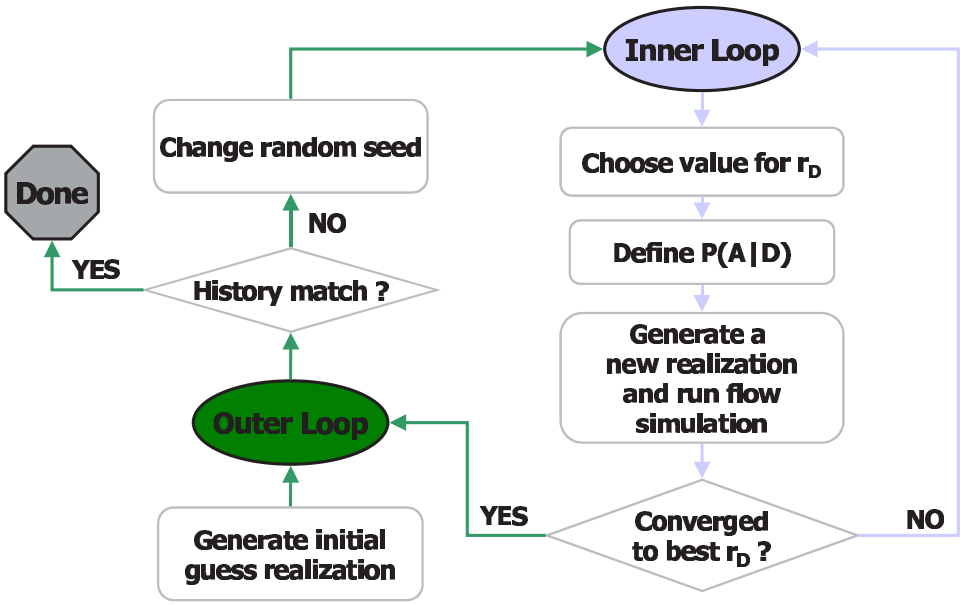

Figure A.6: The basic workflow of the probability perturbation method.

1. First an initial realization is generated, $i^0(\mathbf{u})$.
2. Flow simulation is performed on this realization and the objective function is evaluated. If the objective function is below a threshold value then STOP.
3. The random seed is changed.
4. A value of r is chosen and P(A|**D**) is calculated.
5. Using the calculated P(A|**D**), a new realization is generated.
6. Flow simulation is performed on this realization and the objective function is calculated.
7. Goto step-4 and optimize over the r parameter for minimizing the objective function.
8. Goto step-2.

A.4.1 Regional probability perturbation method

The probability perturbation method, as explained above, provides a global perturbation to a realization. This method would be effective for small reservoirs with few number

of wells. However, in realistic reservoirs with many wells, this technique would not be sufficient to obtain perturbations that would lead to a history match for all wells. In such cases a regional perturbation is necessary. The probability perturbation allows for such regional perturbations. In such a case the P(A|**D**) would be defined through the following relationship:

$$\mathrm{P}(\mathrm{A}|\mathbf{D}) = (1 - r_l)i^0(\mathbf{u}) + r_l\mathrm{P}(\mathrm{A}) \tag{A.14}$$

where l denotes the region number ($l = 1, 2, \cdots, L$) and L denotes the total number of regions. Even though P(A|**D**) is defined globally, it will have different values for each region defined in the reservoir. There exist a number of methods for defining the number and shapes of the regions. For history matching purposes, using streamlines for defining the regions presents an effective way (Hoffman and Caers, 2003) where each region is identified through the streamlines that belong to a single producer.

While performing the history matching, unlike the global probability perturbation method, optimization needs to be performed not just on a single r parameter, but on multiple r_l parameters (where each r_l parameter defines the amount of perturbation performed on region l. Hoffman and Caers (2003) proposes to use L number of 1 dimensional optimizations for each parameter r_l with a criteria to minimize the following objective function for each region l:

$$\forall l = 1, 2, \cdots, L \quad O(r_l) = |\mathbf{D}_l^c - \mathbf{D}_l| \tag{A.15}$$

where $O(r_l)$ denotes the objective function for region l, $\mathbf{D}_l^c$ is the calculated flow response for the well in region l and $\mathbf{D}_l$ is the observed field data for the well in region l.

Appendix B

Upscaling and Upgridding

B.1 Upscaling

Fine scale heterogeneities can have significant effects on flow responses in subsurface formations. Highly detailed geostatistical realizations are needed to capture the quantitative effects of these heterogeneities on flow simulation results. These realizations in some cases may require up to a billion cells, simply unfeasible to perform flow simulation. The common solution is to upscale and compute an equivalent property for the coarsened grid, hence reducing the dimensions of the grid.

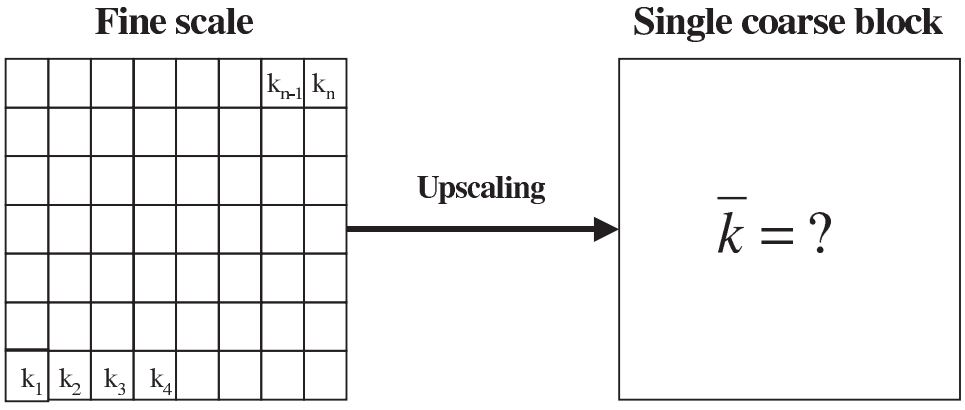

Figure B.1: Upscaling a fine grid of permeability into a coarse block.

Figure-B.1 illustrates the general problem of upscaling. The main challenge is to find an equivalent permeability for a coarsened grid block given the high resolution model,

preserving the flow properties of the high resolution model as much as possible.

The scale up of permeability values has been studied by many number of scientists. The equivalent permeability of a coarsened model grid block is dependent on many factors such as, the flow boundary conditions, spatial arrangement of the high resolution grid cells, anisotropy ratios, to name a few. In this section we provide background information only regarding the upscaling techniques used in this thesis, understanding that many other techniques exist in the literature. Two major types of upscaling techniques have been used: static and flow-based upscaling techniques.

B.1.1 Static upscaling

A simple way for calculating effective properties is by single-point averaging. Most common methods are: arithmetic averaging, harmonic averaging and geometric averaging. The arithmetic averaging gives a higher bound for the upscaled permeability while on the other hand the harmonic averaging gives the lower bound. Any other averaging for determining the equivalent permeability of Figure-B.1 would lie somewhere in between.

The power averaging provides a continuous spectrum of averaging values (see Journel *et al.* (1986), Deutsch (1989), Hernández (1991), Hernandez and Journel (1994)):

$$\overline{k} = \left[\frac{1}{n} \sum_{i=1}^{n} k_i^{\omega} \right]^{\frac{1}{\omega}} \tag{B.1}$$

The arithmetic, harmonic and geometric averaging techniques are special cases of Equation-B.1, where, $\omega = 1$ corresponds to arithmetic averaging, $\omega = -1$ corresponds to harmonic averaging and $\omega \to 0$ corresponds to geometric averaging.

In many cases the type of averaging required for permeability is unknown. In such cases the static averaging provided by Equation-B.1 can not be used since the ω parameter would be unknown.

B.1.2 Flow based upscaling

The upscaling method used in this study is single phase upscaling (Deutsch, 1985; Tran, 1995). The illustration of such an approach is given in Figure-B.2. The method is explained on a 2D system. The extension to 3D systems is straightforward.

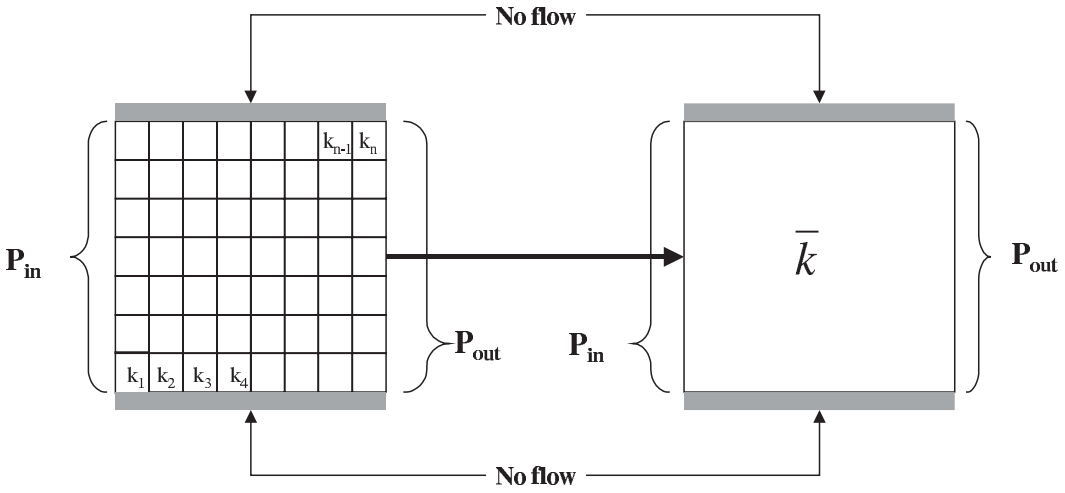

Figure B.2: Illustration of the flow based upscaling.

The aim of the single phase upscaling method is to preserve the overall flow rate of the high resolution grid block given incompressible single phase conditions. The procedure for determining the equivalent permeability value, $\overline{k}_x$, of a single coarsened grid block in the horizontal direction is explained. Given a high resolution grid block, no-flow boundaries are set on the boundaries parallel to flow. Constant pressure boundaries are then set in the direction of interest (the horizontal direction), denoted by P_{in} and P_{out} in Figure-B.2. Given the high resolution grid blocks permeability field denoted by $\mathbf{k}(\mathbf{u}) = \{k(u_1), k(u_2), \cdots, k(u_n)\}$, one can solve the pressure equation given in Relation-B.2 numerically.

$$\nabla.\left[\mathbf{k}(\mathbf{u}).\nabla p(\mathbf{u})\right] = 0 \tag{B.2}$$

The resulting pressure is then used to calculate the flow rate at the outlet grid blocks using Darcy's law:

$$q^{out}_{i=n_x,j} = \frac{k_{i=n_x,j}A}{\mu}\ \frac{P_{out} - P_{i=n_x,j}}{\Delta x/2} \tag{B.3}$$

where A is the cross-sectional area perpendicular to flow and μ is the fluid viscosity, which is taken as 1. The total flow rate is then calculated as:

$$q^{out} = \sum_{j=1}^{n_y} q^{out}_{i=n_x,j} \tag{B.4}$$

Due to the incompressible nature of the fluid the fluid flow rate at the inlet and outlet will be equal.

Using the predetermined flow rates, an equivalent permeability, $\overline{k}_x$ can now be determined through the following relationship.

$$\overline{k}_x = \frac{q^{out}\mu}{A} \frac{\Delta x}{P_{in} - P_{out}} \tag{B.5}$$

A similar approach is taken to determine $\overline{k}_y$, where the flow direction in this case would be in the y direction. In that case the constant pressure boundaries would be set on the top and bottom of the high resolution model and the no-flow boundaries would be set at the borders extending in the y direction.

B.2 Upgridding

In this section we provide a detailed description of the flow based upgridding method that has been used in this thesis. The method is valid for Cartesian grids only. The methodology is adapted from Durlofsky *et al.* (1997). The technique requires a single phase, incompressible flow simulation to be performed on the high resolution geostatistical model. A velocity field $u_{x,y}$ (for 2D reservoirs, with y being the vertical direction) is derived from which a non-uniform grid is determined. Once the velocity field, $u_{i,j}$, (where i and j denote the integer indices for the high resolution model) is determined, they are averaged along each row j as:

$$u^{avg}_j = \frac{\sum_{i=1}^{n_x} u_{i,j}}{n_x} \tag{B.6}$$

where n_x represents the number of grid cells in the x direction. Similarly the average velocity for each column i is calculated as:

$$u_i^{avg} = \frac{\sum_{j=1}^{n_y} u_{i,j}}{n_y} \tag{B.7}$$

where n_y represents the number of grid cells in the y direction. Next the row average velocities are standardized as:

$$u_j^{st} = \frac{u_j^{avg}}{\max_j(u_j^{avg}, j = 1, \cdots, n_y)} \tag{B.8}$$

Similarly for the columns:

$$u_i^{st} = \frac{u_i^{avg}}{\max_i(u_i^{avg}, i = 1, \cdots, n_x)} \tag{B.9}$$

We present first the algorithm for upgridding in only one dimension (uplayering) then proceed to the general case.

In order to preserve important high permeability layers, we preserve layers with high standardized velocity and upgrid layers with low u^{st}. The desired level of upgridding determines the threshold velocity above which high velocity layers should be preserved. For example, for a very coarse upgridding requirement, one would expect high velocity layers to be combined. To achieve an upgridding method that targets a certain coarse grid dimension, we approximately introduce the following tuning parameters:

- u_x^{max} is the maximum acceptable cumulative velocity of all high resolution layers composing any coarsened upgridded layer. If u_x^{max} is set to zero then the corresponding upgridded model will have the same number of layers as that of the high resolution model. As u_x^{max} is increased the dimensions of the coarsened model are decreased until u_x^{max} reaches the sum of all layers. At this point the coarse model would only be composed of a single layer.

- n^{max} is the maximum allowable number of high resolution layers composing any coarsened upgridded layer. If n^{max} is set to 1, then the corresponding upgridded model will have the same number of layers as that of the high resolution model. As n^{max} is increased, then u_x^{max} will become more dominant in determining the gridding.

The gridding algorithm for uplayering can be summarized as follows:

1. For $j = 1, \cdots, n_y$

   (a) Number of grid blocks=1 cumulative $u^{st} = 0$.

   (b) Until (number of grid blocks $> n^{max}$ or cumulative $u^{st} > u_x^{max}$)
   cumulative $u^{st} \leftarrow$ cumulative $u^{st} + u_j^{st}$
   $j \leftarrow j + 1$

   (c) Add grid line at j

The algorithm is described as follows:

- Start from row $j = 1$ until $j = n_x$.
- Cumulatively add u_j^{st} to the previous one as j increases.
- If the number of grid blocks is higher that n^{max} then mark the coarse grid block boundary, or
- if the cumulative u_j^{st}'s exceed u_x^{max} then mark coarse block boundary. However this time the cumulative standard velocities will have to be reset to zero.

The column-wise gridding is done in the same fashion, this time introducing the parameter u_y^{max} which is equivalent to u_x^{max}. In a general 3D case, one would upgrid along the major continuity direction first.

Consider the following 2D synthetic example illustrated in Figure-B.3. The upgridding method described above is performed on a 2D cross section of a permeability field. Figure-B.3a represents the horizontal permeability field and Figure-B.3c represents the vertical permeability field. Given the constant pressure boundary conditions (P_1 and P_2 in Figure-B.3b), an incompressible single phase flow simulation is performed on the given permeability field. As a result the velocity field is obtained in the horizontal and vertical directions, given in Figures-B.3b and B.3d respectively. The horizontal velocity field is similar to the horizontal permeability field. However the vertical velocity field (that indicates the vertical cross flow due to pressure difference in the horizontal) is rather different from the vertical permeability field. Once the velocity field is determined, velocities are averaged along each row for obtaining the average velocity curve for the horizontal velocities. Similarly

the velocities are averaged for each column for obtaining the average velocity profile for the vertical velocities.

Based on the average velocity profiles, the upgridding is performed and the coarse model is obtained as shown in Figure-B.3e. The upscaling method in this case, for obtaining the average properties of the coarsened permeability values, is the flow based upscaling method explained previously. As noted in Figure-B.3, the upgridding method manages to refine the high velocity regions accurately.

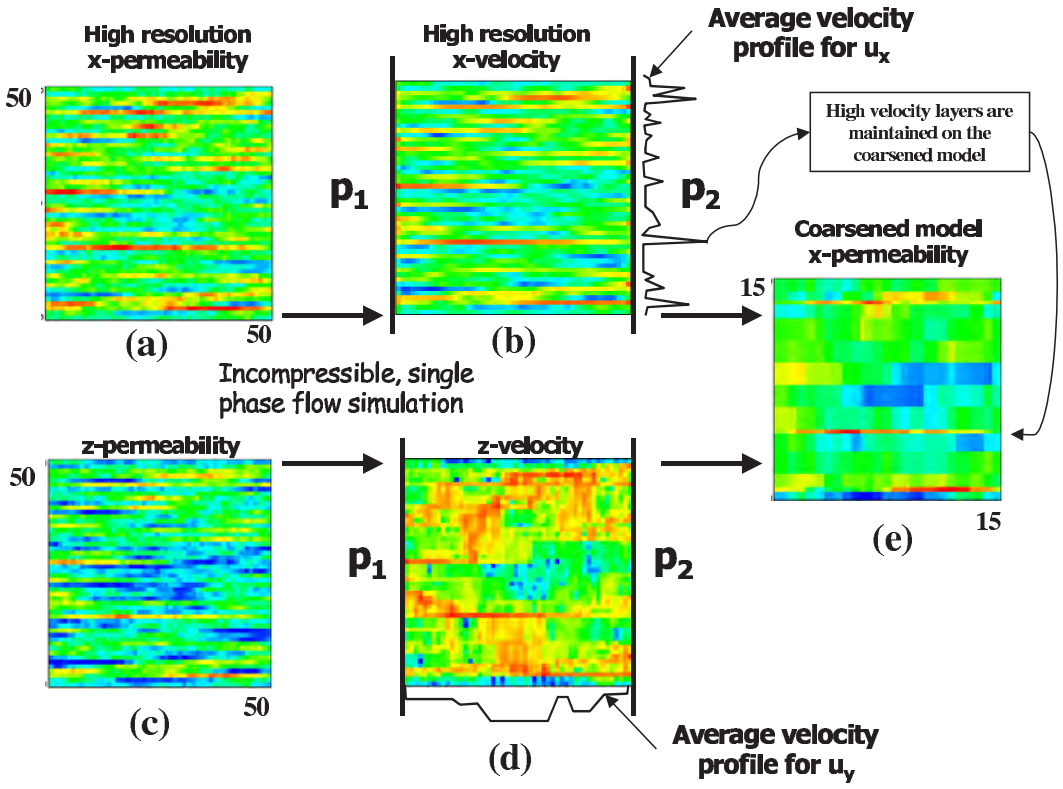

Figure B.3: The flow based upgridding method on a 2D cross section.

Appendix C

3D Discrete Elastic Grid Adjustment

C.1 Introduction

In this thesis we review an existing gridding algorithm, 3D-DEGA (3D Discrete Elastic Grid Adjustment), developed at the Stanford Center for Reservoir Forecasting by Michel Garcia, Andre Journel and Khalid Aziz (Garcia *et al.* (1990), Garcia *et al.* (1992)). This algorithm is devoted to the generation of quadrilateral or hexahedral grids suitable for grid adaptation based on reservoir properties (ϕ, k), pressure fields, saturation fields or any other reservoir variable. The resulting grids are in a corner point geometry fashion and can be used with most commercial simulators.

The main idea behind the 3D-DEGA algorithm is to generate coarsened grid blocks that are as homogeneous in terms of a given input variable or variables (permeability, porosity, facies map, etc.). Next to generating grids that capture the geological variability, 3D-DEGA attempts to obtain grid conformity by disallowing the generation of small small grid blocks next to large grid blocks (the ”suitability” of the grid blocks for flow simulation). 3D-DEGA can preserve the fine scale heterogeneities and flow responses by defining a balance between these two constraints (geology and grid conformity), while reducing significantly the number of grid blocks.

The intent of this chapter is first to give a review of the gridding approach the 3D-DEGA software uses. Then, a detailed explanation is provided on how the program can be run. This is followed by detailed descriptions of the parameters and the structures of the input files. Experience through sensitivities are also provided. Finally updates to the 3D-DEGA

software is discussed.

C.2 Fundamentals of Elastic Gridding

The 3D-DEGA is a software that uses an elastic gridding approach for obtaining grids that fit the underlying fine scale heterogeneity. Figure-C.1 illustrates how the 3D-DEGA algorithm responds to a simple example of fine scale heterogeneity. The high resolution model contains a box of high permeability within a low permeability matrix. In the coarsened model the gridding is refined in the region of high permeability and is coarsened for homogeneous areas. Coarsened grid blocks deviate from orthogonality to better preserve the high permeability region. This is accomplished through an elastic gridding approach. The following sections present some important details of the approach.

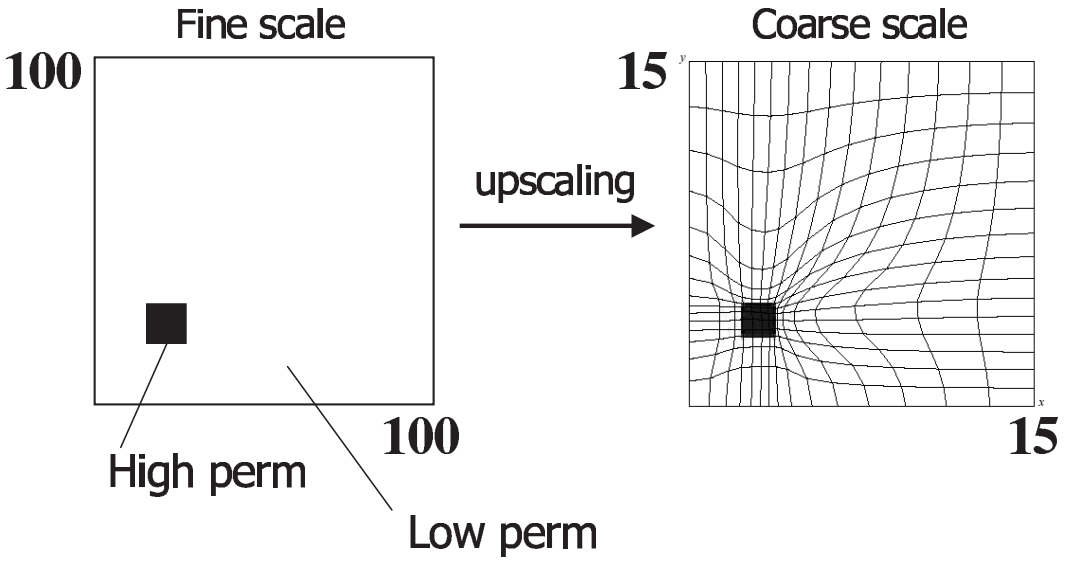

Figure C.1: Typical gridding provided by 3DDEGA.

C.2.1 Components of Elastic Gridding

Consider in Figure-C.2a a high resolution data grid, populated with one or more categorical or continuous property $z_i(\mathbf{u})$ where i=1,2,$\cdots$,N_d (N_d is the number of properties) and $\mathbf{u}$=(x,y,z). The elastic gridding algorithm uses the spatial distribution of these properties as

input. Figure-C.2b represents a typical gridding provided by 3D-DEGA (in this case, only for explanatory purposes since the underlying property field is not given). Figure-C.2c is a detailed description of a part of Figure-C.2b and illustrates all the necessary components of elastic gridding. The main idea behind the elastic gridding method is to consider all grid edges (a grid edge is illustrated in Figure-C.2c) as elastic bands capable of relaxing and contracting. The aim is to contract those elastic bands in areas with important fine scale heterogeneity and relax in mostly homogeneous zones.

Before explaining the necessary steps to obtaining elastic gridding (such as the one shown in Figure-C.2b) some important definitions must be made. Then the overall elastic gridding methodology will be explained through these definitions.

coefficient of elasticity. Each grid edge between vertex *i* and *j* (where a vertex is defined as the intersection points of grid edges, such as the vertex points 1 and 2 in Figure-C.2c) is assigned a coefficient of elasticity (k_{ij}). k_{ij} is made a function of the fine scale heterogeneity within the adjacent coarsened grid blocks. The exact functionality will be explained later. In Figure-C.2c, the coefficient of elasticity for grid edge 1-2 is a function of the fine scale heterogeneity in coarsened blocks 1234 and 1256. In 3D-DEGA, fine scale heterogeneity within a single coarsened block is summarized using the so-called grid-block coefficient of heterogeneity, denoted by β_B of block B, a concept that will be explained in detail in the following section. The coefficient of elasticity k_{ij} is therefore a function of the locations of the grid vertices x_i, y_i, z_i and x_j, y_j, z_j, because they determine the location and geometry of the coarsened grid block.

potential energy. A potential energy for a grid edge can be defined as follows:

$$E_{ij} = \frac{1}{2} k_{ij} d_{ij}^2 \tag{C.1}$$

where d_{ij} is the distance between grid vertices i and j. It is important to note that Equation-C.1 is a function of the coefficient of elasticity k_{ij}, therefore it is also directly proportional to the coefficient of heterogeneity β_B.

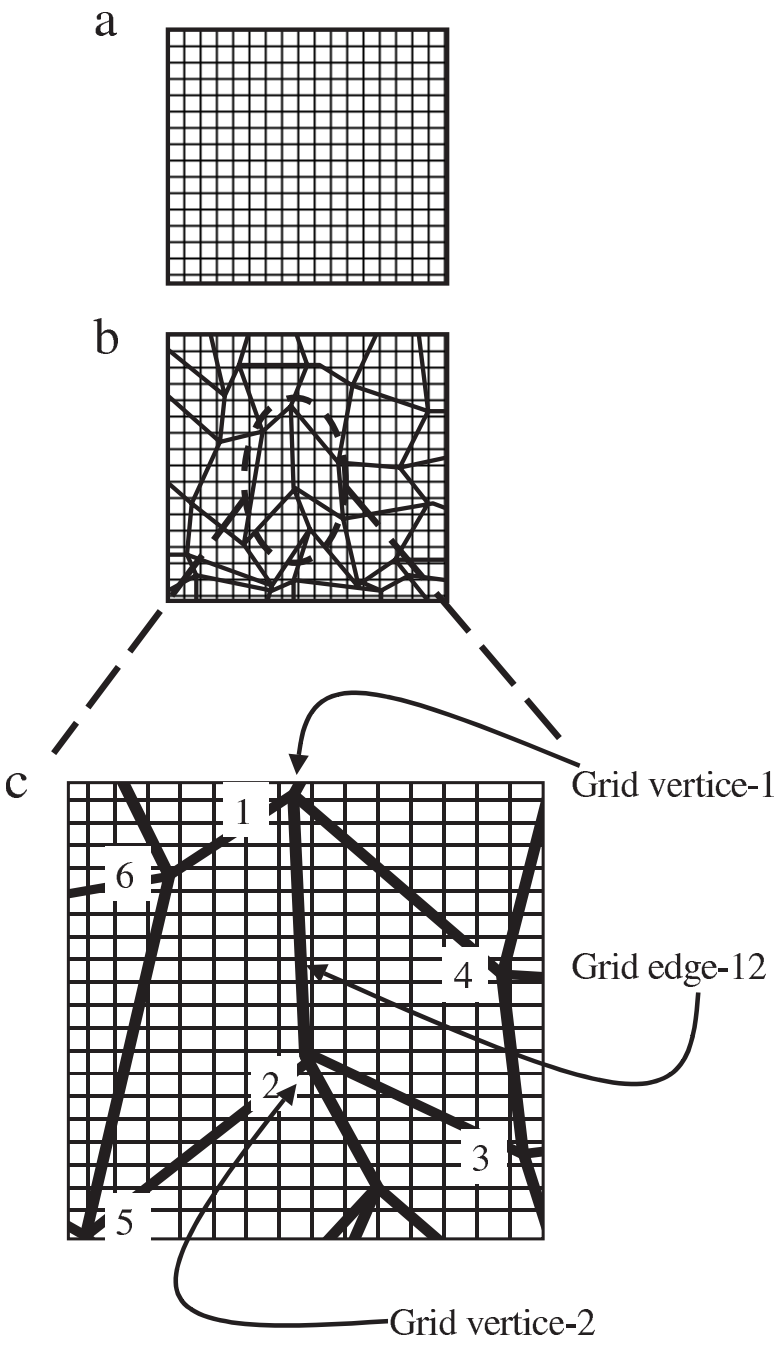

Figure C.2: Various components of the elastic gridding technique. (a)high resolution data grid, (b) typical elastic gridding provided by 3D-DEGA, (c) illustration of grid vertices and grid edges.

global potential energy A global potential energy can be expressed as the sum of all potential energies of all grid edges.

$$E_G(k_{ij}\forall ij) = \sum_{i,j} E_{ij} \tag{C.2}$$

Having made these necessary definitions, we can now proceed with explaining elastic gridding. Figure-C.3 illustrates the flow chart, all steps will be explained through Figure-C.3. The target of the 3D-DEGA algorithm is to minimize the global potential energy (which is a function of the grid vertex positions). This is performed by determining the optimal locations of the grid vertices such that E_G is minimized.

The algorithm starts with an initial arbitrary grid configuration with desired number of coarsened grids and initial coefficients of elasticity, as indicated in box-1 of Figure-C.3. At this point we will assume that the initial grid is Cartesian (with the desired target number of coarsened grids), and that the coefficients of elasticity for all edges are set to one. This assumption will be relaxed later and the importance of choosing the initial grid will be discussed in a forthcoming section. In the next step the grid vertex locations are optimized such that the global potential energy is minimized (the procedure for the minimization is not given here). This step is illustrated in box-2 of Figure-C.3. Once the global potential energy is minimized, the program stops if the maximum number of iterations is reached and the gridding is complete. If not, then we move to box-4 of Figure-C.3. Based on the new vertex locations, the coefficients of heterogeneity are computed. Then (see box-5 of Figure-C.3) the coefficients of elasticity are updated using the following relationship:

$$k_{ij}^{t+1} = k_{ij}^{t} + \Delta k_{ij}^{t+1} \tag{C.3}$$

where t is the previous iteration step, t+1 is the new iteration step and Δk_{ij}^{t+1} is the corrective term given by:

$$\Delta k_{ij}^{t+1} = \frac{1}{n_{ij}} \sum_{l=1}^{n_{ij}} \beta_l \tag{C.4}$$

here, n_{ij} is the total number of coarsened grid blocks adjacent to grid edge *ij*. Equations (C.3) and (C.4) define the basic relation between the coefficients of elasticity and the coefficients of heterogeneity.

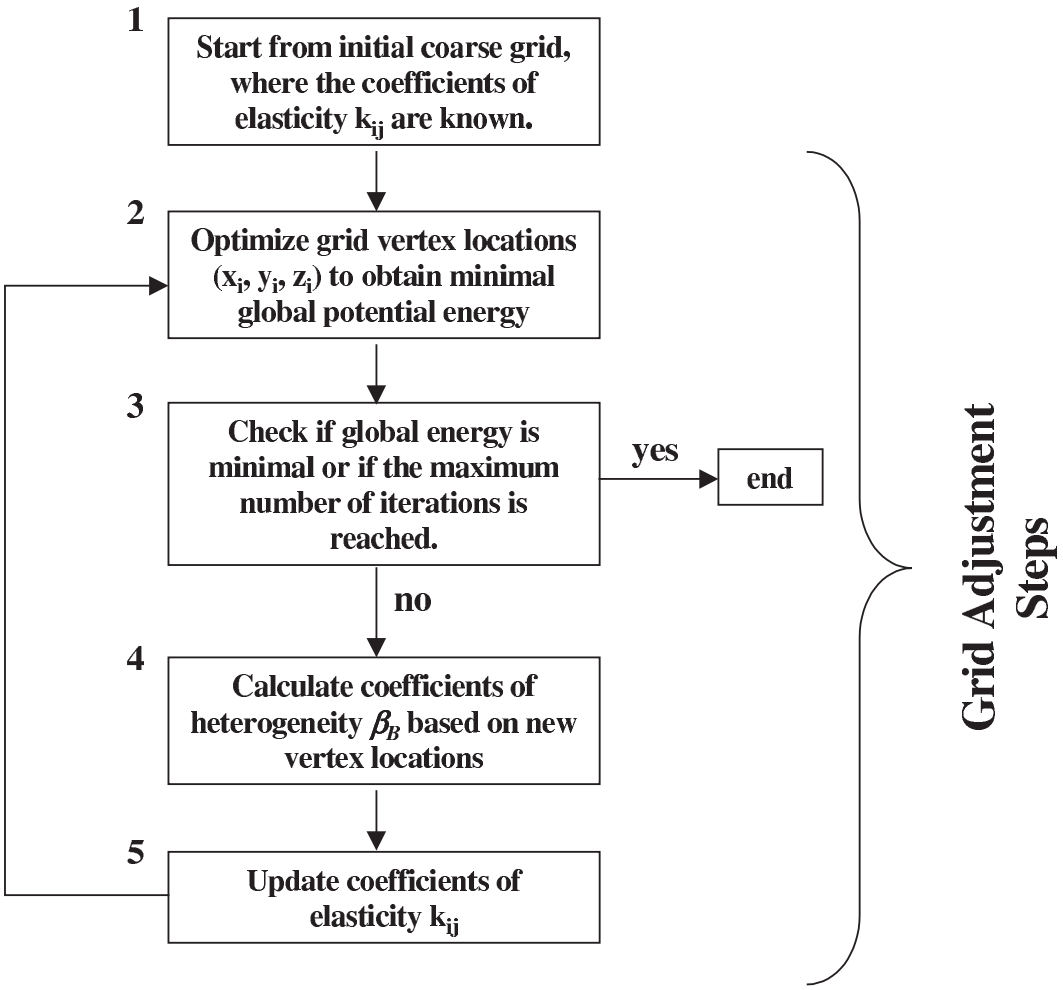

Figure C.3: Flow chart for the fundamental steps of the elastic gridding.

After the coefficients of elasticity are updated we go back to box-2 of Figure-C.3 and repeat the steps until convergence with box-3 of Figure-C.3 is achieved. The next section will focus on the important criterion for quantifying the within grid block heterogeneity, β_B.

C.2.2 Defining Block Heterogeneity, β_B

Up to this point the only missing component regarding the elastic gridding approach is a criteria that needs to be set for defining the coefficient of elasticity, $k_{i,j}$, for all grid edges based on a measure of heterogeneity of neighboring grid blocks. The grid block coefficient

of heterogeneity β_B is a measure of heterogeneity within each coarsened grid block B and is defined as follows:

1. For continuous variables a measure of coarsened grid-block heterogeneity is evaluated by means of the variance of the within high resolution model properties;

$$\sigma_B = \frac{1}{N_B} \sum_{i \in B} (z(\mathbf{u}_i) - m_B)^2 \tag{C.5}$$

where m_B is the mean of the high resolution model grid blocks within a single coarsened block *B*, given by

$$m_B = \frac{1}{N_B} \sum_{i \in B} z(\mathbf{u}_i) \tag{C.6}$$

N_B is the total number of high resolution model grid blocks that fall within a single coarsened grid block B and $z(\mathbf{u}_i)$ is the property assigned to each high resolution model grid block within block B.

2. In the case of categorical variables the coarsened grid-block coefficient of heterogeneity is defined as:

$$\sigma_B = 1 - (\max proportion)_B \tag{C.7}$$

where (max $proportion$)$_B$ is the proportion of internal data-grid nodes belonging to the most frequent category within block B.

The block coefficient of heterogeneity is defined in the following way:

$$\beta_B = \left(\frac{\sigma_B}{\sigma_{max}} \right) \tag{C.8}$$

where σ_B is the variance of the block of interest, σ_{max} is the maximum of all internal block variances (or equivalent expression for a categorical variable). Equation-C.8 can also be extended with a power parameter such that the coefficient of heterogeneity can either be a very strong function of the variance or not a function at all. In this case the coefficient of heterogeneity would take the following form:

$$\beta_B = \left(\frac{\sigma_B}{\sigma_{max}}\right)^{\omega_\sigma} \tag{C.9}$$

where ω_σ is a power weight.

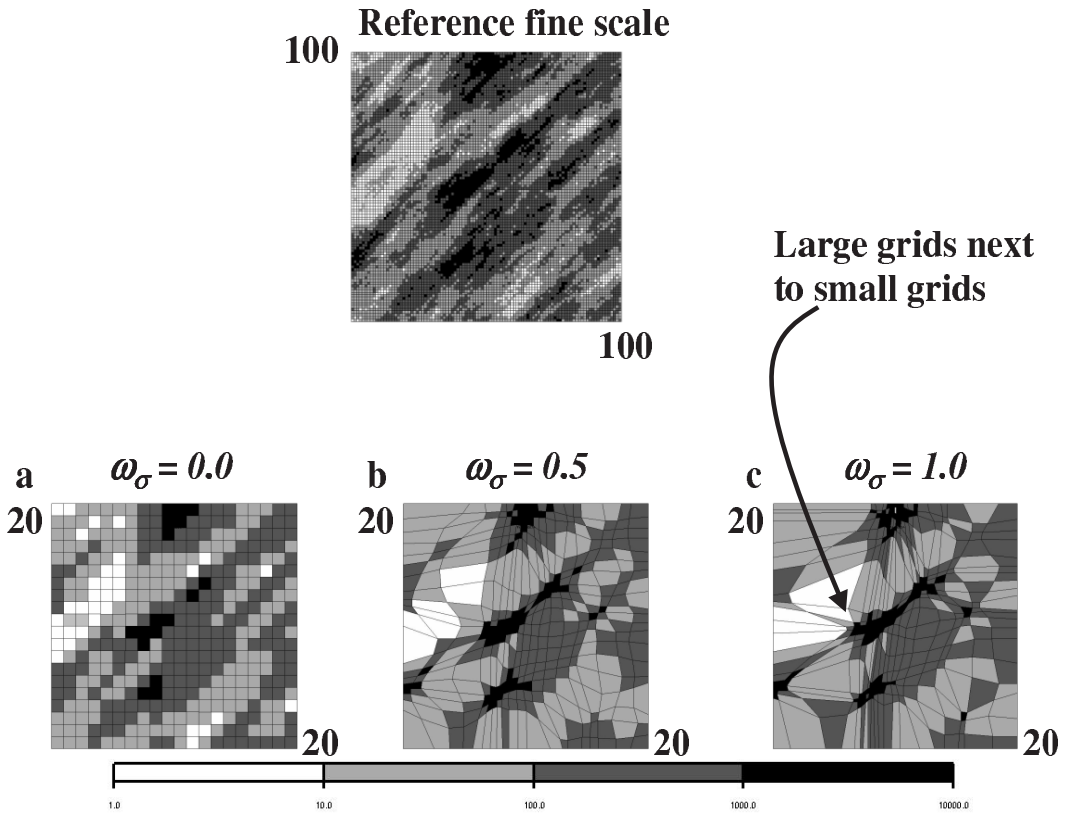

Figure C.4: The reference high resolution model with results of 3D-DEGA gridding for three values of ω_σ, (a) ω_σ=0.0, (b) ω_σ=0.5 and (c) ω_σ=1.0.

In order to understand the effect of the block coefficient of heterogeneity and the parameter ω_σ on the gridding, a sensitivity is performed on a 2D case given in Figure-C.4. The top image is the high resolution continuous permeability map. The permeability in the high resolution model is given on a 100×100 field with a log-normally distributed permeability within a range of 1md and 10000md. In the bottom row, three cases are presented upscaled to a 20×20 grid where (a) ω_σ=0.0, (b) ω_σ=0.5 and (c) ω_σ=1.0. Setting ω_σ=0 results in uniform gridding, since ω_σ=0 sets the block coefficient of heterogeneity to the same constant for every grid block, in other words all blocks are considered equally heterogeneous. Increasing the ω_σ parameter results in an increase in the range of block

coefficients of heterogeneity between various blocks. As a result the grids become more and more deformed in order to better fit the underlying heterogeneity. The ω_σ power can be used to have control on the magnitude of such deformation. This parameter may become useful in the following situation. In cases of highly heterogeneous fields with very large outlier values, the coarsened grid-blocks (containing these fine scale outlier values) would tend to have large values of coefficients of heterogeneity. Hence the resulting grid would refine near isolated possibly disconnected extremes. This can be prevented by decreasing the ω_σ value.

C.2.3 Delivering Flowable Grids

It is favorable in many cases to refine around high or low connected extreme permeability values. These regions most of the time dominate the flow behavior. However, refining high or low permeability in too great detail may result in a grid consisting of small grid blocks next to large grid blocks. This is not favorable in terms of flow simulation, potentially leading to instabilities in the numerical schemes used by flow simulators. An example is shown in Figure-C.4c. Setting the ω_σ value high results in over-refining around high permeability regions, resulting in blocks of considerable volume difference adjacent to each other.

The coefficient of heterogeneity concept needs to be extended for 3D-DEGA to deliver "flowable" grids (putting constraints on the difference of adjacent grid block volumes). For this purpose, the definition of coefficient of heterogeneity is changed as follows:

$$\beta_B = \left(\frac{\sigma_B}{\sigma_{max}}\right)^{\omega_\sigma} \left(\frac{V_B}{V_{norm}}\right)^{\omega_V} \tag{C.10}$$

where β_B is the coefficient of heterogeneity from coarsened grid block *B*, ω_V is a power assigned to the block volume term and V_{norm} is such that;

$$V_{norm}^{\omega_V} = max(V_{min}^{\omega_V}, V_{max}^{\omega_V}) \tag{C.11}$$

Figure-C.5 illustrates the sensitivity of the ω_V parameter on the gridding. Figure-C.5a, C.5b and C.5c give the 3D-DEGA results for ω_V values of -0.5, 0.5 and 2.0 respectively. All examples were obtained by setting the ω_σ value to a constant of 1.

The ω_V parameter can take both positive and negative values. Taking positive values for

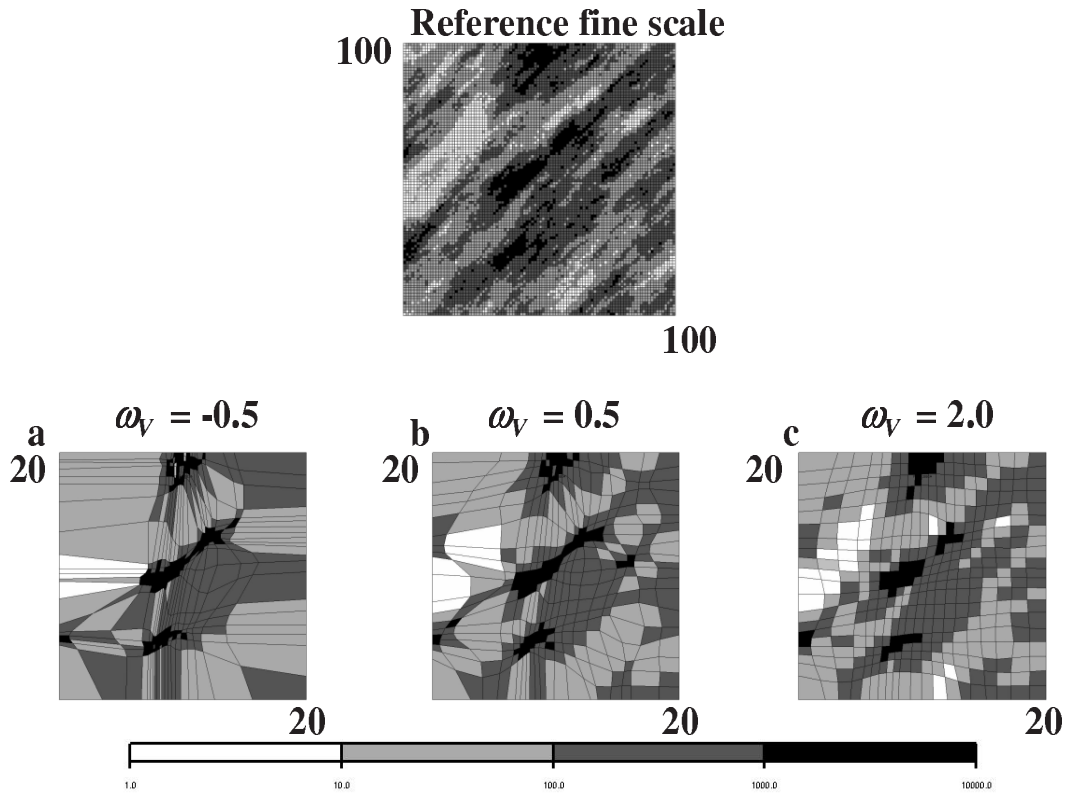

Figure C.5: The reference high resolution model with results of 3D-DEGA gridding for three values of ω_V, (a) ω_σ=-0.5, (b) ω_σ=0.5 and (c) ω_σ=2.0.

this parameter results in a smoothing effect, where large differences in coarsened grid block volumes are not allowed (see Figure-C.5c). Taking negative values results in a roughening effect where in this case, large differences in grid block volumes are allowed (see Figure-C.5a). Taking values very close to zero (either positive or negative), will ignore any effect of coarsened grid block volumes on the gridding. The choice of the ω_V parameter depends highly on the objective of the gridding application.

In many cases it might be necessary to adapt the coarsened grid to multiple fine scale heterogeneities (for example it might be necessary to adapt gridding both to permeability, porosity and the velocity field of fluid particles). For this purpose, the coefficient of heterogeneity may be extended to allow gridding based on multiple properties. In this case the coefficient of heterogeneity takes the following form:

$$\beta_B = \frac{1}{\prod_{i=1}^{N_d=1}(1+\mu_i)-1}\left[\prod_{i=1}^{N_d=1}\left(1+\mu_i\left(\frac{\sigma_B^i}{\sigma_{max}^i}\right)^{\omega_{\sigma i}}\right)-1\right]\left(\frac{V_B}{V_{norm}}\right)^{\omega_V} \tag{C.12}$$

- i = 1,$\cdots$,N_d, refers to the input variables (high resolution model input variables that are within the limits of the coarsened grid block boundaries) where N_d is the total number of variables (such as porosity, permeability, etc.),

- μ_i is a weight assigned to data variable i,

C.2.4 The 3D-DEGA algorithm

The 3D-DEGA algorithm has been explained in the previous sections, through the flow chart in Figure-C.3. As mentioned in Section-C.2.1 the initial and final adjusted grids have the same dimensions (same number of grid blocks). In the actual implementation, 3D-DEGA starts from a much coarser grid, then gradually refines the grid to the desired coarsened grid dimension. This approach is termed ”grid refinement” and needs further elaboration.

The main idea behind the grid refinement approach is to start with an initial set of very coarsened grid blocks. After a first adjustment step, the optimal coarsened grid, established through grid adjustment, is further refined and further grid adjustment applied. This is done until the desired target number of grid blocks are obtained.

To obtain a better understanding of the grid refinement approach, a 2D example is provided in Figure-C.6. In this example, it is assumed that there is an underlying high resolution model with dimensions 100×100. The desired number of coarsened grids is set to 4×4. This example is used to explain the grid refinement approach, hence for simplicity only orthogonal elastic grids are considered. Figure-C.6a represents the initial coarsened grid dimensions taken to be 2×2. The first step in the grid refinement process is to calculate the average block coefficients of heterogeneity for all rows and for all columns. In Figure-C.6 the average block coefficients of heterogeneity for the rows are represented by $\overline{\beta}_r$ and for the columns by $\overline{\beta}_c$.

The next step requires the user to set a limit for the maximum number of grid lines (grid layers or columns) to be added to the existing grid in both directions for the refinement

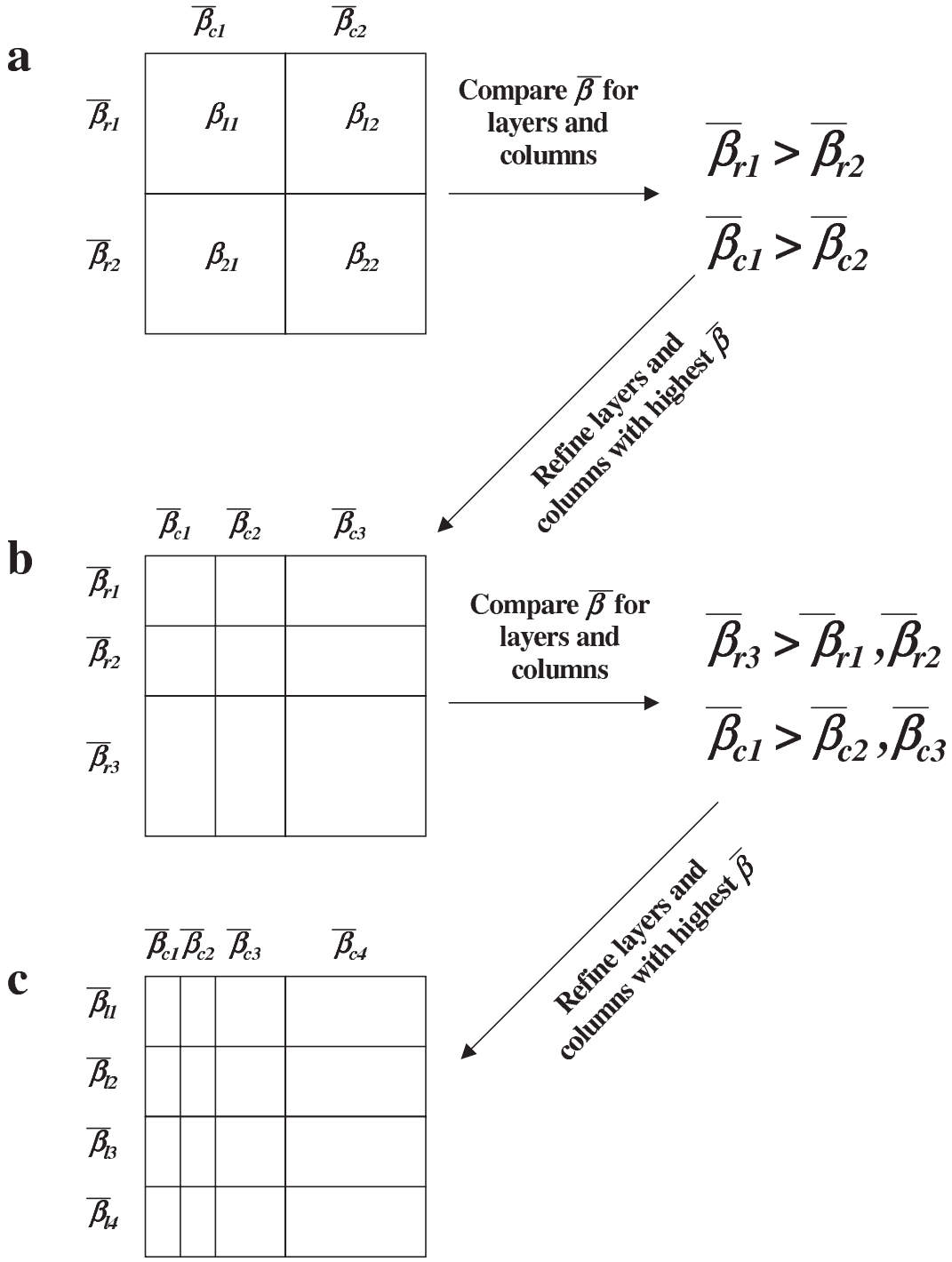

Figure C.6: Example illustrating the fundamental steps of the grid refinement approach, (a)2×2, (b)3×3, (c)4×4.

step. These limits will be denoted by di$_{max}$ (determines how many columns can be added to the existing gridding) and dj$_{max}$ (determines how many rows can be added to the existing gridding). In the current example these limits are set as di$_{max}$=1 and dj$_{max}$=1. Hence at each grid refinement step one generates one additional grid line in both directions.

Given these limits, the average block coefficients of heterogeneity are compared (rows and columns independently). The average block coefficient of heterogeneities are determined in the following two ways (using the notation given in Figure-C.6). The average block coefficient of heterogeneity for the rows are determined by:

$$\overline{\beta}_{ri} = \sum_{j=1}^{n_j} \beta_{ij} \quad (\forall i = 1, ..., n_i) \tag{C.13}$$

The average block coefficient of heterogeneity for the columns are determined by:

$$\overline{\beta}_{cj} = \sum_{i=1}^{n_i} \beta_{ij} \quad (\forall j = 1, ..., n_j) \tag{C.14}$$

where n_i is the total number of grid blocks along a row, n_j is the total number of grid blocks along a column, $\overline{\beta}_{ri}$ is the average block coefficient of heterogeneity for the rows, $\overline{\beta}_{ci}$ is the average coefficient of heterogeneity for the columns and β_{ij} is the coefficient of heterogeneity of each individual coarsened grid block *ij*. The row and column with the highest average block coefficient of heterogeneity is refined. In this case since $\beta_{r1} > \beta_{r1}$, row-1 is refined in the next step. Similarly, since $\beta_{c1} > \beta_{c2}$, column-1 is refined in the next step of the refinement process. These steps are shown in Figure-C.6b. If the limits had been greater or equal to the current grid dimensions (in this case if di$_{max} \geq 2$ or dj$_{max} \geq 2$) then all grid layers and columns would have been refined.

The same steps are repeated on Figure-C.6b to obtain Figure-C.6c. Now row-3 and column-1 are refined in Figure-C.6b since they have the highest average block coefficient of heterogeneity.

The flowchart for the grid refinement approach is given in Figure-C.7. The flowchart is explained in the following way:

1. Set the maximum number of additional grid blocks to be generated in each direction during each step of the grid refinement procedure. These limits will be denoted by di$_{max}$, dj$_{max}$ and dk$_{max}$,

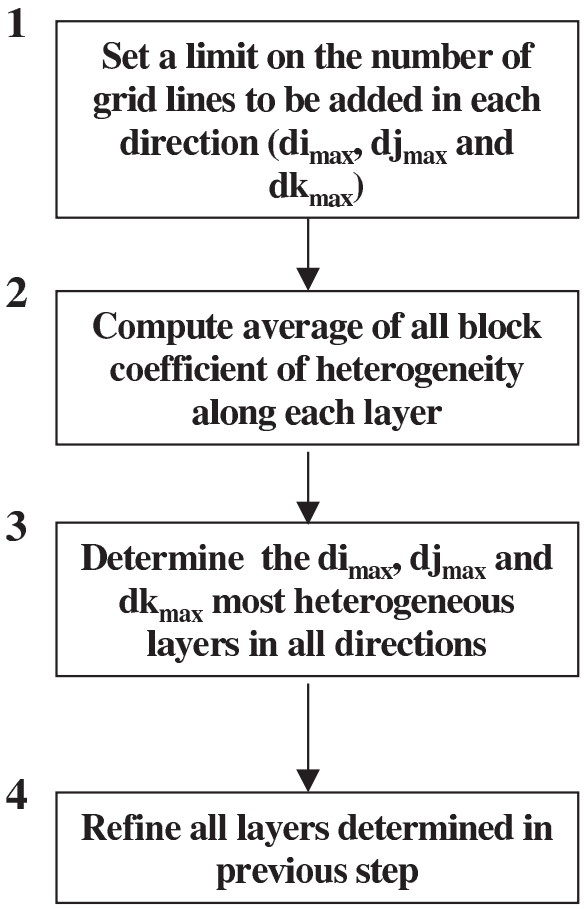

Figure C.7: The flowchart of the grid refinement procedure.

Until desired coarsened grid dimensions nx_c, ny_c and nz_c are reached:

(a) Compute the average block coefficient of heterogeneity for each layer in the i, j and k directions,

(b) Determine the di_{max}, dj_{max} and dk_{max} most heterogeneous layers (based on the block coefficient of heterogeneity) in all directions and refine these layers by adding additional grid lines. If the present number of layers is less then the numbers di_{max}, dj_{max} and dk_{max}, then all layers are refined.

(c) Initialize the coefficients of elasticity of new grid edges belonging to block layers inserted.

Putting it all together, the 3D-DEGA software uses the overall approach given in Figure-C.8. Two loops are now considered. The outer loop is performed for the grid refinement process. Within each outer loop, an inner loop of grid adjustment is present.

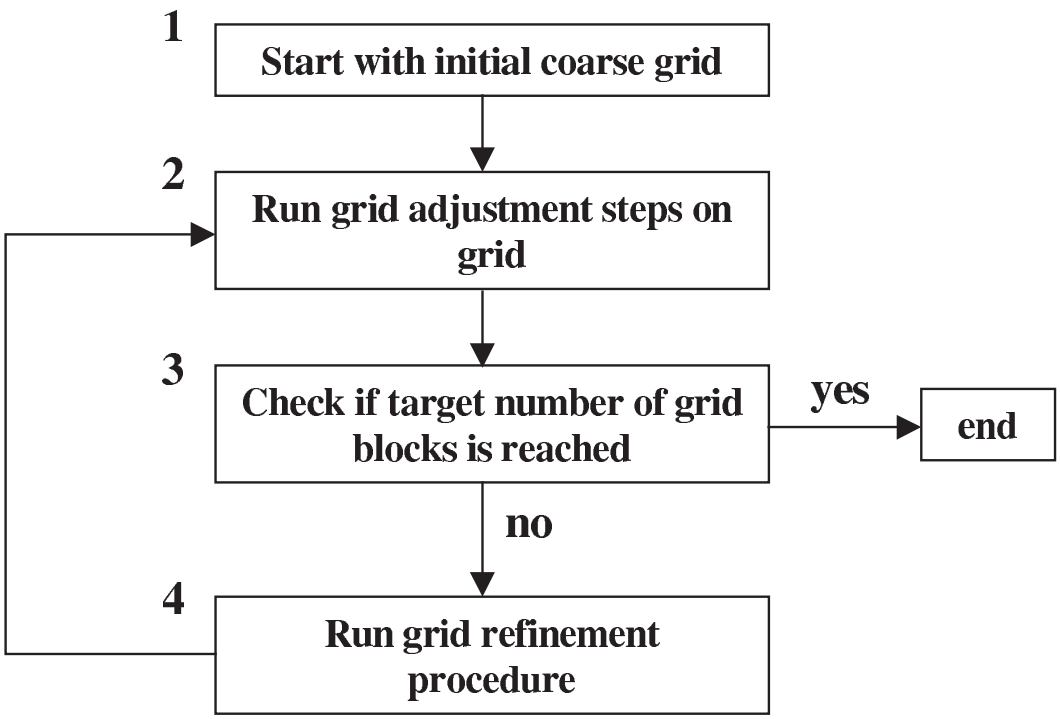

Figure C.8: The overall flow chart for the 3D-DEGA software.

1. In box-1 of Figure-C.8 the algorithm starts with very coarsened initial grids if the use of the grid refinement procedure is intended. However this is optional, the initial grids can be provided with the same dimensions of the desired target grids. In this case the grid refinement procedure will not be used.

2. In box-2 of Figure-C.8 the grid adjustment procedure is performed on the grids. This procedure has been explained in detail in Figure-C.3.

3. In box-3 of Figure-C.8 the current dimensions of the grids are checked. If the target dimensions are reached, then the program stops. If not the next item is performed.

4. In box-4 of Figure-C.8 the grid refinement procedure is performed in order to further

refine the grids for better fitting the underlying heterogeneities. This procedure is explained in detail in Figure-C.7.

5. Finally the program repeats the above steps from box-2 of Figure-C.8 until the target grid dimensions are reached.

As a final remark it is also important to note that although the horizontal coarsened grid lines are allowed to deviate from orthogonality, the 3D-DEGA software is designed to generate straight vertical lines (z-lines).

C.3 Using 3D-DEGA

This section focuses on the practical application of the 3D-DEGA software. First, a detailed description of the parameters are given. Then example cases are presented along with some general suggestions based on experience gained in running the code.

C.3.1 Running the 3D-DEGA Software

In order to run the 3D-DEGA software, five types of files are required, where two of these files are however optional. The three required files are as follows:

- a grid file,
- a data file,
- a data-grid file(s)

The optional files are:

- a project file,
- an initial-grid file

Once the program is run, if the project file does not exist, the program will create a project file with the default name *dega.pro*. The program is accessed by running the executable in the following way: **3ddega** *[project file name]*, where either the 3ddega executable needs to be in the same directory or a path needs to be set to the directory which the executable exists. Each file is described next.

C.3.2 Description of the project file

This file provides the names of the data and grid files. Hence the file contains three names as follows:

grid file name

data file name

initial grid file (optional) name

If the project file is not given, then 3D-DEGA prompts the user for these file names and generates a project file *dega.pro* with the file names provided by the user.

C.3.3 Description of parameters in the grid file

This file provides most of the parameters related to elastic gridding. The file has the following format and parameters:

- I_0 J_0 K_0
- nbds
- nx_c ny_c nz_c
- DI DJ DK
- maxnbas
- N_d
- z_1, z_2,. . ., z_{N_d}
- maxangle
- cexyratio
- cezratio
- vpower

- npx1 npx2 npy1 npy2 npz1 npz2
- xsmooth ysmooth zsmooth

These parameters are explained as follows:

1. I_0, J_0, K_0 are the dimensions of the initial grid. They are taken into account when no initial grid file is input. These dimensions can be equal to the target number of grid blocks, where in such a case the refinement approach would not be used. These dimensions can also be coarser then the target dimensions where in this case the grid refinement approach would be used. The concept of initial grids have been discussed in Section-C.2.4.
2. *nbds* is the number of overall steps. This parameter should be set to one.
3. nx_c, ny_c, nz_c are the desired grid dimensions.
4. *DI, DJ, DK* are the maximum grid dimension increases allowed in a same refinement process (as explained in section-C.2.4).
5. *maxnbas* is the maximum number of iterative steps (for grid adjustment) with the same grid dimensions (flowchart explained in Figure-C.3).
6. N_d is the number of data variables involved for the adjustment step. The default maximum number of data variables is set to 10.
7. $z_1(\mathbf{u}), z_2(\mathbf{u}), \ldots, z_{N_d}(\mathbf{u})$ is the list of data variables. They are labelled with numbers ($\geq$1) corresponding to their rank in the data file (the structure of the data file is explained in the next section).
8. *maxangle* is the maximum z-line (vertical grid-line) tilt angle **given in degrees** (although the 3D-DEGA software is designed to generate straight z-lines, they are allowed to be all tilted in the same direction).
9. *cexyratio* is the maximum elasticity coefficient ratio for x and y edges. This coefficient is yet another control on the coarsened grid block volumes. It is the maximum allowable ratio of the coefficient of elasticity for two successive grid edges in the

same direction both for the x and y. In the case where the actual ratio is higher then this number, then the smaller coefficient of elasticity is set to the highest one divided by *cexyratio*

10. *cezratio* is the maximum elasticity coefficient ratio for z edges. The concept is the same as in *cexratio*.

11. *vpower* (ω_V) is the power value to be applied to block volume terms in the computation of block weights (coefficients of heterogeneity).

12. *npx1, npx2, npy1, npy2, npz1, npz2* are flags that must be set to 1 to account for non-pay data nodes in the corresponding grid direction(s), or 0 otherwise.

13. *xsmooth, ysmooth, zsmooth* are coefficients to control the grid line smoothing along the x, y and z directions, respectively. Coefficients must be greater than or equal to 0. The higher a coefficient, the smoother the grid-lines in the corresponding direction. Examples on using these parameters are also given in the following sections.

C.3.4 Description of the data files, data-grid files and their corresponding parameters

Two data files are required in the data files section. The first file (the *data file*) is used for entering information regarding the high resolution model properties as well as the name of the high resolution model data file (*data-grid file*). The data-grid file is the file where the high resolution model properties are given. The data-file has the following format and parameters:

- N_d
- datatype
- nx ny nz
- x0 y0 z0
- dbx dby dbz

- data-grid file[1]
- vartype[1] varweight[1] varpower[1] varobjvar[1]
- data-grid file[2]
- vartype[2] varweight[2] varpower[2] varobjvar[2]
- . . . . . .
- data-grid file[nbvar]
- vartype[nbvar] varweight[nbvar] varpower[nbvar] varobjvar[nbvar]

The parameters are explained as follows:

1. *nbvar* is the number of data variables.
2. *datatype* is a character string specifying the type of data-grid file(s) to be read. The possible string values are:
   - FSSI,
   - MORE,
   - IRAP,
   - ECL,
   - GSLIB,
   - and HERESIM,
3. *nx*, *ny* and *nz* are the data-grid's dimensions (high resolution model grid dimensions). Correct dimension values are required when the data-grid file type involved is not supposed to provide them (e.g., GSLIB and HERESIM file-types). Otherwise, any values can be given, those being useless.
4. *x0*, *y0* and *z0* are the coordinates of the data grids origin point.
5. *dbx*, *dby* and *dbz* are the high resolution model grid block sizes.

6. For each data variable *i* (*i*=1,2,...,nbvar)

   - *datagridfile*[i] is the name of the data grid file where node values can be found (note that when all data-variable node values are included into a same file, the file name must be declared for each variable),
   - *vartype*[i] is the type (1 for categorical variable, 2 or any other value for continuous variables),
   - *varweight*[i] is the weight,
   - *varpower*[i] ω_σ is the power of the variance term in the block coefficient of heterogeneity,
   - *varobjvar*[i] is the minimum (objective) variance (i.e., threshold value under which blocks are considered homogeneous).

C.3.5 A sensitivity study on various input parameters

This section presents a sensitivity study on various parameters that impact the resulting gridding most. A 2D channel-shale binary field with dimensions of 100×100 on the high resolution model is shown in Figure-C.9. The channel permeability in this case is taken as 10000md and the shale permeability is taken as 100md.

The first sensitivity study is performed on the block orthogonality coefficients *xsmooth*, *ysmooth* and *zsmooth*. This is accomplished by varying only the block orthogonality coefficient in the x direction and keeping all other parameters the same. The results are given in Figure-C.10. In this example four values of the block orthogonality coefficient are used (0.0, 0.1, 1.0 and 10.0). Using a value of 0.0 for this coefficient provides a coarsened grid that is maximally deformed. As this coefficient is increased, grid flexibility is reduced resulting in smoother grid lines in the x direction (see Figure-C.10).

The next sensitivity study is performed on the maximum elasticity coefficient ratios *cexratio*. The maximum elasticity ratio sets a limit on elasticity coefficients of two successive grid edges (for example grid edge 52 and grid edge 23 in Figure-C.2) in either the x or the y directions. This parameter provides another control on the grid conformity. The maximum elasticity coefficient ratios are used to perform a correction of the edge coefficients of elasticity. During gridding, if the ratio of any elasticity coefficient of two successive edges

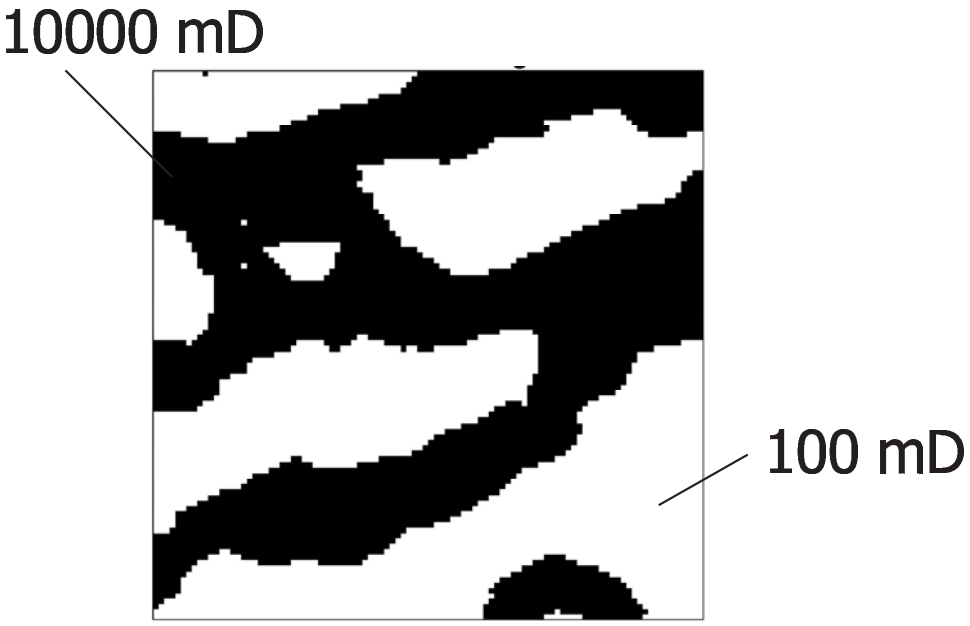

Figure C.9: The reference high resolution model permeability field to be used on the sensitivities of various 3D-DEGA parameters.

lying on a same grid line exceeds this limit (the maximum elasticity coefficient ratio), the smallest coefficient of elasticity is set to the highest one divided by this limit value. The sensitivity study regarding this parameter is given in Figure-C.11. The parameters in this case take the values of 1.0, 2.0 and 5.0. The case where the elasticity ratio is 1.0 causes all the elasticity coefficients of the adjacent edges to be equal to each other. This results in uniform gridding. When this parameter is increased, the grid edges have increasingly different elasticity coefficients, hence the grid is allowed to be deformed further.

Finally a 3D example shows that 3DDEGA works for 3D reservoir heterogeneity. The high resolution model for this example has dimensions of $51\times51\times20$. This model is illustrated in Figure-C.12a. Figure-C.12b illustrates the channel structure of the overall field. The permeability field and the channel structure of the upgridded model (with dimensions of $20\times20\times10$) provided by 3D-DEGA is illustrated in Figures C.13a and C.13b. This example clearly illustrates the efficiency of the 3D-DEGA software especially in preserving the overall channel structures of the high resolution model on the coarsened scale.

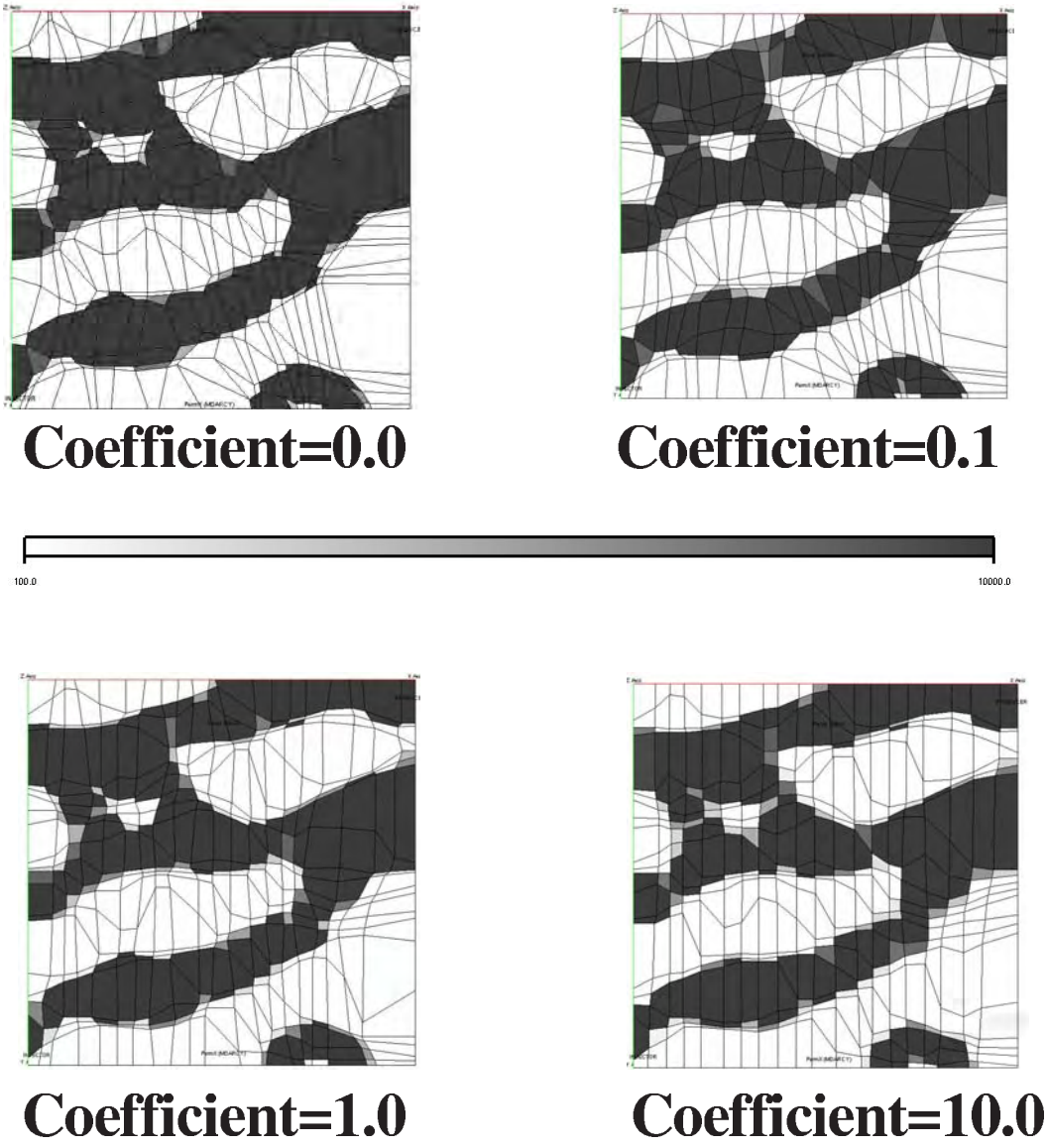

Figure C.10: Sensitivity results regarding the block orthogonality coefficient (all coarsened models are given with 20×20 grid dimensions).

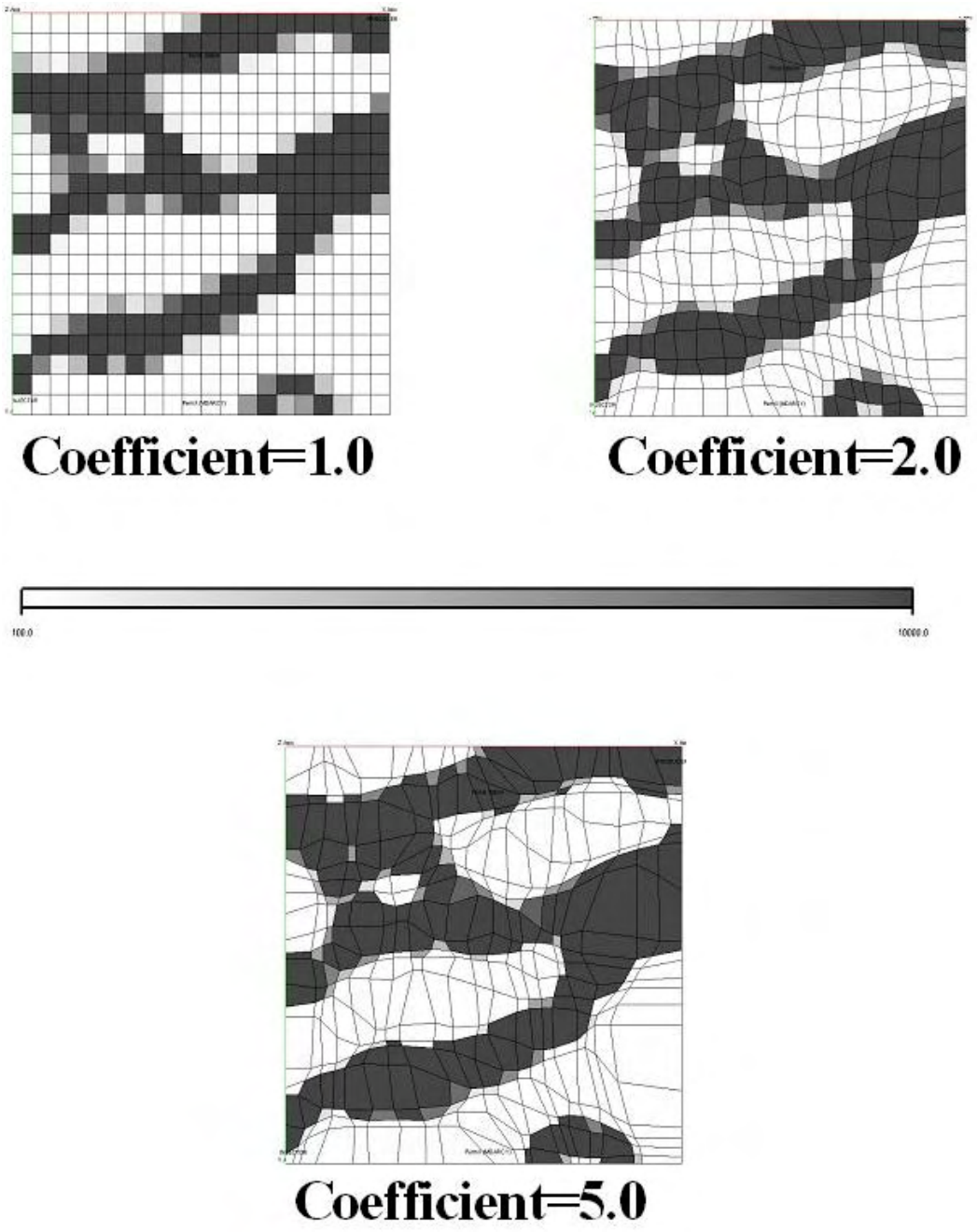

Figure C.11: Sensitivity results regarding the x-y elasticity ratio (all coarsened models are given with 20×20 grid dimensions).

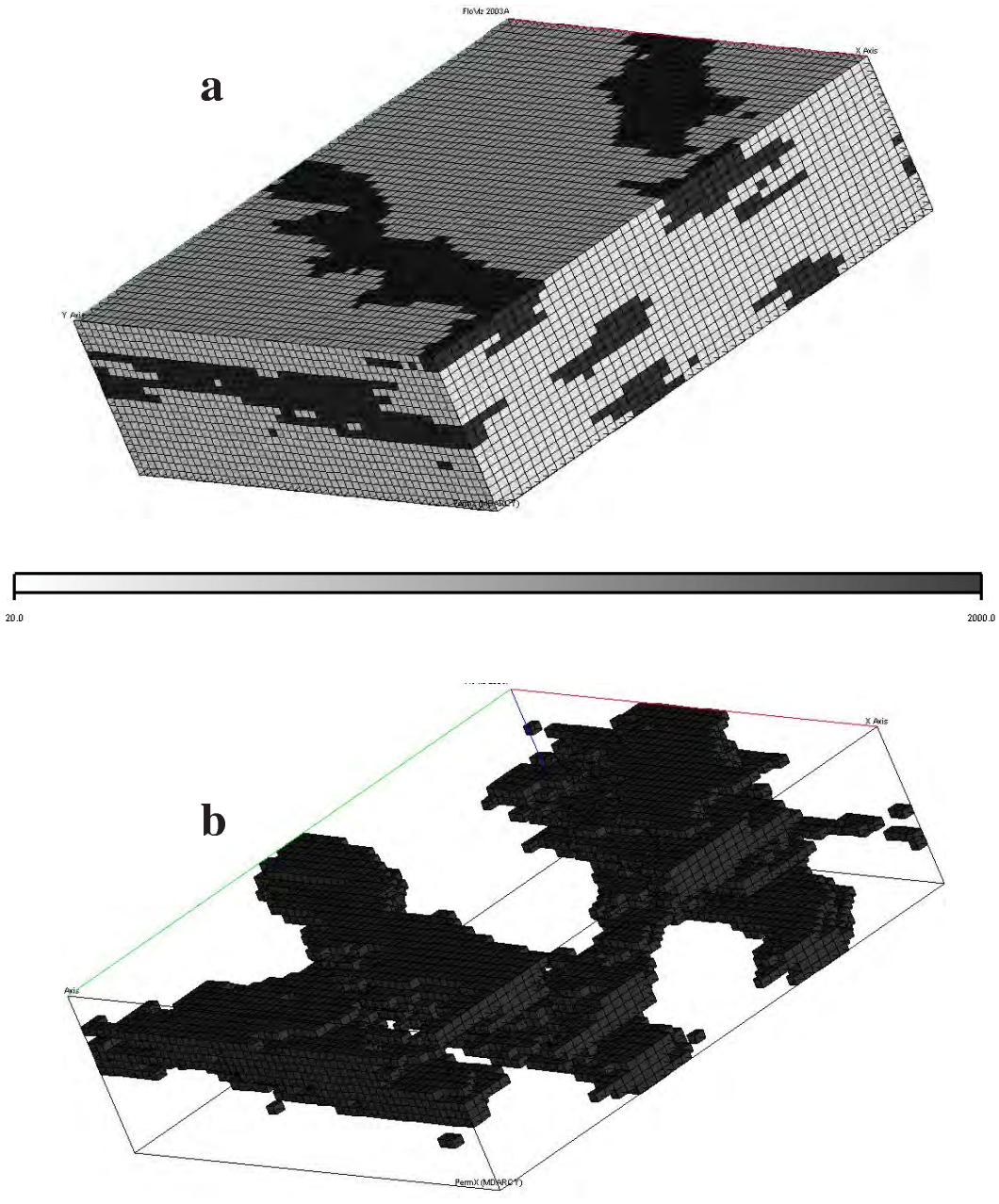

h

Figure C.12: The high resolution model for the 3D example (a) permeability map, (b) channel structure only.

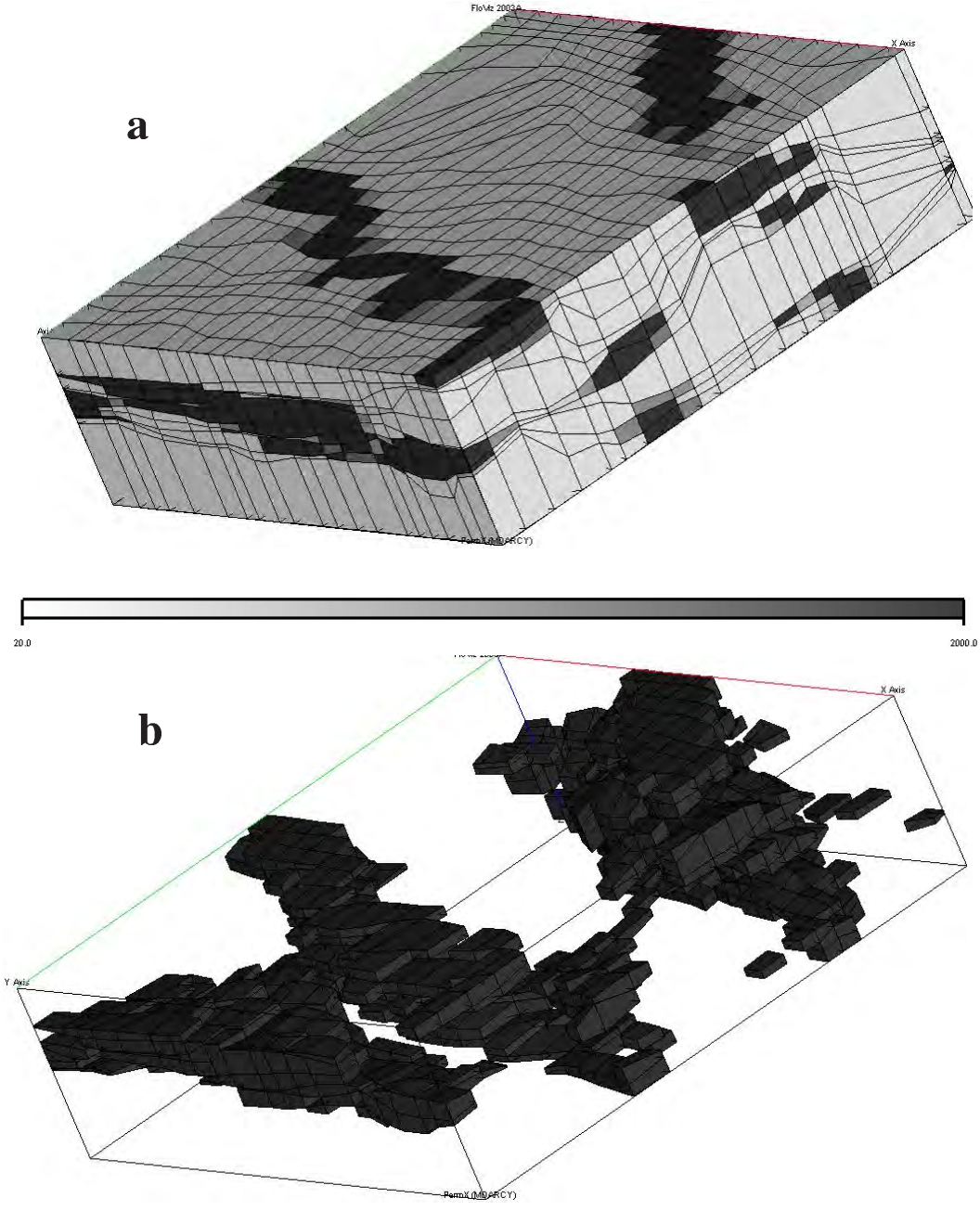

h

Figure C.13: 3D-DEGA gridding for the 3D case (a) permeability field, (b) channel structure.

C.4 Example Parameter Files of the 3D-DEGA Software

In this section we provide the parameter files for the various cases presented in the previous section.

C.4.1 Parameter files of examples given in Figures C.10 and C.11

- *data.int* file

% Number of variables (N_d)
1
% File Type (datatype)
GSLIB
% High resolution model grid dimensions (nx, ny, nz)
100 100 1
% Grid Origin (x0, y0, z0)
0 2000 -8825
% High resolution model grid block dimensions (dbx, dby, dbz)
20 20 200
%name of the data file (data-grid-file)
realization.out
%Type (vartype), Weight (varweight), Power (varpower), Minimum Variance (varobjvar)
2 1.0 0.1 0.0

- *grid.int* file

% Initial Grid Dimensions (I_0, J_0, K_0)
2 2 1
% Number of overall steps (nbds)
1
% final grid dimensions (n_{x_c}, n_{y_c}, n_{z_c})
20 20 1
% Maximum grid refinement in one step (DI, DJ, DK)
4 4 0
% Number of iterative steps (maxnbas)
100
% Number of variables considered (N_d)
1
% Variable number
1
% Maximum tilt angle (maxangle)
40.0
% Maximum xy elasticity coefficient ratio (cexyratio)
20.0
% Maximum z elasticity coefficient ratio
1000.00
%Volume power (ω_V)
0.1
% npx1, npx2, npy1, npy2, npz1, npz2
0 0 0 0 0 0
% xsmooth, ysmooth, zsmooth
0 0 0.1

C.4.2 Parameter files of examples given in Figure-C.13

- *data.int* file

% Number of variables (N_d)
1
% File Type (datatype)
GSLIB
% High resolution model grid dimensions (nx, ny, nz)
51 51 20
% Grid Origin (x0, y0, z0)
0 2040 -8525
% High resolution model grid block dimensions (dbx, dby, dbz)
40 40 10
%name of the data file (data-grid-file)
realization.out
%Type (vartype), Weight (varweight), Power (varpower), Minimum Variance (varobjvar)
2 1.0 0.5 0.0

- *grid.int* file

% Initial Grid Dimensions (I_0, J_0, K_0)
2 2 2
% Number of overall steps (nbds)
1
% final grid dimensions (n_{x_c}, n_{y_c}, n_{z_c})
20 20 10
% Maximum grid refinement in one step (DI, DJ, DK)
6 6 6
% Number of iterative steps (maxnbas)
100
% Number of variables considered (N_d)
1
% Variable number
1
% Maximum tilt angle (maxangle)
0.0
% Maximum xy elasticity coefficient ratio (cexyratio)
20.0
% Maximum z elasticity coefficient ratio
20.00
%Volume power (ω_V)
-0.1
% npx1, npx2, npy1, npy2, npz1, npz2
0 0 0 0 0 0
% xsmooth, ysmooth, zsmooth
0 0 0